UNIVERSITY OF SOUTHAMPTON

FACULTY OF ENGINEERING, SCIENCE AND MATHEMATICS

Institute of Sound and Vibration Research

Theoretical Modelling of Railway Curve Squeal

by

Zhenyu Huang

Thesis submitted for the degree of Doctor of Philosophy

September 2007

UNIVERSITY OF SOUTHAMPTON

ABSTRACT

FACULTY OF ENGINEERING, SCIENCE AND MATHEMATICS
INSTITUTE OF SOUND AND VIBRATION RESEARCH

DOCTOR OF PHILOSOPHY

THEORETICAL MODELLING OF RAILWAY CURVE SQUEAL

by Zhenyu Huang

Railway curve squeal is an environmental noise problem occurring occasionally when a vehicle is negotiating a sharp curve. A theoretical study is carried out to develop a complete model, which can predict curve squeal and may provide useful approaches to control it.

The curve squeal results from a kind of self-excited vibration existing in the wheel/rail contact system, mainly due to the falling friction coefficient when sliding occurs between the wheel and rail surfaces. The central work of this thesis is to build a self-excited feedback loop model, representing relations between the wheel/rail motions and the contact forces. The stability analysis of this loop can predict the possibility of squeal, while the time-domain integration of the loop can provide the intensity of squeal. To implement this loop model in a general way, all the possible degrees of freedom involved in the wheel/rail contact are considered. A non-linear friction model is established, considering the adhering friction at small creepages and falling friction in sliding. The parametric study of the wheel/rail squeal model shows that the most important parameters involved in the squeal are the steady-state creepages, dynamic properties of the wheel, and the friction characteristic. Some of these parameters are related to the steady-state curving behaviour. To calculate this, a dedicated steady-state curving program has been developed and validated using a commercial vehicle dynamic package.

A twin-disc rig, with a wheel disc rolling on a rail disc, was used to investigate the squeal phenomenon and validate the wheel/rail squeal model. With this rig, the lateral forces acting on the discs due to varying amounts of lateral creepage can be measured in a controlled environment, as well as the acoustic and vibration responses of the discs. According to the experimental results, the falling friction in sliding is closely related to the self-excited vibration and hence the occurrence of squeal. The experimental results also show that squeal can be controlled using friction modification, e.g. lubricating contact surfaces. By using the measured friction curves and adjusted modal parameters of the discs, the unstable vibration and squeal radiation can be predicted.

In order to apply the model to predict the occurrence of curve squeal, the curving behaviour of a typical UK passenger vehicle on various tight curves is calculated using the steady-state curving program. The curve squeal prediction is applied for all four wheel/rail contacts in a bogie. The results show that squeal is prone to occur at the leading wheels of a bogie, mainly due to the large lateral steady-state creepage. The leading outer wheel in flange contact has less possibility for squeal than the leading inner one. The trailing wheels are unlikely to squeal. Both a wheel damping treatment and friction modification can be used to control the squeal, but will not always be effective.

DECLARATION OF AUTHORSHIP

I, Zhenyu Huang, declare that the thesis entitled THEORETICAL MODELLING OF RAILWAY CURVE SQUEAL and the work presented in it are my own. I confirm that:

- this work was done wholly while in candidature for a research degree at this University;
- no part of this thesis has previously been submitted for a degree or any other qualification at this University or any other institution;
- where I have consulted the published work of others, this is always clearly attributed;
- where I have quoted from the work of others, the source is always given. With the exception of such quotations, this thesis is entirely my own work;
- I have acknowledged all main sources of help;
- where the thesis is based on work done by myself jointly with others, I have made clear exactly what was done by others and what I have contributed myself;
- parts of this work have been published as:

- Hsu, S.S., Huang, Z.Y., Iwnicki, S.D., Thompson, D.J., Jones, C.J.C., Xie, G. and Allen, P.D., Experimental and theoretical investigation of railway wheel squeal. *Proceedings of the Institution of Mechanical Engineers*, 221 Part F, 59-73, 2007.
- Huang, Z.Y., Thompson, D.J. and Jones, C.J.C., Squeal prediction for a bogied vehicle in a curve. *Ninth International Workshop on Railway Noise and Vibration*, Munich, Germany, 2007.
- Huang, Z.Y., Thompson, D.J. and Jones, C.J.C., A general model for wheel/rail curve squeal. *Ninth International Conference on Recent Advances in Structural Dynamics*, Southampton, UK, 2006.
- Xie, G., Allen, P.D., Iwnichi, S.D., Alonso, A., Thompson, D.J., Jones, C.J.C. and Huang, Z.Y., The introduction of falling coefficients into curving calculations for studying curve squeal noise. *IAVSD*, Milan, Italy, 2005.

Signed: .

Date: .

ACKNOWLEDGEMENTS

I would like to gratefully acknowledge the enthusiastic supervision of David Thompson and Chris Jones during this work. It was a pleasure to work with them.

I would like to thank the members of my internal review panel, Simon Iwnicki and Tim Waters. I have benefited much from their helpful comments.

This project was funded by Rail Research UK and involved cooperation with Rail Technology Unit, Manchester Metropolitan University. Thanks are due also to my colleagues in Manchester Metropolitan University, in particular, the help from Sin-Sin Hsu for experiments and the work of Gang Xie for the validation of my vehicle dynamic program.

I cannot forget Tian-Xing Wu who recommended me to study in ISVR. Many thanks to him. I also acknowledge the generous financial support from ISVR.

Finally, I am forever indebted to my parents for their understanding and encouragement when they were most required.

CONTENTS

LIST OF FIGURES

LIST OF TABLES

ABBREVIATIONS

DOF	Degree(s) of freedom
FE	Finite element
FFT	Fast Fourier transform
FRF	Frequency response function
MDOF	Multi-degrees of freedom
MIMO	Multiple-input, multiple-output (system)
MMU	Manchester Metropolitan University
PSD	Power spectral density
SDOF	Single degree of freedom
SISO	Single-input, single-output (system)
SPL	Sound pressure level
TFM	Transfer function matrix

SYMBOLS

a, b	Semi-axes of the Hertz contact ellipse along the rolling and transverse directions.
a_c	Centripetal acceleration required on the curve.
a_g	Centripetal acceleration provided by the gravity.
a_k, b_k	Coefficients of the denominator and numerator in a transfer system.
A, B	Parameters in the function of separation between two contact surfaces, (Appendix B).
A_1	Amplitude of the oscillation in the mass-on-moving-belt system.
$[\mathbf{A}_\mathrm{v}]$	Inertia matrix of the vehicle.
$[\mathbf{A}^\mathrm{r}]$	State matrix of the rail equivalent system.
$[\mathbf{A}^\mathrm{w}]$	State matrix of the wheel system.
$[\mathbf{A}_\mathrm{c}^\mathrm{w}]$	System matrix of the simplified self-excited vibration loop.
$[\mathbf{B}_\mathrm{v}]$	Damping matrix of the vehicle.
$[\mathbf{B}^\mathrm{r}]$	Input matrix of the rail equivalent system.
$[\mathbf{B}^\mathrm{w}]$	Input matrix of the wheel system.
$[\mathbf{B}_1^\mathrm{w}]$	Input matrix of the simplified self-excited vibration loop.
c	Half distance between the centre lines of two bogies in a vehicle; parameter representing the size of contact ellipse, (Appendix B).
c_0	Speed of sound in air, (Appendix G).
c_1	Damper in the mass-on-moving-belt system.
c_c	Maximum value of the control damping in the mass-on-moving-belt system.
c_e	Equivalent damping coefficient of the friction force.
c_i	Modal damping of mode *i*.
C_{ij}	Kalker constant.
$[\mathbf{C}^\mathrm{r}]$	Output matrix of the rail equivalent system.
$[\mathbf{C}^\mathrm{w}]$	Output matrix of the wheel system
$[\mathbf{C}_1^\mathrm{w}]$	Output matrix of the simplified self-excited vibration loop.
d_1	Distance between the mass centre of bogie and the primary suspensions.
d_2	Distance between the mass centre of bogie and the secondary suspensions.

d_3	Distance between the mass centre of the vehicle body and the secondary suspensions.
D_ϑ	Directivity factor in one spatial direction ϑ, (Appendix G).
DI	Directivity index, (Appendix G).
$[\mathbf{D}_\mathrm{v}]$	Damping matrix of the vehicle.
$[\mathbf{D}^\mathrm{r}]$	Direct output matrix of the rail equivalent system.
e	Eccentricity of the contact ellipse, (Appendix B).
E^*	Composite elastic modulus, (Appendix B).
$\mathbf{E}(e)$	Complete elliptical integral in terms of eccentricity of contact ellipse e, (Appendix B).
f_i, $i=1,2$	Contact surface function of contacting body i, (Appendix B).
f_i, $i=1$ to 6	Dynamic forces (and moments) in the wheel/rail contact system.
f_{itot}, $i=1$ to 6	Total forces (and moments) in the wheel/rail contact system.
f_{i0}, $i=1$ to 6	Steady forces (and moments) in the wheel/rail contact system.
f_s	Rotational frequency of a stationary disc.
f_{ytot}	Total friction force in the mass-on-moving-belt system.
f_y	Dynamic friction force in the mass-on-moving-belt system.
f_{y0}	Steady friction force in the mass-on-moving-belt system.
f_y'	Disturbance of friction force in the mass-on-moving-belt system.
$\{\mathbf{f}^\mathrm{w}\}$	Wheel force vector.
F_1, F_2, F_3	Longitudinal, lateral and vertical forces acting on the rail disc.
F_f	Static friction force.
F_i, $i=1$ to 6	Amplitude of harmonic forces in the wheel/rail contact system.
$\{\mathbf{F}^\mathrm{f}\}$	Vector of friction forces: $\{F_1 \quad F_2 \quad M_3\}$.
$\{\mathbf{F}'\}$	Vector of the disturbing forces.
$g_{1,2}(i,j)$	Rigid components in the surface (sliding) velocities of the element (i,j) in the longitudinal (denoted 1) and lateral (denoted 2) directions, (Appendix C).
G^*	Composite shear modulus of two contacting bodies.
G_i, $i=1,2$	Shear modulus of contact body i.
$[\mathbf{G}]$	Mobility matrix.
h	Half distance between the centre lines of two wheelsets in a bogie; separation

	between the two surfaces (before deformation), (Appendix B).
h_0	Initial length of the contacting body.
$H(s)$	Equivalent system of the rail system.
$[\mathbf{H}_1]$	Matrix of the derivatives of non-dimensional friction forces in the self-excited loop.
$[\mathbf{H}_2]$	Matrix of the fluctuation of normal force in the self-excited loop.
I	Sound intensity, (Appendix G).
$j=\sqrt{-1}$	Imaginary unit.
k_1	Stiffness in the mass-on-moving-belt system.
k_H	Stiffness of the Hertz contact spring.
$\mathbf{K}(e)$	complete elliptical integral in terms of eccentricity of the contact ellipse e, (Appendix B).
$[\mathbf{K}_1]$	Feedback matrix of the simplified loop.
l_0	Half track gauge.
l_1, l_2, l_3	Offset distances of contact points, along the x (1), y (2) and z (3) directions.
L, L_1, L_2, L_3	Flexibilities of the linear springs in Kalker's simplified theory, (Appendix A and Appendix C).
L_W	Sound power level, (Appendix G).
m, n	Intermediate parameters in the calculation of Hertz contact, (Appendix B).
m_1	Mass in the mass-on-moving-belt system.
N	Normal load in the contact area.
N_0	Steady normal load in the contact area.
N_x	Number of elements in a slice of contact ellipse, (Appendix C).
N_y	Number of slices in the contact ellipse, (Appendix C).
p	Normal pressure; sound pressure, (Appendix G).
p_0	Maximum normal pressure, (Appendix B).
$p^s(i,j)$	Normal pressure of element (i, j), provided by Kalker's simplified theory, (Appendix C).
p^*	Yield pressure of material.
P	Normal load.
P_{in}	Power input to the mass-on-moving-belt system from the friction force.
P_s	Power increment of the mass-on-moving-belt system.
q, q_i	Tangential stresses at contact.

$q(\omega)$	Frequency-dependent open-loop gain of a SISO feedback system, (Chapter 5).
$q_i(\omega)$	Frequency-dependent eigenvalues of $\left[\mathbf{Q}(\omega)\right]$, (Chapter 5).
$q_{1,2}(i,j)$	Tractions of an element (*i*, *j*) in the longitudinal (denoted 1) and lateral (denoted 2) directions, (Appendix C).
$q^H_{1,2}(i,j)$	Hypothetical tractions of an element (*i*, *j*) in the longitudinal (denoted 1) and lateral (denoted 2) directions, (Appendix C).
$\left[\mathbf{q}(\omega)\right]$	Diagonal matrix with diagonal terms $\{q_1(\omega), q_2(\omega), \cdots, q_n(\omega)\}$.
Q^s	Resultant saturated tangential force, (Appendix A).
Q^J_1, Q^J_2	Linear tangential forces of Johnson: longitudinal and lateral, (Appendix A).
Q^L_1, Q^L_2, M^L	Linear tangential forces and moment calculated using Kalker's linear theory: longitudinal, lateral and moment about the normal, (Appendix A).
$\left[\mathbf{Q}(\omega)\right]$	Frequency-dependent open-loop TFM of the general squeal loop.
r	Wheel radius; distance from the sound source, (Appendix G).
r_0	Nominal radius of the wheel.
r_l, r_r	Left and right wheel rolling radii.
r_r, r_w	Rolling radii of the rail and wheel discs.
$\{\mathbf{r}\}, \{\mathbf{r}_{i,j}\}$	Vectors of the rail state-space variables, and rail state-space variables of one of equivalent system.
R_0	Curve radius.
R_e	Equivalent relative curvature radius, (Appendix B).
R'_i, R''_i	Principal radii of curvature, (Appendix B).
s	Parameter in the *S* domain.
s, s_1, s_2	Reduced creepages in the Shen-Hedrick-Elkins formula: resultant, longitudinal and lateral, (Appendix A).
s^*	Critical shear strength of the contact junction.
S	Sound radiation surface area of the structure, (Appendix G).
S_i	Roots of the closed-loop of a simplified self-excited vibration loop.
T	Oscillation cycle period.
$[\mathbf{T}_{\mathbf{rot}}]$	Rotation matrix in the rigid transform of structural dynamics.
$[\mathbf{T}_{\mathbf{off}}]$	Offset matrix in the rigid transform of structural dynamics.
$[\mathbf{T}_{\mathbf{tot}}]$	Total transform matrix in the rigid transform of structural dynamics.
u_2	Lateral offset of the wheelset in the reference coordinates.
$\overline{u}_i,\ i = 1,2$	Contact surface displacement of a contact body *i*.

v_0	Wave speed in the disc.
v_s	Sliding velocity.
$v^s_{i,tot}$, $i=1,2,6$	Total sliding velocity.
v^s_{ytot}	Sliding velocity of the mass in the mass-on-moving-belt system.
v^s_{y0}	Steady sliding velocity of the mass in the mass-on-moving-belt system.
v_i^w, v_i^r, v_i^c,	Dynamic velocities of the wheel, rail, contact spring, $i=1\sim6$.
v_i^s, $i=1,2,6$	Dynamic sliding velocities between the rail and wheel.
$\mathbf{v}^i$, $i=1,2$	Linear velocity vector of a contact body *i*.
$\{\mathbf{v}^w\}$	Wheel velocity response vector.
$\overline{\langle v^2\rangle}$	Squared normal velocity averaged over the surface, (Appendix G).
V	Resultant speed of the wheel at the wheel centre.
V_0	Rolling speed; speed of the centre of the wheelset.
V_1, V_2	Longitudinal and lateral surface velocities in the contact area, (Chapter 2); longitudinal and lateral speeds of the wheel at the wheel centre, (Chapter 3).
V_l, V_r	Resultant speeds of the left and right wheels at the wheel centre.
V^r_{0i}, $i=1$ to 6	Rail velocities in the contact frame.
V^w_{0i}, $i=1$ to 6	Wheel velocities in the contact frame.
V^s_{0i}, $i=1$ to 6	Sliding velocities between the wheel and rail in the contact frame.
V_1^r, V_1^w	Longitudinal velocities of the rail and wheel discs.
V_2^r, V_2^w	Lateral velocities of the rail and wheel discs.
V_b	Moving speed of the mass in the mass-on-moving-belt system.
V_i^w, V_i^r, V_i^c	Amplitudes of dynamic velocities of the wheel, rail and contact spring.
V_i^s	Amplitudes of dynamic sliding velocities between the wheel and rail.
$\{\mathbf{V}^s\}$	Vector of sliding velocities: $\{V_1^S \quad V_2^S \quad \Omega_3^S\}$.
$w_{1,2}(i,j)$	Surface (sliding) velocity of the element (*i*, *j*) in the longitudinal (denoted 1) and lateral (denoted 2) directions, (Appendix C).
$\{\mathbf{w}\}$, $\{\dot{\mathbf{w}}\}$	Vectors of wheel state-space variables and its first deviation to time.
W_{rad}	Radiated sound power, (Appendix G).
$[\mathbf{W}(\omega)]$	Eigenvector matrix of $[\mathbf{Q}(\omega)]$.

y	Lateral motion of the components in a bogied vehicle, (Chapter 3); dynamic displacement of the mass in the mass-on-moving-belt system, (Chapter 4).
y_0	Steady displacement of the mass in the mass-on-moving-belt system.
y_{tot}	Total displacement of the mass in the mass-on-moving-belt system.
Y_{ij}	Resultant mobilities of the wheel, rail and contact spring.
Y_{ij}^w, Y_{ij}^r, Y_{ij}^c	Mobilities of the wheel, rail and contact spring.

α	Angle between the actual rolling direction and the nominal rolling direction.
$\alpha_{i,j}$	Receptance.
γ, γ_1, γ_2, γ_6	Resultant creepage and its components in the longitudinal, lateral and spin directions.
γ_{10}, γ_{20}, γ_{60}	Steady-state creepages in the longitudinal, lateral and spin directions.
γ_{1tot}, γ_{2tot}, γ_{6tot}	Total creepages in the longitudinal, lateral and spin directions.
γ_c	Creepage where the slope of the friction curve turns over.
γ_p	Creepage where the derivative of the friction curve is maximum.
γ_1^*, γ_2^*, γ_6^*	Longitudinal, lateral and spin creepages, (Chapter 3).
δ	Compression displacement of contacting bodies, (Appendix B).
δ_H	Approach distance between the contacting bodies.
δ_i, $i=1,2$	Rigid displacement in the contacting body i.
δ_l, δ_r	Left and right wheel/rail contact angles.
$\delta_{i,j}$	Diagonal terms of upper sub-matrices of $[\mathbf{A}_c^w]$.
ε	Ratio of saturation of tangential friction force, (Appendix A).
$\zeta_{e,i}$	Equivalent damping ratio of the friction force for the mode i.
$\zeta_{e,\max}$	Maximum value of the equivalent damping ratio of the friction force.
ζ_c	Maximum value of the control damping ratio in the mass-on-moving-belt system.
ζ_r	Damping ratio of the modal mode r.
η	Intermediate angle in the calculation of Hertz contact, (Appendix B).
ϑ	Spatial direction in the calculation of sound pressure, (Appendix G).
θ_1	Rotation angle in the rigid body about the x-axis.
θ_i, $i=1,2$	Angle between the principal radii along the x_i direction of two contact surfaces, (Appendix B).

κ	Saturation coefficient in the heuristic falling friction function; Timoshenko shear coefficient, (Appendix K).
λ	Falling ratio in the heuristic falling friction function.
λ_i	Term related to the effect of the vertical force.
λ_s	Wavelength in a stationary rotating disc.
λ_v^1	Wavelength of the wave moving in the same direction with the rotating disc.
λ_v^2	Wavelength of the wave moving in the opposite direction to the rotating disc.
μ	Non-dimensional friction force.
μ_0	Coulomb friction coefficient.
μ_1, μ_2, μ_6	Longitudinal, lateral and spin non-dimensional friction forces.
μ_k	Kinetic friction coefficient.
υ	Poisson's ratio.
ξ, ξ_1, ξ_2	Reduced creepages in Vermeulen and Johnson formula: resultant, longitudinal and lateral, (Appendix A).
σ	Radiation ratio, (Appendix G).
ϕ_0	Track cant angle.
$\phi_{i,r}$	Mass normalised modeshape parameters of mode *r* in the *i* direction.
$[\boldsymbol{\phi}^p], p = 0,1,2$	Modal matrices at points 0, 1 and 2.
$\chi_{i,j}$	Off-diagonal terms of upper sub-matrices of $[\mathbf{A}_\mathbf{c}^\mathbf{w}]$.
ψ	Yaw angle.
ω	Frequency in radians; rotational speed in the wheel.
ω_1	Oscillation frequency in the mass-on-moving-belt system.
ω_r	Natural frequency of modal mode *r*.
ω_r, ω_w	Angular speeds of the rail and wheel discs.
$\boldsymbol{\omega}^i,\ i = 1,2$	Angular velocity vector of contacting body *i*.

1. INTRODUCTION

1.1 Background

Railways, which made use of steam locomotives from the 1820s and 1830s, were the first practical form of mechanised land transport. They remain an important form of transport and will remain so in the near future. Nowadays, due to their advantages of high capacity and efficiency, railways are the best solution to the problem of congestion in densely populated areas. Furthermore, the development of high-speed rail networks will win back railway passengers who have been lost to other modes of travel on long-distance journeys.

However, the environmental effects of noise and vibration can work against this promotion of railways. Railway noise can be generated by two main mechanisms: (1) structural vibration due to the wheel and rail contact; (2) aerodynamic fluctuations due to the air turbulence when wind flows over solid objects. Aerodynamic noise is only a dominant source of noise for high-speed trains moving at speeds of 300 km/h and above. For most trains running below the speed of 300 km/h, wheel and rail rolling contact is the main mechanism of noise source [1].

Thompson and Jones [2] reviewed wheel/rail contact noise and divided this noise into three main categories. (1) Rolling noise is the main source on straight track and is predominantly caused by undulations of the wheel and rail surfaces which induce a vertical relative vibration. (2) Impact noise occurs at discontinuities of the wheel or rail surface. The non-linear vertical excitation plays a greater role. (3) Squeal noise, occurring on tight curves, is usually induced by a lateral excitation mechanism.

Railway curve squeal, the main topic of this thesis, is an environmental noise problem occurring where rail transport systems such as mainline railways, tramways and metro rail networks exist in populated areas. Typically, the noise is radiated from the wheels and has most of its energy between 400 Hz and 10 kHz (in the frequency band where human beings are most sensitive to noise) and is strongly tonal in nature (i.e. dominated by a single frequency) [3]. Noise levels can exceed 130 dB at positions close to the wheel, and up to 100-110 dB at 7.5 metres from the track centre [3]. This means that the noise level of curve squeal can exceed the usual rolling noise level by more than 15 to 20 dB.

Since the noise level of railway curve squeal is so high, the only meaningful control method is at source. Known practical solutions for railway squeal in a particular curve include friction modification [4] and wheel damping treatments [5]. These solutions can reduce the occurrence of squeal for some specified cases. However, to understand their operation and optimise their use, theoretical models are required. Many theoretical models have appeared in the last 30 years. These are reviewed in the following section.

1.2 Literature survey

Various mechanisms can result in squealing – a kind of high-level and tonal noise radiated from structural vibration. For railway curve squeal, it undoubtedly arises from the wheel/rail contact. Another squeal phenomenon, automotive brake squeal, has an analogy to railway curve squeal with its strong relation with solid contact. In the literature survey on squeal, these two kinds of squeal are introduced in turn.

1.2.1 Railway curve squeal

Curve squeal has been found to originate from the unstable response of a railway wheel and rail that are subject to large creep forces in the region of contact between the wheel and the rail when negotiating curved track. The creep force is the tangential friction force produced between two bodies in rolling contact due to the creepage - a kind of micro-slippage within the contact region. The wheel is thought to be easily excited into vibration under the creep forces, particularly at frequencies corresponding to the wheel's axial modes. Most previous research considered that the main mechanism of curve squeal is a kind of self-excited vibration due to the non-linear creep forces [6-17].

Rudd [7] in 1976 proposed that the curve squeal might be excited by the following wheel/rail contact conditions: (1) lateral creepage at the contact between the wheel tyre and rail crown, (2) wheel flange rubbing on the rail gauge face, and (3) longitudinal creepage at the contact on the wheel tyre due to differential slip. He discredited the theory that squeal noise can be excited by differential longitudinal slip or flange contact alone, partly through experimental findings and partly from the hypothesis that the noise radiation due to the excitation by differential slip and flange rubbing is negligible as the forces act within the plane of the wheel. Despite occasional conflicting results, almost all curve squeal noise experiments carried out reinforce the hypothesis that the lateral creep forces are responsible for generating squeal. Generally, the literature since Rudd has given little attention to differential slip or flange rubbing as mechanisms for squeal and most work has been focused on the lateral creepage excitation mechanism. Rudd indicated that the wheel response is unstable due to the decreasing friction forces at large sliding velocities when the friction forces are saturated. The slope of the friction curve in the falling regime is not constant [18] and this nonlinearity limits the unstable response to a stable amplitude (limit cycle). Many of the subsequent models that appear in the literature adopted parts of Rudd's approach to the theoretical modelling of squeal. Most of the models begin by assuming a characteristic of the creepage-dependent friction coefficient. Van Ruiten [8], for example, applied Rudd's model to trams.

In a review article, Remington [9] described the state of knowledge of railway curve squeal up to 1985. Based on the analyses of published curve squeal literature and related experimental results, he pointed out that to resolve questions on curve squeal noise it would be necessary to develop a comprehensive analytical model of squeal. He suggested that this model should include finite element models of railway wheel dynamics, numerical models for the dynamics of bogies in curves and details of the friction coefficient versus creepage. Since then, a number of increasingly complex models for curve squeal, consisting of various sub-models, have been published.

Fingberg [11] included a finite element model of the wheelset and an equivalent modal model of the rail. The creep force formula is derived from Kalker's theory [19] of rolling contact, extended to include a falling regime based on Kraft's formula [18] to resemble experimental findings more closely at large creepages. Fingberg used this to couple the wheel and rail vibration in the time domain. A frequency-domain prediction of squeal noise radiation was obtained using the vibration response of the wheel as an input to a boundary element analysis. The model was used to assess the level of damping required to eliminate squeal under a range of creepage configurations. Périard [12], who included vehicle dynamics simulations in a time-domain curve squeal calculation, extended Fingberg's work further.

Heckl [13] presented the findings of a theoretical investigation into the vibration response of an annular disc model, which was excited at a point on the edge by an oscillating lateral force. The disc had a uniform thickness and several out-of-plane modes. This model is analogous to a railway wheel with large lateral creepages as it negotiates curved track. Heckl took a numerical approach in the time domain. The purpose of this work was to gain an understanding of the vibration response and modal behaviour of the disc under conditions where it generates squeal noise due to lateral creepage. The model is not a generalised model and does not allow for variation in the geometric parameters of the wheel. The contact patch was assumed a single point on the disc circumference, and the friction characteristic was simplified to a bi-linear behaviour. The numerical simulations of time histories showed two distinctly different wheel oscillation responses: (1) with a linear lateral creep force, slip but no stick is induced, whereas (2) with a non-linear lateral creep force, a stick-slip oscillation occurs with limit velocity amplitude determining the intensity of the squeal. The second part of Heckl's investigation [20] presented a frequency-domain method of using the modal parameters of the disc to assess which modes of a friction-driven wheel will be unstable, but only for the case of pure slip and not considering a non-linear friction force. The final part of this investigation [21] developed a means of preventing the instabilities associated with squeal noise generation using active control.

De Beer *et al.* [14] presented a frequency-domain model of curve squeal noise due to lateral creepages. This frequency-domain model was derived on the basis that the forces and displacements can be expressed as a quasi-static part and a fluctuating part that can be linearised for low vibration amplitudes. The interrelationship between contact forces and wheel/rail responses was described by a loop, which starts from the lateral contact force and feeds back to it. The Nyquist criterion was used to assess the stability of this positive feedback and identify squeal frequencies. This model predicts that squeal depends on the lateral position of the contact on the wheel tread. This result has also been demonstrated in scale model experiments. Noise radiation can be predicted using the standard components of the TWINS software [22]. The model of de Beer was extended by Monk-Steel and Thompson [15] by including the case of wheel flange contact, which occurs at the leading outer wheel (and possibly the trailing inner wheel) in sharp curves. This model is more general in that it allows for an arbitrary wheel/rail contact angle, including lateral, longitudinal, and spin creepages, but the results of including these effects have not been fully explored.

Chiello *et al.* [16] presented a curve squeal model including not only tangential dynamics (friction force) but also normal dynamics on the wheel/rail contact zone (also included by de Beer [14]). The model can predict the unstable wheel modes and the corresponding squeal level and spectrum. The numerical results agreed satisfactorily with the experimental results given in a companion paper [23]. However, although the numerical results showed that only a friction coefficient decreasing with increasing creepage is able to destabilise the system and induce wheel vibrations, the measurement of the corresponding friction was not able to identify this negative slope. A hypothesis was proposed to explain this phenomenon that the instantaneous friction coefficient may decrease with contact velocity whereas the average friction coefficient remains constant with the angle of attack, but this has not been validated.

1.2.2 Automotive brake squeal

Automotive brake squeal is produced in the disc brake system of automobiles. For a modern (spot-type) disc brake, there are several major components: the rotor, caliper, brake pad assemblies and a hydraulic actuation system [24]. The rotor (or disc) is rigidly mounted on the axle and therefore rotates with the automobile's wheel. A pair of brake pads consisting of friction material are assembled on the backing plates. A caliper is attached to the vehicle and houses the hydraulic pistons. The pistons actuate the brake pads to press against the disc in order to generate a frictional torque to slow the disc (and wheel) rotation when braking. It is generally agreed that the brake squeal results from a sustained, high frequency (more than 1000 Hz) vibration of braking components during a braking action and produces sound levels of over 100 dB, as measured at a reasonable distance from the source [24]. It causes customer dissatisfaction and increases environmental noise.

Kinkaid *et al.* [24] reviewed a large volume of literature up to the year 2001 from which they categorized six central mechanisms of brake squeal, and the most popular three mechanisms are introduced as follows.

a) Decreasing kinetic friction coefficient with increasing sliding velocity

Mills [25] in 1938 examined various occurrences of brake squeal and concluded that the brake squeal was most probably set up by a type of 'stick-slip' action between the rubbing surfaces due to a necessary condition that the relationship between the kinetic (dynamic) friction and the sliding velocity has a negative slope. His work led to a school of thought based on this condition [26,27,28]. However, this theory of brake squeal has not received much attention in recent years, partly because further experimental findings showed that the brake squeal can still exist without the condition of decreasing kinetic friction at large sliding velocity, and partly because other proposed squeal mechanisms are more reasonable under some specific conditions.

b) Sprag-slip

Spurr [29] in 1961 used the term 'sprag-slip' to describe his theory of brake squeal. This theory considers that squeal can be generated independently of the relationship between the dynamic friction and the sliding velocity, and actually it is associated with the unstable oscillations of the components involved in sprag-slip action in braking. If, during braking, one of the sliding components is oriented with respect to another with an angle θ, then the friction force applied by the latter to the former causes the normal force (and hence the friction force) to increase. The total process can be described by a positive feedback loop. If no flexible member exists in the system, the contact forces can become unbounded when the angle is about $\theta = \tan^{-1}(1/\mu)$, where μ is the friction coefficient; then the system is in the situation of sprag. However, the flexibility of some components allows them to free themselves from the sprag by sufficiently deforming under the large normal and friction forces. Once the sprag has been relieved and the original contact situation re-established, the contact forces again start to build up. Thus, sprag in an elastic system can lead to a sprag-slip self-excited vibration. The terms 'geometrically induced' or 'kinematic constraint' for this type of instability can be found in the sprag-slip theory of brake squeal.

c) Self-excited vibration with constant friction coefficient

North [30] in 1972 presented an eight-degree-of-freedom model for a particular disc brake system (pads symmetrically mounted on both sides of the disc) and concluded that self-excited vibration can be induced by friction forces with constant μ. The flutter instability of the brake system can be investigated in terms of the eigenvalues of the equation of motion of this brake system. He found that larger values of μ can induce instability, a phenomenon found in many experiments. The threshold of friction coefficient for brake squeal is determined by the parameters of the brake system components. Ouyang *et al.* [31] used a finite element model to show that brake squeal is the consequence of the unstable parametric resonances induced by the rotating dry friction between the disc and the pads.

1.2.3 Summary of squeal models

The literature survey introduces several squeal theories based on different relationships between the vibration (sliding velocity) and the contact forces (friction and normal contact force) at the contact region. It is clear that these relationships result in self-excited vibration, a kind of system vibration induced by the movement of this system itself. Thus, a squealing system, which has many components coupled to each other, can always be described by a feedback loop. If the feedback loop is stable under certain conditions, no squeal will happen. Thus, the stability analysis of this loop can predict the possibility of squeal.

In the self-excited vibration process, the relationship between the motion and exciting forces is very important, which is determined by the squeal mechanism. For the curve squeal research, this relationship is mainly investigated based on the wheel/rail structural dynamics and the rolling friction in the wheel/rail contact system. Compared with the wheel/rail system, the constitution and contact conditions of a braking system are much more complex. For example, the materials of braking components, disc and pads, are diversely chosen to satisfy the needs of braking, while the material of the wheel and rail is normally quasi-identical steel. Hence, some mechanisms of self-excited vibration, which are important for investigating brake squeal, may not be readily applicable to the problem of railway curve squeal. For instance, the sprag-slip phenomenon is a kind of geometrically induced self-excited vibration, which needs a contact angle to satisfy the sprag situation, and is therefore difficult to meet in wheel/rail contact. Another mechanism, self-excited vibration with a constant friction coefficient, is a kind of flutter, which is dependent on the special vibration structures, and therefore appears unlikely to be realised in the railway contact system.

Curve squeal is widely considered as a good example of 'stick-slip' self-excited vibration, which is induced by a decreasing friction coefficient at large creepages.

Although other mechanisms may exist in the curve squeal simultaneously, this mechanism is generally believed to be dominant.

1.2.4 Shortcomings of current curve squeal models

The existing theoretical curve squeal models are mostly focused on the unstable vibration resulting from the large lateral sliding, but ignore the differential longitudinal slip or the flange contact, following the hypotheses presented by Rudd [7]. To investigate the possible inter-relations between the longitudinal, lateral creepages and spin, a general wheel/rail contact model, including all the possible degrees of freedom, should be considered.

Although several squeal models in the literature survey have included the curving behaviour in their squeal models, the links between the vehicle dynamics package and the curve squeal model are weak. Hence, the relations between the curving conditions and the curve squeal have not been further investigated.

To implement the curve squeal prediction, either time-domain squeal calculation or frequency-domain stability analysis is adopted in the surveyed literature. Normally, frequency-domain stability analysis is more practical in engineering applications. However, due to the strong nonlinearities existing in the wheel/rail rolling friction, the question of how effective the stability analysis is should be answered before using it.

1.3 Aim and scope of the thesis

The aim of the thesis is to develop a complete curve squeal model, which can predict curve squeal and will allow useful approaches to control it to be studied. As the curve squeal results from a kind of self-excited vibration existing in the wheel/rail contact system, the central work of this thesis is to build a self-excited feedback loop model, representing relations between the wheel/rail motions and the contact forces. Furthermore, since squealing takes place under some specified curving conditions, a vehicle dynamics model is required to provide necessary parameters related with steady-state curving behaviour. Finally, an acoustic radiation module can qualify squealing by predicting the noise level. Thus, this curve squeal model contains four sub-models: wheel and rail structural dynamics, wheel/rail rolling contact dynamics including the friction, vehicle dynamics, and acoustic radiation. These sub-models together constitute a loop, as shown in Figure 1-1. Although it is beyond the scope of the current work to validate the whole model, each sub-model has been fully or partly validated.

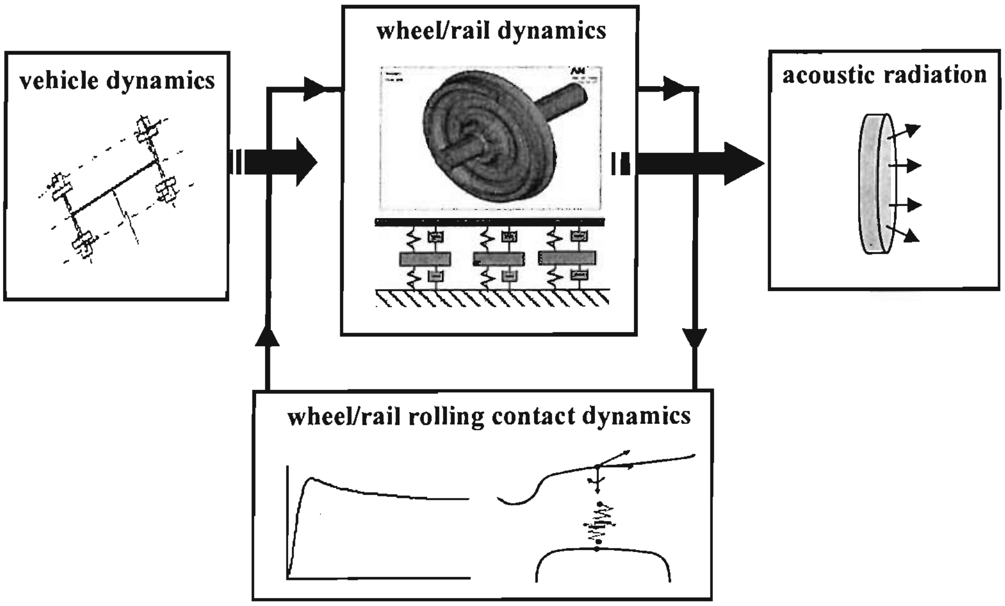

Figure 1-1 Sub-models in the general curve squeal model.

1.4 Structure of the thesis

The structure of the thesis is introduced as follows.

Chapter 2. Rolling friction model. This chapter presents the creepage-friction relationship, which is applicable in both contact dynamics and vehicle dynamics at different levels of complexity.

Chapter 3. Vehicle dynamics – steady-state curving. To obtain the parameters of vehicle dynamics on curves, a bogied vehicle with 17 degrees of freedom (DOF) is modelled in this chapter. This model is validated by comparison with a commercial vehicle dynamic package.

Chapter 4. Self-excited vibration. In this chapter the classic self-excited vibration problem, a mass on a moving belt, is studied. Through the analysis of this simple model, some important points in the self-excited vibration are proposed, i.e. the feedback loop, the stability problem and the limit-cycle response.

Chapter 5. Squeal model for wheel/rail contacts. This chapter introduces a general curve squeal model. The wheel and rail are both multi-DOF (MDOF) systems, which can be represented in either the time domain or the frequency domain. Stability analysis of the loop can predict squeal in terms of all possible DOF. The time-domain responses are available by step-by-step integration according to the general self-excited loop. The acoustic calculation considers the noise radiation from the main source in squealing – the vibrating wheel. Following the theoretical portion, a parametric study of the curve squeal is provided to show the role of each component involved in squeal.

Chapter 6. Squeal experiments on a twin-disc rig. Experimental results are obtained to show the relationship between the squealing and the lateral friction force. The curve squeal model is partly validated using this rig.

Chapter 7. Application of the model to curve squeal prediction. The curve squeal model is applied to predict the squeal of a particular vehicle (Class 158 DMU). The possibility of squeal and the dominant squeal frequency are predicted for each wheel in a bogie negotiating curves with different curve radii. The relations between the curving conditions and the curve squeal are investigated.

Chapter 8. Conclusions and further work. This chapter summarises the main findings of the thesis and considers further work that might improve the model.

1.5 Main original contributions

The main original contributions are as follows.

(i) Establishment of a complete curve squeal model, including the steady-state curving calculation, the time-domain and frequency-domain wheel/rail squeal models and the acoustic radiation calculation. This model can be used to predict the squeal noise of a specific vehicle under any steady-state curving conditions.

(ii) Thorough investigation of the occurrence of curve squeal at arbitrary wheel/rail contact in the presence of all the possible creepages. The simulations show that a large longitudinal creepage can induce audible squeal noise, in some situations as for a large lateral creepage; flange contact with a large contact angle and spin may eliminate the occurrence of squeal; and variations of the contact position and contact angle may change the dominant squeal frequency.

(iii) Validation of the stability analysis by comparing the squeal prediction results from both the frequency-domain and the time-domain models. This shows that the stability analysis can effectively predict the possible unstable modes if the nonlinearities of friction around the steady-state creepages are limited.

(iv) Investigation of the relations between the curving behaviour and the occurrence of squeal. The most important parameters of curving behaviour are the steady-state creepages (spin), the contact positions and contact angles.

(v) Consideration of the effects of the conventional squeal methods, i.e. friction modification and wheel damping treatments using the wheel/rail squeal model. Using either control method, it is possible to stabilise the wheel vibration and control the squeal. Under some conditions, these two methods should be combined to successfully control the curve squeal.

2. ROLLING FRICTION MODEL

2.1 Introduction

Rolling contact is a topic of tribology and is mainly studied in relation to contact mechanics. In rolling contact, the friction force generated between the contact surfaces provides the traction or braking force, driving or stopping one contacting body relative to another. Since the rolling contact area is normally very small compared with the contacting bodies, at least for steel-on-steel contact, the motion-force relations can be studied at two levels. One level is between the rigid motions of the contacting bodies and the resultant friction forces. The other level is between the local motions, i.e. surface motion and normal approach of contact bodies in the contact region, and the contact stresses, i.e. traction and normal pressure. An appropriate friction model is required to determine these relations. For the application of squeal analysis, the phenomenon of falling friction in sliding, although it is not important in existing rolling contact theories, must be considered in the friction model. In this chapter, the friction in rolling contact is reviewed to provide a basis for the applications of friction in both vehicle dynamics and the curve squeal model.

2.2 Review of friction of elastic solids

2.2.1 Coulomb friction

The classic study of friction carried out by Coulomb (1785) [32] shows that the friction force F_f is proportional to the load and independent of the velocity of sliding v^s, which is represented as

$$\left|F_f\right| = \mu_0 P, \quad \left|v^s\right| > 0 \tag{2.1}$$

where $\mu_0 > 0$ is the Coulomb friction coefficient, which is an empirical property of the contacting materials, $P \geq 0$ is the normal force exerted between the contact surfaces, and $\mu_0 P$ is termed the Coulomb force.

2.2.2 Static friction

Before gross sliding (macroscopic sliding) starts, elastic deformation may exist in the contact surface. This state is considered as 'static', with $v^s = 0$. The elastic force in static contact is exactly what it must be in order to prevent motion between the surfaces and balance the net force tending to cause such motion. Rather than providing an estimate of the actual friction force, the Coulomb force provides a threshold value for this static friction, above which sliding would commence. Hence, the static friction force may take any value from zero up to the Coulomb force:

$$\left|F_f\right| \le \mu_0 P, \quad v^s = 0. \tag{2.2}$$

The direction of the static friction force on a surface is opposite to the direction of motion that the surface would experience in the absence of this friction.

2.2.3 Kinetic friction

For sliding motion, under most circumstances, the friction force in sliding is a function of the sliding velocity, instead of a constant Coulomb friction force. The kinetic friction coefficient μ_k, a dimensionless scalar value, can be adopted to describe the ratio of the friction force between two bodies and the force pressing them together:

$$\mu_k\left(v^s\right) \equiv \frac{F_f}{P}, \quad \left|v^s\right| > 0, \tag{2.3}$$

where the sign of μ_k is always opposite to the sign of sliding velocity v^s, because the friction force F_f is exerted in the opposite direction to that of sliding velocity v^s.

The physical processes that occur during sliding are too complex to yield a simple mathematical model. By carrying out experiments, Bowden [32] showed some important friction phenomena with his intuitive explanations. Some of them may be useful to the understanding of the squeal phenomenon in terms of falling friction. These are restated in the following subsections.

2.2.4 Friction due to junction growth

Bowden found that, under the intense pressure which acts at the summits of the surface irregularities, junction growth (a localised adhesion and welding together of the metal surfaces) occurs. The friction is thus due to the shearing of adhered junctions. For uncontaminated contact surfaces, the friction coefficient in Eq.(2.3) can be rewritten in terms of the bulk properties of the materials [32]:

$$|\mu| = \frac{s^*}{p^*}, \tag{2.4}$$

where s^* is the critical shear strength of the contact junction and p^* is the yield pressure of material. Experiments [32] also showed that the region of contact junctions may actually cover a small percentage of the nominal contact area. If the normal force increases, more contact junctions will be built and the friction force will increase proportionally. Consequently, the friction coefficient will remain constant. If a contaminant film weaker than the bulk metal separates the surfaces, the shear stress s^* normally decreases and is no longer dependent on the material [32]. However, since the friction between surfaces depends on so many other factors, the friction coefficient will have to be determined by experimental measurements.

2.2.5 Stick-slip in sliding

Experiments of Bowden [32] showed that, at extremely slow speeds of sliding, the resultant strength of the adhered junctions is often greater than that occurring at higher speeds of sliding. This means, as many workers have shown, that the static friction limit is often higher than the kinetic friction. As gross sliding commences, there appears to be a tendency for the surfaces to slide until, as they slow down, the junction between them has time to establish again [32]. This type of behaviour is associated with 'intermittent' or 'stick-slip' motion. Bowden used a method of electrical conductance to show the 'stick-slip' motion. Although the friction variations with respect to sliding velocity are not of great interest in tribology, there is one special interest from the standpoint of stability of tribological systems [32]: if a sliding system has a friction coefficient which reduces as the velocity increases, a situation may exist, which can lead to harmonic oscillations and even squeal.

2.2.6 Other friction mechanisms

Other friction mechanisms may play significant roles in the process of sliding. For example [32], if one contacting surface is harder than the other, the asperities of the harder surface plough out the softer material to an appreciable depth below the surface. However, for contacting surfaces with quasi-identical materials, e.g. those of normal wheels and rails, the effect of ploughing is not significant.

2.3 Rolling contact of elastic solids

2.3.1 Rigid motion in rolling

2.3.1.1 Coordinates

In Figure 2-1, two elastic bodies, body (1) and body (2), contact each other at an instantaneous contact point **c**, which is assumed to be at the centre of the contact surface. Choosing the rolling direction as the direction of the x-axis, an instantaneous contact frame 01-02-03 can then be established in a plane including the contact surface. The contact frame has its origin at the point **c** and its 01-axis in the rolling direction, forming a contact (tangent) plane with the 02-axis, and the 03-axis is normal and downward to this contact plane. A reference frame 1-2-3 is coincident with the contact frame but its origin is fixed at the instantaneous contact point **c** at a particular time. If the wheel is rolling on the rail, the instantaneous contact point **c** and the contact frame will shift in the reference frame.

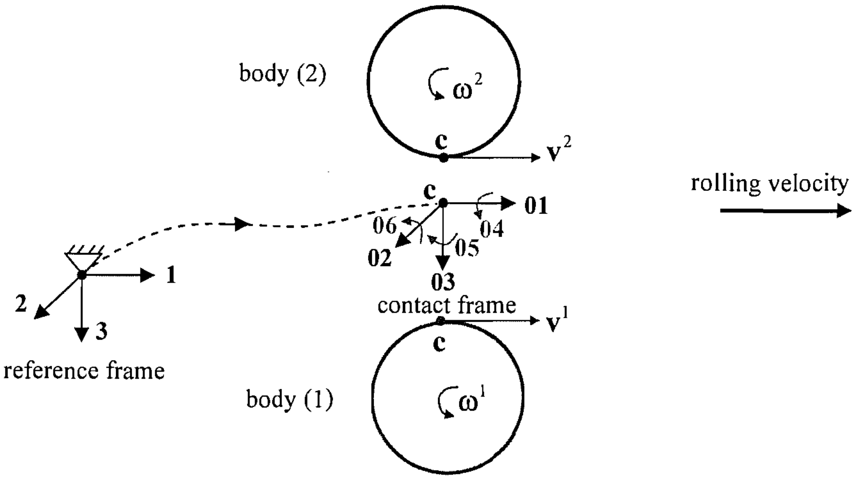

Figure 2-1 Schematic diagram of rolling contact.

2.3.1.2 Rigid motion

The rigid motion of a body at any instantaneous time can be defined by the linear velocity vector of an arbitrarily chosen point in the body together with the angular velocity vector of the body. In the contact frame 01-02-03, the reference can be the contact point **c**. The rigid motion of body i, $i=1,2$, can be described by its linear velocity vector $\mathbf{v}^i:(v^i_{01},v^i_{02},v^i_{03})$ and angular velocity $\omega^i:(v^i_{04},v^i_{05},v^i_{06})$. The linear or angular velocities of the two bodies in or about the same axis may be different. The difference is called the sliding velocity, $v^s_{0j}=v^1_{0j}-v^2_{0j}$, $j=1$ to 6.

2.3.1.3 Rolling speed

In the contact frame, the tangential motion of the two bodies at the contact point **c** is mainly the longitudinal one, along the 01-axis. Although the longitudinal velocity of each body may be different, the difference between them is very small compared with either longitudinal velocity. A rolling speed $V_0>0$ is defined by averaging the longitudinal velocities of the two bodies, the value of which is

$$V_0 \equiv \frac{\left|v^1_{01}+v^2_{01}\right|}{2}. \qquad (2.5)$$

2.3.1.4 Creepage

In the contact frame, the contact surfaces 'flow' through the contact area with tangential velocities v^i_{01} (in the longitudinal direction) and v^i_{02} (in the lateral direction), $i=1,2$. If

$v_{01}^1 \neq v_{01}^2$ and/or $v_{02}^1 \neq v_{02}^2$, the rolling motion is accompanied by 'sliding'. The sliding is evaluated by a dimensionless parameter, the creepage γ. The longitudinal and lateral creepages γ_1, γ_2 are defined as

$$\gamma_1 \equiv (v_{01}^1 - v_{01}^2)/V_0 \equiv v_{01}^s/V_0, \tag{2.6}$$

and

$$\gamma_2 \equiv (v_{02}^1 - v_{02}^2)/V_0 \equiv v_{02}^s/V_0. \tag{2.7}$$

2.3.1.5 Spin

The bodies may also have angular velocities about the normal to the contact plane, the 03-axis in the contact frame. This angular velocity, denoted v_{06}^i, $i = 1,2$, is actually a component of the rolling angular velocity when the contact plane has an angle relative to the plane including the axis of rotation. If $v_{06}^1 \neq v_{06}^2$, a relative spin motion will exist, which leads to rotational sliding around a particular centre point. Spin can be evaluated in terms of spin creepage γ_6. This definition is similar to that of the above creepages but it has dimension [m^{-1}]:

$$\gamma_6 \equiv (v_{06}^1 - v_{06}^2)/V_0 \equiv v_{06}^s/V_0. \tag{2.8}$$

2.3.1.6 Normal approach

Under the normal load P, the two contacting bodies will approach each other in the direction normal to the contact surfaces. The 'approach' velocity is

$$\frac{d\delta_H}{dt} \equiv -(v_{30}^1 - v_{30}^2) \equiv -v_{30}^s, \tag{2.9}$$

where δ_H is the approach distance which is a function of normal load P according to the Hertz theory [33, 34].

2.3.2 Surface motion in the contact area: 'stick' and 'slip'

Although 'sliding' exists due to the rigid velocity difference between the two bodies in rolling contact, the relative motion of two adjacent surface particles in each contacting body may 'stick' or 'slip', as shown schematically in Figure 2-2(a) and (b), following Johnson [35].

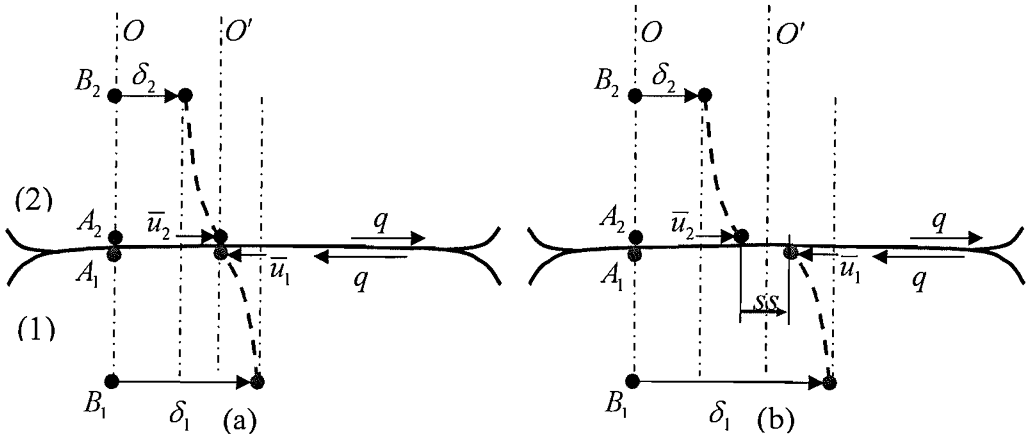

Figure 2-2 Relative motion of surface particles at contact: (a) stick, (b) slip, Johnson [35].

2.3.2.1 Elastic surface deformation

In Figure 2-2, A_1 and A_2 are two surface points of body (1) and body (2). They are initially coincident at rest (without elastic tangential stress). B_1 and B_2 are points inside body (1) and body (2), which are distant from the contact interface and represent the rigid motion of the corresponding body. After a small interval of time, B_1 and B_2 move through effectively rigid displacements δ_1 and δ_2, while A_1 and A_2 experience tangential elastic displacements $\bar{u}_1$ and $\bar{u}_2$ relative to B_1 and B_2. The slip distance (micro sliding) between A_1 and A_2 can be written as the sum of rigid motions and elastic surface deformation of the contacting bodies:

$$ss \equiv (\delta_1 + \bar{u}_1) - (\delta_2 + \bar{u}_2) = (\delta_1 - \delta_2) + \delta\bar{u}\,, \tag{2.10}$$

where the elastic surface deformation is

$$\frac{\delta\bar{u}}{h_0} = \frac{\bar{u}_1}{h_0} - \frac{\bar{u}_2}{h_0} = \frac{q_1}{G_1} - \frac{q_2}{G_2}, \tag{2.11}$$

where q_i are tangential stresses (shear stresses or traction), h_0 is initial length of the contacting surface under q_i, and G_i are shear moduli.

Writing the tangential stress

$$q \equiv q_1 = -q_2, \tag{2.12}$$

and the composite shear modulus

$$\frac{1}{G^*} = \frac{1}{G_1} + \frac{1}{G_2}, \tag{2.13}$$

the elastic surface deformation in Eq.(2.11) can be rewritten to be

$$\delta\bar{u} = \frac{q}{G^*} h_0 . \tag{2.14}$$

2.3.2.2 Stick

If the elastic surface deformation $\delta\bar{u}$ is sufficient to compensate the relative rigid displacement $(\delta_1 - \delta_2)$, A_1 and A_2 will remain 'stuck' with $ss = 0$, see Figure 2-2(a). During this interval Δt, from Eq.(2.10), the elastic deformation should equal the sliding distance:

$$\delta\bar{u} = -(\delta_1 - \delta_2) = -v^s \Delta t . \tag{2.15}$$

According to the strain and stress relationship given in Eq.(2.14), Eq.(2.15) can be used to determine the tangential stress:

$$q = -G^* v^s \Delta t / h_0 , \tag{2.16}$$

the value of which should be less than the Coulomb friction:

$$|q| < \mu_0 p , \tag{2.17}$$

where p is the normal pressure.

2.3.2.3 Slip

'Slip' may occur when the value of tangential stress reaches the Coulomb friction limit, $\mu_0 p$, and cannot increase to sustain further elastic deformation. In Figure 2-2(b), two initially sticking points A_1 and A_2 will slip, if they are still in the contact area after a time interval Δt. The critical time interval can be calculated from Eq.(2.16):

$$\Delta t = \frac{\mu_0 p h_0}{|G^* v^s|} . \tag{2.18}$$

At the slip point, the traction is the same as the Coulomb friction, with the direction opposite to the sliding velocity v^s:

$$q = -\mu_0 p \frac{v^s}{|v^s|} . \tag{2.19}$$

2.3.3 Surface slip velocity in rolling contact

The surface velocities are formulated in the contact frame, 01-02-03. For the general case, the surface velocities $\bar{v}^i_{01}, \bar{v}^i_{02}$ of contacting bodies i ($i = 1,2$) are combinations of rigid motions $v^i_{01}, v^i_{02}, v^i_{06}$ and surface elastic motions $d\bar{u}^i_{01}/dt, d\bar{u}^i_{02}/dt$. In Figure 2-3, for time instant t, at the contact point (x, y), the longitudinal surface velocities are

$$\bar{v}^i_{01}(x,y,t) = \left(v^i_{01}(t) - v^i_{06}(t)y\right) + \frac{d\bar{u}^i_{01}(x,y,t)}{dt}, \quad i = 1,2, \tag{2.20}$$

and the lateral surface velocities are

$$\bar{v}^i_{02}(x,y,t) = \left(v^i_{02}(t) + v^i_{06}(t)x\right) + \frac{d\bar{u}^i_{02}(x,y,t)}{dt}, \quad i = 1,2. \tag{2.21}$$

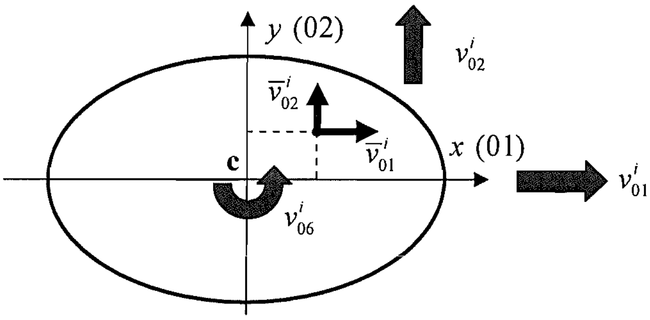

Figure 2-3 Surface velocities in the contact region.

The elastic velocities in Eq.(2.20) and Eq.(2.21) are

$$\frac{d\bar{u}^i_{01}(x,y,t)}{dt} = \frac{\partial \bar{u}^i_{01}}{\partial x}\frac{dx}{dt} + \frac{\partial \bar{u}^i_{01}}{\partial y}\frac{dy}{dt} + \frac{\partial \bar{u}^i_{01}}{\partial t} = \left(V_1 \frac{\partial \bar{u}^i_{01}}{\partial x} + V_2 \frac{\partial \bar{u}^i_{01}}{\partial y}\right) + \frac{\partial \bar{u}^i_{01}}{\partial t}, \tag{2.22}$$

and

$$\frac{d\bar{u}^i_{02}(x,y,t)}{dt} = \frac{\partial \bar{u}^i_{02}}{\partial x}\frac{dx}{dt} + \frac{\partial \bar{u}^i_{02}}{\partial y}\frac{dy}{dt} + \frac{\partial \bar{u}^i_{02}}{\partial t} = \left(V_1 \frac{\partial \bar{u}^i_{02}}{\partial x} + V_2 \frac{\partial \bar{u}^i_{02}}{\partial y}\right) + \frac{\partial \bar{u}^i_{02}}{\partial t}. \tag{2.23}$$

In the elastic velocities, the terms in the bracket are related to the 'flow' velocities V_1 and V_2 of the surface particle. The last term involves the rate of change of strain with time. If there is a small angle $\alpha \le 5^\circ$ between the rolling direction and the nominal rolling direction, the instantaneous flow velocities in the longitudinal and lateral directions are

$$V_1 = \frac{dx}{dt} = V_0 \cos\alpha \approx V_0 , \tag{2.24}$$

and

$$V_2 = \frac{dy}{dt} = V_0 \sin\alpha \approx V_0\alpha . \tag{2.25}$$

Writing the longitudinal and lateral elastic surface deformations as $\delta\bar{u}_{01} = \bar{u}^1_{01} - \bar{u}^2_{01}$ and $\delta\bar{u}_{02} = \bar{u}^1_{02} - \bar{u}^2_{02}$, respectively, the longitudinal and lateral slip velocities of coincident surface particles, given in Eqs.(2.20) and (2.21), can be rewritten as

$$\begin{aligned} \bar{v}^s_{01}(x,y) &= \bar{v}^1_{01} - \bar{v}^2_{01} \\ &= \left(v^s_{01} - v^s_{06}y\right) + \left(V_1 \frac{d\left(\delta\bar{u}_{01}\right)}{\partial x} + V_2 \frac{d\left(\delta\bar{u}_{01}\right)}{\partial y} + \frac{d\left(\delta\bar{u}_{01}\right)}{\partial t}\right), \end{aligned} \tag{2.26}$$

and

$$\begin{aligned} \bar{v}^s_{02}(x,y) &= \bar{v}^1_{02} - \bar{v}^2_{02} \\ &= \left(v^s_{02} + v^s_{06}x\right) + \left(V_1 \frac{d\left(\delta\bar{u}_{02}\right)}{\partial x} + V_2 \frac{d\left(\delta\bar{u}_{02}\right)}{\partial y} + \frac{d\left(\delta\bar{u}_{02}\right)}{\partial t}\right). \end{aligned} \tag{2.27}$$

As in the previous discussion, a point with zero slip, $\bar{v}^s_{01} = \bar{v}^s_{02} = 0$, means 'stick', and the corresponding elastic deformation is directly related to the traction. A point with non-zero slip, $\bar{v}^s_{01} \neq 0$ and/or $\bar{v}^s_{02} \neq 0$, has a limiting Coulomb friction. The resultant friction forces and possible spin moment are the sum of the tractions in the contact area.

2.3.4 Steady rolling before gross sliding

In the rolling contact area, there are two significant forces: the normal load P and the resultant tangential force Q, and one important moment: the spin moment M_3. Their relations before gross sliding have been widely studied in the field of elastic contact mechanics. Some important theoretical models involved in this field are reviewed in Appendix A. For analytical studies, the contact problem is usually treated as Hertz contact. Consequently, the dimensions of the contact area and the distribution of normal contact pressure are obtained from Hertz theory, as given in Appendix B. With appropriate numerical methods, e.g. Kalker's FASTSIM algorithm [36], the surface condition (stick or slip at any contact point) and the distribution of traction in the steady-state rolling contact problem can be determined. Detailed information about the FASTSIM algorithm can be found in Appendix C. Some typical rolling contact cases from FASTSIM are shown in Figure 2-4 and Figure 2-5; related parameters listed in Table C-1, Appendix C.

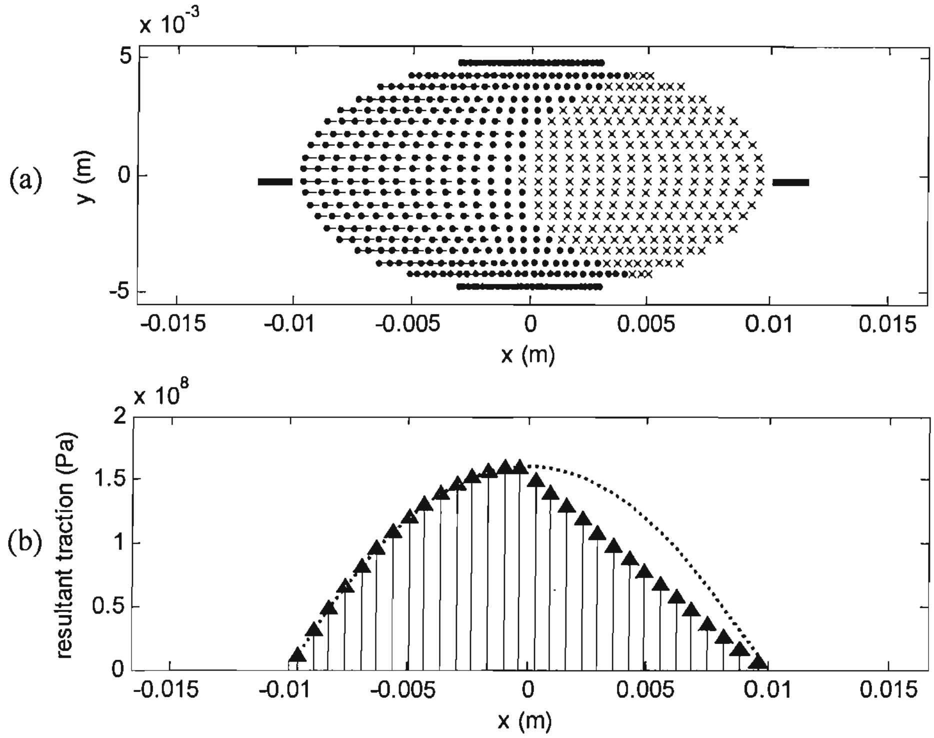

Figure 2-4 Contact area under a longitudinal creepage, calculated by FASTSIM. (a) × stick element, • slip element, – slip direction; (b) tractions for the central strip in (a), indicated by lines —, ↑ resultant traction, ----- limiting Coulomb force.

In Figure 2-4, a gentle creepage is involved. The leading zone in the contact area, where surface particles 'flow' into contact area, from right side to left side, is under 'stick'. The trailing zone in the contact area, where surface particles leave the contact area, is under 'slip'. In the 'stick' position, the traction is less than the corresponding Coulomb friction, while in the 'slip' position, the traction is equal to the Coulomb friction. Since the distribution of normal pressure in the contact area is a paraboloid, the Coulomb friction may be different from one position to another. If the creepage increases, more regions in the contact area will turn from 'stick' to 'slip', starting from the trailing area, until the whole area is under slip for a significantly large creepage. During this process, the resultant tangential force Q will increase, initially linearly, until it is saturated and becomes equal to the Coulomb friction force $\mu_0 P$.

If a large spin is involved in the rolling contact, the surface condition and consequently the distribution of traction is more complex. In Figure 2-5, results are shown for a pure spin which leads to a stick region in the centre and large slip in the peripheral region. A spin moment will exist. Due to the small dimensions of the contact area compared with the contacting bodies, this spin moment is so small that it normally plays a negligible role on the dynamic performances of the contacting bodies. Besides the spin moment, a transverse resultant force may also be generated, which may be significant for the tangential forces.

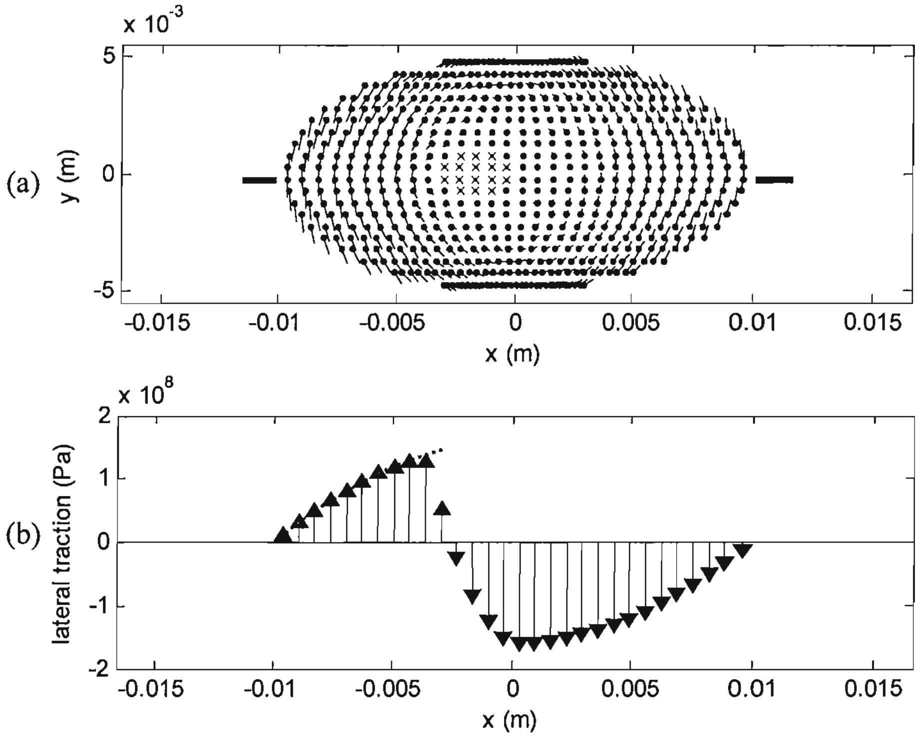

Figure 2-5 Contact area under a large pure spin, calculated by FASTSIM: (a) × stick element, • slip element, – slip direction; (b) tractions for the central strip in (a), indicated by lines —, ↑ lateral traction, ----- limiting traction.

2.3.5 Rolling with unsteady sliding velocity

If the sliding velocities are unsteady, the surface velocities at each surface point, as given in Eq.(2.26) and Eq.(2.27), will obviously vary together. Nevertheless, the elastic deformation may become time varying. Hence, the steady rolling theory, which mainly concerns the relationship of force-motion in adhesion, cannot strictly be applied accurately to unsteady cases. For simplicity, it will be retained here.

2.4 Friction model

2.4.1 Friction curve

For engineering applications, the relations between forces and sliding velocities involved in steady rolling contact can be represented by sliding velocity - force curves, as shown in Figure 2-6. If the sliding velocity is very small, the friction force increases linearly from zero, until it saturates at the Coulomb friction. This is the adhering zone, where more and more of the contact turns from stick to slip until the whole contact area is under slip. After the adhering zone, the rolling contact is under gross sliding. In some cases, e.g. lubricated contact surfaces, no significant downward slope can be found in sliding. However, for most cases, the friction force is a function of sliding velocity. Often, the friction curve will slope down from the Coulomb friction and then may reach a constant value or even slope up at some large sliding velocities [32].

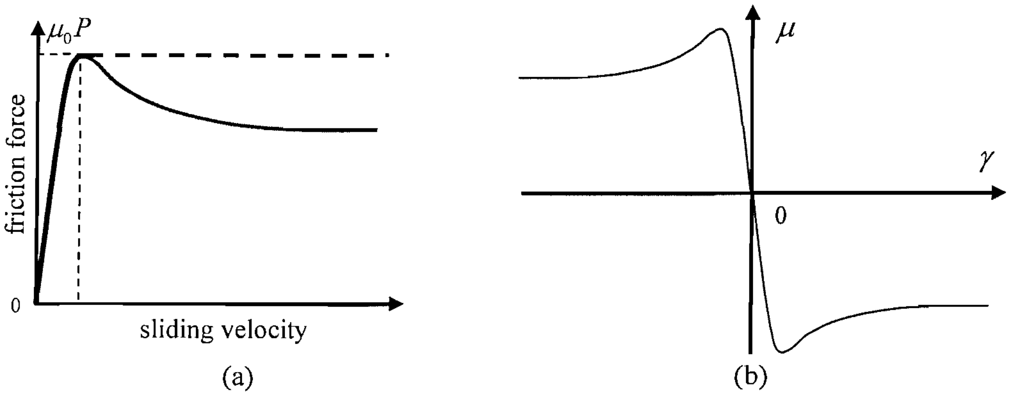

Figure 2-6 Schematic diagram of friction curve, (a) friction force with respect to the sliding velocity, (b) non-dimensional friction force with respect to the creepage.

Since the friction force is also related to the normal force, the non-dimensional friction force represents the friction property better than the friction force. Eliminating the influence of the normal force, and choosing creepage instead of sliding velocity, the friction curve in Figure 2-6(a) can be changed into a curve in terms of non-dimensional friction force and creepage. The non-dimensional friction force μ_i, $i = 1,2,6$, represents the non-dimensional ratio between the friction force (moment) in the *i* direction and the normal force. The non-dimensional friction force can be given a sign to indicate that the direction of the friction force is opposite to that of sliding velocity, as shown in Figure 2-6(b).

2.4.2 Theoretical model adopted for the friction curve in adhering

The curve in adhering, especially for clean surfaces, can be well explained from rolling contact mechanics. As shown in Appendix A, for the general case, i.e. creepages with spin, Kalker's numerical method, FASTSIM algorithm [36] based on his simplified theory [37], can provide good computational speed with small cost in terms of accuracy. The FASTSIM algorithm is discussed in Appendix C. Alternatively, if the spin effect is small, the Shen-Hedrick-Elkins formula [38] is an appropriate analytical model for cases with creepages and small spin. This is described in Appendix A. In Figure 2-7, using the parameters in Table C-1, it is shown that their results are quite consistent at small spin $\gamma_6 = 0.076$ m^{-1} (wheel/rail contact angle is 2° and wheel rolling radius is 0.46 m), but very different at large spin $\gamma_6 = 1.7$ m^{-1} (wheel/rail contact angle is 45° and wheel rolling radius is 0.46 m). Since FASTSIM is an approximation of Kalker's exact theory, the result from FASTSIM is closer to the real condition. The result from the Shen-Hedrick-Elkins formula is acceptable for the cases with small spin when wheel/rail contact angle is less than 5°.

The sign of the spin may not influence the longitudinal friction very much, but it can play a great role on the lateral friction, as shown in Figure 2-8. Due to the effect of large spin, the slope in the adhering zone decreases significantly. This results in the saturation of friction force taking place at larger creepage. If the sign of the spin is the same as that of the lateral creepage, the lateral friction force will increase and reach the limiting Coulomb force at smaller creepages. Conversely, if the spin has the opposite sign to that of the lateral creepage, it will decrease, or even change the direction of the lateral friction force.

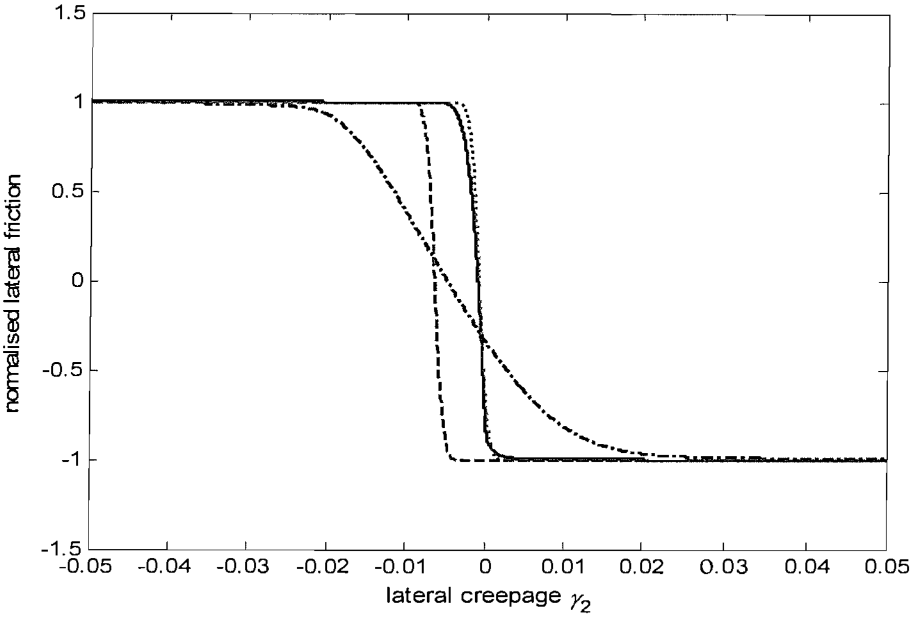

Figure 2-7 Comparison of friction curves calculated by FASTSIM and Shen-Hedrick-Elkins formula, —— FASTSIM with small spin $\gamma_6 = 0.076$ m^{-1}, ······ Shen-Hedrick-Elkins formula with small spin $\gamma_6 = 0.076$ m^{-1}, — · — FASTSIM with large spin $\gamma_6 = 1.7$ m^{-1}, ------ Shen-Hedrick-Elkin formula with large spin $\gamma_6 = 1.7$ m^{-1}.

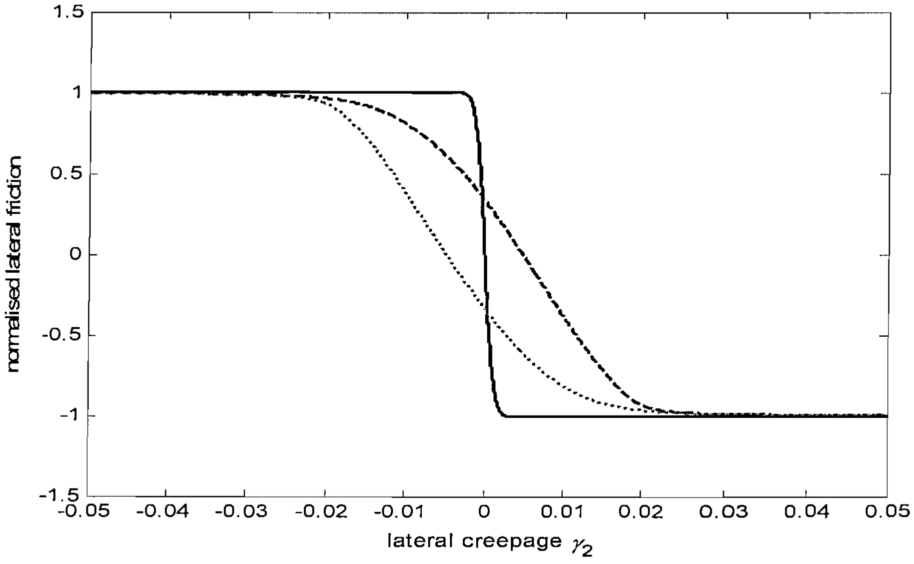

Figure 2-8 Influence of spin on the lateral friction, calculated by FASTSIM, —— no spin, ······ large positive spin $\gamma_6 = 1.7$ m^{-1}, ------ large negative spin $\gamma_6 = 1.7$ m^{-1}.

2.4.3 Heuristic formula for falling friction in sliding

The friction curve in gross sliding can only be partly explained in terms of tribology. The knowledge of the downward slope of the friction curve relies mainly on experimental findings. Accounting for the falling characteristics for large creepages, a heuristic approach is adopted in this thesis, which was first proposed by Kraft [18], then adopted by Fingberg [11], de Beer *et al.* [14] and Monk-Steel *et al.* [39] for their curve squeal calculations. However, the falling function used in this thesis is slightly different [1], which is

$$\tau(\gamma)=1-\lambda e^{-\kappa/|\gamma|}, \tag{2.28}$$

where λ is termed falling ratio here, defined as

$$\lambda \equiv \frac{\mu_0-|\mu_k(\gamma)|}{\mu_0}, \quad \gamma \to \infty, \tag{2.29}$$

and κ is the saturation coefficient which determines the creepage where the friction curve goes into saturated and falling regions. According to the friction measurement in Chapter 6, $\kappa=0.005$ is appropriate for clean and dry contact surfaces at a rolling speed of about 3 m/s. The coefficient λ can also be obtained from related experiments. The effects of different coefficients in the falling function are shown in Figure 2-9. It can be found that the falling ratio λ influences the friction curve at large creepages, while the saturation coefficient κ mainly influences the friction curve at small creepages, close to the saturation zone.

---

[1] The differences are (i) only one decaying exponential term is included as the second term in the formula of Kraft [18] applies for large gross sliding and is not relevant here; (ii) the factor λ is introduced whereas Kraft used a constant value of 0.5; (iii) for convenience, Eq.(2.28) is written in terms of creepage rather than sliding velocity, although in practice κ will be related to the rolling velocity (but not exactly proportional to the rolling velocity).

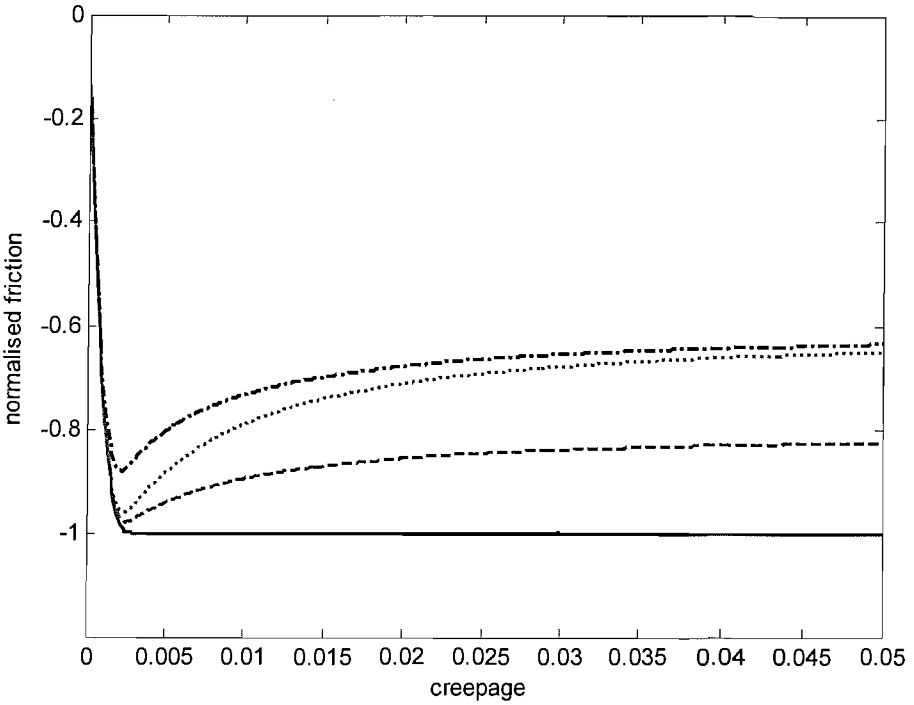

Figure 2-9 Influence of coefficients in the falling function, —— not weighted with falling function, ------ $\lambda = 0.2$, $\kappa = 0.005$, ······ $\lambda = 0.4$, $\kappa = 0.005$, - · - $\lambda = 0.2$, $\kappa = 0.005$.

2.4.4 Coulomb friction coefficient

The Coulomb friction is the maximum friction force in the friction curve. In the theoretical rolling contact model, i.e. FASTSIM algorithm, the Coulomb friction coefficient μ_0 is used to calculate the local Coulomb friction and determine the surface condition, 'stick' or 'slip'. Related experiments are required for the measurement of the Coulomb friction coefficient.

2.4.5 Hertz contact spring

Besides the friction coefficient, the normal force is another important parameter for the friction force. The normal force may not be steady. When any fluctuation of the two contacting bodies takes place in the normal direction, they will approach each other in the direction normal to the contact surface without penetration. Due to the stiffness of the material, an additional normal force will be generated and added to the nominal load. The relation between the normal force $P > 0$ and the normal approach $\delta_H > 0$ can be represented by the stiffness of the Hertz spring k_H

$$k_H = \frac{\partial P}{\partial \delta_H} > 0. \tag{2.30}$$

According to Hertz theory (see Appendix B), this Hertz spring is non-linear, although for small fluctuations it can be linearised around the steady normal force.

2.5 Summary

For the purpose of squeal analysis, a friction model, considering adhering friction at small creepages, falling friction at large creepages and normal force fluctuation, is established. The adhering friction is mainly based on the numerical rolling contact model, Kalker's FASTSIM algorithm, which is appropriate for the condition with large spin. A heuristic falling function is used to weight the friction force in the gross sliding region. The coefficients in the falling function rely on the experimental results. The normal fluctuating force can be calculated using the Hertz contact spring.

However, there are two limitations associated with this friction model. One is that the adhering friction model, FASTSIM algorithm, is based on steady rolling contact, which may not be accurate in the stick-slip motion. Hence, the friction model is an approximation, especially when the sliding velocities are small in the 'stick' phase. The other limitation is related to the falling friction force in sliding. Although it is a common phenomenon and has been widely accepted, no theoretical model is available due to the complex mechanisms involved in the sliding process.

3. VEHICLE DYNAMICS – STEADY-STATE CURVING

3.1 Introduction

In the curve squeal modelling, some steady-state curving parameters, such as creepages, contact positions and normal contact forces, are required. A dedicated steady-state curving model presented in this chapter can provide these parameters. This is mainly based on the introduction in the book of Wickens [40]. Before the formulation of this model, it is necessary to review the long history of research on vehicle dynamics.

3.1.1 Review of railway vehicle dynamics

Redtenbacher [41] provided the first theoretical analysis of railway vehicle dynamics in 1855. His formula showed that a wheelset will be able to move laterally in a curve from the track centreline to the line termed the equilibrium line, because of the conicity on the wheel treads. However, this formula only represents the situation of an unconstrained wheelset in a moderate curve. For stability reasons, the wheelsets in a vehicle must be constrained in some way, such as by the wheel flange and suspension stiffnesses connecting them to the rest of the vehicle. It can be seen that the guidance is provided by the linear conicity only for very slightly curved track, whereas on sharper curves, switches and crossings the flanges become the essential mode of guidance [40].

The first practical theories, considering the friction forces, stemmed from the work by Mackenzie in 1883 [42]. His discussion was based on sliding friction but neglected the effects of wheelset conicity on curving. His calculations showed that the outer wheel flange exerts a lateral force, termed the gravity force, against the rail. This force is sufficient to overcome the friction of the wheel treads. It was generally supposed that all wheelsets run in flange contact with the outer rails of curves.

Many subsequent researchers developed the ideas of Mackenzie. Porter in 1935 [43] gave the most complete development of Mackenzie's theory. The principal considerations were that a vehicle consists of one or more axles, each with a rigid wheelbase connecting two wheels with conicity, and that wheel/rail forces are developed at the flange contacts and by sliding friction forces at all the wheel treads. For smaller curve radii, the leading outer and trailing inner flanges contact the rails. This was referred to as “constrained curving”. For greater curve radii, only the leading wheelset is in flange contact, referred to as “free curving”.

Boocock in 1969 [44] and Newland in 1968 [45] considered vehicles with coned wheelsets, and with yaw flexibility between the axles and the vehicle body or bogie frame. The wheel conicity enables a friction yaw torque to be developed which tends to yaw the wheelset to a ‘radial’ position, although this situation is usually not achieved owing to the presence of yaw restraining springs. It was assumed in this idea that the suspension elements, the wheel/rail contact geometry, and the relationships of creep force and creepages could be approximated by linear functions, outside which the theory became invalid.

On most curves, the analysis of curving of conventional vehicles must involve a consideration of important nonlinearities, i.e. the saturation of the friction forces and realistic wheel/rail geometric interaction in flange contact [40]. Elkins and Gostling gave the first comprehensive non-linear treatment of practical vehicles on curves in 1977 [46], in which numerical solutions were shown to give good agreement with full-scale experiments. Their treatment covered the nonlinearities caused by the movement of the contact patch across the rail and its subsequent change in shape, friction saturation and large wheel/rail contact angles in flange contact. Since their research was focused on steady-state curving behaviour, the inertia terms were not included.

From the 1980s, the simulations of vehicle dynamics gradually became available in powerful, validated and user-friendly commercial software packages, such as ADAMS, Vampire and Simpack. It is possible to carry out simulations of the dynamic behaviour of railway vehicles running on a real track. These software packages are now widely used in designing and improving railway vehicles.

3.1.2 About the steady-state curving model

Although the commercial software packages are available, to satisfy the demands of curve squeal research and to provide insight into the squeal excitation, it is preferable to have a self-contained vehicle simulation model, which can be programmed and integrated into the curve squeal model. Some important characteristics of this steady-state curving model are introduced as follows.

According to the survey of curve squeal experiments [7,9,14,16], squeal noise is the result of high frequency vibration of the wheel, up to several kilo-Hertz, but with very small vibration displacement in the scale of less than a millimetre. Compared with this high frequency vibration, vehicle dynamics concerns the responses of the vehicle at much lower frequencies, normally less than 100 Hz. Thus, the quasi-steady analysis of the vehicle dynamics is applicable for the squeal model, providing quasi-steady parameters related with wheel/rail interaction.

In this steady-state curving model, rigid bodies of the vehicle are connected to each other by flexible components of suspensions, i.e. springs and dampers, representing the vehicle. The vehicle is considered to run on a constant track section, which has a fixed curve radius and cant angle. The cross-section profiles of the contacting wheel tread and railhead are based on measured data that are assumed constant through the whole simulation process. The non-linear creepage-friction relationship adopted in the squeal analysis is also considered in the steady-state curving but not including the falling region. However, the definitions of sliding velocities and creepages are slightly different. Under most circumstances, the rigid motion of a wheelset is much more significant than that of the track. Therefore, for vehicle dynamics, the rail motion can be ignored. This is a treatment consistent with the definitions in the commercial software, e.g. Vampire [47].

3.2 Wheel/rail interaction

3.2.1 Wheel/rail geometry

Figure 3-1 shows the rear view of a wheelset on a track in a right-hand curve with a cant angle ϕ_0. The wheelset reference frame *oxyz* is defined on the track, with the origin *o* at the centre point of the line that connects the top points on the two rail profiles. The *z*-axis is normal to the cant plane and the *y*-axis is parallel to the cant. The lateral offset of the wheelset in the reference coordinates is u_2, and the roll angle about the *x*-axis is ϕ.

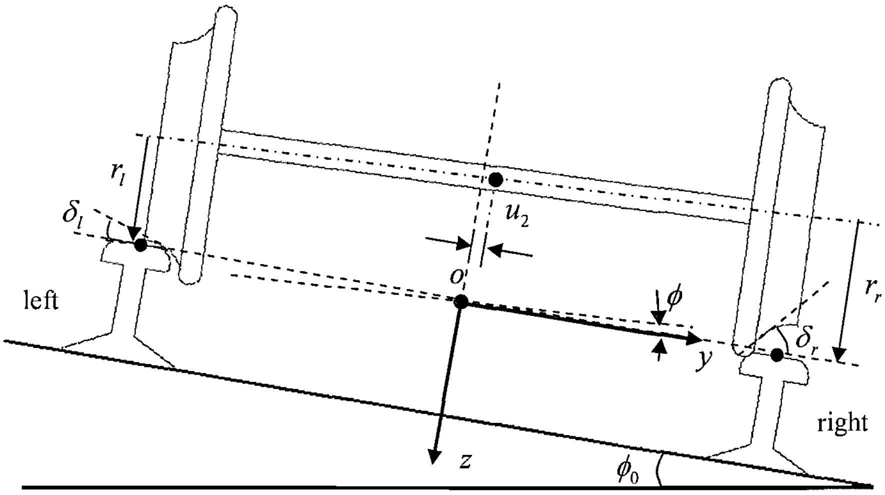

Figure 3-1 Lateral offset of a wheelset on a canted track.

The lateral offset of the wheelset will result in variations in the wheel/rail contact positions. The procedure for finding the wheel/rail contact positions is based on an iterative process with the following steps.

(i) Keep a sufficient gap between the wheelset and rails, which allows the wheelset to move and roll freely.

(ii) Move the wheelset laterally with a particular offset distance.

(iii) Rotate the wheelset with an assumed roll angle.

(iv) Find the possible contact points by determining the nearest distances between the corresponding wheel and rail profiles.

(v) Calculate the wheelset roll angle using the information of the two possible contact positions.

(vi) Check the difference between the assumed roll angle and the calculated one. If this difference is smaller than a specified tolerance, the possible contact points are correct. Otherwise, replace the assumed roll angle with the calculated one and go to step (iii).

Variations in the wheel/rail contact positions will lead to changes in other contact parameters. These contact results are calculated using the measured profiles of a Class 158 wheel (s1002 wheel profile) and a standard UIC 60 rail (installed on a canted ground plane with 1:20 slope). The parameters of the wheelset and track can be found in Appendix D and Appendix E, respectively. Figure 3-2 provides the wheel/rail contact positions with respect to the lateral offset of the wheelset. Additionally, the rolling radii of left and right wheels, r_l, r_r, are shown in Figure 3-3. The contact angles of left and right wheel/rail contacts, δ_l, δ_r, are shown in Figure 3-4. Finally, the rolling angles between the wheelset and track, ϕ, are shown in Figure 3-5. The wheel/rail contact results have been smoothed with a curve fit method and tabulated in terms of the lateral offset of the wheelset. In the simulations of this vehicle dynamics package, the contact results for each wheelset are searched out in this table according to the lateral position of the wheelset.

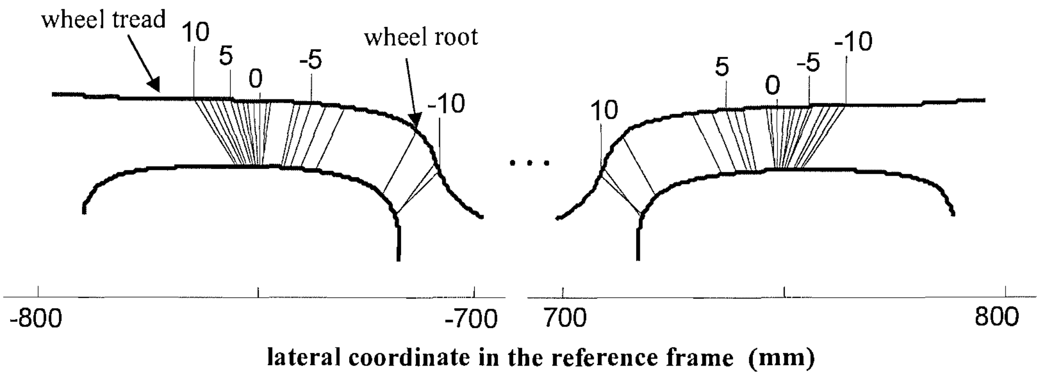

Figure 3-2 Wheel/rail contact positions in their own profiles with respect to the lateral displacement of the wheelset, from -10 mm to 10 mm with 1 mm interval. The wheel is unworn.

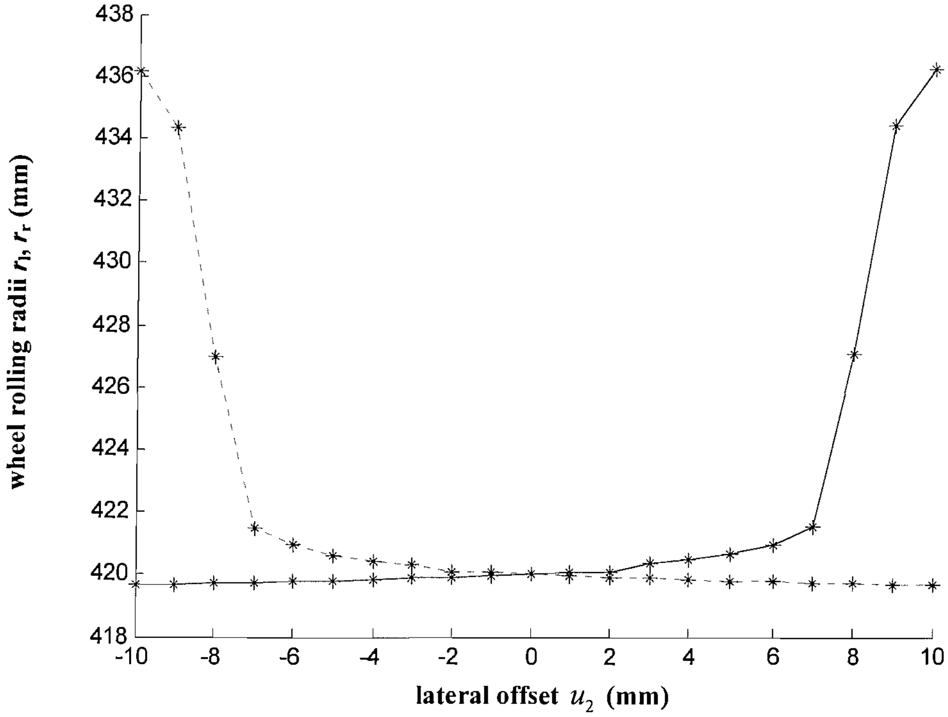

Figure 3-3 Wheel rolling radii with respect to the lateral displacement of the wheelset, —— right wheel, ------- left wheel.

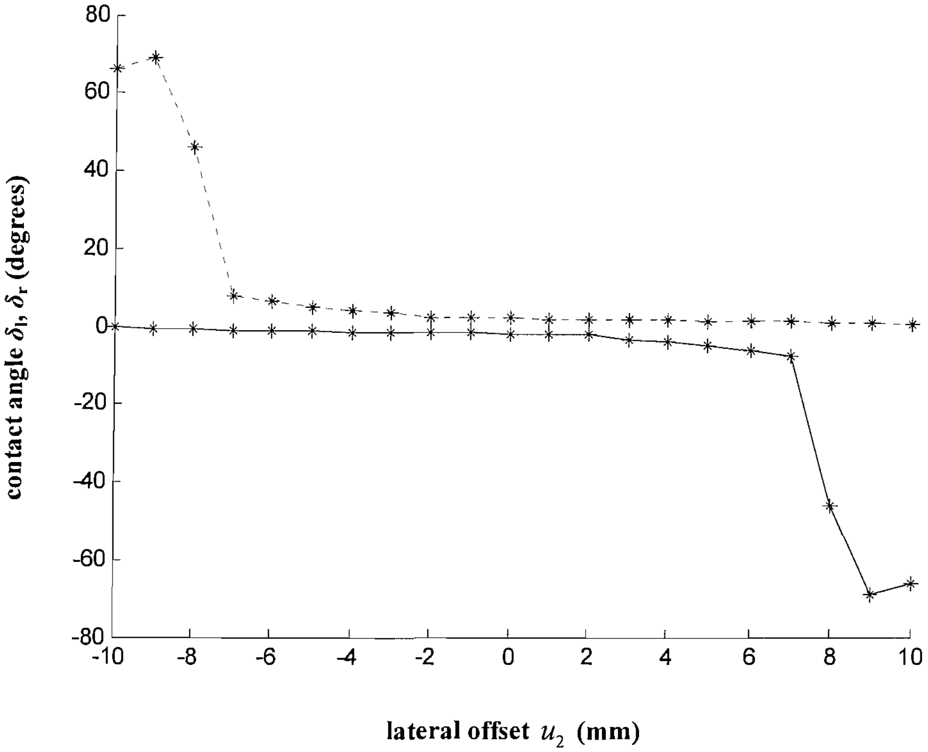

Figure 3-4 Wheel/rail contact angles with respect to the lateral displacement of the wheelset, —— right wheel, ------- left wheel.

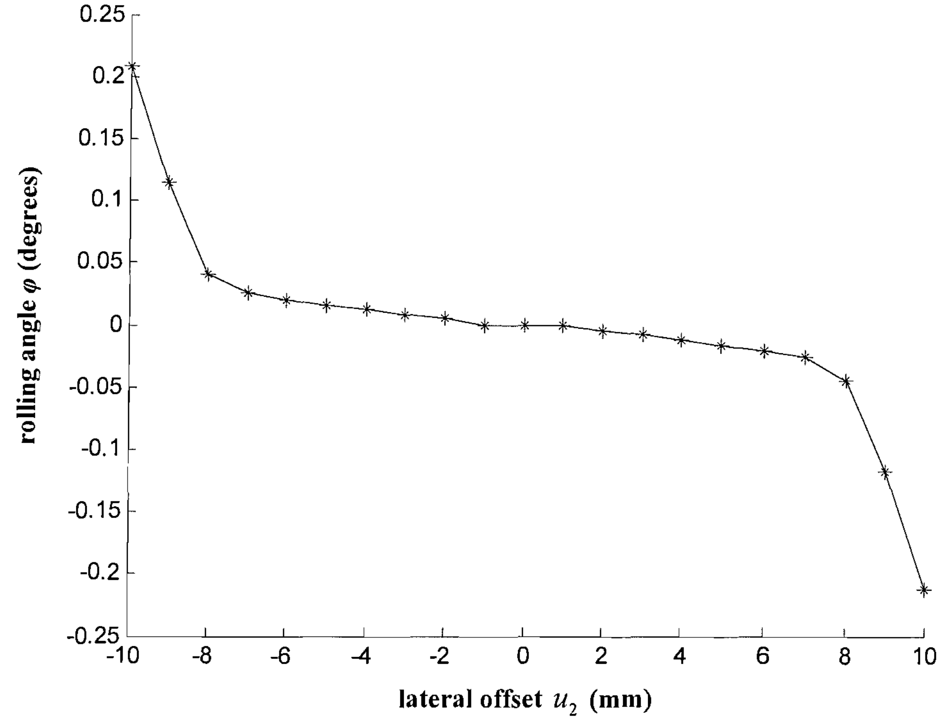

Figure 3-5 Wheelset rolling angle with respect to the lateral displacement of the wheelset.

Two significant zones, i.e. the linear zone and the flange zone, can be easily identified from the possible contact areas shown in Figure 3-2. In the linear zone, the coned region of the wheel treads contacts on the top of the railhead, so that the contact parameters, as shown in Figure 3-3 to Figure 3-5, are approximately in linear relationships with the lateral displacement. In the flange zone, one of the contact positions is concentrated on a small region of the wheel root and rail head with a contact angle of up to 70°, see Figure 3-4. Consequently, the contact parameters are all nonlinearly related to the lateral displacement. Since the left and right wheels are connected on a rigid axle, when one wheel is in the linear or transition zone, the other one may be in the flange zone.

3.2.2 Hertz contact patch

When a wheel is pressed against a rail, a normal load is transmitted and a contact area is formed. As the elastic deformation in the vicinity of the contact area is small compared with the contacting bodies, i.e. wheel and rail, its effect on the geometrical analysis described above can be neglected. Then, assuming that the wheel and rail are smooth, the curvatures of wheel and rail are approximately constant in the vicinity of the contact patch. The conditions for using Hertz's solution for contact patch calculation are satisfied. Under these assumptions, the contact area is elliptical, with the shape and orientation depending on the wheel and rail curvatures in the vicinity of the contact, and with the size depending on the normal load in the contact area. If a constant normal load of 42500 N is assumed to act on the Class 158 wheel and a standard UIC 60 rail, the semi-axes of the contact area, a (along the rolling direction) and b (transverse the rail), can be calculated with the Hertz theory as described in Appendix B. Figure 3-6 shows the results with respect to the lateral wheelset displacement, from -15 mm to 15 mm.

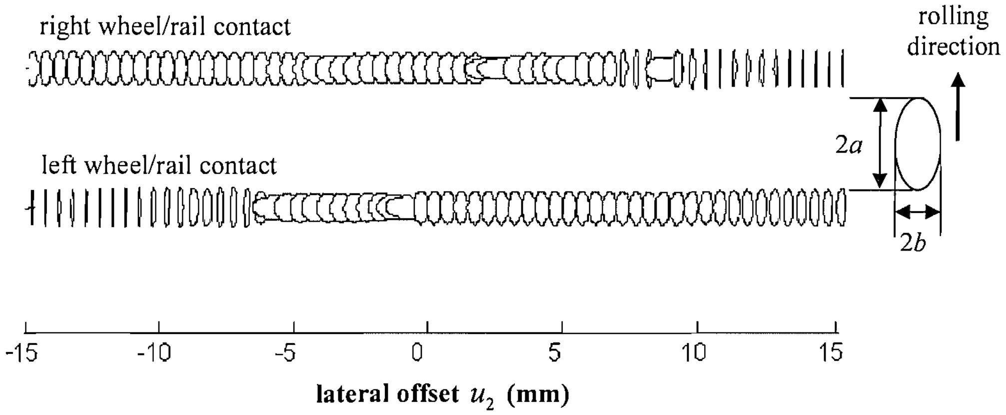

Figure 3-6 Schematic shape of contact patch with respect to the wheelset lateral displacement, with a constant normal force of 42500 N.

In the linear and transition zones, the contact patch shapes are elliptical and correspond to the assumptions of Hertz theory. The shape of contact patch is sensitive to the curvatures at the wheel/rail contact point. For the measured wheel/rail profiles adopted in the current simulations, the curvatures of the wheel and rail are not continuous. Therefore, the form of the contact patch may be discontinuous at some positions. In practice, the elastic deformation in the vicinity of the contact may lessen this discontinuity. In the flange zone with lateral offset $|u_2| > 10$ mm, however, the contact patch shapes have a large aspect ratio, i.e. $a/b > 10$. The assumptions of the Hertz theory are not strictly satisfied in this zone. Methods of analysis have been developed for this case by Nayak and Paul [48] and by Kalker [49]. Since this extreme flange contact does not occur in the normal curving behaviour, only Hertz theory is adopted in the steady-state curving model.

3.2.3 Creepages in the steady-state curving

The steady-state creepages at the wheel/rail contacts are important parameters in the squeal model. They are realised in the steady-state curving as follows.

3.2.3.1 Longitudinal creepage

In Figure 3-7(a), the instantaneous reference frame 1-2-3 is fixed at the instantaneous wheel/rail contact point **c**, with the 1-axis along the tangential direction of the track, the 2-axis along the transverse direction of the track, and the 3-axis normal to the track plane (with a cant angle to the horizontal plane). In this instantaneous reference frame, the translational speed of the wheel is measured at its centre, denoted by V ($V > 0$). This is consistent with the longitudinal velocity of the wheel if the yaw angle is very small ($< 2^\circ$), giving $V_1 = V$. The velocity of the rail is assumed zero, as discussed in Subsection 3.1.2. The wheel/rail contact point **c** will move with the wheel, so that the longitudinal velocity of the contact point **c** is also V_1.

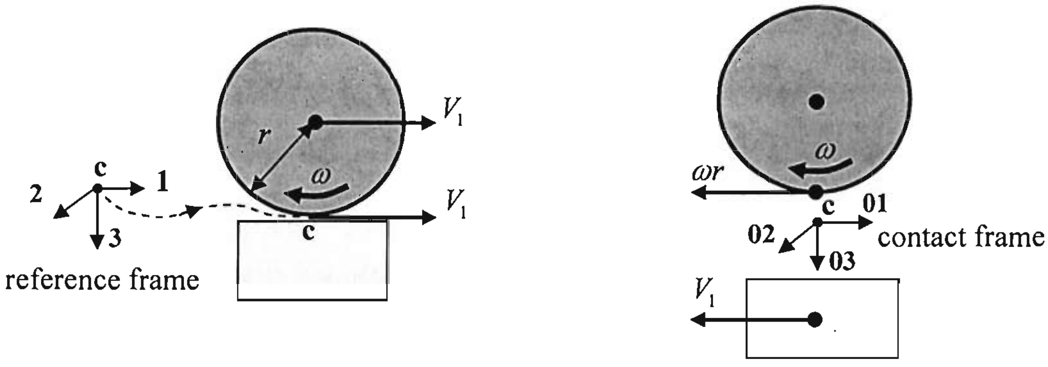

(a) (b)

Figure 3-7 Longitudinal sliding velocity between the wheel and rail, (a) in the reference frame, (b) in the contact frame.

The sliding velocities are formulated in the instantaneous contact frame 01-02-03 at the contact point **c**, as shown in Figure 3-7(b), with the 01-axis along the tangential direction of the curved track, the 02-axis along the transverse direction in the contact plane, and the 03-axis normal to the contact plane. The contact plane may have a contact angle inclined relative to the canted plane. In this contact frame, the rail is moving backwards through the contact point **c** with a velocity

$$V_{01}^{r} = -V_1 . \tag{3.1}$$

The wheel, which is rolling with a rotational speed ω ($\omega > 0$), has zero centre velocity in this contact frame, so that the wheel velocity at the contact point, V_{01}^{w}, can be expressed as:

$$V_{01}^{w} = -\omega r , \tag{3.2}$$

where r is the wheel radius. The sliding velocity V_{01}^{s} between wheel and rail at the contact point is defined as the wheel velocity minus the rail velocity [2]

$$V_{01}^{s} \equiv V_{01}^{w} - V_{01}^{r} = -\omega r + V_1 . \tag{3.3}$$

According to this definition, the longitudinal sliding velocity is negative for a wheel in traction (the extreme is $V_1 = 0$) and positive for a braked wheel (the extreme is $\omega = 0$). If the sliding velocity is zero, termed free rolling, from Eq.(3.3), the rotational speed will be given as

$$\omega = V_1 / r . \tag{3.4}$$

For a pair of wheels installed in a rigid wheelset axle, the longitudinal creepages on both wheels can be defined in a similar way as follows.

In a short time interval Δt, the vehicle will travel around a track segment corresponding to a curve angle $\Delta\Psi$. During this process, the speeds of the left wheel, V_l, the centre of the wheelset (considered as rolling velocity of the wheelset), V_0, and the right wheel, V_r, are different due to the different curve radii experienced:

$$\frac{V_l}{R_0 + l_0} = \frac{V_r}{R_0 - l_0} = \frac{V_0}{R_0} = \frac{\Delta\Psi}{\Delta t} , \tag{3.5}$$

---

[2] Note that this definition is conventional for the vehicle dynamics but has the opposite sign to those introduced in Chapter 2 (rolling friction model), Chapter 5 (squeal model) and Chapter 6 (squeal experiments on the twin-disc rig).

where l_0 is the half track gauge, representing the distance from the centre of the wheelset to the nominal wheel/rail contact point. From Eq.(3.5), the speed at the centre of the wheelset is

$$V_0 = (V_l + V_r)/2 . \tag{3.6}$$

If the left and right wheels are both under free rolling, from Eq.(3.4), there is the following relationship

$$\omega = \frac{V_l}{r_l} = \frac{V_r}{r_r}, \tag{3.7}$$

where r_l and r_r are the rolling radii of left and right wheels. Substituting V_l and V_r from Eq.(3.7) into Eq.(3.6), the rotational speed can be expressed by the speed at the centre of the wheelset:

$$\omega = 2V_0/(r_l + r_r), \tag{3.8}$$

which is an approximation for the rotational speed, because free rolling is not actually practical in tight curves. According to the definition of the longitudinal sliding velocity in Eq.(3.3), substituting V_l, V_r from Eq.(3.5) and ω from Eq.(3.8) into Eq.(3.3), the left and right longitudinal creepages in the vehicle dynamics are defined as [3]

$$\gamma_{1,l}^{*} \equiv \frac{V_{01,l}^{s}}{V_0} = \frac{V_l - \omega r_l}{V_0} = \left(\frac{R_0 + l_0}{R_0} V_0 - \frac{2V_0}{r_l + r_r} r_l\right) \Big/ V_0 = -\left(\frac{r_l - r_r}{r_l + r_r}\right) + \frac{l_0}{R_0}, \tag{3.9}$$

and

$$\gamma_{1,r}^{*} \equiv \frac{V_{01,r}^{s}}{V_0} = \frac{V_r - \omega r_r}{V_0} = \left(\frac{R_0 - l_0}{R_0} V_0 - \frac{2V_0}{r_l + r_r} r_r\right) \Big/ V_0 = \left(\frac{r_l - r_r}{r_l + r_r}\right) - \frac{l_0}{R_0} = -\gamma_{1,l}^{*} . \tag{3.10}$$

The longitudinal creepages of the left and right wheel/rail contacts have the same values but opposite signs. Hence, the approximation of rotational speed in Eq.(3.8) has limited error, because the sliding of the left and right wheels can be counteracted in the averaging calculation. In the above equations for longitudinal creepage, the first terms are due to the difference of the wheel rolling radii, and the second terms are due to the

---

[3] The * is used due to the difference in sign of the creepage definitions from Chapters 2, 5 and 6.

difference of curve radii between the contact points and the wheelset centre. If the wheelset is positioned in the centre of the track, the rolling radii are almost equal, $r_l = r_r$, therefore the left (outer in the curve) wheel has a positive creepage (in braking), while the right wheel (inner in the curve) has a negative creepage (in traction). A frictional torque is then generated to yaw the wheelset. When the wheelset moves to the left from the centre position (moving outwards in the curve), due to the conicity of the wheel treads the relationship between rolling radii is $r_l > r_r$. Obviously, the wheel profile conicity can somewhat reduce the wheel radii difference, which makes both left and right longitudinal creepages smaller.

3.2.3.2 Lateral creepage

If there is a yaw angle ψ between the rolling direction and the tangent of the curve, as shown in Figure 3-8(a), the rolling speed of the wheel has a component in the lateral direction. The yaw angle is normally very small, less than 2°, so that it will not influence the velocity of the wheel along the tangential direction of the track

$$V_1 = V\cos\psi \approx V. \tag{3.11}$$

However, the yaw angle will produce an additional lateral velocity of the wheel, which is expressed as

$$V_2 = V\sin\psi \approx V\psi. \tag{3.12}$$

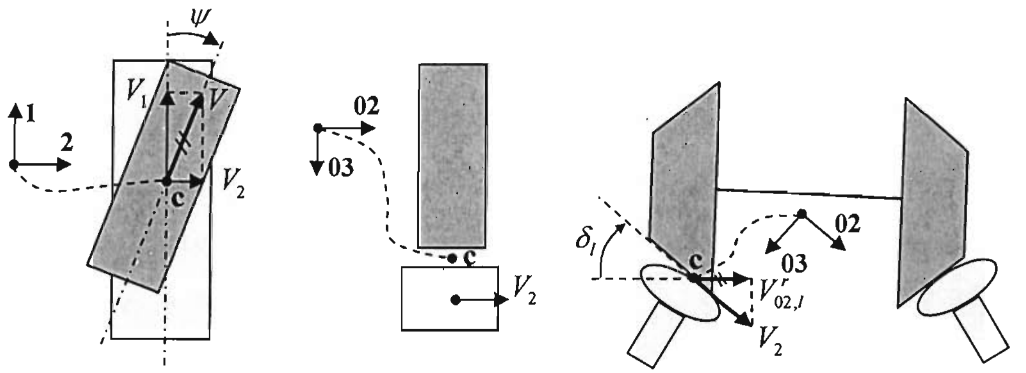

in the reference frame (a) | in the contact frame (b) | left with a contact angle right (c)

Figure 3-8 Lateral sliding velocities between the wheel and rail, (a) in the reference frame (plan view), (b) in the contact frame (rear view), and (c) in the contact frame with a contact angle (rear view).

In the reference frame 1-2-3, the lateral rail velocity is zero, while the lateral velocity of the contact point is the same as the moving wheel. In the contact frame 01-02-03, as shown in Figure 3-8(b), the lateral velocities of the wheel and rail are

$$V_{02}^{w} = 0, \tag{3.13}$$

and

$$V_{02}^{r} = V_2 = V\psi . \tag{3.14}$$

Considering a significant contact angle δ between the contact plane and the plane parallel to the axle of the wheelset, as shown in Figure 3-8(c), Eq.(3.14) must be revised to include the effect of the contact angle:

$$V_{02}^{r} = V\psi / \cos\delta . \tag{3.15}$$

Thus, the lateral sliding velocity is

$$V_{02}^{s} \equiv V_{02}^{w} - V_{02}^{r} = -V\psi / \cos\delta . \tag{3.16}$$

The lateral creepages for the left and right wheels in a wheelset can be expressed as

$$\gamma_{2,l}^{*} \equiv \frac{V_{02,l}^{s}}{V_0} = \frac{-V_l\psi / \cos\delta_l}{V_0} = -\frac{V_l\psi / \cos\delta_l}{V_0} \approx -\psi / \cos\delta_l , \tag{3.17}$$

and

$$\gamma_{2,r}^{*} \equiv \frac{V_{02,r}^{s}}{V_0} = \frac{-V_r\psi / \cos\delta_r}{V_0} = -\frac{V_r\psi / \cos\delta_r}{V_0} \approx -\psi / \cos\delta_r . \tag{3.18}$$

Obviously, the lateral creepages for left and right wheel/rail contacts are both determined by the yaw angle ψ. However, due to the possible difference between the left and right contact angles, as shown in Figure 3-4, the one with the larger contact angle (contact closer to the flange zone), will have a larger lateral creepage.

3.2.3.3 Spin creepage

Figure 3-9 shows that the spin sliding velocity is the component of the wheel rotational velocity ω, with its direction normal to the contact plane. For a contact angle δ

between the contact plane and the track plane, the spin creepages for the left and right contacts are

$$\gamma_{6,l}^{*} \equiv \frac{v_{06,l}^{w} - v_{06,l}^{r}}{V_0} = \frac{0-(-\omega \sin \delta_l)}{V_0} = \frac{2\sin \delta_l}{r_l + r_r}, \tag{3.19}$$

and

$$\gamma_{6,r}^{*} \equiv \frac{v_{06,r}^{w} - v_{06,r}^{r}}{V_0} = \frac{0-(-\omega \sin \delta_r)}{V_0} = \frac{2\sin \delta_r}{r_l + r_r}. \tag{3.20}$$

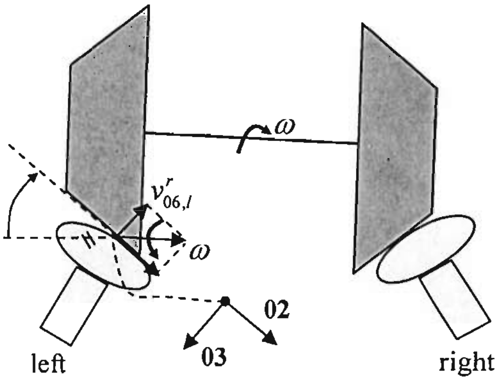

Figure 3-9 Spin motion between the wheel and rail

The spin creepages in the steady-state condition are mainly determined by the wheel/rail contact angles, with units: [m^{-1}]. Only when the wheel/rail contact takes place close to the wheel flange zone is the contact angle so large that the spin creepage cannot be ignored.

3.2.4 Friction model adopted in the calculations of the vehicle dynamics

When creep occurs in any of the three creep coordinates, longitudinal, lateral or spin, shear stresses are generated in the contact patch and creep forces are produced. The relations between the creepages and friction forces were discussed in Section 2.3. For small values of creepage, without spin, adhesion occurs over almost the complete wheel/rail contact area and there is a linear relationship between the friction forces and creepages. For large values of creepage, the wheel nearly or totally slips on the railhead surface. The relationships between the friction forces and creepages are then no longer linear. The friction forces are in the saturation zone and the values are limited by the

Coulomb friction force. If the spin is large, the friction is also non-linear. For vehicle dynamic analysis on straight track, the Shen-Hedrick-Elkins formula [38] is an appropriate creep-force model. This is analytical and includes the effects of small spin but is not accurate enough for the case with large spin. However, in the curving analysis, flange contact with large spin occurs at some wheel/rail contacts. Hence, FASTSIM [36], which accounts for the effects of large spin, is required in the steady-state curving model.

Although it is very important for the squeal analysis that the friction forces fall for large sliding velocities, this property does not play a significant role in the vehicle dynamics. Xie *et al.* [51] introduced the falling friction into curving calculations by using Simpack. The curving results were almost the same as those from the friction model without falling friction. Hence, the conventional FASTSIM algorithm, without falling friction, is adopted for the current steady-state curving model.

3.2.5 Wheel/rail interaction forces

When a vehicle is running on the track, the external forces are mainly due to the interaction between the wheel and rail. The wheel/rail interaction forces exist in the contact plane, including the contact force normal to the contact plane, the spin moment about the normal to the contact plane and the tangential friction forces in the contact plane. To calculate the friction forces, the normal contact force that determines the size of the contact patch is determined first. In steady-state curving analysis, if the position of a wheelset is near the track centreline, the contact angles of both left and right contacts are small and the normal forces are approximately equal to the resultant value of gravity and centripetal forces. However, if one of the contact points is close to the flange zone, the difference between left and right wheel/rail contact angles is great enough to make the normal force at each contact patch different. The assumed normal force is therefore adjusted using an iteration process, see Appendix F.

3.3 Vehicle dynamics

Most modern railway vehicles are four-axle vehicles with a body and two bogies. Each bogie has a frame and two wheelsets. The wheelsets and the bogie frame are connected through a primary suspension. The bogies support the vehicle body usually by means of a secondary suspension, but there is no direct connection between the bogies. The bogied vehicle model discussed here is used to reveal the basic principles of the steady curving motion. In Figure 3-10 and Figure 3-11, a bogied vehicle is shown under its initial conditions in a curve. The curving behaviour of all components, including four wheelsets (denoted '1 to '4'), two bogies (denoted 'b' and 'd') and the vehicle body (denoted 'c'), are analysed in their local coordinates, with the origins at their mass centre, the *y*-axes along the radial direction of the curved track and pointing inwards, and the *z*-axes normal to the canted track plane and pointing downwards. The positions of suspension components are shown in Figure 3-10 and Figure 3-11, by springs with dampers (not shown) installed in parallel. It is obvious that the bogied vehicle under these initial conditions may not be in equilibrium. The steady-state curving behaviour can be obtained by step-by-step integration.

The minimum number of DOF required to describe the steady-state curving behaviour of this bogied vehicle is 17, including the lateral motion y, yaw ψ and roll ϕ of one vehicle body, two bogies, and the lateral motion and yaw of four wheelsets [4]. Hence, the motion of the bogied vehicle is defined by a set of 17 generalised coordinates, $\{\mathbf{Q}_\mathrm{v}\}=[y_1,\psi_1,y_b,\phi_b,\psi_b,y_2,\psi_2,y_c,\phi_c,\psi_c,y_3,\psi_3,y_d,\phi_d,\psi_d,y_4,\psi_4]^\mathrm{T}$. The equations of motion in these generalised coordinates are

$$[\mathbf{A}_\mathrm{v}]\{\ddot{\mathbf{Q}}_\mathrm{v}\}+[\mathbf{D}_\mathrm{v}]\{\dot{\mathbf{Q}}_\mathrm{v}\}+[\mathbf{E}_\mathrm{v}]\{\mathbf{Q}_\mathrm{v}\}=\{\mathbf{F}_\mathrm{v}\}, \tag{3.21}$$

---

[4] In the commercial software, e.g. Vampire and Simpack, a conventional vehicle model will include the vertical motions of wheelsets, bogies and vehicle bodies, and the pitch motions of vehicle bodies, as well as those motions included in the current steady-state curving model. These additional motions mainly result from the vertical undulation of the track in the running direction. This is avoided in the steady-state curving analysis by assuming a constant smooth profile of track.

where $[\mathbf{A}_v]$ is the inertia matrix, $[\mathbf{D}_v]$ is the damping matrix, $[\mathbf{E}_v]$ is the stiffness matrix and $\{\mathbf{F}_v\}$ is the external force vector, provided in Appendix D.

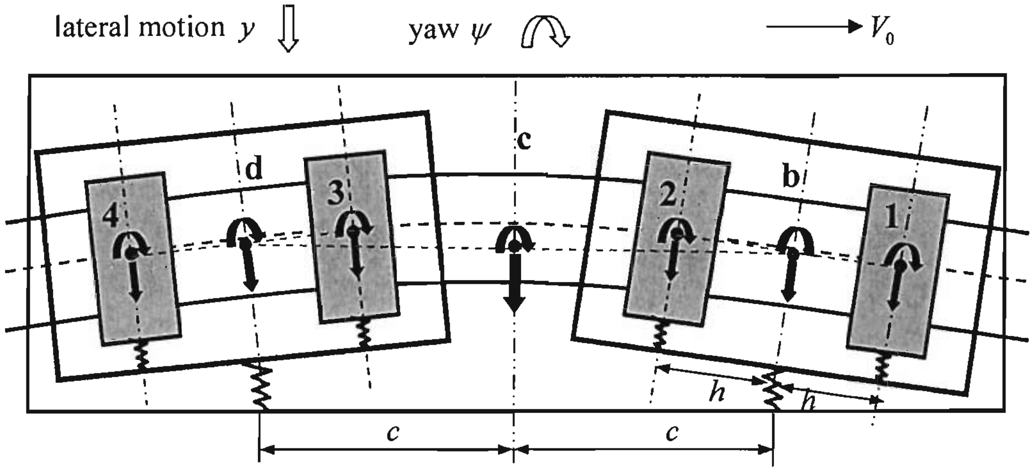

Figure 3-10 Definition of the reference points and coordinate systems of main components of an idealised bogied vehicle: under the condition in which the primary suspension springs are relaxed and the secondary suspension springs are in their initial positions.

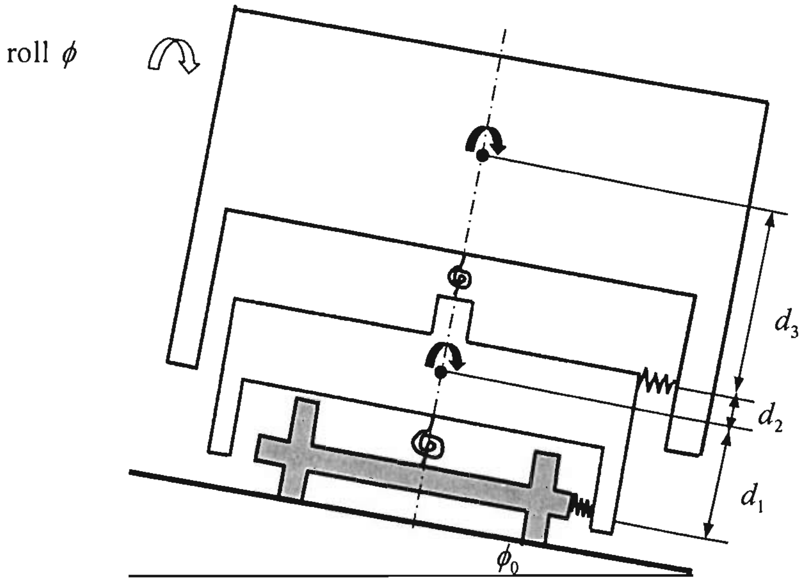

Figure 3-11 Rear view of the bogied vehicle.

The track in a curve has an appropriate cant angle ϕ_0, providing all or part of the centripetal force for curving. In Figure 3-12, the centripetal acceleration a_g provided by the gravity is

$$a_g = g\tan(\phi_0)\,, \tag{3.22}$$

where g is the acceleration due to gravity. For the case with a vehicle speed V_0 and a curve radius R_0, the centripetal acceleration a_c required for the curving vehicle is

$$a_c = \frac{V_0^2}{R_0}. \tag{3.23}$$

If the centripetal acceleration can be totally provided by the gravity, having $a_c = a_g$, the cant angle must be

$$\phi_0 = \arctan\left(\frac{V_0^2}{R_0 g}\right). \tag{3.24}$$

On a specified curved track with a curve radius R_0, for different vehicle speeds V_0, the fixed cant angle ϕ_0 may provide less (cant deficiency) or more (cant surplus) centripetal acceleration than that required. Under these circumstances, the wheel/rail contact forces will be involved in the balance of lateral forces.

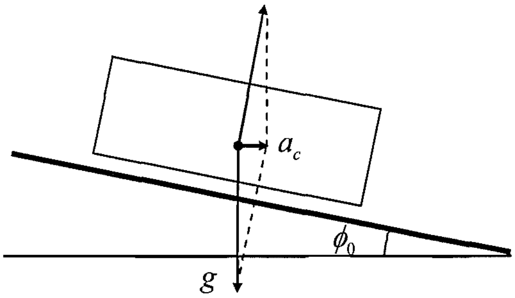

Figure 3-12 Effects of cant angle in a curve.

3.4 Results and discussion

The steady-state curving simulation involves simulating a quasi-steady time-history of vehicle motion in a curve via step-by-step integration. If the simulation process is convergent, the integration process can start from arbitrary reasonable initial positions and finally provide the quasi-steady results. Considering the non-linear characteristics of the wheel/rail contact forces, a fourth order Runge-Kutta integration algorithm is applied in the integration.

An unconstrained wheelset, a single bogie and a bogied vehicle are considered in turn. The unconstrained wheelset is the simplest model used to explain the curving behaviour of a wheelset that is driven only by the wheel/rail interaction forces, without the constraint of suspensions. The curving behaviour of a bogie is not only affected by the wheel/rail interaction forces but also constrained by the stiffness forces from the primary suspensions. For the bogied vehicle, since the resistance of the secondary suspension to the bogie rotation is relatively low, the curving behaviour of the leading and trailing bogies is similar. The analysis of the bogied vehicle is focused on a comparison with the curving behaviour of a single bogie.

3.4.1 Curving behaviour of an unconstrained wheelset

An unconstrained wheelset has two degrees of freedom, the lateral movement y of the centre of the wheelset mass, and the yaw angle ψ about the axis normal to the track plane. Its curving behaviour converges in a process shown in Figure 3-13.

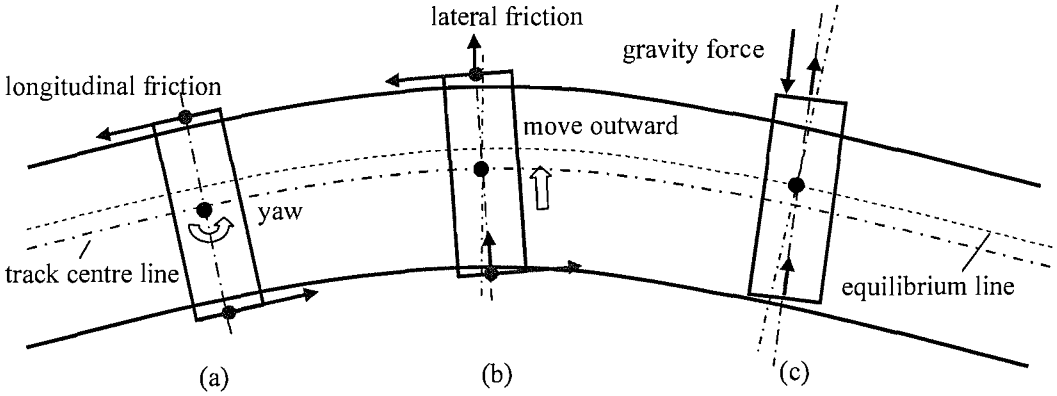

Figure 3-13 An unconstrained wheelset on a curve: (a) yawing motion; (b) moving outward; (c) the conditions of force balance.

When a wheelset is running from a straight track into the curved track, as shown in Figure 3-13(a), the wheelset is initially positioned in the track centreline without yaw, having $y = \psi = 0$. Both wheel/rail contacts are limited to the linear zone, having $r_l = r_r$ and $\delta_l = \delta_r = 0$. According to the longitudinal creepage given in Eq.(3.9) and Eq.(3.10), the left longitudinal creepage is positive and the right longitudinal creepage is negative. The corresponding friction forces (opposite to the creepage) will thus produce a torque.

In Figure 3-13(b), the torque rotates the wheelset to generate a yaw angle. According to the lateral creepages given in Eq.(3.17) and Eq.(3.18), this yaw angle results in a lateral creepage and consequently a resultant lateral friction force, forcing the wheelset to move outward in the curve.

In Figure 3-13(c), the outward movement of the wheelset will increase the left contact angle, which results in a gravity force (which can be considered as a component of the normal contact force) preventing the wheelset from further outward movement. Hence, the force balance in the lateral direction can be reached. In the yaw direction, the yaw torque can be eliminated only if the longitudinal friction forces are zero. This condition can be satisfied when the wheelset is located at the position of the so-called equilibrium line, outward of the track centreline, where the difference of left and right rolling radii due to the coned wheel profile can counteract the difference of the curve radii between the left and right contacts. The tighter the curve, the greater becomes the distance between the equilibrium line and the track centreline, and consequently the yaw angle.

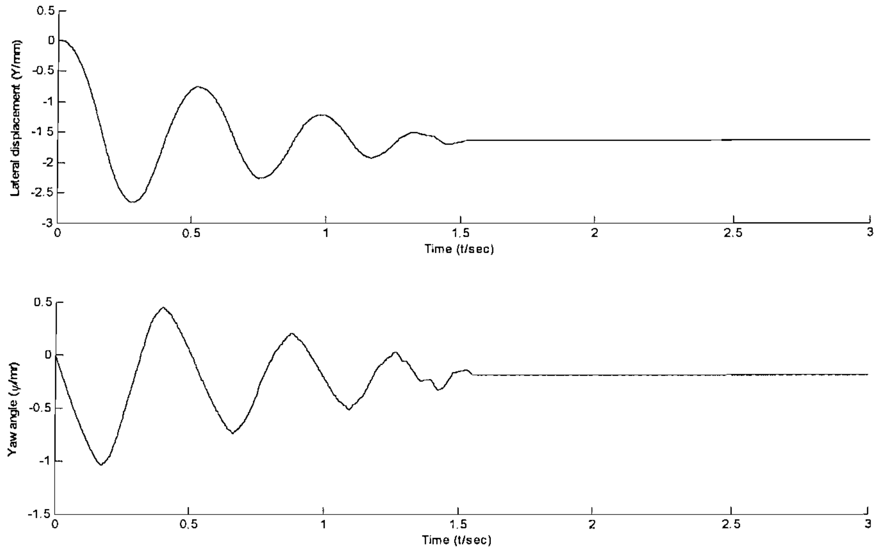

Figure 3-14 Steady-state curving behaviour of an unconstrained wheelset in a uniform curve with zero cant deficiency. The curve radius is 2000 m, the wheelset speed is 20 m/s and the parameters of the wheelset are listed in Appendix D.

Due to the strong coupling between the lateral motion and yaw, the nonlinearity of the wheel/rail contact geometry and the saturation of friction, the converging process is complex. In Figure 3-14, the simulation results of a unconstrained wheel negotiating a large curve radius of 2000 m are provided. The wheelset is initially positioned at the centre of the track without yaw, $y=\psi=0$. After several decaying oscillations, it converges to the steady-state curving behaviour, with a small negative lateral offset (outward in the curve) and a very small negative yaw angle because of the large curve radius. If the curve is very tight, however, the amplitude of fluctuation in the yaw and lateral motions will increase to reach the flange contact.

In general, in the steady-state curving behaviour of an unconstrained wheelset at its balance speed (zero cant deficiency), the wheelset axis is kept near the radial line while it moves towards the outside of the curve. Obviously, the creep forces help the unrestrained wheelset move to its steady-state position.

3.4.2 Curving behaviour of a bogie

In practice, vehicles are assembled with several wheelsets in a frame, e.g. two wheelsets in a bogie. These wheelsets are connected to the frame by suspensions that include springs and dampers. The simplest 'vehicle' is a bogie with two wheelsets, a frame and a primary suspension connecting the wheelsets and the frame, the same form as a two-axle vehicle. In curving, the wheelsets in the bogie cannot move freely to the equilibrium position or rotate to achieve radial alignment like unconstrained wheelsets, but they are constrained by the stiffnesses.

3.4.2.1 Under general conditions

In general, each wheelset in a bogie tends to be driven by its friction forces from arbitrary initial conditions to its steady-state curving conditions, as discussed for the unconstrained wheelset. However, these two wheelsets are actually coupled by the stiffnesses between the bogie frame and the wheelsets. The steady-state curving behaviour of the bogie can be reached when all of the external forces and torques acting on both wheelsets are balanced. The converging process from the relaxed initial conditions in a straight track to the particular curving conditions in a curved track is shown schematically in Figure 3-15.

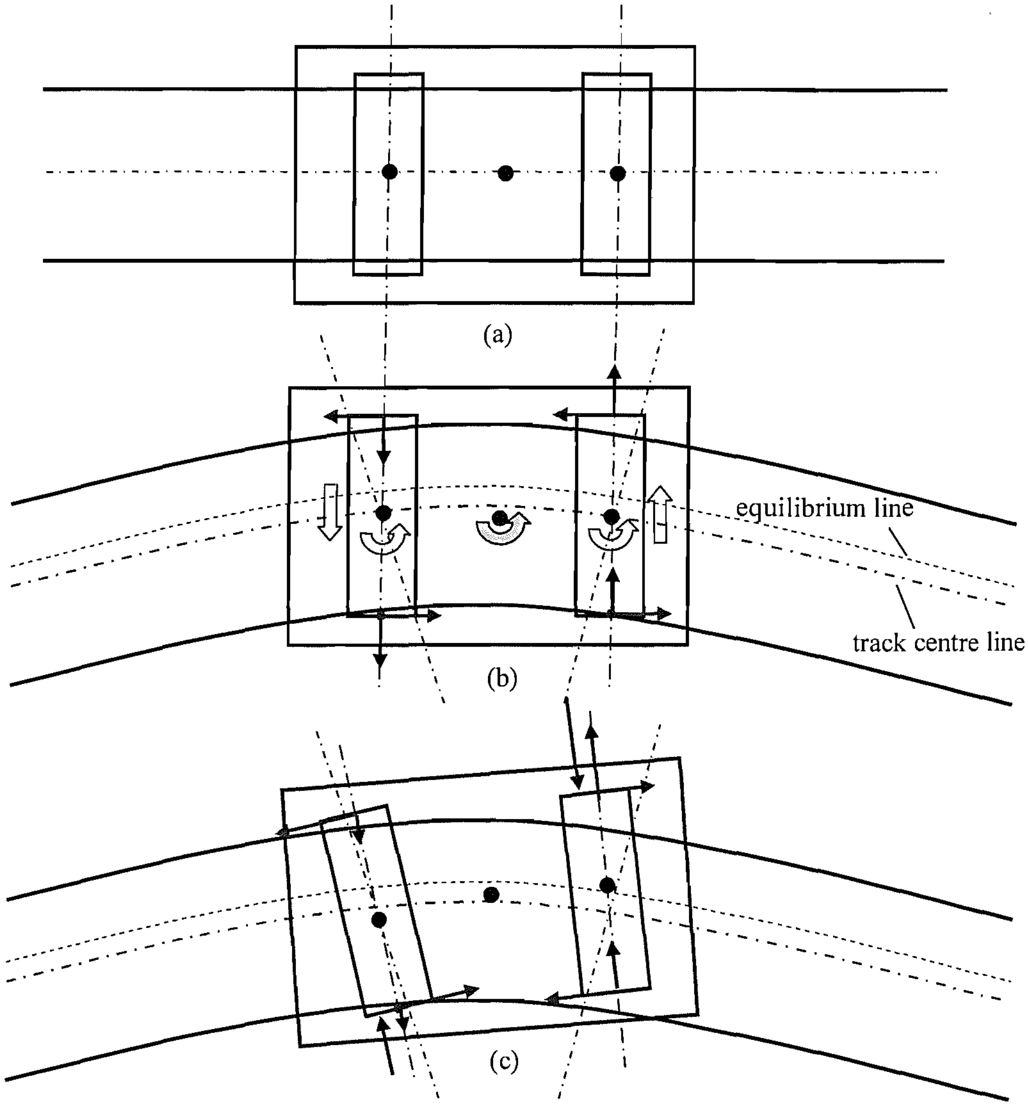

Figure 3-15 A bogie on a curve, (a) bogie on the straight track before entering the curve, (b) friction forces acting on the bogie before it is in balance, (c) curving behaviour when the bogie is in balance.

In Figure 3-15, a bogie runs from a straight track suddenly into a curved track. The initial conditions of the bogie in a curve can be considered the same as those in the straight track, as shown in Figure 3-15(a). On the curve, the equilibrium line is not coincident with the track centreline, which leads both wheelsets to produce (negative) frictional torques and consequently a resultant torque acting on the bogie through the suspensions, as shown in Figure 3-15(b). Initially, the leading wheelset experiences a negative yaw angle while the trailing wheelset experiences a positive one, which produces opposite lateral creepages and corresponding friction forces on the wheelsets, pushing the leading one outwards and the trailing one inwards.

The negative frictional torque at each wheelset then increases the negative yaw angle of the leading wheelset while it decreases the positive yaw angle of the trailing wheelset. This results in the increment of the outward lateral friction force at the leading wheelset but the decrease of the inward lateral friction forces at the trailing wheelset. Hence, the leading wheelset moves outwards quickly and may reach the left flange contact zone. If the leading wheelset moves outward beyond the equilibrium line, its frictional torque will change from negative to positive, while the trailing wheelset will remain and even increase its negative frictional torque. Finally, the balance of these two frictional torques acting on the bogie will be achieved, as shown in Figure 3-15(c).

In the lateral direction, due to the larger lateral friction force, the leading wheelset will move closer to the flange zone than the trailing one, and consequently the outer wheel will have a greater contact angle and a greater gravity force. The balance of lateral forces in the whole bogie normally relies on the leading wheelset, and the trailing wheelset is 'free'. If the curve is very tight, the positive yaw angle of the trailing wheelset may be large enough to produce a friction force to push it into flange contact at the right wheel. Normally, however, only the leading wheelset experiences flange contact.

3.4.2.2 Cant deficiency

Curving at high speeds with cant deficiency means that the wheelsets must generate additional lateral forces to compensate for part of the centrifugal force. Compared with the case of no cant deficiency, the leading and trailing wheelsets move outwards to achieve higher positive gravity forces. Both wheelsets tend to yaw in the positive direction, decreasing the negative yaw angle of the leading wheelset and increasing the positive yaw angle of the trailing one. This tends to lessen a bit the negative lateral friction forces (pointing outwards in the curve) and consequently make the resultant lateral force acting on the bogie positive (pointing inwards in the curve). A comparison of the curving behaviour between the cases with and without cant deficiency is shown schematically in Figure 3-16.

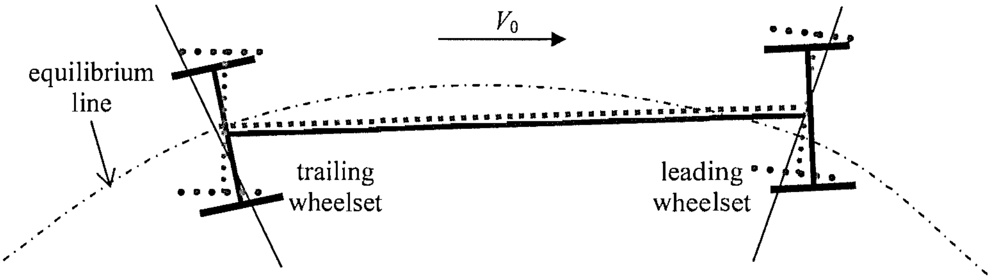

Figure 3-16 Schematic curving behaviour of the wheelsets of a bogie, —— no cant deficiency, ----- with cant deficiency.

3.4.2.3 Non-linear analysis

On sharp curves, the displacements of all or some of the wheelsets take up a significant proportion of the flange-way clearance, which means that flange contact can exist. The wheel/rail geometry cannot be represented by simple linear functions and the actual curvatures, contact angles and rolling radii must be taken into account. The contact angles may be large, giving rise to large amounts of spin, and the difference between left and right contact angles results in the normal contact forces having significant components in the lateral direction. When the contact patch moves across the rail and changes in shape, as shown in Figure 3-6, the variation of the contact patch influences the magnitude of the creep forces. As the creepages and spin may be large, creep saturation may occur. Hence, it is necessary to consider the solutions of the full non-linear equations of motion and adopt numerical methods to solve these complex non-linear cases.

3.4.3 Curving behaviour of a bogied vehicle

3.4.3.1 General analysis

A bogied vehicle described by the parameters in Appendix D, is simulated here. It has two bogies connected by the vehicle body through secondary suspensions. The curve radius is $R_0 = 225\,\mathrm{m}$, which is so tight that squeal may happen. The vehicle speed is $V_0 = 15\,\mathrm{m/s}$ and the cant deficiency is zero. The Coulomb friction coefficient is taken as $\mu_0 = 0.3$. The friction model is using FASTSIM. The simulation is started from the initial conditions with every coordinate in its zero position and lasts 1 second. In this case, the yaw stiffness between the bogies and the vehicle body is zero, so that the curving behaviour of the leading and trailing bogies is similar. Only the results of the leading bogie and the vehicle body are shown in Figure 3-17 to Figure 3-20.

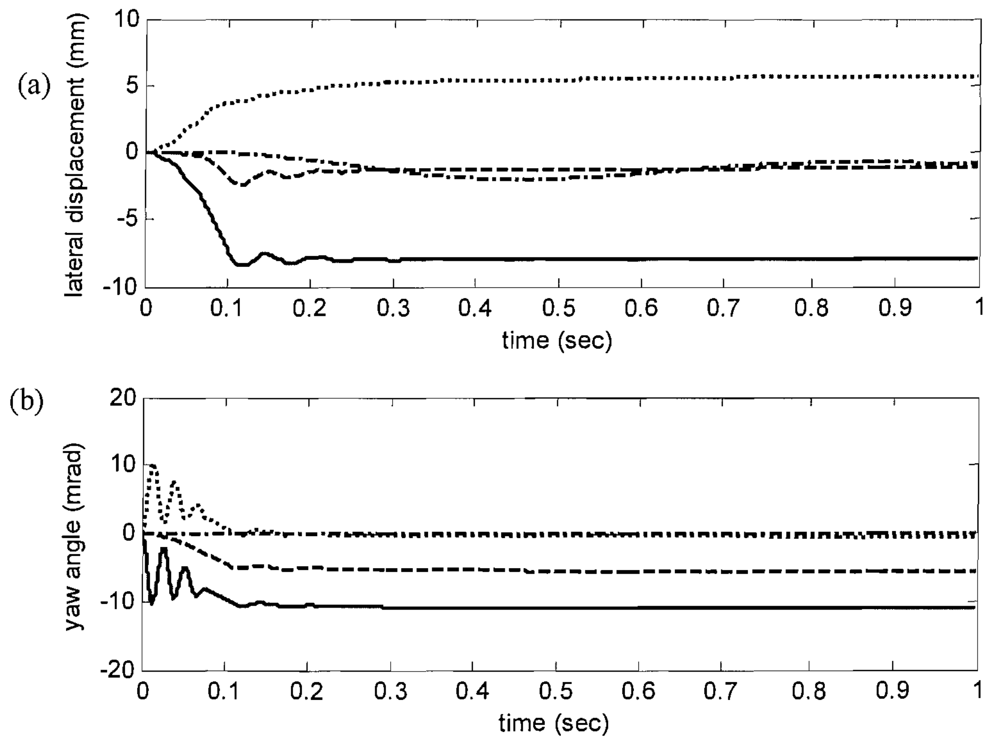

Figure 3-17 Curving behaviour of a bogied vehicle, —— leading wheelset, ······ trailing wheelset, ------ leading bogie, — · — vehicle body, (a) lateral displacement, (b) yaw angle.

In Figure 3-17, the leading wheelset moves outward (negative displacement) into flange contact and has a yaw angle of -12 mrad or -0.7°, while the trailing wheelset moves inward in the curve without the flange contact and has almost zero yaw angle (along the radial direction in the curved track). The behaviour of the bogie frame is almost the average of that of the two wheelsets. Since there is no yaw stiffness in the secondary suspensions, the vehicle body can remain radial to the track whatever the yaw angles of the two bogies. The lateral offset of the vehicle body is also close to zero, which means its mass centre stays in its initial position, as shown in Figure 3-11. The steady-state results are reached after about 0.5 second, as shown in Figure 3-18 to Figure 3-20. These show the creepages, wheel/rail normal contact forces and contact positions respectively.

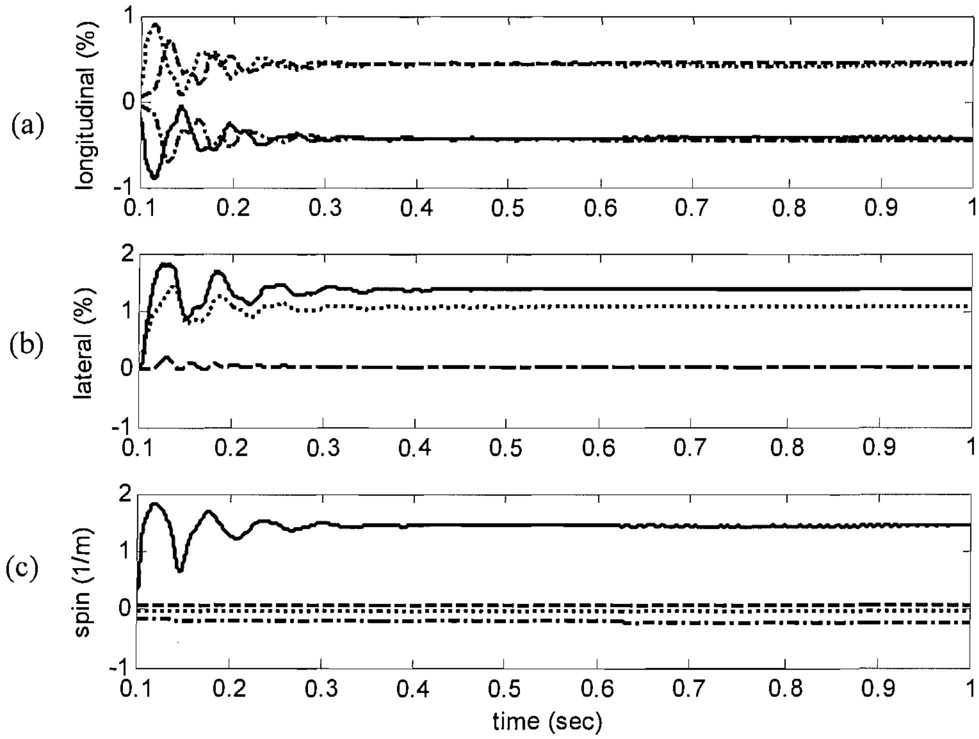

Figure 3-18 Steady-state creepages of a bogied vehicle at wheel/rail contacts: —— leading outer, ······ leading inner, ------ trailing outer, — · — trailing inner, (a) longitudinal creepage; (b) lateral creepage, (c) spin creepage.

In Figure 3-18(a), as in the discussion in the curving behaviour of a bogie, the left and right longitudinal creepages of the leading wheelset are opposite to the corresponding ones in the trailing wheelset. Thus, two frictional torques with opposite directions are in balance within the bogie. In Figure 3-18(b), the negative yaw angle of the leading wheelset produces negative lateral creepages at both left and right wheel/rail contacts. As the leading left wheel is in flange contact with a large contact angle, the lateral creepage at the leading left contact is greater than that at the leading right contact. The zero yaw angle of the trailing wheelset indicates no lateral creepage. Significant spin can be found in the leading outer (left) wheel/rail contact, as shown in Figure 3-18(c).

Besides these creepages, the normal contact forces at each wheel/rail contact patch are required to determine the friction forces. Because of the different contact angles, the normal force in each wheel/rail contact is different, as shown in Figure 3-19.

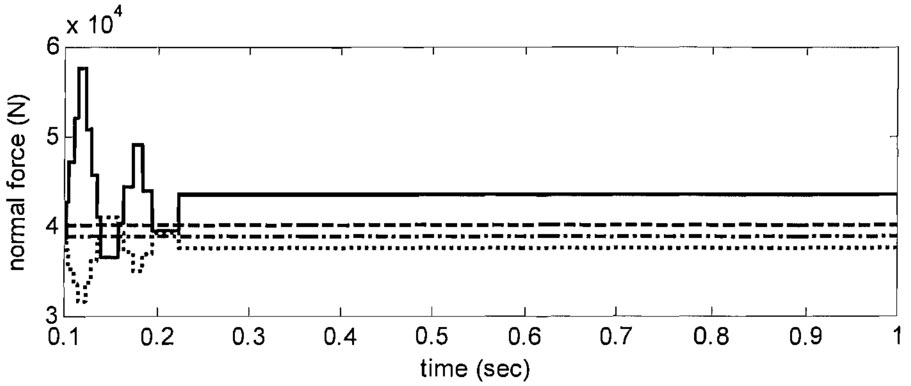

Figure 3-19 Steady-state normal contact forces of a bogied vehicle, —— leading outer, ······ leading inner, ------ trailing outer, — · — trailing inner.

The normal force is obtained through iteration described in Appendix F, which is started from the nominal normal force – the weight of the whole vehicle averaged on each wheel/rail contact patch. The nominal normal force of the current case is about 40 kN. Normally the greater the contact angle, the larger the normal force, i.e. a large normal force at the leading outer contact due to flange contact. Additionally, the flange contact at the leading outer wheel can induce roll of the leading wheelset, and consequently the bogie. In the trailing wheelset, because each wheel/rail contact is far from the flange, there is a small difference between the left and right normal forces. This difference is mainly due to the vertical suspension forces from the bogie in roll. Since the normal forces converge to their steady-state values in the check of the normal force, the 'stair steps' in the initial time steps are due to the error allowance, here set to be 10%.

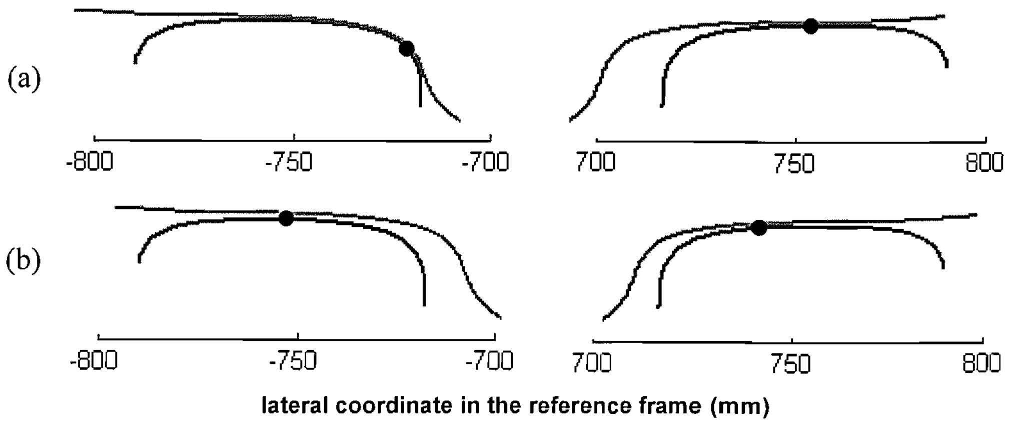

Figure 3-20 Steady-state wheel/rail contact positions in the reference (track) frame, (a) leading wheelset, (b) trailing wheelset.

The wheel and rail profiles in the steady-state curving are assumed to be constant and known. If the contact positions are obtained, as shown in Figure 3-20, after some necessary transforms between wheelset and wheel/rail coordinates, the parameters of wheel/rail interaction, e.g. contact angles, dimensions of contact patches, can be obtained.

3.4.3.2 Influence of curve radius

The curving behaviour for two cases with different curve radii, $R_0 = 225$ m and $R_0 = 150$ m, are compared with each other in Figure 3-21. Other parameters are the same: the vehicle speed is $V_0 = 15\,\text{m/s}$, the dynamic friction coefficient is $\mu_0 = 0.3$ and the cant deficiency is zero. The simulations are started from the initial conditions of every coordinate in its zero position and last 1 second.

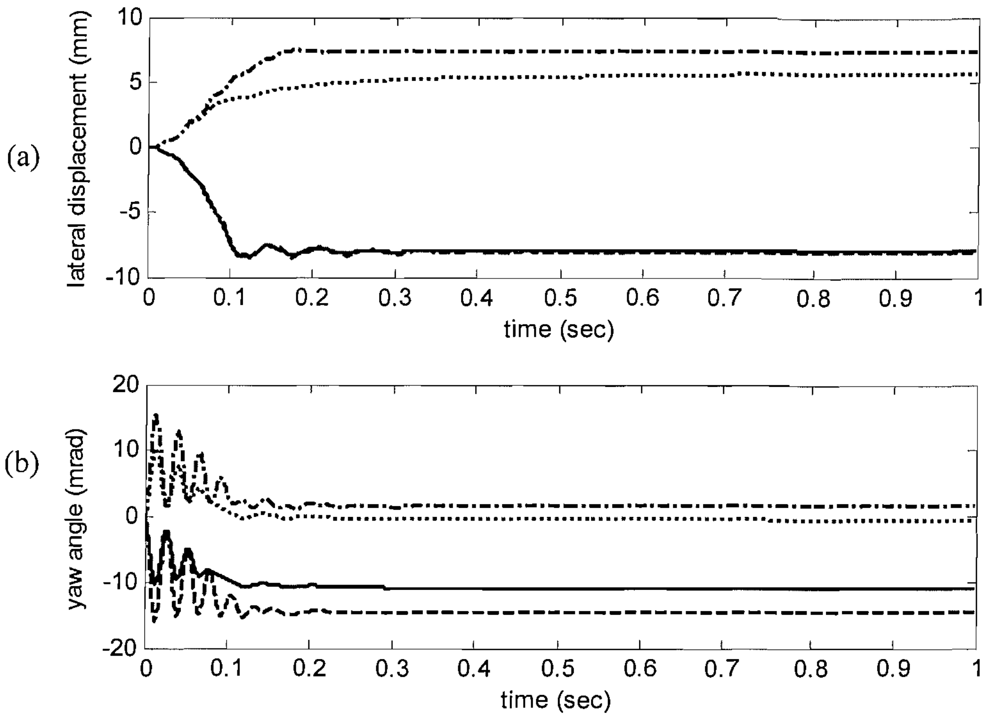

Figure 3-21 Comparison of the curving behaviour of the leading and trailing wheelsets in a bogie vehicle with different curve radii: —— leading wheelset, R_0 = 225 m, ------ leading wheelset, R_0 = 150 m, ······ trailing wheelset, R_0 = 225 m, — · — trailing wheelset, R_0 = 150 m; (a) lateral displacement; (b) yaw angle.

In the case of 150 m curve radius, both the leading and trailing wheelsets are in flange contact, termed 'constrained curving'. However, in the case of the larger curve radius of 225 m, only the leading wheelset is in flange contact, termed 'free curving'. The smaller curve radius increases the yaw angles of both wheelsets. Hence, a smaller curve radius means a larger yaw angle of the leading wheelset and a possible yaw angle and flange contact in the trailing wheelset. If the cant deficiency exists in curving, the tendency discussed in the single bogie case, as shown in Figure 3-16, is still valid for the bogied vehicle.

3.5 Validation of the vehicle-dynamic model

The validation of the current steady-state curving model is carried out in two ways: (1) comparison of the curving behaviour with a 17-DOF vehicle provided by Wickens [40] (called the Wickens model); (2) comparison of the curving behaviour with an accompanying example in Vampire [47], i.e. Class 158 DMU vehicle (called the Vampire model).

3.5.1 Comparisons of the curving behaviour with the Wickens model

The advantage of adopting the first way is that the parameters of the Wickens model can be directly used for validation, as given in Appendix D. The validation is carried out by adopting the curving case with the following parameters: curve radius $R_0 = 225$ m, vehicle speed $V_0 = 15$ m/s, Coulomb friction coefficient $\mu_0 = 0.3$ and zero cant deficiency. The results of curving behaviour of the Wickens model, including the lateral displacements and yaw angles, are shown in Figure 3-22 and Figure 3-23, respectively.

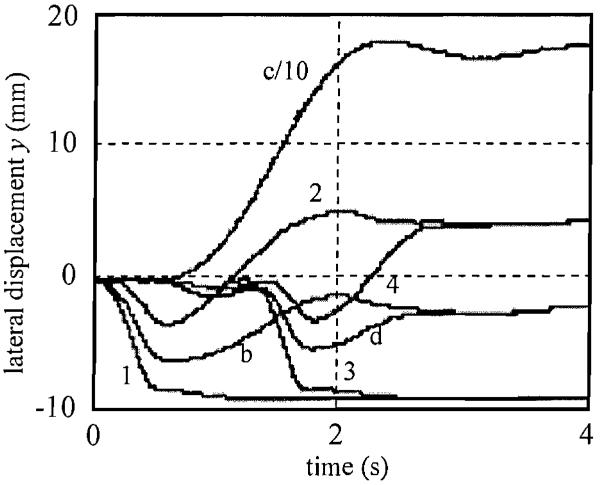

Figure 3-22 Lateral displacements in the steady-state curving behaviour of the Wickens vehicle under curving conditions of R_0 = 225 m, V_0 = 15 m/s, μ_0 = 0.3 and zero cant deficiency: 1 - leading wheelset of the front bogie, 2 - trailing wheelset of the front bogie, 3 - leading wheelset of the rear bogie, 4 - trailing wheelset of the rear bogie, b – front bogie, d – rear bogie and c – car body, (from Wickens, Figure 6.6 in [40]).

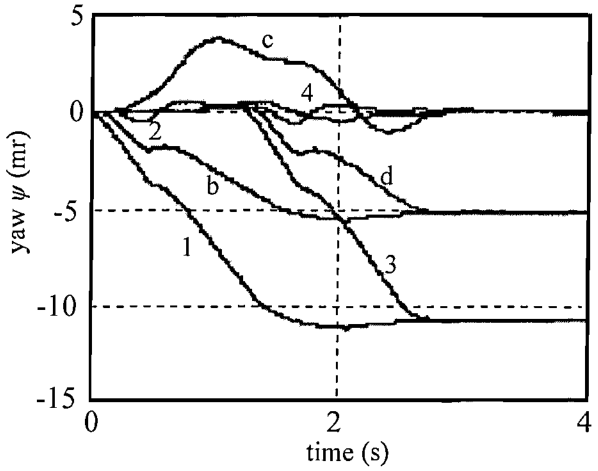

Figure 3-23 Yaw angles in the steady-state curving behaviour of the Wickens vehicle under curving conditions of R_0 = 225 m, V_0 = 15 m/s, μ_0 = 0.3 and zero cant deficiency: 1 - leading wheelset of the front bogie, 2 - trailing wheelset of the front bogie, 3 - leading wheelset of the rear bogie, 4 - trailing wheelset of the rear bogie, b – front bogie, d – rear bogie and c – car body, (from Wickens, Figure 6.6 in [40]).

It is obvious that the curving behaviour of the front bogie and its wheelsets is the same as that of the rear one. It is therefore sufficient to compare the curve behaviour of the front bogie and its wheelsets. Comparisons of the curving behaviour between the present model (see Figure 3-17) and the Wickens model show that the lateral displacements and yaw angles of the front two wheelsets '1 , '2 and the front bogie 'b' are consistent, with less than 10% difference. Since wheel/rail profiles are not known precisely, this difference is acceptable. However, the lateral displacement of the car body of the Wickens model is much greater than that of the present model. This may be due to a difference in coordinate system but will not influence the study of curve squeal.

3.5.2 Comparisons of the curving behaviour with the Vampire model

The Vampire model of the Class 158 vehicle was originally established for the general study of vehicle dynamics, so that it includes all the important motions, some of which are not included in the present model. Moreover, the Vampire model uses parameters of a practical vehicle, which includes the suspensions in detail. The components in its suspensions have conventional installation positions and necessary non-linear properties. Due to these general or practical considerations, the Vampire model is much more complex than the present model. For instance, the Vampire model has more than 30

DOF to represent the behaviour below 100 Hz, whereas the present model has only 17 DOF. Thus, only an equivalent Class 158 DMU vehicle with reduced DOF can be simulated in the present model. By checking the modeshapes of the Class 158 DMU vehicle in Vampire, those modes corresponding to 17 DOF in the present model can be identified. Through eigenvalue analysis of the equations of motion in Eq.(3.21), by adjusting the stiffnesses of suspensions, the current model can have the equivalent dynamic characteristics as the Vampire model in terms of the specified 17 DOF. The parameters of this equivalent Class 158 DMU vehicle are given in Appendix D.

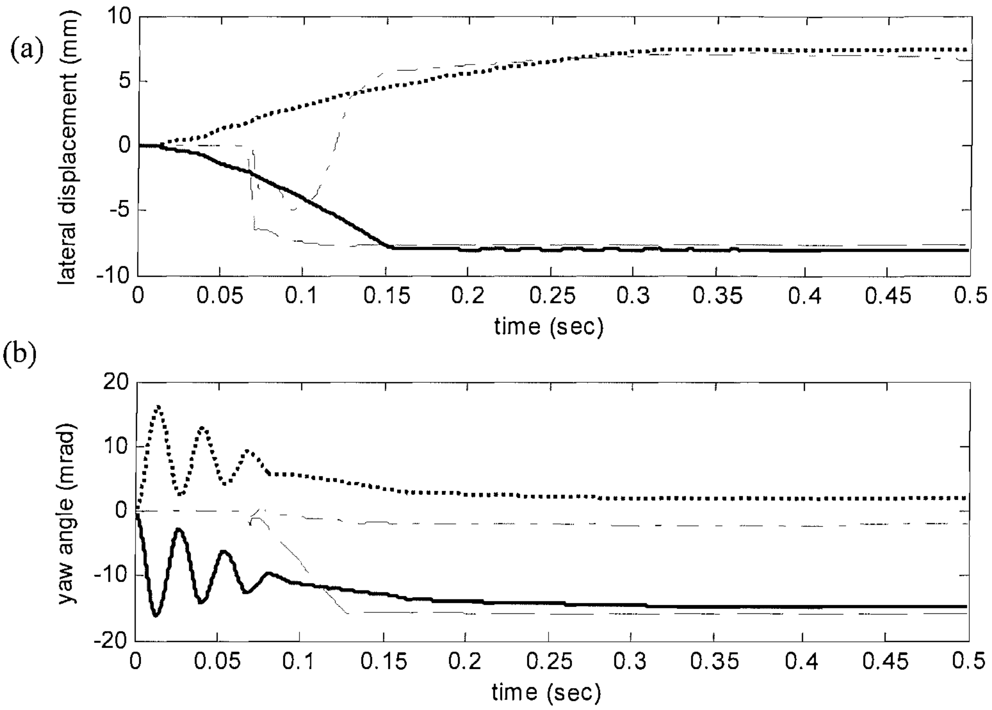

Figure 3-24 Comparisons of curving behaviour of the present model and the Vampire model, —— leading wheelset of the present model, ······ trailing wheelset of the present model, ------ leading wheelset of the Vampire model, — · — trailing wheelset of the Vampire model, (a) lateral displacement, (b) yaw angle.

The validation is carried out by adopting the curving case in a sharp right-hand curve with the following parameters: curve radius $R_0 = 150$ m, vehicle speed $V_0 = 6$ m/s, Coulomb friction coefficient $\mu_0 = 0.3$ and zero cant deficiency. The curving results of the Vampire model, including the lateral displacements and yaw angles of the leading and trailing wheelsets in the front bogie, are shown in Figure 3-24. The important curving results calculated by the present model and Vampire model are listed and compared in Table 3-1. It should be noted that the Vampire model allows two-point wheel/rail contacts, while the present model considers only one-point wheel/rail contacts. Furthermore, the curving behaviour of the front and rear bogies in the Vampire model are slightly different due to the asymmetric layout of the suspensions, while this does not happen in the present model with an exactly symmetric layout of the suspensions. From the results provided in Table 3-1, the curving results for the leading wheelset are very consistent between these two models, but the curving results for the trailing wheelset show some differences, especially the yaw angle and consequently the longitudinal creepages.

Table 3-1 Comparisons of curving behaviour between the present model and Vampire model

Equivalent / Vampire	Leading wheelset		Trailing wheelset	
Lateral displacement (mm)	-8.0 / -7.8		-7.2 / -6.2	
Yaw angle (mrad)	-15.3 / -15.2		2.2 / -0.8	
	Left wheel	Right wheel	Left wheel	Right wheel
Longitudinal creepage (%)	-0.3 / 0.0	0.3 / 0.3	0.9 / -0.3	-0.9 / 0.3
Lateral creepage (%)	1.9 / 1.8	1.5 / 1.5	-0.2 / -0.2	-0.2 / -0.2
Spin creepage (m^{-1})	1.5 / 1.5	0.0 / 0.0	0.1 / 0.0	-0.6 / -0.4
Normal force (kN)	64 / 72	59 / 55	61 / 59	61 / 62

As a comparison, the Class 158 DMU vehicle has also been modelled in Simpack using the same set of parameters as in the Vampire model. The curving behaviour calculated by these two commercial software packages exhibits quite large differences, especially in the results related to the creepages. These are important parameters in the squeal analysis. The differences between the present model and Vampire are smaller than the differences between Vampire and Simpack.

3.6 Summary

Some general conclusions of curving behaviour can be drawn based on the previous discussions. On tight curves, the outer (left) wheel in the leading wheelset is in flange contact, therefore it experiences a large spin (due to large contact angle) as well as a large lateral creepage. The inner (right) wheel in the leading wheelset is in the linear contact zone, with a large lateral creepage but a negligible spin. Either wheel in the trailing wheelset has a much smaller lateral creepage but a greater longitudinal creepage than the corresponding creepages in either leading wheel. Sharp curves may place the trailing inner wheel also in flange contact, so that there may be spin creepage at the trailing inner wheel. The cant deficiency can move the trailing wheelset outwards in the curve.

The detailed values of steady-state curving parameters can be obtained by using the dedicated steady-state curving model. As discussed, this model has been validated by comparisons with the results of both the Wickens model and the Vampire model.

4. SELF-EXCITED VIBRATION

4.1 Introduction

For ease of set-up and interpretation of the possible self-excited vibration in the wheel/rail contact system, an idealised mass-on-moving-belt model is established. This can represent the stick-slip motion of a one-mode wheel transversely sliding on a rail due to falling friction. The equations of motion of the mass and the relationship between the motion and friction can build the self-excited vibration, represented by a feedback loop. The stability of the wheel can then be studied analytically. If the self-excited vibration is unstable, a limit-cycle response of the wheel can be obtained by numerical integration in terms of the feedback loop.

4.2 Mass-on-moving-belt system

4.2.1 Equations of motion

A mass-spring-damper system (with parameters m_1, k_1 and c_1) is shown schematically in Figure 4-1. In this system, the belt is assumed to move with a constant lateral sliding speed V_b and the mass m_1 has a velocity of $\dot{y}_{tot}$. Thus, the sliding velocity between the mass and belt is

$$v_{ytot}^{s} \equiv \dot{y}_{tot} - V_b . \tag{4.1}$$

If the normal contact force between the mass and belt is N_0, the sliding friction force acting on the mass can be obtained:

$$f_{ytot} = N_0 \mu(v_{ytot}^{s}) , \tag{4.2}$$

where the non-dimensional friction force μ includes a sign opposite to that of the sliding velocity.

If the system is under equilibrium conditions, the mass should be motionless:

$$\dot{y}_{tot} = 0 . \tag{4.3}$$

Thus, the equilibrium sliding velocity v_{y0}^s, given from Eq.(4.1), is only related to the velocity of moving belt:

$$v_{y0}^s = -V_b, \tag{4.4}$$

and consequently the equilibrium friction force f_{y0} given from Eq.(4.2) is

$$f_{y0} = N_0 \mu(v_{y0}^s). \tag{4.5}$$

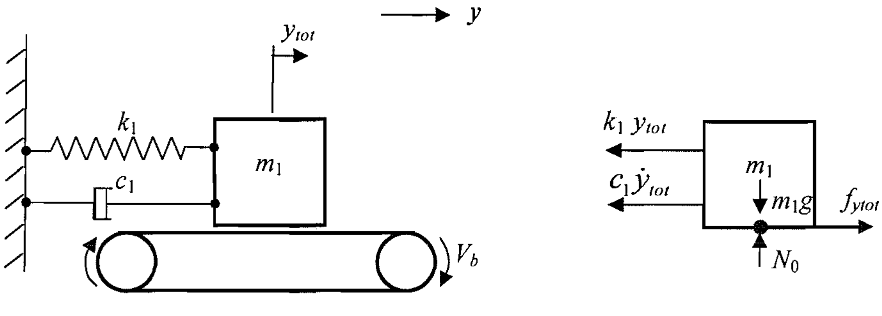

(a) (b)

Figure 4-1 Mass-on-moving-belt system, (a) friction driven mass-spring-damper system, (b) schematic diagram of the forces acting on the mass.

To maintain the force balance, the spring k_1 must stretch an equilibrium length $y_{tot} = y_0$ from its relaxed position to balance the equilibrium friction force f_{y0}, giving

$$f_{y0} = k_1 y_0. \tag{4.6}$$

If there is a disturbance, i.e. a transient force, which moves the mass from its steady-state position, the mass will start to oscillate. The displacement of the mass can be written as the sum of an equilibrium part y_0 and a dynamic part y:

$$y_{tot} \equiv y_0 + y, \tag{4.7}$$

and the velocity and acceleration are

$$\dot{y}_{tot} = \dot{y}, \tag{4.8}$$

$$\ddot{y}_{tot} = \ddot{y}. \tag{4.9}$$

Then the sliding velocity from Eq.(4.1) is

$$v_{ytot}^s = \dot{y} - V_b, \tag{4.10}$$

which can be rewritten into a general form by substituting $-V_b$ with v^s_{y0}:

$$v^s_{ytot} = v^s_{y0} + \dot{y}, \qquad (4.11)$$

so that the sliding velocity is the sum of an equilibrium part v^s_{y0} and a dynamic part $\dot{y}$.

The friction force f_{ytot} can also be written as the sum of an equilibrium part f_{y0} and a dynamic part f_y:

$$f_{ytot} \equiv f_{y0} + f_y. \qquad (4.12)$$

The governing equation of this mass-damper-spring system is

$$m_1\ddot{y}_{tot} + c_1\dot{y}_{tot} + k_1 y_{tot} = f_{ytot}. \qquad (4.13)$$

Combining Eqs.(4.6), (4.7), (4.8), (4.9) and (4.12) to eliminate the equilibrium parts in Eq.(4.13) gives the following equation of motion as a single-degree-of-freedom (SDOF) system.

$$m_1\ddot{y} + c_1\dot{y} + k_1 y = f_y. \qquad (4.14)$$

Substituting Eqs.(4.1), (4.2) and (4.5) into Eq.(4.12), the dynamic friction force is actually related to the vibration of the mass, $\dot{y}$:

$$f_y = f_{ytot} - f_{y0} = N_0\left(\mu(\dot{y} + v^s_{y0}) - \mu(v^s_{y0})\right). \qquad (4.15)$$

Combining the equation of motion in Eq.(4.14) and the friction force in Eq.(4.15), the system is a self-excited one, which is excited by a force determined by its own motion:

$$m_1\ddot{y} + c_1\dot{y} + k_1 y = N_0\left(\mu(\dot{y} + v^s_{y0}) - \mu(v^s_{y0})\right). \qquad (4.16)$$

4.2.2 Self-excited vibration

The interaction between the sliding velocity and the friction force in the mass-on-moving-belt system can be described as a positive feedback loop, see Figure 4-2. The input of the loop is a disturbance, which is assumed a transient signal. The output of the loop is the vibration of the mass. The block in the forward route is a linear mass-spring-damper system. The block in the feedback route can be considered as a generator for the friction force. The input signal of the block is the sliding velocity between the mass and the belt, and the output signal of the block is the dynamic friction force acting on the mass.

As discussed in the previous section, the equilibrium of the mass-spring-damper system is that the mass should be motionless. For any possible equilibrium sliding velocity v_{y0}^s, which is only determined by the velocity of belt, the stability in question is whether the system can eliminate fluctuations resulting from any small disturbances of $f_y^{'}$ and therefore maintain its equilibrium, i.e. $\dot{y}=0$.

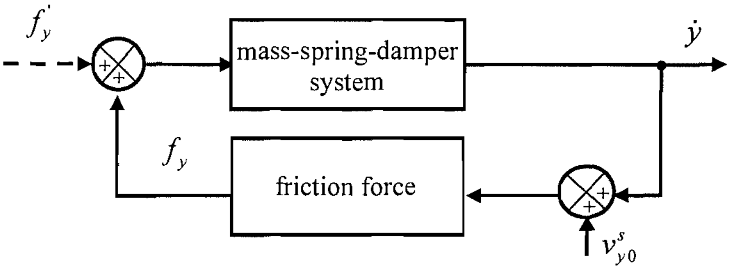

Figure 4-2 Feedback loop of the mass-on-moving-belt system.

For the purpose of stability analysis of the loop at one possible equilibrium sliding velocity v_{y0}^s, the non-linear friction force can be considered as being proportional to the sliding velocity in a very small range around v_{y0}^s. Since the derivative of the friction force with respect to the sliding velocity is similar to the definition of viscous damping (the damping force over relative velocity), an equivalent damping coefficient about v_{y0}^s can be defined as follows:

$$c_e(v_{y0}^s) = -\left.\frac{\partial f_y}{\partial v_y^s}\right|_{v_{y0}^s} . \qquad (4.17)$$

Unlike the viscous damping, which is always positive and dissipates the vibration of the structure, the equivalent damping coefficient of the friction force can be positive or negative. A negative sign of c_e (a positive derivative of friction force with respect to sliding velocity) means the friction force will increase the vibration energy of the structure.

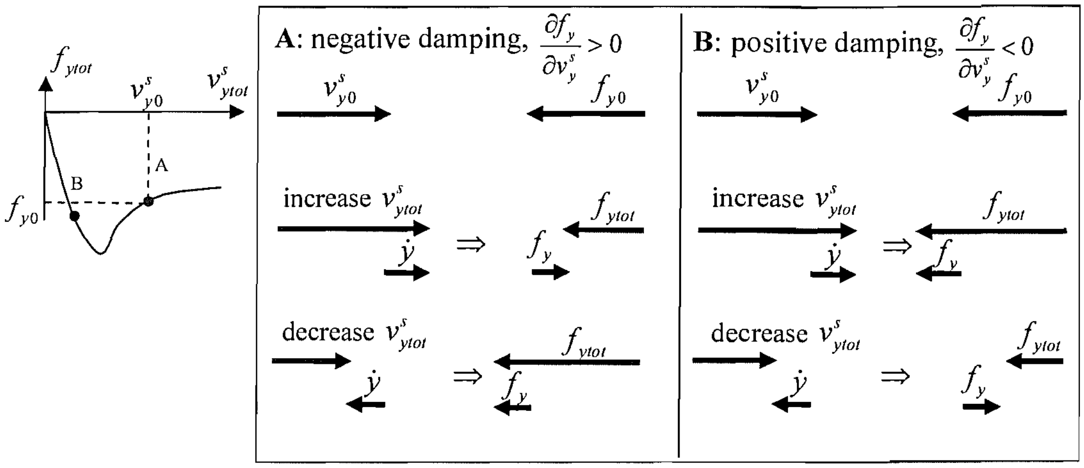

Figure 4-3 Equivalent damping effects of the friction force.

In Figure 4-3, two possible equilibrium points, **A** and **B**, are chosen on a friction curve with falling zone. At point **A**, the friction curve has a negative c_e (a positive derivative). It is found that the dynamic friction force $f_y = f_{ytot} - f_{y0}$ is always in the same direction as the increment of sliding velocity $\dot{y} = v^s_{ytot} - v^s_{y0}$. This will tend to increase the amplitude of vibration and in turn increase the friction force. Therefore, the system may be unstable at point **A**. However, at point **B**, the friction force has a positive c_e (a negative derivative) and the direction of dynamic friction force f_y is always opposite to that of the increment of sliding velocity $\dot{y}$. Thus, the dynamic friction force will tend to decrease the vibration and maintain the system at the equilibrium point **B**.

If the oscillation of $\dot{y}$ is very small compared with v^s_{y0}, the dynamic friction force f_y in Eq.(4.15) can be evaluated with the equivalent frictional damping c_e as follows:

$$f_y = \dot{y}\lim_{\dot{y}\to 0}\frac{N_0\left(\mu(\dot{y}+v^s_{y0})-\mu(v^s_{y0})\right)}{\dot{y}} = \dot{y}N_0\left.\frac{\partial\mu}{\partial\dot{y}}\right|_{v^s_{y0}} = -c_e\dot{y}\,. \qquad (4.18)$$

Substituting Eq.(4.18) into Eq.(4.14) gives

$$m_1\ddot{y} + c_1\dot{y} + k_1 y = -c_e\dot{y}\,. \qquad (4.19)$$

Assuming the oscillation is harmonic with frequency ω_1 and very small amplitude A_1,

$$y = A_1 \cos(\omega_1 t), \tag{4.20}$$

in an oscillation cycle T, the averaged power input to the system by the dynamic friction force f_y is

$$P_{in} = \frac{1}{T}\int_T f_y \dot{y} dt = -c_e \frac{1}{T}\int_T \dot{y}^2 dt = -\frac{A_1^{\ 2}\omega_1^{\ 2}}{2} c_e . \tag{4.21}$$

Since structural damping exists in the mass-spring-damper system, the increment of vibration should also consider the energy dissipated by the structural damping (the potential energy in the system is conserved). Shifting the damping part in Eq.(4.19) from left to right gives

$$m_1 \ddot{y} + k_1 y = -c_e \dot{y} - c_1 \dot{y} = \left(-c_e - c_1\right)\dot{y} , \tag{4.22}$$

where the structural damping coefficient c_1 is always greater than zero. The averaged power increment of the system in a harmonic oscillation is thus

$$P_s = \frac{1}{T}\int_T \left[\left(-c_e - c_1\right)\dot{y}\right]\dot{y} dt = \frac{A_1^{\ 2}\omega_1^{\ 2}}{2}\left(-c_e - c_1\right). \tag{4.23}$$

The stability criterion from the viewpoint of power increment is

$$P_s < 0 . \tag{4.24}$$

Combining Eq.(4.23) and Eq.(4.24), the stability of the mass-on-moving-belt system is judged by the following criterion:

$$\begin{cases} c_1 \geq 0, & c_e > 0 \\ c_1 > \left|c_e\right|, & c_e \leq 0 \end{cases} , \tag{4.25}$$

which means the structural damping can keep the system stable if the equivalent damping of the friction force is not negative, or the structural damping should be greater than the value of the negative equivalent damping.

However, since the friction force is non-linear, the unstable response will not increase indefinitely and a limit-cycle response will finally be achieved. The limit-cycle phenomenon can be studied by the step-by-step integration in terms of the feedback loop in Figure 4-2.

4.2.3 Self-excited vibration in a single-mode wheel

The mass-on-moving-belt model can be used directly to simulate the self-excited behaviour of one of the modes of a curving wheel sliding on a rigid rail in one direction. The feedback loop described in Figure 4-2 can be adopted for the wheel/rail simulation. A wheel with only one mode is represented by the mass-spring-damper system. The belt can be considered as a rail with rigid surface. The belt velocity V_b is represented by the possible equilibrium lateral sliding velocity between the wheel and rail. In each simulation step, the sliding velocity fed back from the output of the previous step will update the friction force. Only the dynamic response of the wheel is considered in the loop; that of the rail is ignored because the rail is assumed rigid.

As the rail is assumed to be motionless, the equilibrium sliding velocity v^s_{y0} now corresponds to the lateral component of rolling speed of the wheel, which is evaluated from its creepage. The lateral creepage γ_2 is defined as the lateral sliding velocity v^s_y in Eq.(4.11) normalised by the rolling velocity of the vehicle V_0. The total lateral creepage is defined as

$$\gamma_{2tot} = v^s_{ytot} \big/ V_0 \,. \tag{4.26}$$

As discussed in Chapter 3, the lateral creepage in steady-state curving is quasi-static, denoted as γ_{20} in the squeal model. Hence, the possible equilibrium sliding velocity can be expressed in terms of the steady-state lateral creepage:

$$v^s_{y0} = \gamma_{20} V_0 \,. \tag{4.27}$$

Substituting Eq.(4.27) into Eq.(4.18) gives

$$f_y = \dot{y} N_0 \left.\frac{d\mu}{d\dot{y}}\right|_{v^s_{y0}} = \dot{y}\frac{N_0}{V_0}\left.\frac{d\mu}{d(\dot{y}/V_0)}\right|_{v^s_{y0}/V_0} = \dot{y}\frac{N_0}{V_0}\left.\frac{d\mu}{d\gamma}\right|_{\gamma_{20}} = \dot{y}\frac{N_0}{V_0}\mu'(\gamma_{20}) \,. \tag{4.28}$$

The equivalent damping coefficient defined in Eq.(4.17) can thus be expressed as

$$c_e(\gamma_{20}) = -\frac{f_y}{\dot{y}} = -\frac{N_0}{V_0}\mu'(\gamma_{20}). \tag{4.29}$$

From the stability analysis in Eq.(4.25), if enough structural damping is added to the unstable system, it is possible to make the system stable. Since the curve of non-dimensional friction force is non-linear, the minimum damping ratio needed to make the unstable wheel into a stable one is dependent on the steady-state creepage and the friction curve. To ensure the stability of the wheel, a damping coefficient is required that is as large as the maximum value of the equivalent damping coefficient of the friction force:

$$c_c = \frac{N_0}{V_0}\left|\mu'(\gamma_p)\right|, \tag{4.30}$$

or in terms of the damping ratio

$$\zeta \geq \zeta_c = \frac{N_0}{V_0}\left|\mu'(\gamma_p)\right| \Big/ 2\sqrt{m_1 k_1}, \tag{4.31}$$

where the peak value of the derivative of friction force is at the creepage of γ_p.

4.3 Results and discussion

4.3.1 Parameters

The parameters in the mass-spring-damper system are chosen from one mode [5] of the finite element (FE) model of a UIC 920mm freight wheel [50]. They are natural frequency f_1 = 90.2 Hz, mass m_1 = 298.3 kg, stiffness k_1 = 9.6×10^7 N/m and damping coefficient c_1 = 3386.8 Ns/m (damping ratio $\zeta_1 = 0.01$). Other parameters are the normal contact force $N_0 = 42$ kN and the rolling velocity $V_0 = 12.25$ m/s.

---

[5] This mode is coupled with the motion of the wheelset, called the axle (bending) mode of the UIC 920 mm freight wheel. Although it may not be the mode at which squeal occurs, it still can be selected to show the self-excited vibration of one-mode wheel under falling friction.

One case of non-dimensional friction force and its derivative is shown in Figure 4-4. The parameters of the falling function in Eq.(2.28) are $\mu_0 = 0.4$, $\lambda = 0.4$ and $\kappa = 0.005$. It is found that the slope turning point is $\gamma_c = 1.825 \times 10^{-3}$. The peak value of the derivative is $d\mu/d\gamma = 25.5$ at $\gamma_p = 2.1 \times 10^{-3}$.

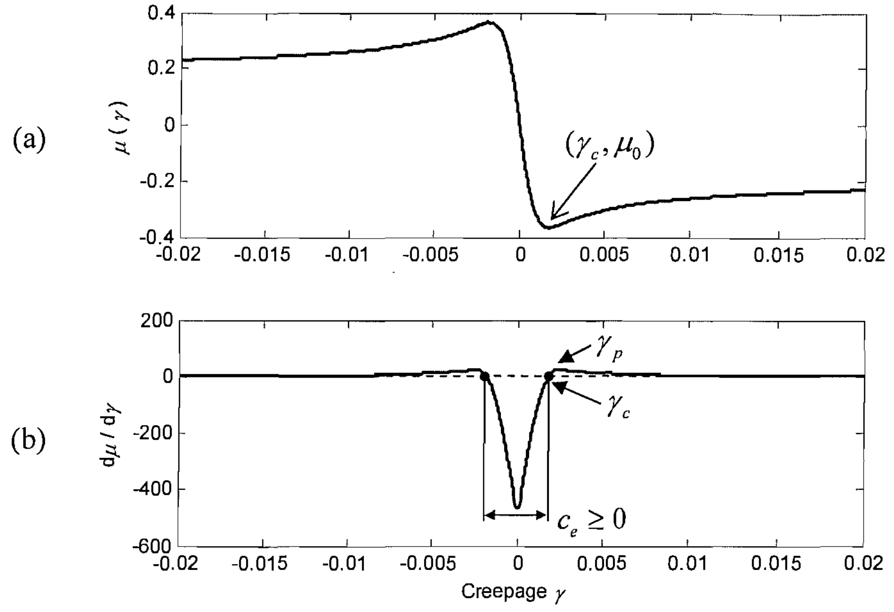

Figure 4-4 Non-dimensional friction force curve and its derivative, (a) creepage-dependent non-dimensional friction force; (b) derivative of the non-dimensional friction force.

4.3.2 Stability

In Figure 4-5, two trajectories are shown with the same steady-state creepage $\gamma_{20} = 1.5 \times 10^{-3}$ but different initial conditions. Both trajectories can tend asymptotically to the equilibrium point on the phase plane, which means the wheel is stable at this steady-state creepage. The stability criterion in Eq.(4.25) is satisfied, because c_e is positive if the steady-state creepage γ_{20} is less than the critical one γ_c, as shown in Figure 4-4.

In Figure 4-6, four trajectories with the same steady-state creepage $\gamma_{20} = 5 \times 10^{-3}$ but different initial conditions are shown on the phase plane. All trajectories tend asymptotically to one closed limit cycle, not the steady-state point. Therefore, the wheel is not stable at this steady-state creepage.

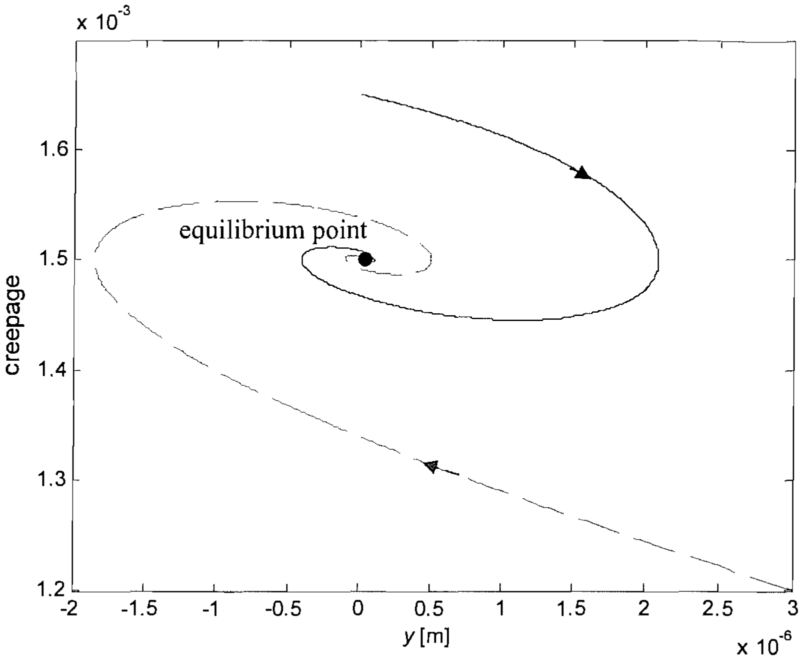

Figure 4-5 Phase-plane plot for the one-mode wheel under steady-state conditions: $y_0 = 0$, $\gamma_{20} = 1.5\times10^{-3}$; **initial conditions:** —— $y = 0, \gamma_2 = 1.65\times10^{-3}$, — — $y = 3\times10^{-6}$ m, $\gamma_2 = 1.2\times10^{-3}$.

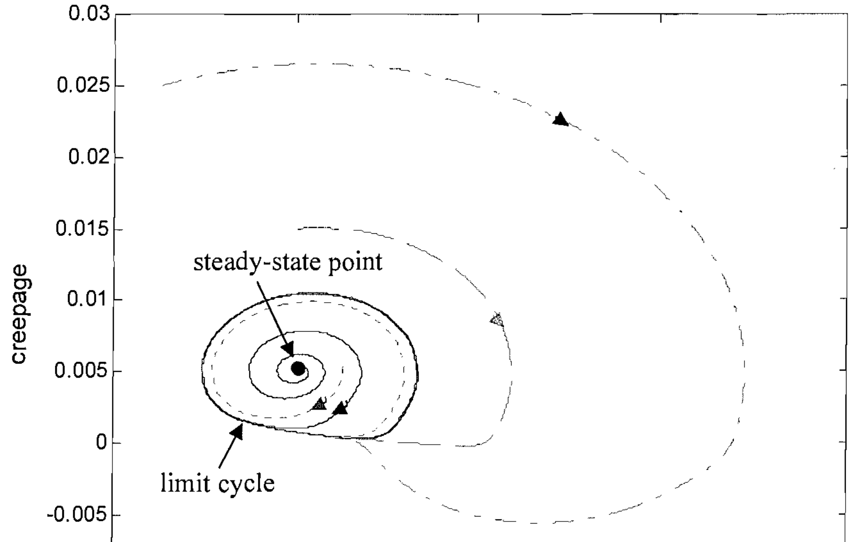

Figure 4-6 Phase-plane plot for the one-mode wheel system under steady-state conditions: $y_0 = 0$, $\gamma_{20} = 5\times10^{-3}$; **initial conditions:** —— $y = 5\times10^{-6}$ m, $\gamma_2 = 5\times10^{-3}$, ------ $y = 0.5\times10^{-4}$ m, $\gamma_2 = 5\times10^{-3}$, — — $y = 0, \gamma_2 = 1.5\times10^{-2}$ **and** — · — $y = -1.5\times10^{-4}$ m, $\gamma_2 = 2.5\times10^{-2}$.

4.3.3 Limit-cycle response

The non-linear characteristic of the friction force is the only reason for the limit-cycle response of the unstable case seen in Figure 4-6. The first several oscillations and steady-state limit-cycle oscillations of this unstable wheel are shown in Figure 4-7. The initial conditions are chosen to be very close to the steady-state point; therefore, the self-excited oscillation can slowly develop into the limit cycle. The sliding velocity and friction force seen in Figure 4-7(a) are the dynamic components, $\dot{y}$ and f_y, normalised by corresponding maximum values.

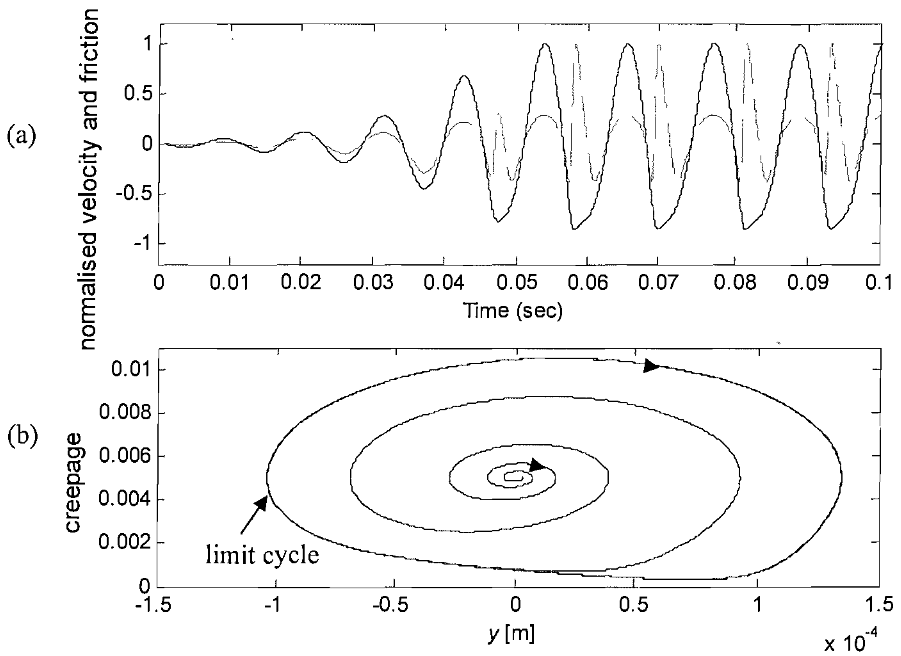

Figure 4-7 Initial response of the one-mode wheel system under steady-state creepage: $y_0 = 0$ and $\gamma_{20} = 5\times10^{-3}$; initial conditions: $y = 5\times10^{-6}$ m, $\gamma_2 = 5\times10^{-3}$; (a) time histories of the wheel dynamic velocity and friction force, —— velocity normalised by its maximal amplitude, — — friction force normalised by its maximal amplitude; (b) phase-plane plot.

In Figure 4-7(a), the friction force always has the same sign as the velocity in the initial several oscillations, so that the friction force gives a negative damping effect on the wheel system and consequently enlarges the amplitude of oscillation. However, this tendency decreases gradually as the amplitude of the wheel becomes large enough to reach the zone where the corresponding friction force has positive damping effects. Then the friction force has both negative and positive damping effects in every oscillation cycle, as shown in the last several oscillations. Finally, the power balance between the friction force and structural damping force is reached within an oscillation cycle, and the stable limit-cycle response is reached. Due to nonlinearity of the friction force, the frequency of the steady-state oscillation is about 87 Hz, not the natural frequency $f_1 = 90.3$ Hz.

In Figure 4-7(b), the limit-cycle curve distorts at very small creepages due to the significant positive damping effect of the friction force in this zone. The 'stick-slip' motion can also be found in the limit-cycle oscillation. In the distortion zone, the sliding velocity is very small so that the wheel is almost sticking on the rail. In the zone with large creepage, the wheel is slipping on the rail with large amplitudes.

4.3.4 Control of the vibration with structural damping

If the structural damping ratio of the wheel is increased to the critical value $\zeta_c = 0.253$, calculated by using Eq.(4.31), the wheel is stable for any steady-state creepage. Actually, a slightly smaller value of damping is enough to make the system stable depending on γ_{20}. For example, if the damping ratio ζ_1 can be improved from 0.01 to 0.15, the case shown in Figure 4-7 will be stable, as shown in Figure 4-8. However, if the disturbance is very large, this smaller control damping may not be enough. So the control damping should be greater than ζ_c to make the wheel stable for all creepages.

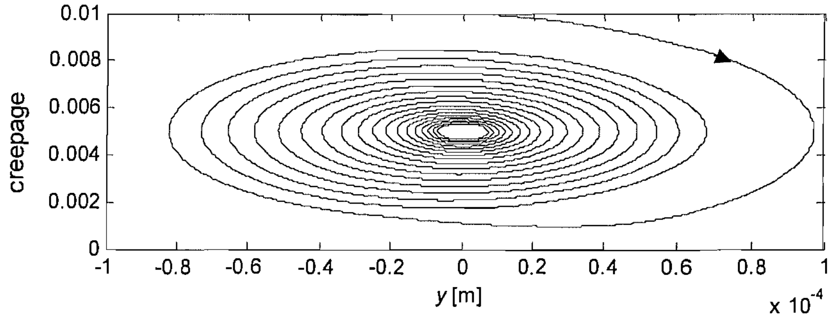

Figure 4-8 Phase-plane plot for the one-mode wheel system with structural damping ratio 0.15, where the steady-state creepage: $y_0 = 0$, $\gamma_{20} = 5\times10^{-3}$; initial conditions: $y = 3\times10^{-6}$ m, $\gamma_2 = 1\times10^{-2}$.

4.4 Summary

The wheel and rail contact system can be properly described as a self-excited vibration loop, because the excitation force (friction) sustaining the vibration is determined by the vibration (sliding velocity) itself. The falling friction can be considered as a negative equivalent damping, which may result in instability of the contact system if it is greater than the structural damping. For unstable cases, a limit-cycle response will occur with a stick-slip type of motion at a frequency close to (but not exactly at) the natural frequency of the unstable system.

5. SQUEAL MODEL FOR WHEEL/RAIL CONTACTS

5.1 Introduction

The self-excited vibration of a single-mode wheel system, as discussed in Chapter 4, can provide some important insights into the phenomena of self-excited vibration in terms of the falling friction force. However, this model is too simple to reach the purpose of squeal analysis in the practical wheel/rail contact system. In this chapter, a general self-excited vibration loop is established by including models of the wheel and rail structural dynamics and the wheel/rail rolling contact dynamics. By modelling the wheel/rail systems in state-space form, it is possible to study the squeal phenomenon in the time-domain. In addition, the stability analysis of the self-excited vibration loop can show which wheel modes are prone to squeal using a frequency-domain approach. This frequency-domain approach was originally presented by de Beer *et al.* [14], and then was extended by Monk-Steel and Thompson [15] to make it more general. As an important part of the current squeal model, the frequency-domain model is restated in this chapter. The effectiveness of the stability analysis is investigated in the parametric case study.

To predict squeal noise, the acoustic calculation for the steady-state response of the structures must be included. However, since the purpose of the acoustic radiation calculation here is to evaluate the squeal amplitude by including the acoustic radiation efficiency, an engineering approach to the acoustic radiation of the wheel, the dominant noise source, is described in Appendix G. The radiation from the rail is neglected.

5.2 Wheel/rail structural dynamics

Structural dynamic analysis is concerned with the effects of forces on the motion of solids. If the relationships between input forces and output motions are linear, the dynamic properties of a solid can be described with frequency response functions (FRFs), e.g. mobility or receptance. In modelling squeal, the wheel and rail are assumed to have linear dynamics, but the excitation forces (friction forces) acting on them are non-linear. For such non-linear problems, the method of step-by-step integration in the time domain is appropriate. This requires the dynamic properties of the wheel and rail to be described in the state-space form.

5.2.1 Wheel structural dynamics

A wheel can be modelled by finite element (FE) analysis. This provides the modal parameters (natural frequencies and modeshapes) as well as the mobility or receptance at the wheel/rail contact point. As an example, a Class 158 wheel has been modelled in ANSYS. This provides the modal parameters, for frequencies up to 10 kHz. The modal parameters of modes below 5 kHz are listed in Appendix H. The wheel mobilities can be derived from these modal parameters by using the method of modal synthesis. As shown in Figure H-2 to Figure H-5, using only 27 modes below 5 kHz (omitting some insignificant modes) the FRFs can be reliably predicted up to around 4 kHz.

Besides the mobilities, a state-space model of the wheel is required for the step-by-step simulation. If the number of wheel modes is small, a lumped-parameter system and corresponding state-space model can be designed to have dynamic characteristics equivalent to those of the wheel, as described in Appendix I. Alternatively, a modal analysis method can be adopted, as introduced in Appendix J. These two methods have been validated by comparison with each other. They are both applicable to the time-domain simulation. However, the state-space model provided by the modal analysis method can retain recognisable modal information, which is of benefit to the analysis, so this method is adopted and the state-space model is built as follows.

Consider a wheel with n modes, j input dynamic forces $\{\mathbf{f}^{\mathbf{w}}\}=[f_1^w, f_2^w, \cdots, f_j^w]^{\mathrm{T}}$, and i output dynamic velocities $\{\mathbf{v}^{\mathbf{w}}\}=[v_1^w, v_2^w, \cdots, v_i^w]^{\mathrm{T}}$. This can be represented by a state equation, Eq.(5.1), and an output equation, Eq.(5.2):

$$\{\dot{\mathbf{w}}\}=[\mathbf{A}^{\mathbf{w}}]\{\mathbf{w}\}+[\mathbf{B}^{\mathbf{w}}]\{\mathbf{f}^{\mathbf{w}}\}, \tag{5.1}$$

$$\{\mathbf{v}^{\mathrm{w}}\} = [\mathbf{C}^{\mathrm{w}}]\{\mathbf{w}\}, \tag{5.2}$$

where the $2n$-order state-variable vector consists of the modal velocity $\dot{q}_r$ and the modal displacement q_r of modes r (1 to n)

$$\{\mathbf{w}\} = \left[\dot{q}_1, \dot{q}_2, \cdots, \dot{q}_n, q_1, \cdots, q_n\right]^{\mathrm{T}} = \left[w_1, w_2, \cdots, w_{2n}\right]^{\mathrm{T}}. \tag{5.3}$$

The system matrix $[\mathbf{A}^{\mathrm{w}}]$ is

$$[\mathbf{A}^{\mathrm{w}}] \equiv \left[\begin{array}{cccc|cccc} -2\zeta_1\omega_1 & & & & -\omega_1^2 & & & \\ & -2\zeta_2\omega_2 & & & & -\omega_2^2 & & \\ & & \ddots & & & & \ddots & \\ & & & -2\zeta_n\omega_n & & & & -\omega_n^2 \\ \hline 1 & & & & & & & \\ & 1 & & & & & [0] & \\ & & \ddots & & & & & \\ & & & 1 & & & & \end{array}\right], \tag{5.4}$$

where ζ_r is the damping ratio of mode r (1 to n) and ω_r is the natural frequency (in radians/sec) of mode r. The input matrix $[\mathbf{B}^{\mathrm{w}}]$ can transform external forces into modal forces for each mode, while the output matrix $[\mathbf{C}^{\mathrm{w}}]$ sums modal velocities of each mode into external velocities. Both matrices are formed with modeshapes of the wheel:

$$[\mathbf{B}^{\mathrm{w}}] \equiv \left[\underbrace{\begin{matrix} \phi_{11} & \phi_{12} & \cdots & \phi_{1n} \\ \phi_{21} & \phi_{22} & \cdots & \phi_{2n} \\ \vdots & \vdots & \ddots & \vdots \\ \phi_{j1} & \phi_{j2} & \cdots & \phi_{jn} \end{matrix}}_{n} \left| \underbrace{\begin{matrix} 0 & 0 & \cdots & 0 \\ 0 & 0 & \cdots & 0 \\ \vdots & \vdots & \ddots & \vdots \\ 0 & 0 & \cdots & 0 \end{matrix}}_{n} \right.\right]^{\mathrm{T}}, \tag{5.5}$$

and

$$[\mathbf{C}^{\mathrm{w}}] \equiv \left[\underbrace{\begin{matrix} \phi_{11} & \phi_{12} & \cdots & \phi_{1n} \\ \phi_{21} & \phi_{22} & \cdots & \phi_{2n} \\ \vdots & \vdots & \ddots & \vdots \\ \phi_{i1} & \phi_{i2} & \cdots & \phi_{in} \end{matrix}}_{n} \left| \underbrace{\begin{matrix} 0 & 0 & \cdots & 0 \\ 0 & 0 & \cdots & 0 \\ \vdots & \vdots & \ddots & \vdots \\ 0 & 0 & \cdots & 0 \end{matrix}}_{n} \right.\right], \tag{5.6}$$

where ϕ_{ir} and ϕ_{jr} are the mass-normalised modeshape of mode r in the i and j directions. In a Cartesian coordinate system, there are 6 forces (and moments) and 6 corresponding motions. Hence, i and $j = 1$ to 6.

5.2.2 Rail structural dynamics

The rail can also be modelled by FE analysis, but an analytical rail model is preferred, because it can represent different kinds of rails simply by changing a small number of parameters. Most of the work related to the analytical rail model has been done and validated by other researchers, i.e. Wu and Thompson [52] for vertical and lateral motions and Lurcock [53] for longitudinal motion. The spin motion of the rail is additionally modelled for squeal analyses, and is introduced in Appendix K. This spin model has not been validated by experiments. Hence, the point mobility curves (with force and response at the same point) in the longitudinal, lateral, vertical and spin directions are available.

These analytical rail models, however, are too complex to apply directly to the step-by-step integration in the time domain. Compared with the wheel system, the rail has much higher damping and therefore has smoother mobility curves, which makes it possible to find a low order equivalent system corresponding to each mobility curve, using the method introduced by Wu and Thompson [52] as described in Appendix L. The state-space rail model can then be derived from these equivalent systems with the method introduced in Appendix M. The state-space model of the rail is built as follows.

The equivalent system adopted here is assumed to have a transfer function expressed in the form of a ratio of two polynomials

$$H(s) \equiv \frac{b_1 s^{m-1} + b_2 s^{m-2} + \cdots + b_m}{s^m + a_1 s^{m-1} + a_2 s^{m-2} + \cdots + a_m}, \tag{5.7}$$

where the order of the denominator is one order higher than that of numerator. Determining the coefficients in this transfer function is actually a process of system identification. For a given complex frequency response, i.e. mobility or receptance, the coefficients obtained for the equivalent system, a_k, b_k, are not unique but depend on how much error is allowed in the application. Normally, the higher the order of the equivalent system assumed, the less is the error of the system identification results. However, if the order of the system is very high, the performance of the equivalent system is sensitive to the coefficients and may be unstable. A trial-and-error process of seeking appropriate coefficients has been used by making use of '*invfreqs*', a function provided by the Signal Processing Toolbox of MATLAB [54].

For any particular input force f_j^r and output response v_i^r, their dynamic relationship can be described in a mobility function Y_{ij}^r. A corresponding equivalent system with the form in Eq.(5.7) can be calculated, with coefficients $a_{ij,k}$ and $b_{ij,k}$, $k=1,\cdots,m$. Then, the state-space model can be written as

$$\{\dot{\mathbf{r}}_{ij}\}=[\mathbf{A}_{ij}^{\mathbf{r}}]\{\mathbf{r}_{ij}\}+[\mathbf{B}_{ij}^{\mathbf{r}}]f_j, \tag{5.8}$$

$$v_i^r=[\mathbf{C}_{ij}^{\mathbf{r}}]\{\mathbf{r}_{ij}\}+[\mathbf{D}_{ij}^{\mathbf{r}}]f_j, \tag{5.9}$$

where the vector of state variables is

$$\{\mathbf{r}_{ij}\}\equiv\left[r_{ij,1},r_{ij,2},\cdots,r_{ij,m}\right]^{\mathrm{T}}. \tag{5.10}$$

The system matrix is

$$[\mathbf{A}_{ij}^{\mathbf{r}}]\equiv\begin{bmatrix}-a_{ij,1} & -a_{ij,2} & \cdots & \cdots & -a_{ij,m}\\ 1 & 0 & \cdots & \cdots & 0\\ 0 & 1 & & \cdots & 0\\ \vdots & & \ddots & \vdots & \vdots\\ 0 & 0 & \cdots & 1 & 0\end{bmatrix}, \tag{5.11}$$

the input matrix is

$$[\mathbf{B}_{ij}^{\mathbf{r}}]\equiv[1,0,\cdots,0]^{\mathrm{T}}, \tag{5.12}$$

and the output matrix is

$$[\mathbf{C}_{ij}^{\mathbf{r}}]\equiv\left[b_{ij,1},b_{ij,2},\cdots,b_{ij,m}\right]. \tag{5.13}$$

The direct output matrix is zero

$$[\mathbf{D}^{\mathrm{r}}_{ij}] = 0\,. \tag{5.14}$$

The whole rail model is a multiple-input, multiple-output (MIMO) system. The sub-models corresponding to each force input and each velocity output can be assembled to give the complete state-space model. It is not necessary to include all the possible FRFs, because the rail is normally much more damped than the wheel and consequently has much less response than it. Since the rail has quasi-symmetry in its cross-section, four point FRFs and no cross FRF are retained to describe the dynamic properties at the nominal contact position, as shown in Figure 5-1(a). These FRFs are longitudinal, lateral, vertical and spin, Y^r_{ij}, $i = j = 1,2,3,6$. However, in the flange contact, as shown in Figure 5-1(b), the contact position offsets from the nominal contact position to the rail corner, and the contact plane rotates by a large contact angle. Hence, in the contact frame, the cross-relation between the lateral and vertical motions should be considered. This cross-mobility can be obtained by transforming the point mobilities at the nominal contact point, as introduced in the following section.

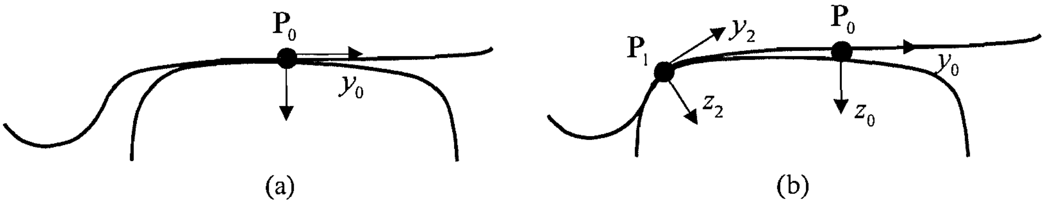

Figure 5-1 Typical wheel/rail contact positions: (a) nominal contact position P_0, (b) flange contact position P_1 and the relative relation between two frames.

The whole rail model, with 6 input forces $\{\mathbf{f}^{\mathrm{r}}\} = [f^r_1, f^r_2, \cdots, f^r_6]^{\mathrm{T}}$ and 6 output velocities $\{\mathbf{v}^{\mathrm{r}}\} = [v^r_1, v^r_2, \cdots, v^r_6]^{\mathrm{T}}$, is obtained by assembling these sub-models as follows:

$$\{\dot{\mathbf{r}}\} = [\mathbf{A}^{\mathrm{r}}]\{\mathbf{r}\} + [\mathbf{B}^{\mathrm{r}}]\{\mathbf{f}^{\mathrm{r}}\}, \tag{5.15}$$

and

$$\{\mathbf{v}^{\mathrm{r}}\} = [\mathbf{C}^{\mathrm{r}}]\{\mathbf{r}\}, \tag{5.16}$$

where the vector of state variables and matrices in Eq.(5.15) and Eq.(5.16) are assembled to be

$$\{\mathbf{r}\} \equiv [\{\mathbf{r}_{11}\} \quad \{\mathbf{r}_{22}\} \quad \cdots \quad \{\mathbf{r}_{66}\}]^T, \tag{5.17}$$

the system matrix is

$$[\mathbf{A}^r] \equiv \begin{bmatrix} [\mathbf{A}^r_{11}] & & & \\ & [\mathbf{A}^r_{22}] & & \\ & & \ddots & \\ & & & [\mathbf{A}^r_{66}] \end{bmatrix}, \tag{5.18}$$

the input matrix is

$$[\mathbf{B}^r] \equiv \begin{bmatrix} [\mathbf{B}^r_{11}] & & & \\ & [\mathbf{B}^r_{22}] & & \\ & & \ddots & \\ & & & [\mathbf{B}^r_{66}] \end{bmatrix}, \tag{5.19}$$

and the output matrix is

$$[\mathbf{C}^r] \equiv \begin{bmatrix} [\mathbf{C}^r_{11}] & & & \\ & [\mathbf{C}^r_{22}] & & \\ & & \ddots & \\ & & & [\mathbf{C}^r_{66}] \end{bmatrix}. \tag{5.20}$$

5.2.3 Rigid transformation of structural dynamics

Under different curving conditions, the contact position of wheel and rail may shift significantly from the centre position to the flange position and consequently the contact plane will rotate by a large contact angle, as shown in Figure 5-1. Since the dynamic properties of a structure may be different from one position to another, the wheel and rail mobilities obtained at the nominal contact point cannot be applied for the analysis of other positions, e.g. the position in the flange. Unfortunately, it is sometimes difficult to get the mobilities at arbitrary points of a structure. For the wheel, the FE model can be used to provide a new set of modal parameters for any new position, but this involves a large amount of work. For the analytical rail models, since they are only modelled at the nominal contact position, it is impossible for them to provide additional dynamic properties at any new positions. Hence, a method is required to make the transformation of dynamic properties possible, for both wheel and rail models.

For vibration in steel with a frequency up to 5000 Hz, the minimum wavelength of shear waves is about 640 mm (the shear wave speed is about 3200 m/s). Since the distance between the nominal contact point and the flange contact point is about 50 mm (about 1/12 of the wavelength at the highest frequency vibration), the structural motion between them can be considered as rigid.

From the modeshape of a Class 158 wheel, as shown in Appendix H, no flexible deflection takes place on the wheel tread up to 5000 Hz. The rigid transformation can probably be used reliably up to about 10 kHz but can be expected to become less reliable at higher frequencies than this. The rail system has significant resonances of the cross-section in the frequency range higher than 1000 Hz, e.g. the pinned-pinned resonance of vertical bending and lateral bending of the rail web [55]. However, these flexible modes contain only rigid motion of the railhead. Thus, the assumption of a rigid transformation is valid for the wheel and railhead below at least 5000 Hz, which is the upper limit of the current curve squeal analyses. The application of this method is as follows.

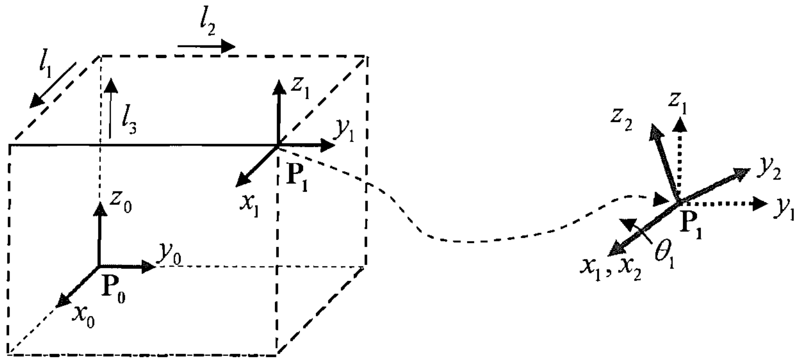

Figure 5-2 Rigid transform: translating from P_0 to P_1 and then rotating about the x-axis.

If the modeshapes of an n-mode system are available, e.g. the wheel system modelled by FE analysis, the modal matrix can be created with the modeshapes of all modes:

$$[\phi]=\begin{bmatrix}\phi_{1,1} & \phi_{1,2} & \cdots & \phi_{1,n}\\ \phi_{2,1} & \phi_{2,2} & \cdots & \phi_{2,n}\\ \vdots & \vdots & & \vdots\\ \phi_{6,1} & \phi_{6,2} & \cdots & \phi_{6,n}\end{bmatrix}. \tag{5.21}$$

The modal matrix $[\phi^0]$ at point $\mathbf{P}_0$ in the frame $x_0y_0z_0$ can translate to the new position $\mathbf{P}_1$ in the frame $x_1y_1z_1$ by distances (l_1, l_2, l_3), then rotate by an angle θ_1 about the x_1-axis to give the new modal matrix $[\phi^2]$ in the frame $x_2y_2z_2$, as shown in Figure 5-2. The total transform is expressed as

$$[\phi^2]=[\mathbf{T}_{\mathbf{rot}}][\mathbf{T}_{\mathbf{off}}]\cdot[\phi^0]\equiv[\mathbf{T}_{\mathbf{tot}}]\cdot[\phi^0], \tag{5.22}$$

where the translation matrix $[\mathbf{T}_{\mathbf{off}}]$ is

$$[\mathbf{T}_{\mathbf{off}}]=\left[\begin{array}{ccc:ccc}1 & & & 0 & l_3 & -l_2\\ & 1 & & -l_3 & 0 & l_1\\ & & 1 & l_2 & -l_1 & 0\\ \hdashline & & & 1 & & \\ & [0] & & & 1 & \\ & & & & & 1\end{array}\right], \tag{5.23}$$

the rotation matrix $[\mathbf{T}_{\mathbf{rot}}]$ is

$$[\mathbf{T}_{\mathbf{rot}}]=\left[\begin{array}{ccc:ccc}1 & 0 & 0 & & & \\ 0 & \cos\theta_1 & \sin\theta_1 & & [0] & \\ 0 & -\sin\theta_1 & \cos\theta_1 & & & \\ \hdashline & & & 1 & 0 & 0\\ & [0] & & 0 & \cos\theta_1 & \sin\theta_1\\ & & & 0 & -\sin\theta_1 & \cos\theta_1\end{array}\right], \tag{5.24}$$

and the total transformation matrix $[\mathbf{T}_{\mathbf{tot}}]$ is

$$[\mathbf{T}_{\mathbf{tot}}]=\left[\begin{array}{ccc:ccc}1 & 0 & 0 & 0 & l_3 & -l_2\\ 0 & \cos\theta_1 & \sin\theta_1 & -l_3\cos\theta_1+l_2\sin\theta_1 & -l_1\sin\theta_1 & l_1\cos\theta_1\\ 0 & -\sin\theta_1 & \cos\theta_1 & l_3\sin\theta_1+l_2\cos\theta_1 & -l_1\cos\theta_1 & -l_1\sin\theta_1\\ \hdashline & & & 1 & 0 & 0\\ & [0] & & 0 & \cos\theta_1 & \sin\theta_1\\ & & & 0 & -\sin\theta_1 & \cos\theta_1\end{array}\right]. \tag{5.25}$$

In some cases (e.g. the rail system here), if only the FRFs (mobility and/or receptance) but not the modeshapes are available, the transformation in terms of FRFs is needed. For the case shown in Figure 5-2, with mobilities Y_{ij}^0 at $\mathbf{P}_0$ in the frame $x_0y_0z_0$ and Y_{ij}^2 at $\mathbf{P}_1$ in the frame $x_2y_2z_2$, the following relation exists

$$\begin{bmatrix} Y_{1,1}^2 & Y_{1,2}^2 & \cdots & Y_{1,6}^2 \\ Y_{2,1}^2 & Y_{2,2}^2 & \cdots & Y_{2,6}^2 \\ \vdots & \vdots & \ddots & \vdots \\ Y_{6,1}^2 & Y_{6,2}^2 & \cdots & Y_{6,6}^2 \end{bmatrix} = [\mathbf{T}_{\mathrm{tot}}] \begin{bmatrix} Y_{1,1}^0 & Y_{1,2}^0 & \cdots & Y_{1,6}^0 \\ Y_{2,1}^0 & Y_{2,2}^0 & \cdots & Y_{2,6}^0 \\ \vdots & \vdots & \ddots & \vdots \\ Y_{6,1}^0 & Y_{6,2}^0 & \cdots & Y_{6,6}^0 \end{bmatrix} [\mathbf{T}_{\mathrm{tot}}]^{\mathrm{T}} . \tag{5.26}$$

5.3 Wheel/rail rolling contact dynamics

5.3.1 Wheel/rail rolling contact dynamics in the time domain

The general wheel/rail contact system is shown in Figure 5-3.

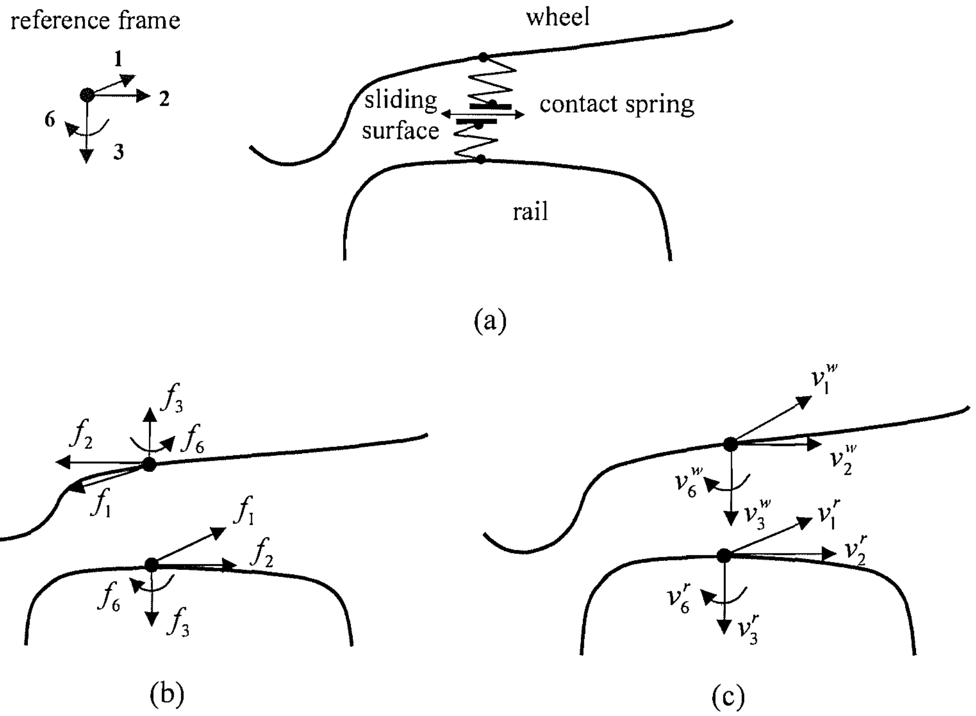

Figure 5-3 Forces and velocities of the wheel/rail contact system: (a) schematic diagram of the wheel/rail contact system, (b) forces acting on the wheel and rail in the contact area, (c) velocities of the wheel and rail.

The reference frame is established at the contact patch, as shown in Figure 5-3(a), where there are four DOF: the longitudinal and lateral directions (with index **1** and **2**) are located in the contact plane, the vertical direction (with index **3**) is normal to the contact plane, and the spin (with index **6**) rotates about the vertical direction. In the normal direction, the massless Hertz contact spring represents local dynamic behaviour of the contact zone. The dynamic contact forces (including the spin moment) and the dynamic velocities (including the spin motion) involved in the wheel/rail contact system are shown in Figure 5-3(b) and Figure 5-3(c), respectively.

The dynamic contact forces f_1, f_2 and the spin moment f_6 are the dynamic part of the friction forces. The vertical dynamic contact force f_3 results from the deformation of the contact spring. The vector of dynamic contact forces $\{\mathbf{f}\}$ includes four forces

$$\{\mathbf{f}\} \equiv [f_1 \quad f_2 \quad f_3 \quad f_6]^{\mathrm{T}}. \tag{5.27}$$

In Figure 5-3(b), the dynamic contact forces acting on the rail have the same values as, but opposite directions to, those acting on the wheel. Assuming the rail has positive contact forces, the contact force vectors of wheel $\{\mathbf{f}^{\mathrm{w}}\}$ and rail $\{\mathbf{f}^{\mathrm{r}}\}$ are therefore

$$\{\mathbf{f}^{\mathrm{w}}\} \equiv -\{\mathbf{f}\}, \tag{5.28}$$

$$\{\mathbf{f}^{\mathrm{r}}\} \equiv \{\mathbf{f}\}. \tag{5.29}$$

In Figure 5-3(c), the velocity vectors of wheel $\{\mathbf{v}^{\mathrm{w}}\}$ and rail $\{\mathbf{v}^{\mathrm{r}}\}$ are formed with their velocities (and rotational velocity) in the longitudinal direction $v_1^{w,r}$, in the lateral direction $v_2^{w,r}$, in the vertical direction $v_3^{w,r}$ and in the spin direction $v_6^{w,r}$:

$$\{\mathbf{v}^{\mathrm{w}}\} \equiv [v_1^w \quad v_2^w \quad v_3^w \quad v_6^w]^{\mathrm{T}}, \tag{5.30}$$

$$\{\mathbf{v}^{\mathrm{r}}\} \equiv [v_1^r \quad v_2^r \quad v_3^r \quad v_6^r]^{\mathrm{T}}. \tag{5.31}$$

The dynamic contact forces, as discussed in Section 5.2, can determine the dynamic responses of wheel and rail. The relative motions between wheel and rail in turn determine the dynamic contact forces. This process is formulated as follows.

In the vertical direction, no sliding exists because the wheel and rail will maintain contact vertically due to the load, but will not penetrate each other. The dynamic approach of wheel and rail can be considered as the compression of the contact spring,

$$d_3^c \equiv -(d_3^r - d_3^w) = -\int_0^t (v_3^r - v_3^w)dt, \tag{5.32}$$

where the compression of the contact spring is assumed to be positive. Consequently, the relative velocity of the contact spring is

$$v_3^c \equiv -(v_3^r - v_3^w). \tag{5.33}$$

A vertical sliding velocity can then be determined, which is obtained from Eq. (5.33) and must be equal to zero,

$$v_3^s \equiv (v_3^r - v_3^w) + v_3^c = 0. \tag{5.34}$$

In the longitudinal, lateral and spin directions, the dynamic sliding velocities exist, and are defined as the velocities of the rail relative to those of the wheel [6]. Combining the vertical sliding velocity given in Eq.(5.34), the sliding velocities are written in matrix form as

$$\begin{bmatrix} v_1^s \\ v_2^s \\ v_3^s \\ v_6^s \end{bmatrix} \equiv \begin{bmatrix} v_1^r \\ v_2^r \\ v_3^r \\ v_6^r \end{bmatrix} - \begin{bmatrix} v_1^w \\ v_2^w \\ v_3^w \\ v_6^w \end{bmatrix} + \begin{bmatrix} 0 \\ 0 \\ v_3^c \\ 0 \end{bmatrix}. \tag{5.35}$$

The dynamic sliding velocities v_1^s, v_2^s, v_6^s and the normal fluctuating force f_3 can result in the dynamic friction forces f_1, f_2 and the spin moment f_6. These relations are determined by the wheel/rail rolling friction, which is treated as a non-linear problem in the squeal analyses. For a general situation, during steady-state curving for a rolling

---

[6] The contact spring is only included in the vertical direction, representing the elastic deformation under the normal contact. As discussed in Chapter 2, the elastic strain also exists in the tangential direction in the contact. This tangential strain-stress relation has been considered in the friction forces calculated by the ready rolling friction models, e.g. FASTSIM algorithm. However, since these models are based on the condition of steady-state rolling, errors may exist due to neglect of the tangential contact spring.

speed V_0, the longitudinal sliding v^s_{1tot}, lateral sliding v^s_{2tot} and spin v^s_{6tot} are present simultaneously.

The spin sliding velocity can be considered as the component of the wheel rotation vector in the direction normal to the contact patch. For a contact angle θ between the plane of the contact and the ground plane (which may be canted in curve), the spin is

$$v^s_{6tot} = \frac{V_0}{r_0}\sin\theta, \tag{5.36}$$

where r_0 is the nominal radius of the wheel, so that the spin creepage is considerable in flange contact with large contact angle.

The sliding velocities are normally evaluated in terms of the creepages,

$$\begin{bmatrix} \gamma_{1tot} \\ \gamma_{2tot} \\ \gamma_{6tot} \end{bmatrix} \equiv \frac{1}{V_0}\begin{bmatrix} v^s_{1tot} \\ v^s_{2tot} \\ v^s_{6tot} \end{bmatrix}, \tag{5.37}$$

where γ_{1tot}, γ_{2tot}, γ_{6tot} are the longitudinal, lateral and spin creepages. These sliding velocities and corresponding creepages can be split into a steady-state component and a dynamic (time-varying) component,

$$\begin{bmatrix} \gamma_{1tot} \\ \gamma_{2tot} \\ \gamma_{6tot} \end{bmatrix} \equiv \frac{1}{V_0}\begin{bmatrix} v^s_{10}+v^s_1 \\ v^s_{20}+v^s_2 \\ v^s_{60}+v^s_6 \end{bmatrix} = \begin{bmatrix} \gamma_{10}+v^s_1/V_0 \\ \gamma_{20}+v^s_2/V_0 \\ \gamma_{60}+v^s_6/V_0 \end{bmatrix}, \tag{5.38}$$

where the steady-state components v^s_{10}, v^s_{20}, v^s_{60} and γ_{10}, γ_{20}, γ_{60} are determined by the steady-state curving behaviour, and the dynamic components v^s_1, v^s_2, v^s_6 are determined by the dynamic sliding velocities of the wheel and the rail at the contact patch, as given in Eq.(5.35).

The longitudinal and lateral friction forces f_{1tot}, f_{2tot} and the spin moment f_{6tot} can be written as the product of the normal contact force f_{3tot} and corresponding non-dimensional friction forces:

$$\begin{bmatrix} f_{1tot} \\ f_{2tot} \\ f_{6tot} \end{bmatrix} = \begin{bmatrix} \mu_1(\gamma_{1tot}, & \gamma_{2tot}, & \gamma_{6tot}, & f_{3tot}) \\ \mu_2(\gamma_{1tot}, & \gamma_{2tot}, & \gamma_{6tot}, & f_{3tot}) \\ \mu_6(\gamma_{1tot}, & \gamma_{2tot}, & \gamma_{6tot}, & f_{3tot}) \end{bmatrix} f_{3tot}, \tag{5.39}$$

where the non-dimensional friction forces μ_1, μ_2, μ_6 are non-linear functions of all three creepages and the normal contact force determined using FASTSIM. The normal contact force f_{3tot} fluctuates due to the compression or extension of the contact spring. Thus, it can also be considered as the sum of a nominal contact force $f_{30} = N_0$ and a dynamic vertical force f_3:

$$f_{3tot} \equiv N_0 + f_3. \tag{5.40}$$

The stiffness of the Hertz contact spring k_H is a non-linear function of the normal load f_{3tot}. It can be linearised around the steady-state approach d_{30}^c due to normal load N_0. Hence, for a small dynamic vertical approach d_3^c given in (5.32), the dynamic vertical force is

$$f_3 = k_H d_3^c = -k_H \int_0^t v_3^s dt. \tag{5.41}$$

According to Eq.(5.39), the friction forces and spin moment at the steady-state point can be expressed as

$$\begin{bmatrix} f_{10} \\ f_{20} \\ f_{60} \end{bmatrix} = \begin{bmatrix} \mu_1(\gamma_{10}, & \gamma_{20}, & \gamma_{60}, & N_0) \\ \mu_2(\gamma_{10}, & \gamma_{20}, & \gamma_{60}, & N_0) \\ \mu_6(\gamma_{10}, & \gamma_{20}, & \gamma_{60}, & N_0) \end{bmatrix} N_0. \tag{5.42}$$

During steady-state curving, these steady-state components of friction forces and moment are balanced by the vehicle suspension forces, which means only the dynamic components are directly related to squealing. From Eq.(5.39) and Eq.(5.42), writing each component as the sum of a steady-state component and a dynamic component, the dynamic friction forces are given as

$$\begin{bmatrix} f_1 \\ f_2 \\ f_6 \end{bmatrix} = \begin{bmatrix} f_{1tot} \\ f_{2tot} \\ f_{6tot} \end{bmatrix} - \begin{bmatrix} f_{10} \\ f_{20} \\ f_{60} \end{bmatrix} =$$

$$\begin{bmatrix} \mu_1\left(\gamma_{10}+\dfrac{v_1^s}{V_0},\ \gamma_{20}+\dfrac{v_2^s}{V_0},\ \gamma_{60}+\dfrac{v_6^s}{V_0},\ N_0+f_3\right) \\ \mu_2\left(\gamma_{10}+\dfrac{v_1^s}{V_0},\ \gamma_{20}+\dfrac{v_2^s}{V_0},\ \gamma_{60}+\dfrac{v_6^s}{V_0},\ N_0+f_3\right) \\ \mu_6\left(\gamma_{10}+\dfrac{v_1^s}{V_0},\ \gamma_{20}+\dfrac{v_2^s}{V_0},\ \gamma_{60}+\dfrac{v_6^s}{V_0},\ N_0+f_3\right) \end{bmatrix}(N_0+f_3) - \begin{bmatrix} \mu_1(\gamma_{10},\ \gamma_{20},\ \gamma_{60},\ N_0) \\ \mu_2(\gamma_{10},\ \gamma_{20},\ \gamma_{60},\ N_0) \\ \mu_6(\gamma_{10},\ \gamma_{20},\ \gamma_{60},\ N_0) \end{bmatrix} N_0 \quad .(5.43)$$

This is a non-linear friction equation. Combining it with the state-space wheel and rail models given in Section 5.2, and the contact spring formulation in Eq.(5.41), the time-domain squeal analyses can be obtained.

5.3.2 Wheel/rail rolling contact dynamics in the frequency domain

Besides the time-domain formulations, the wheel/rail rolling contact dynamics can also be described in the frequency domain, as given by Thompson and Monk-Steel [15]. In the quasi-steady condition, the dynamic forces and velocities can be converted into the frequency domain by assuming they are harmonically oscillating at frequency ω. Hence, the dynamic components of contact forces, wheel velocities, rail velocities, contact spring velocity, and sliding velocities are written as

$$f_i = F_i e^{j\omega t},\ v_i^w = V_i^w e^{j\omega t},\ v_i^r = V_i^r e^{j\omega t},\ v_3^c = V_3^c e^{j\omega t},\ v_i^s = V_i^s e^{j\omega t},\ \ i = 1,2,3,6 \ .(5.44)$$

In the frequency domain, the ratio of the velocity amplitude V_i to the force amplitude F_j at one frequency ω is termed mobility $Y_{ij}(\omega)$. The wheel and rail mobilities are provided by the corresponding structural models. Hence, the dynamic velocities and the dynamic forces can be connected by the mobility matrix. For the wheel and rail systems, this gives

$$\begin{bmatrix} V_1^w \\ V_2^w \\ V_3^w \\ V_6^w \end{bmatrix} \equiv - \begin{bmatrix} Y_{11}^w & Y_{12}^w & Y_{13}^w & Y_{16}^w \\ Y_{21}^w & Y_{22}^w & Y_{23}^w & Y_{26}^w \\ Y_{31}^w & Y_{32}^w & Y_{33}^w & Y_{36}^w \\ Y_{61}^w & Y_{62}^w & Y_{63}^w & Y_{66}^w \end{bmatrix} \begin{bmatrix} F_1 \\ F_2 \\ F_3 \\ F_6 \end{bmatrix}, \qquad (5.45)$$

and

$$\begin{bmatrix} V_1^r \\ V_2^r \\ V_3^r \\ V_6^r \end{bmatrix} \equiv \begin{bmatrix} Y_{11}^r & Y_{12}^r & Y_{13}^r & Y_{16}^r \\ Y_{21}^r & Y_{22}^r & Y_{23}^r & Y_{26}^r \\ Y_{31}^r & Y_{32}^r & Y_{33}^r & Y_{36}^r \\ Y_{61}^r & Y_{62}^r & Y_{63}^r & Y_{66}^r \end{bmatrix} \begin{bmatrix} F_1 \\ F_2 \\ F_3 \\ F_6 \end{bmatrix}, \tag{5.46}$$

where Y_{ij}^w and Y_{ij}^r are the mobilities of wheel and rail at the contact point.

Similar to Eq.(5.35), the amplitudes of the sliding velocities are

$$\begin{bmatrix} V_1^s \\ V_2^s \\ V_3^s \\ V_6^s \end{bmatrix} = \begin{bmatrix} V_1^r \\ V_2^r \\ V_3^r \\ V_6^r \end{bmatrix} - \begin{bmatrix} V_1^w \\ V_2^w \\ V_3^w \\ V_6^w \end{bmatrix} + \begin{bmatrix} 0 \\ 0 \\ V_3^c \\ 0 \end{bmatrix}. \tag{5.47}$$

The vertical compression velocity can be expressed by the contact spring mobilities Y_{33}^c,

$$V_3^c = Y_{33}^c F_3, \tag{5.48}$$

where the mobility of vertical contact spring is

$$Y_{33}^c = \frac{j\omega}{k_H}. \tag{5.49}$$

Substituting Eq.(5.45), Eq.(5.46) and Eq.(5.48) into the sliding velocities in Eq.(5.47), the dynamic relationship between wheel and rail is

$$\begin{bmatrix} V_1^s \\ V_2^s \\ V_3^s \\ V_6^s \end{bmatrix} = \begin{bmatrix} Y_{11} & Y_{12} & Y_{13} & Y_{16} \\ Y_{21} & Y_{22} & Y_{23} & Y_{26} \\ Y_{31} & Y_{32} & Y_{33} & Y_{36} \\ Y_{61} & Y_{62} & Y_{63} & Y_{66} \end{bmatrix} \begin{bmatrix} F_1 \\ F_2 \\ F_3 \\ F_6 \end{bmatrix}, \tag{5.50}$$

where $Y_{ij} = Y_{ij}^w + Y_{ij}^r + Y_{ij}^c$ is the sum of mobilities of wheel, rail, and contact spring.

In this dynamic relationship, the vertical sliding velocity should be zero, which gives

$$V_3^s = Y_{31}F_1 + Y_{32}F_2 + Y_{33}F_3 + Y_{36}F_6 = 0. \tag{5.51}$$

Thus, the vertical dynamic force is not independent and can be expressed in terms of the other three dynamic friction forces,

$$F_3 = -\begin{bmatrix} \frac{Y_{31}}{Y_{33}} & \frac{Y_{32}}{Y_{33}} & \frac{Y_{36}}{Y_{33}} \end{bmatrix} \begin{bmatrix} F_1 \\ F_2 \\ F_6 \end{bmatrix}. \tag{5.52}$$

This allows V_3^s to be eliminated from Eq.(5.50):

$$\begin{bmatrix} V_1^s \\ V_2^s \\ V_6^s \end{bmatrix} = \begin{bmatrix} Y_{11} & Y_{12} & Y_{16} \\ Y_{21} & Y_{22} & Y_{26} \\ Y_{61} & Y_{62} & Y_{66} \end{bmatrix} \begin{bmatrix} F_1 \\ F_2 \\ F_6 \end{bmatrix} + \begin{bmatrix} Y_{13} \\ Y_{23} \\ Y_{63} \end{bmatrix} F_3. \tag{5.53}$$

Substituting Eq.(5.52) into Eq.(5.53) for F_3 gives

$$\begin{bmatrix} V_1^s \\ V_2^s \\ V_6^s \end{bmatrix} = \begin{bmatrix} Y_{11} - \frac{Y_{13}Y_{31}}{Y_{33}} & Y_{12} - \frac{Y_{13}Y_{32}}{Y_{33}} & Y_{16} - \frac{Y_{13}Y_{36}}{Y_{33}} \\ Y_{21} - \frac{Y_{23}Y_{31}}{Y_{33}} & Y_{22} - \frac{Y_{23}Y_{32}}{Y_{33}} & Y_{26} - \frac{Y_{23}Y_{36}}{Y_{33}} \\ Y_{61} - \frac{Y_{63}Y_{31}}{Y_{33}} & Y_{62} - \frac{Y_{63}Y_{32}}{Y_{33}} & Y_{66} - \frac{Y_{63}Y_{36}}{Y_{33}} \end{bmatrix} \begin{bmatrix} F_1 \\ F_2 \\ F_6 \end{bmatrix}. \tag{5.54}$$

In this relation, only the friction forces and sliding velocities are involved. So the dynamic relationship of wheel/rail contact system can be written as

$$\{\mathbf{V}^s\} = [\mathbf{G}]\{\mathbf{F}^f\}, \tag{5.55}$$

where the vector of dynamic sliding velocities is

$$\{\mathbf{V}^s\} \equiv \begin{bmatrix} V_1^s & V_2^s & V_6^s \end{bmatrix}^{\mathrm{T}}, \tag{5.56}$$

the vector of dynamic friction forces is

$$\{\mathbf{F}^f\} \equiv [F_1 \quad F_2 \quad F_6]^{\mathrm{T}}, \tag{5.57}$$

and the mobility matrix is

$$[\mathbf{G}] = \begin{bmatrix} Y_{11} - \frac{Y_{13}Y_{31}}{Y_{33}} & Y_{12} - \frac{Y_{13}Y_{32}}{Y_{33}} & Y_{16} - \frac{Y_{13}Y_{36}}{Y_{33}} \\ Y_{21} - \frac{Y_{23}Y_{31}}{Y_{33}} & Y_{22} - \frac{Y_{23}Y_{32}}{Y_{33}} & Y_{26} - \frac{Y_{23}Y_{36}}{Y_{33}} \\ Y_{61} - \frac{Y_{63}Y_{31}}{Y_{33}} & Y_{62} - \frac{Y_{63}Y_{32}}{Y_{33}} & Y_{66} - \frac{Y_{63}Y_{36}}{Y_{33}} \end{bmatrix}. \tag{5.58}$$

The friction equation in Eq.(5.43) can be linearised at the steady-state point $(\gamma_{10},\ \gamma_{20},\ \gamma_{60},\ N_0)$ by assuming that the dynamic quantities are small and ignoring terms of second order in small quantities:

$$\begin{bmatrix} f_1 \\ f_2 \\ f_6 \end{bmatrix} = \frac{N_0}{V_0} \begin{bmatrix} \frac{\partial \mu_1}{\partial \gamma_1} & \frac{\partial \mu_1}{\partial \gamma_2} & \frac{\partial \mu_1}{\partial \gamma_6} & \frac{\partial \mu_1}{\partial f_3} \\ \frac{\partial \mu_2}{\partial \gamma_1} & \frac{\partial \mu_2}{\partial \gamma_2} & \frac{\partial \mu_2}{\partial \gamma_6} & \frac{\partial \mu_2}{\partial f_3} \\ \frac{\partial \mu_6}{\partial \gamma_1} & \frac{\partial \mu_6}{\partial \gamma_2} & \frac{\partial \mu_6}{\partial \gamma_6} & \frac{\partial \mu_6}{\partial f_3} \end{bmatrix} \begin{bmatrix} v_1^s \\ v_2^s \\ v_6^s \\ V_0 f_3 \end{bmatrix} + \begin{bmatrix} \mu_1 \\ \mu_2 \\ \mu_6 \end{bmatrix} f_3 . \qquad (5.59)$$

To convert the relationship, as given in Eq.(5.59), into the frequency domain, the dynamic forces and sliding velocities are assumed to be in harmonic form. Thus, the relationship between the amplitudes of the harmonic forces and velocities can be written as

$$\begin{bmatrix} F_1 \\ F_2 \\ F_6 \end{bmatrix} = \frac{N_0}{V_0} \begin{bmatrix} \frac{\partial \mu_1}{\partial \gamma_1} & \frac{\partial \mu_1}{\partial \gamma_2} & \frac{\partial \mu_1}{\partial \gamma_6} & \frac{\partial \mu_1}{\partial f_3} \\ \frac{\partial \mu_2}{\partial \gamma_1} & \frac{\partial \mu_2}{\partial \gamma_2} & \frac{\partial \mu_2}{\partial \gamma_6} & \frac{\partial \mu_2}{\partial f_3} \\ \frac{\partial \mu_6}{\partial \gamma_1} & \frac{\partial \mu_6}{\partial \gamma_2} & \frac{\partial \mu_6}{\partial \gamma_6} & \frac{\partial \mu_6}{\partial f_3} \end{bmatrix} \begin{bmatrix} V_1^s \\ V_2^s \\ V_6^s \\ V_0 F_3 \end{bmatrix} + \begin{bmatrix} \mu_1 \\ \mu_2 \\ \mu_6 \end{bmatrix} F_3 . \qquad (5.60)$$

The terms related to F_3 can be brought together to give,

$$\begin{bmatrix} F_1 \\ F_2 \\ F_6 \end{bmatrix} = \frac{N_0}{V_0} \begin{bmatrix} \frac{\partial \mu_1}{\partial \gamma_1} & \frac{\partial \mu_1}{\partial \gamma_2} & \frac{\partial \mu_1}{\partial \gamma_6} \\ \frac{\partial \mu_2}{\partial \gamma_1} & \frac{\partial \mu_2}{\partial \gamma_2} & \frac{\partial \mu_2}{\partial \gamma_6} \\ \frac{\partial \mu_6}{\partial \gamma_1} & \frac{\partial \mu_6}{\partial \gamma_2} & \frac{\partial \mu_6}{\partial \gamma_6} \end{bmatrix} \begin{bmatrix} V_1^s \\ V_2^s \\ V_6^s \end{bmatrix} + \begin{bmatrix} \mu_1 + N_0 \frac{\partial \mu_1}{\partial f_3} \\ \mu_2 + N_0 \frac{\partial \mu_2}{\partial f_3} \\ \mu_6 + N_0 \frac{\partial \mu_6}{\partial f_3} \end{bmatrix} F_3 . \qquad (5.61)$$

Eliminating F_3 using Eq.(5.52), the dynamic friction forces can be rewritten as

$$\begin{bmatrix} F_1 \\ F_2 \\ F_6 \end{bmatrix} = \frac{N_0}{V_0} \begin{bmatrix} \frac{\partial \mu_1}{\partial \gamma_1} & \frac{\partial \mu_1}{\partial \gamma_2} & \frac{\partial \mu_1}{\partial \gamma_6} \\ \frac{\partial \mu_2}{\partial \gamma_1} & \frac{\partial \mu_2}{\partial \gamma_2} & \frac{\partial \mu_2}{\partial \gamma_6} \\ \frac{\partial \mu_6}{\partial \gamma_1} & \frac{\partial \mu_6}{\partial \gamma_2} & \frac{\partial \mu_6}{\partial \gamma_6} \end{bmatrix} \begin{bmatrix} V_1^s \\ V_2^s \\ V_6^s \end{bmatrix} - \begin{bmatrix} \mu_1 + N_0 \frac{\partial \mu_1}{\partial f_3} \\ \mu_2 + N_0 \frac{\partial \mu_2}{\partial f_3} \\ \mu_6 + N_0 \frac{\partial \mu_6}{\partial f_3} \end{bmatrix} \begin{bmatrix} \frac{Y_{31}}{Y_{33}} & \frac{Y_{32}}{Y_{33}} & \frac{Y_{36}}{Y_{33}} \end{bmatrix} \begin{Bmatrix} F_1 \\ F_2 \\ F_6 \end{Bmatrix} . \quad (5.62)$$

This relationship between the dynamic friction forces and dynamic sliding velocities can be written as

$$\{\mathbf{F}^{\mathrm{f}}\} = [\mathbf{H}_1]\{\mathbf{V}^{\mathrm{s}}\} + [\mathbf{H}_2]\{\mathbf{F}^{\mathrm{f}}\}, \quad (5.63)$$

where the frictional impedance matrix $[\mathbf{H}_1]$ is related with the derivatives of non-dimensional friction forces with respect to creepages,

$$[\mathbf{H}_1] = \frac{N_0}{V_0} \begin{bmatrix} \frac{\partial \mu_1}{\partial \gamma_1} & \frac{\partial \mu_1}{\partial \gamma_2} & \frac{\partial \mu_1}{\partial \gamma_6} \\ \frac{\partial \mu_2}{\partial \gamma_1} & \frac{\partial \mu_2}{\partial \gamma_2} & \frac{\partial \mu_2}{\partial \gamma_6} \\ \frac{\partial \mu_6}{\partial \gamma_1} & \frac{\partial \mu_6}{\partial \gamma_2} & \frac{\partial \mu_6}{\partial \gamma_6} \end{bmatrix} = \begin{bmatrix} \frac{\partial f_1}{\partial v_1^s} & \frac{\partial f_1}{\partial v_2^s} & \frac{\partial f_1}{\partial v_6^s} \\ \frac{\partial f_2}{\partial v_1^s} & \frac{\partial f_2}{\partial v_2^s} & \frac{\partial f_2}{\partial v_6^s} \\ \frac{\partial f_6}{\partial v_1^s} & \frac{\partial f_6}{\partial v_2^s} & \frac{\partial f_6}{\partial v_6^s} \end{bmatrix}, \quad (5.64)$$

and the matrix $[\mathbf{H}_2]$ determines the influence from the fluctuation of vertical force on the friction forces,

$$[\mathbf{H}_2] = -\begin{bmatrix} \mu_1 + N_0 \frac{\partial \mu_1}{\partial f_3} \\ \mu_2 + N_0 \frac{\partial \mu_2}{\partial f_3} \\ \mu_6 + N_0 \frac{\partial \mu_6}{\partial f_3} \end{bmatrix} \begin{bmatrix} \frac{Y_{31}}{Y_{33}} & \frac{Y_{32}}{Y_{33}} & \frac{Y_{36}}{Y_{33}} \end{bmatrix}. \quad (5.65)$$

5.4 Self-excited vibration in the wheel/rail contact system

5.4.1 Self-excited vibration loop in the time domain

A general self-excited vibration model can be developed by combining wheel/rail structural models and the wheel/rail rolling contact model in a loop shown in Figure 5-4.

This loop is running on a set of steady-state conditions. If some small transient disturbances $\{\mathbf{f}'\}$ are introduced, the wheel and rail will produce dynamic responses $\{\mathbf{v}^w\}$ and $\{\mathbf{v}^r\}$, which can give dynamic sliding velocities $\{\mathbf{v}^s\}$ and the dynamic velocity of the contact spring v_3^c. In the contact area, the dynamic friction forces may be produced due to either the dynamic sliding velocities or the normal fluctuating force. Consequently, the contact forces $\{\mathbf{f}\}$, including friction forces and normal fluctuating force, are updated and fed back to the wheel and rail system. For the simulation in the time domain, the general loop can be realised in state space, as shown in Figure 5-5.

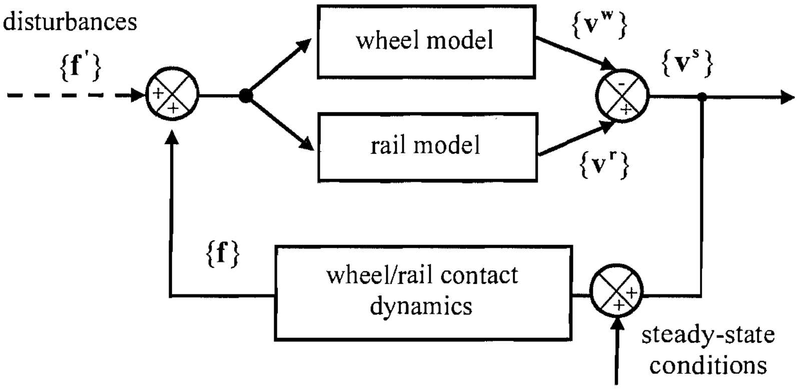

Figure 5-4 General self-excited vibration loop of the wheel/rail contact system.

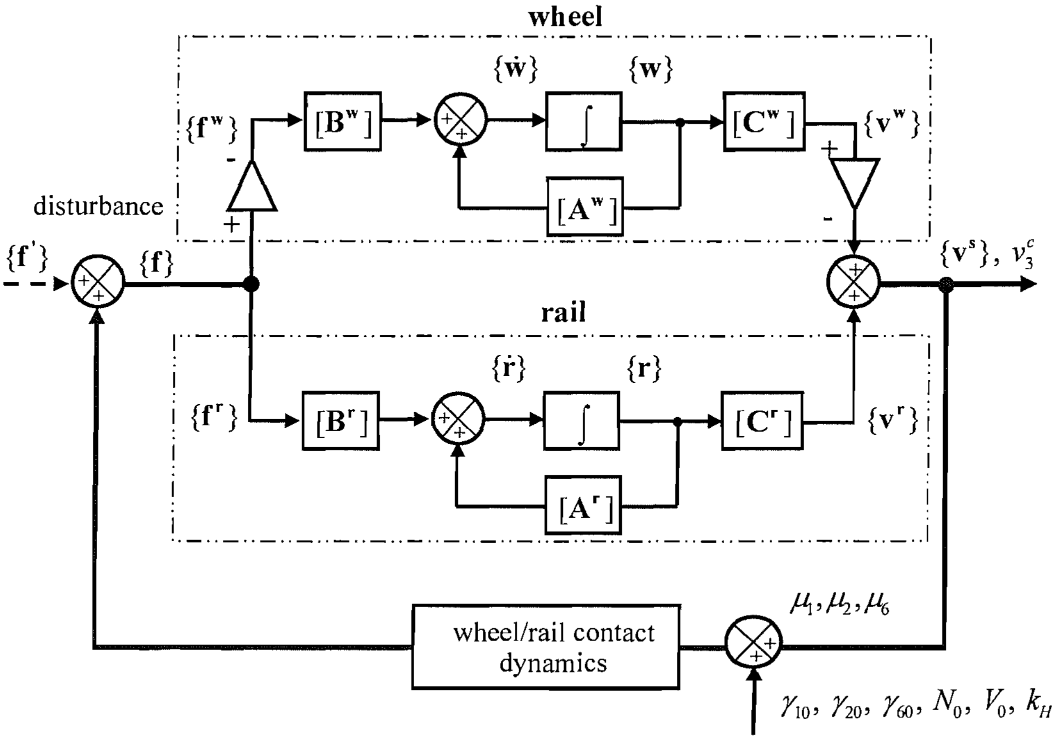

Figure 5-5 State-space self-excited vibration loop of the wheel/rail contact system.

In the state-space model of the wheel, the state variables $\{\mathbf{w}\}$ have physical meanings, i.e. the dynamic displacement and velocity of each mode. For the wheel, according to the definition of wheel forces $\{\mathbf{f}^{\mathrm{w}}\}$ in Eq.(5.28), the contact forces $\{\mathbf{f}\}$ are reversed in sign and applied to the wheel. To obtain the sliding velocities $\{\mathbf{v}^{\mathrm{s}}\}$ defined in Eq.(5.35), the velocities of the wheel $\{\mathbf{v}^{\mathrm{w}}\}$ need to be reversed again. Hence, these negative signs can be eliminated.

In the state-space model of the rail, the state variables $\{\mathbf{r}\}$ are derived from the coefficients of equivalent systems, so they have no clear physical meaning. According to the definition in Eq.(5.29), the forces acting on the rail are the same as the contact forces $\{\mathbf{f}\}$. The velocities of rail $\{\mathbf{v}^{\mathrm{r}}\}$ can be used directly to calculate the sliding velocities $\{\mathbf{v}^{\mathrm{s}}\}$, as given in Eq.(5.35).

The dynamic friction forces f_1, f_2, f_6 can be calculated in Eq.(5.43), with creepage-dependent non-dimensional friction forces μ_1, μ_2, μ_6 and steady-state conditions γ_{10}, γ_{20}, γ_{60}, N_0, V_0, k_H. The vertical fluctuating force f_3 is updated by the dynamic vertical approach velocity v_3^s, as given in Eq.(5.41).

The whole state-space feedback loop includes the non-linear relationship between the sliding velocities and the friction forces as well as the linear relationships in the wheel/rail contact system. The time-domain simulation is implemented by the step-by-step integration from any small disturbance $\{\mathbf{f}'\}$.

5.4.2 Self-excited vibration loop in the frequency domain

The general state-space loop is appropriate for numerical integration in the time-domain, but it is not suitable for analyses of the stability. This shortcoming can be overcome by establishing the general self-excited loop in the frequency domain.

From Eq.(5.55), the wheel/rail dynamic equation gives the relationship between the dynamic friction forces and the dynamic sliding velocities:

$$[\mathrm{G}]\{\mathrm{F^f}\} \to \{\mathrm{V^s}\}, \tag{5.66}$$

where $\{\mathrm{F^f}\}$ is formed of the friction forces and spin moment, and $\{\mathrm{V^s}\}$ includes the dynamic sliding velocities in the longitudinal, lateral and spin directions. It should be pointed out that the arrow signs in Eq.(5.66) to Eq.(5.69) cannot be replaced by equal signs because the steady-state conditions are not achieved.

Similarly, the linearised dynamic friction forces in Eq.(5.63) give the relationship between the dynamic sliding velocities and the dynamic friction forces:

$$[\mathrm{H_1}]\{\mathrm{V^s}\}+[\mathrm{H_2}]\{\mathrm{F^f}\} \to \{\mathrm{F^f}\}. \tag{5.67}$$

Thus, these two relationships can establish an MIMO system, as shown in Figure 5-6.

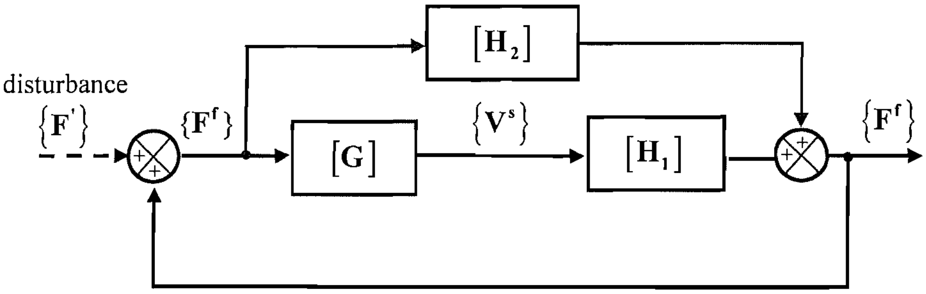

Figure 5-6 Frequency-domain self-excited vibration loop of the wheel/rail contact system.

Substitution of the vector of dynamic sliding velocity from Eq.(5.66) into Eq.(5.67) gives

$$([\mathrm{H_1}][\mathrm{G}]+[\mathrm{H_2}])\{\mathrm{F^f}\} \to \{\mathrm{F^f}\}. \tag{5.68}$$

So the open-loop transfer function is

$$[\mathrm{Q}]\{\mathrm{F^f}\} \to \{\mathrm{F^f}\}, \tag{5.69}$$

where $[\mathrm{Q}]=[\mathrm{H_1}][\mathrm{G}]+[\mathrm{H_2}]$ is the open-loop transfer function matrix (TFM).

5.5 Stability analysis of the loop in the time-domain

5.5.1 Reduced time-domain loop for the lateral motion

The general state-space loop is difficult for parametric analysis, because it includes several DOF and the state variables of the rail system have no physical meaning. To gain an insight into the self-excited vibration, the stability analysis of only an *n*-mode wheel with a reduced set of DOF is more practical. The assumptions are (1) the wheel system in the feedback loop is represented in state-space form; (2) the rail system is assumed rigid, which means no rail response contributes to the loop; (3) only the response and force in one possible sliding direction are considered, e.g. in the lateral direction; (4) the vertical fluctuating force is considered; (5) the friction force is linearised at the steady-state sliding velocity, e.g. v_{20}^s (or creepage γ_{20}).

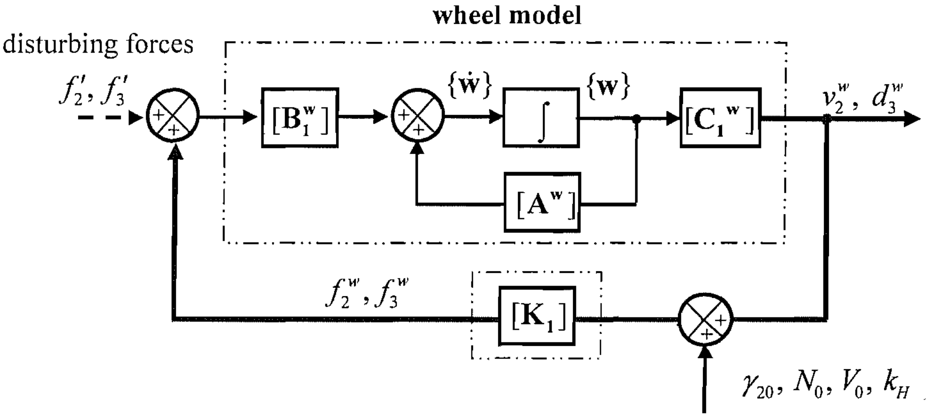

Figure 5-7 State-space self-excited vibration loop for only wheel system.

According to these assumptions, the general self-excited vibration loop in Figure 5-5 is revised to give the one shown in Figure 5-7. Compared with the general loop, there are the following differences between them: (1) two inverse blocks in the wheel route have been eliminated; (2) the output matrix of the wheel $[C^w]$ has been replaced by a reduced matrix $[C_1^w]$ which provides the lateral velocity v_2^w and vertical displacement d_3^w; (3) the contact dynamics are reduced to be a simple constant matrix for linearised lateral friction.

The state variables of the wheel then have following relationship

$$\begin{aligned}\{\dot{\mathbf{w}}\} &= \left([\mathbf{A}^{\mathrm{w}}]+[\mathbf{B}_1^{\mathrm{w}}][\mathbf{K}_1][\mathbf{C}_1^{\mathrm{w}}]\right)\{\mathbf{w}\} \\ &= [\mathbf{A}_{\mathrm{c}}^{\mathrm{w}}]\{\mathbf{w}\}\end{aligned}. \tag{5.70}$$

In this relationship, $[\mathbf{A}_{\mathrm{c}}^{\mathrm{w}}]$ is the system matrix of the feedback loop. $[\mathbf{A}^{\mathrm{w}}]$ is the system matrix that represents the dynamic properties of the wheel, as given in Eq.(5.4). $[\mathbf{B}_1^{\mathrm{w}}]$ is the input matrix, which stems from $[\mathbf{B}^{\mathrm{w}}]$ in Eq.(5.5), but only considers the lateral and vertical forces:

$$[\mathbf{B}_1^{\mathrm{w}}] \equiv \left[\begin{array}{cccc|cccc} \phi_{2,1} & \phi_{2,2} & \cdots & \phi_{2,n} & 0 & 0 & \cdots & 0 \\ \hline \phi_{3,1} & \phi_{3,2} & \cdots & \phi_{3,n} & 0 & 0 & \cdots & 0 \end{array}\right]^{\mathrm{T}}, \tag{5.71}$$

and $[\mathbf{C}_1^{\mathrm{w}}]$ is the output matrix, which stems from $[\mathbf{C}^{\mathrm{w}}]$ in Eq.(5.6), but only outputs the lateral velocity v_2^w and the vertical displacement d_3^w instead of the velocity v_3^w, which is

$$[\mathbf{C}_1^{\mathrm{w}}] \equiv \left[\begin{array}{cccc|cccc} \phi_{2,1} & \phi_{2,2} & \cdots & \phi_{2,n} & 0 & 0 & \cdots & 0 \\ \hline 0 & 0 & \cdots & 0 & \phi_{3,1} & \phi_{3,2} & \cdots & \phi_{3,n} \end{array}\right]. \tag{5.72}$$

Ignoring the rail components, the wheel vertical dynamic force can be obtained from Eq.(5.41),

$$f_3^w = -k_H d_3^w . \tag{5.73}$$

Ignoring the longitudinal and spin friction, and assuming the lateral non-dimensional friction force is only a function of lateral creepage $\mu_2(\gamma_2)$, the linearised lateral dynamic force of the wheel can be obtained from Eq.(5.59),

$$f_2^w = \frac{N_0}{V_0}\frac{d\mu_2}{d\gamma_2} v_2^w + \mu_2 f_3^w . \tag{5.74}$$

Substituting f_3^w from Eq.(5.73) into Eq.(5.74), the wheel lateral dynamic force can be expressed by

$$f_2^w = \frac{N_0}{V_0}\frac{d\mu_2}{d\gamma_2} v_2^w - \mu_2 k_H d_3^w = -c_e v_2^w - \mu_2 k_H d_3^w , \tag{5.75}$$

where the equivalent damping coefficient is

$$c_e \equiv -\frac{N_0}{V_0}\frac{d\mu_2}{d\gamma_2}, \tag{5.76}$$

which is the same definition and physical meaning as that in Eq.(4.29). Thus, the feedback matrix can be formed with Eq.(5.73) and Eq.(5.75),

$$[\mathbf{K}_1] \equiv \begin{bmatrix} -c_e & -\mu_2 k_H \\ 0 & -k_H \end{bmatrix}. \tag{5.77}$$

5.5.2 Root equation of the closed loop

The system described by the state-space model is stable if and only if the eigenvalues of the system matrix $[\mathbf{A}_c^w]$, that is, the roots of the system characteristic equation Γ

$$\Gamma: \ \left| s\mathbf{I} - [\mathbf{A}_c^w] \right| = 0, \tag{5.78}$$

all lie in the left-half s-plane [56].

Substitution of $[\mathbf{A}_c^w]$ given in Eq.(5.70) into Eq.(5.78), after some algebraic calculations, Γ is rewritten as

$$\begin{vmatrix} s^2+(\chi_{1,1}+2\zeta_1\omega_1)s+\delta_{1,1}+\omega_1^2 & \chi_{1,2}s+\delta_{1,2} & \cdots & \chi_{1,n}s+\delta_{1,n} \\ \chi_{2,1}s+\delta_{2,1} & \ddots & & \chi_{2,n}s+\delta_{2,n} \\ \vdots & \vdots & \ddots & \vdots \\ \chi_{n,1}s+\delta_{n,1} & \chi_{n,2}s+\delta_{n,2} & \cdots & s^2+(\chi_{n,n}+2\zeta_n\omega_n)s+\delta_{n,n}+\omega_n^2 \end{vmatrix} = 0, \tag{5.79}$$

where $\chi_{i,j}$ indicates the damping effect of the lateral friction force

$$\chi_{i,j} \equiv c_e \phi_{2,i}\phi_{2,j} \qquad i,j = 1,\cdots,n, \tag{5.80}$$

and $\delta_{i,j}$ indicates the effect of the vertical fluctuating force

$$\delta_{i,j} \equiv \mu_2 k_H \phi_{2,i}\phi_{3,j} + k_H \phi_{3,i}\phi_{3,j} \qquad i,j = 1,\cdots,n, \tag{5.81}$$

with the first term related to the lateral friction force and the second term related to the vertical force. Based on results of numerical calculations, the roots of Γ are found to be almost the same as those of Γ_1, which is obtained from Γ in Eq.(5.79) by eliminating all the off-diagonal terms,

$$\Gamma_1 : \begin{vmatrix} s^2+\left(\chi_{1,1}+2\zeta_1\omega_1\right)s+\delta_{1,1}+\omega_1^2 & 0 & \cdots & 0 \\ 0 & \ddots & & 0 \\ \vdots & & \ddots & \vdots \\ 0 & 0 & \cdots & s^2+\left(\chi_{n,n}+2\zeta_n\omega_n\right)s+\delta_{n,n}+\omega_n^2 \end{vmatrix} = 0 . \quad (5.82)$$

For illustrative purposes, the off-diagonal terms are temporarily eliminated in the following analytical analyses of the system roots.

Γ_1 has roots S_{i1}, S_{i2} from each diagonal term i

$$s^2+\left(\chi_{i,i}+2\zeta_i\omega_i\right)s+\left(\delta_{i,i}+\omega_i^2\right)=(s-S_{i1})(s-S_{i2})=0, \tag{5.83}$$

where

$$S_{i1,2}=\frac{-\left(\chi_{i,i}+2\zeta_i\omega_i\right)\pm\sqrt{\left(\chi_{i,i}+2\zeta_i\omega_i\right)^2-4\left(\delta_{i,i}+\omega_i^2\right)}}{2}. \tag{5.84}$$

Substituting $\chi_{i,i}$ from Eq.(5.80), the term $\left(\chi_{i,i}+2\zeta_i\omega_i\right)$ can be written as

$$\left(\chi_{i,i}+2\zeta_i\omega_i\right)=\phi_{2,i}^2\left(c_e+\frac{2\zeta_i\omega_i}{\phi_{2,i}^2}\right)=\phi_{2,i}^2\left(c_e+c_i\right), \tag{5.85}$$

where c_i is the modal damping coefficient, which is related to the damping ratio ζ_i by

$$c_i=\frac{2\zeta_i\omega_i}{\phi_{2,i}^2}. \tag{5.86}$$

Substituting for $\chi_{i,i}$ and $\delta_{i,i}$ from Eq.(5.80) and Eq.(5.81), the square root term in Eq.(5.84) can be rewritten as

$$\begin{aligned} &\sqrt{\left(\chi_{i,i}+2\zeta_i\omega_i\right)^2-4\left(\delta_{i,i}+\omega_i^2\right)} \\ &=\sqrt{\left(c_e\phi_{2,i}^2+2\zeta_i\omega_i\right)^2-4\omega_i^2-4\left(\mu_2k_H\phi_{2,i}\phi_{3,i}+k_H\phi_{3,i}\phi_{3,i}\right)}, \\ &=2\omega_i\sqrt{\left(\left(\zeta_{e,i}+\zeta_i\right)^2-1\right)-\lambda_i} \end{aligned} \tag{5.87}$$

where $\zeta_{e,i}$ is the equivalent damping ratio of the friction force for the mode i,

$$\zeta_{e,i} \equiv \frac{\phi_{2,i}^2}{2\omega_i} c_e , \tag{5.88}$$

and λ_i is the term related to the effect of the vertical force,

$$\lambda_i \equiv \frac{k_H \phi_{3,i}^{\ 2}}{\omega_i^2}\left(\mu_2 \frac{\phi_{2,i}}{\phi_{3,i}} + 1\right). \tag{5.89}$$

Substitution of Eq.(5.85) and Eq.(5.87) into Eq.(5.84) gives

$$S_{i1,2} = -\frac{\phi_{2,i}^2 \left(c_e + c_i\right)}{2} \pm \omega_i \sqrt{\left(\left(\zeta_{e,i} + \zeta_i\right)^2 - 1\right) - \lambda_i} . \tag{5.90}$$

Some discussions about the roots follow.

5.5.3 Stability analysis without vertical fluctuation

The effect of fluctuating normal force can be suppressed by setting the Hertz spring to be zero, $k_H = 0$. Hence, λ_i in the root equation in Eq.(5.90) is eliminated. Since the damping ratios $\zeta_{e,i}, \zeta_i$ are much less than unity, Eq.(5.90) can be rewritten as

$$S_{i1,2} = -\frac{\phi_{2,i}^2 \left(c_e + c_i\right)}{2} \pm \omega_i j \sqrt{1 - \left(\zeta_{e,i} + \zeta_i\right)^2} . \tag{5.91}$$

To ensure the stability of the feedback system, the real part of $S_{i1,2}$ must be negative, which gives

$$c_e + c_i > 0, \quad i = 1, \cdots, n . \tag{5.92}$$

This conclusion is the same as the stability criterion of the one-mode wheel system, as discussed in Chapter 4. Since the structural damping coefficient $c_i > 0$, if the friction damping coefficient c_e is positive, the wheel system is stable with all of its system roots on the left-half s-plane. If c_e is negative, the stability of the wheel is dependent on the value of structural damping coefficient c_i.

Heckl [20] presented a stability formula to show similar relations to that given in Eq.(5.92), although some parameters involved in Heckl's formula, such as the growth rate of the free wheel (related to the modal damping) and Green's function amplitude (related to the modeshape), are in different forms.

If the system is unstable at mode i, giving $c_e + c_i < 0$, the response grows with $e^{g_i t}$,

$$g_i = -\frac{\phi_{2,i}^2}{2}(c_e + c_i) > 0, \tag{5.93}$$

where g_i is called the increment gain in this thesis.

Hence, a larger increment gain can arise from the following factors: (1) larger value of negative equivalent damping coefficient c_e, (2) smaller value of positive structural damping, and (3) large mass-normalised lateral modeshape $\phi_{2,i}$.

The unstable oscillation frequency $\omega_{d,i}$ will not shift obviously from the natural frequency ω_i due to the relatively small damping ratio

$$\omega_{d,i} = \omega_i \sqrt{1 - (\zeta_i + \zeta_{ei})^2} \approx \omega_i . \tag{5.94}$$

5.5.4 Stability analysis for the vertical mode with vertical fluctuation

If the effect of the vertical contact force is included, the root equation in Eq.(5.87) can be discussed in terms of the modeshape. Considering first the case where the wheel mode i is a vertical mode, having

$$\left|\frac{\phi_{2,i}}{\phi_{3,i}}\right| \ll 1, \tag{5.95}$$

the vertical force term can be reduced to

$$\lambda_i \equiv \frac{k_H \phi_{3,i}{}^2}{\omega_i^2}\left(\mu_2 \frac{\phi_{2,i}}{\phi_{3,i}} + 1\right) \approx \frac{k_H \phi_{3,i}{}^2}{\omega_i^2} > 0 . \tag{5.96}$$

Hence, the roots are

$$S_{i1,2} = -\frac{\phi_{2,i}^2(c_e + c_i)}{2} \pm \omega_i j \sqrt{(1 + \lambda_i) - (\zeta_{e,i} + \zeta_i)^2} . \tag{5.97}$$

The stability analysis is the same as the analysis for $\lambda_i = 0$. The effect of λ_i is mainly on the possible oscillation frequency, especially for those low frequency modes:

$$\omega_{d,i} = \omega_i \sqrt{(1+\lambda_i) - (\zeta_i + \zeta_{ei})^2} \approx \omega_i \sqrt{(1+\lambda_i)}. \tag{5.98}$$

5.5.5 Stability analysis for the lateral mode with vertical fluctuation

If the mode i is a lateral mode, with larger lateral modeshape and smaller vertical modeshape

$$\left| \frac{\phi_{2,i}}{\phi_{3,i}} \right| \gg 1. \tag{5.99}$$

The vertical force term in can then be reduced to

$$\lambda_i \equiv \frac{k_H \phi_{3,i}{}^2}{\omega_i^2} \left(\mu_2 \frac{\phi_{2,i}}{\phi_{3,i}} + 1 \right) \approx \mu_2 \frac{k_H \phi_{3,i} \phi_{2,i}}{\omega_i^2}. \tag{5.100}$$

As the non-dimensional friction force has a negative sign for a positive steady-state creepage, $\mu_2 < 0$, if the signs of lateral and vertical modeshapes are opposite, giving $\phi_{2,i}\phi_{3,i} < 0$, the vertical force term will be positive

$$\lambda_i = \mu_2 \frac{k_H \phi_{3,i} \phi_{2,i}}{\omega_i^2} > 0. \tag{5.101}$$

Thus, the stability analysis is the same as that for the vertical mode. Compared with the vertical mode, the lateral mode has larger lateral modeshape and smaller vertical modeshape, so that it has larger increment gain and smaller shift of oscillation frequency.

It is quite interesting to note that if the lateral and vertical modeshapes have the same sign, giving $\phi_{2,i}\phi_{3,i} > 0$, the following condition may be satisfied for sufficiently large modeshape values (or low frequencies)

$$\lambda_i = \mu_2 \frac{k_H \phi_{3,i} \phi_{2,i}}{\omega_i^2} < -1, \tag{5.102}$$

so that the term related with oscillation is positive

$$\left(\left(\zeta_{e,i}+\zeta_i\right)^2-1\right)-\lambda_i>0, \tag{5.103}$$

thus, the root equation in Eq.(5.90) will have two real values and no oscillation will take place in this mode.

5.5.6 Discussion

The stability of one wheel mode is mainly dependent on the damping condition, which is a combination of the structural damping and the equivalent friction damping. Negative equivalent damping may lead the mode to become unstable, while positive structural damping always lessens and may even eliminate this tendency. In the stability analysis, the equivalent friction damping coefficient c_e is the same for all modes, while the structural damping c_i may be different. Both friction and structural damping play important roles in stability.

If several modes are unstable, the one with the largest increment gain will develop its oscillation more quickly than any other. In the process of self-excited vibration, this means the generated dynamic friction force also has a larger component at this oscillation frequency. Finally, this mode will develop to be the dominant one with the largest amplitude of response. Nevertheless, the oscillation frequency may shift slightly from the natural frequency of this mode. From the analysis of the root equation, the mode with the largest increment gain is expected to have a flexible lateral modeshape (due to the lateral friction force) and small structural damping. The shift of natural frequency is related to the vertical force effect.

However, in the system involving only the wheel, the effect of the vertical force is overestimated. Since the motion of the rail is ignored by considering it as rigid, the compression of the contact spring is equal to the vertical fluctuation of the wheel. In practice, the rail vertical mobility is greater than that of the contact spring for much of the frequency range below 1000 Hz [55], so that the contact spring will deflect less than this model (with rigid rail) suggests. The vertical fluctuating force is actually very limited. The previous analysis related with the vertical force is thus only qualitative.

The stability analysis is based on the linearised friction at one steady-state value of creepage. The mode with largest increment gain at steady-state creepage may not have the largest increment gain at creepages far from the steady-state creepage. The growth of oscillation for an unstable mode is dependent on the nonlinearity of the friction.

The current stability analysis has ignored the off-diagonal terms in the system matrix, which are related to the coupling effects between modes. This simplification will make the actual results change a bit. Hence, a numerical analysis is necessary for the general self-excited wheel/rail contact model.

5.6 Stability analysis for the frequency-domain loop

5.6.1 Stability analysis for the lateral motion

For a linear system, the output to a sinusoidal input is a sinusoid of the same frequency but with a different amplitude and phase. Therefore, in a single-input-single-output (SISO) linear system, the open-loop response to a sinusoidal input at varying frequencies is represented by a transfer function with respect to the frequency. This open-loop transfer function can be used to predict the behaviour of the closed-loop system via classic frequency-domain techniques, e.g. Nyquist stability criterion, Bode plot and root locus (see Figure 5-8).

For a case where only lateral creepage is of interest, the terms involving V_1^s, V_6^s, F_1 and F_6 can be eliminated. This leads to the following reduced wheel/rail dynamic equation from Eq.(5.54),

$$V_2^s = \left(Y_{22} - \frac{Y_{23}Y_{32}}{Y_{33}} \right) F_2 = GF_2, \tag{5.104}$$

and the linearised friction force from Eq.(5.61),

$$F_2 = \frac{N_0}{V_0}\frac{\partial \mu_2}{\partial \gamma_2} V_2^s - \left(\mu_2 + N_0 \frac{\partial \mu_2}{\partial f_3} \right) \frac{Y_{32}}{Y_{33}} F_2 = H_1 V_2^s + H_2 F_2 . \tag{5.105}$$

In this case, the general system described in Figure 5-6 is reduced to a SISO system with open loop

$$\begin{aligned}(H_1G+H_2)\cdot F_2 &\to F_2\\ Q\cdot F_2 &\to F_2\,.\end{aligned} \tag{5.106}$$

where the open-loop transfer function is

$$Q = H_1G + H_2\,. \tag{5.107}$$

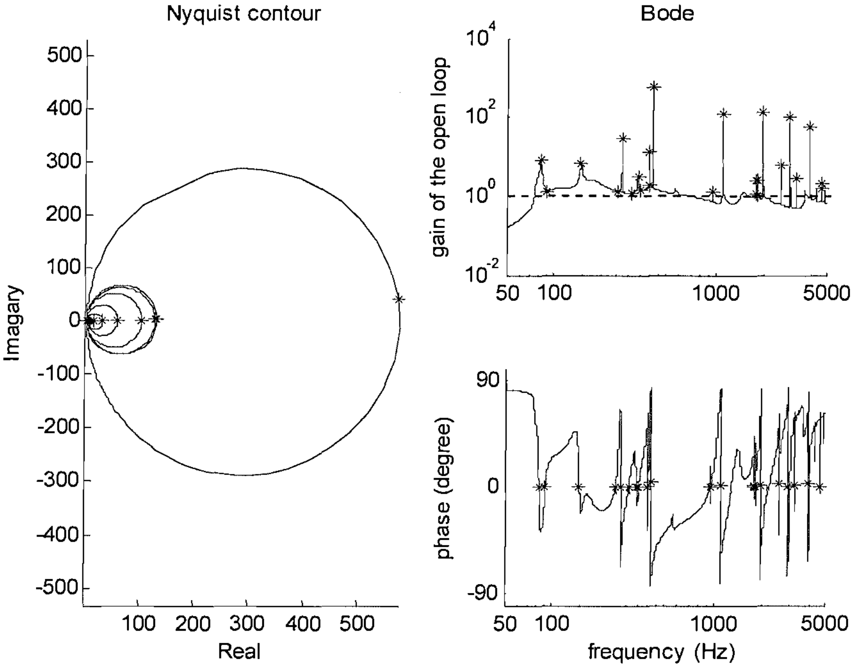

Figure 5-8 Stability analysis in the lateral direction, * unstable frequencies.

If a system is stable, the response of the system to a disturbance (such as an impulse input) will asymptotically tend to the equilibrium. In the self-excited vibration, the equilibrium is at the steady-state condition. In this frequency-domain loop, the stability of the wheel/rail system is a function of frequency. For a SISO system, if an open-loop system is stable (e.g., the dynamic response of the wheel/rail system is always stable in the absence of the feedback mechanism), the stability analysis of its closed-loop system can be considered using its open-loop Bode plot. The Bode plot with gain and phase lag of the system is introduced here to illustrate the conditions for instability of the corresponding closed feedback loop. According to the Nyquist criterion, instability occurs in the closed loop system if the polar plot of the open loop frequency response crosses the real axis beyond the critical point $(-1/k, j0)$, where for a negative feedback, $k=1$, and for a positive feedback, $k=-1$. Since the self-excited vibration is described as a positive feedback loop, see Figure 5-4, the critical point for the current stability analysis is $(1, j0)$. That is to say, in the Bode plot, if the amplitude of the open loop transfer function H_1G+H_2 exceeds unity when the phase angle is 0°, the positive feedback loop is unstable, as shown in Figure 5-8.

The physical meaning can be explained intuitively as follows. Assume that the feedback system is linear and the input signal is a small amplitude oscillation at one frequency. Only if the feedback signals are in phase with the reference input, will the output amplitude increase steadily. Thus, for the positive and negative feedback systems, the output signal should have 0° and 180° phase lag respectively to make the feedback signals occur in phase with the reference inputs.

Besides the condition of phase match between input and output signals, the amplitude of the open loop gain in the SISO Nyquist stability criterion is also meaningful. If the reference input may be stopped, e.g. some transient signals, the feedback system can still run. Normally, the in-phase positive feedback system can also be termed a self-sustaining system. If the gain is less than unity at this frequency, the output will die away to zero. If the gain is unity, the oscillation will be maintained at this frequency with steady amplitude. If the open loop gain is greater than unity at this frequency, the output increases without limit, that is to say, the amplitude increases in magnitude each time the signal passes around the loop. This means that the closed loop of positive feedback systems in Figure 5-6 will be unstable if the open loop frequency response has a gain $q(\omega)$ greater than unity at the frequency giving an open loop phase lag of 0°. Therefore, the unstable frequencies must satisfy the following condition:

$$\mathrm{Re}\{q(\omega)\} > 1, \qquad (5.108)$$

and

$$\mathrm{Im}\{q(\omega)\}=0\,. \tag{5.109}$$

In the SISO Nyquist criterion, the value of the open-loop gain $q(\omega)$ at the unstable frequency can be used to judge the increment of unstable amplitude.

5.6.2 Stability analysis for the general system

For a general MIMO loop, in which the open-loop responses are represented by a transfer function matrix (TFM) (see Section 5.4.2), these techniques for SISO systems may not be appropriate and need to be generalised for MIMO problems. For example, the Nyquist stability criterion was developed using eigenloci of the open-loop TFM. This generalised Nyquist criterion was proved in 1970s by several researchers with different methods [57,58,59,60].

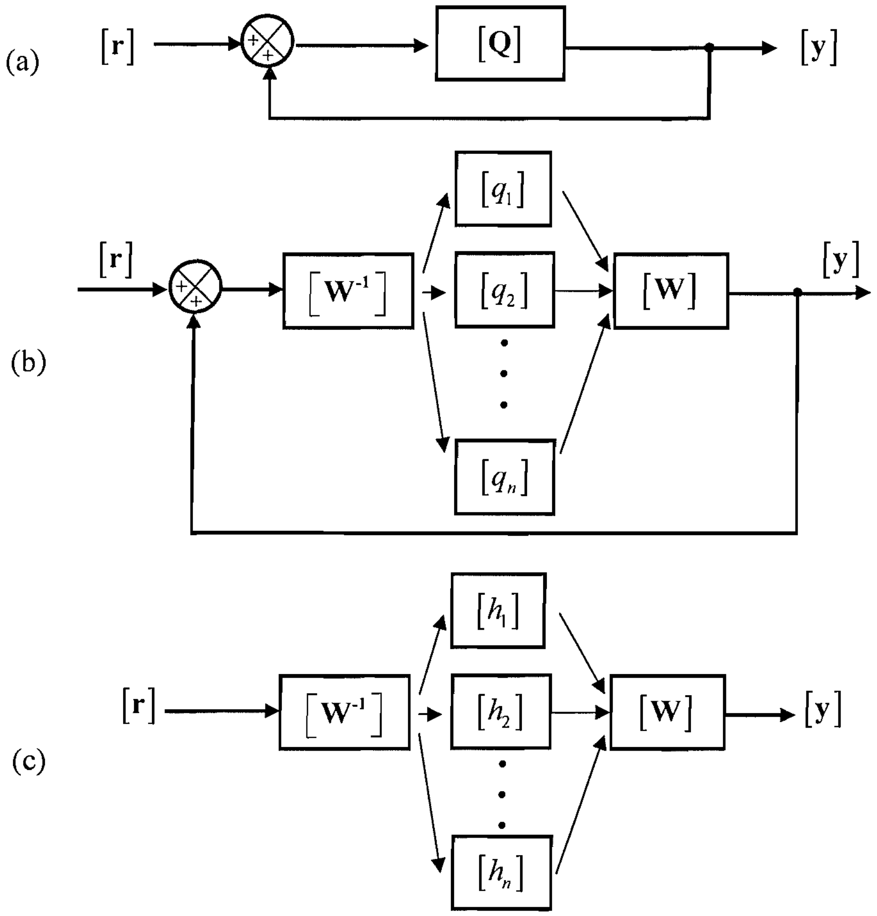

Figure 5-9 Decoupling an MIMO system for stability analysis, (a) original system; (b) modal decomposition of TFM; (c) an equivalent system.

From a straightforward engineering point of view, the eigenvalue analysis involved in the generalised Nyquist criterion actually decouples the TFM. In Figure 5-9, the open-loop TFM, $[\mathbf{Q}]$ (square matrix), can be regarded as the result of applying a transform to obtain a diagonal matrix containing its eigenvalues.

If $q_1(\omega)$, $q_2(\omega)$, $\cdots$ $q_n(\omega)$ represent the frequency-dependent eigenvalues of $[\mathbf{Q}(\omega)]$, then the appropriate diagonal eigenvalue matrix is

$$[\mathrm{q}(\omega)] = \mathrm{diag}\{q_1(\omega), q_2(\omega), \cdots, q_n(\omega)\}, \tag{5.110}$$

and it is possible to write

$$[\mathbf{Q}(\omega)] = [\mathbf{W}(\omega)]^{-1} [\mathrm{q}(\omega)][\mathbf{W}(\omega)], \tag{5.111}$$

where $[\mathbf{W}(\omega)]$ is the eigenvector matrix of $[\mathbf{Q}(\omega)]$ corresponding to each eigenvalue. Eq.(5.111) suggests a mathematically equivalent forward loop, see Figure 5-9(b). Since the transfer function of the closed loop in Figure 5-9(a) is

$$[\mathbf{H}(\omega)] = \{\mathbf{I}_n - [\mathbf{Q}(\omega)]\}^{-1} [\mathbf{Q}(\omega)] \tag{5.112}$$

substituting $[\mathbf{Q}(\omega)]$ from Eq.(5.111) into Eq.(5.112) gives

$$\begin{aligned}
[\mathbf{H}(\omega)] &= \left\{\mathbf{I}_n - \left\{[\mathbf{W}(\omega)]^{-1}[\mathrm{q}(\omega)][\mathbf{W}(\omega)]\right\}\right\}^{-1} \left\{[\mathbf{W}(\omega)]^{-1}[\mathrm{q}(\omega)][\mathbf{W}(\omega)]\right\} \\
&= \left\{[\mathbf{W}(\omega)]^{-1}\left\{[\mathbf{W}(\omega)] - [\mathrm{q}(\omega)][\mathbf{W}(\omega)]\right\}\right\}^{-1} \left\{[\mathbf{W}(\omega)]^{-1}[\mathrm{q}(\omega)][\mathbf{W}(\omega)]\right\} \\
&= \left\{[\mathbf{W}(\omega)]^{-1}\{\mathbf{I}_n - [\mathrm{q}(\omega)]\}[\mathbf{W}(\omega)]\right\}^{-1} \left\{[\mathbf{W}(\omega)]^{-1}[\mathrm{q}(\omega)][\mathbf{W}(\omega)]\right\} \\
&= [\mathbf{W}(\omega)]^{-1} \left\{\{\mathbf{I}_n - [\mathrm{q}(\omega)]\}^{-1}[\mathrm{q}(\omega)]\right\}[\mathbf{W}(\omega)] \\
&= [\mathbf{W}(\omega)]^{-1} \mathrm{diag}\{h_1(\omega), h_2(\omega), \cdots, h_n(\omega)\}[\mathbf{W}(\omega)]
\end{aligned} \quad ,(5.113)$$

where

$$h_i(\omega) = \frac{q_i(\omega)}{1 - q_i(\omega)}. \tag{5.114}$$

It can be shown that the closed-loop TFM for the entire system of Figure 5-9(a) can be replaced by the non-interacting closed-loop sub-systems as shown in Figure 5-9(c).

Thus, the classic Nyquist stability criterion for SISO systems can be applied on this decoupled MIMO system. Hence, the generalised Nyquist stability criterion applied for a feedback system can be stated as follows. The system will be closed-loop stable if and only if the net sum of anti-clockwise encirclements of the critical point $(-1/k+j0)$ by the set of eigenloci of the open-loop TFM is equal to the total number of right-half plane poles of the TFM, where for a negative feedback, $k=1$, and for a positive feedback, $k=-1$. In the frequency-domain squeal loop, the open-loop TFM is established using the mobilities of the wheel/rail system, with bounded input and bounded output (BIBO stable). So this system is physically stable, which means no pole of the open-loop TFM is located in the right-half plane. Thus, the eigenloci of the open-loop TFM must not encircle the critical point $(1+j0)$ (the positive feedback loop with $k = -1$) to make sure the closed-loop system is stable, when the frequency is varied from zero to infinity.

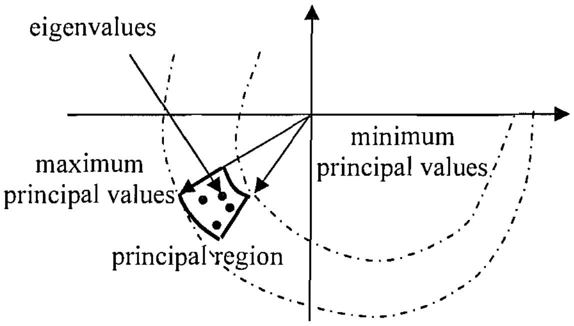

Figure 5-10 Principal region on the complex plane and the eigenvalues inside it.

However, although this mathematical generalization of the classic Nyquist stability criterion is possible, the application of this method has some limitations. One is that the graphical appeal requires constructions in higher dimensional spaces and thus some of the graphical properties may be lost. For example, for predicting the possible unstable frequencies in the squeal loop, only the eigenvalue with maximum modulus at each frequency is chosen to judge the stability. The other limit is, for those unstable frequencies, the magnitude of the eigenvalues may not represent the increment gain. The magnitudes of the eigenvalues of the TFM at one frequency are bounded above and below by the corresponding maximum and minimum principal gains. The arguments of the eigenvalues of the TFM at one frequency are bounded above and below by the maximum and minimum principal phases, if the principal phases of the TFM have a spread of less than π. Thus, at one frequency, m eigenvalues of this TFM ($m \times m$ squeal matrix) are located in a curvilinear rectangle region (segment of annular region) determined by corresponding maximum and minimum principal values [61], as shown in Figure 5-10. Actually the magnitude of the eigenvalue is the increment gain if the input signal vector is the same as the corresponding eigenvector. Hence, the eigenloci in the generalised Nyquist criterion can be used to judge the stability of the MIMO system, but cannot be used to indicate the increment at the unstable frequency.

5.7 Parametric study

A parametric study has been carried out to investigate the roles of some important parameters involved in the generation of curve squeal. Parameters studied include the steady-state creepages, the wheel/rail contact position and contact angle, and the falling ratio in the friction function. The effectiveness of using stability analysis for squeal prediction is investigated by comparing results with those from the time-domain predictions. Practical squeal control methods, i.e. friction modification and wheel damping treatment, are also investigated generically by suitable parameter variations.

5.7.1 Parameters of cases in study

The cases considered in the parametric study are listed in Table 5-1. The wheel is a right-hand Class 158 wheel in the wheelset. The rail is a standard UIC 60 rail with a pad of following parameters: traverse stiffness 1.7×10^7 N/m, vertical stiffness 5.8×10^8 N/m and loss factor 0.25. The normal contact force between wheel and rail is $N_0 = 62$ kN. The rolling velocity of the vehicle is $V_0 = 10$ m/s. The semi-axes of the contact ellipse are $a = b = 5$ mm. The Coulomb friction coefficient is $\mu_0 = 0.3$, with a falling ratio $\lambda = 0.3$ and saturation coefficient $\kappa = 0.005$ (see Eq.(2.28)). The nominal wheel/rail contact positions and contact angle are $l_y^w = l_z^w = 0$, $l_y^r = l_z^r = 0$, $\delta = 0^\circ$. Some of these parameters are varied from these nominal values as indicated in Table 5-1.

Table 5-1 Description of cases in study

No.	γ_{10} [%]	γ_{20} [%]	γ_{60} [m^{-1}]	particular parameters [7]
1	0	2	0	
2	0	0.5	0	
3	2	0	0	
4	0.5	0	0	
5	0.5	2	0	
6	0.5	0.5	0	
7	0	2	1.5	
8	0	2	0	$l_y^w = 30\,\text{mm}$
9	0	2	0	$l_y^w = -30$ mm
10	0	2	0	$\delta = -30^\circ$
11	0	2	1.5	$l_y^w = l_y^r = -30\,\text{mm}$, $\delta = -30^\circ$
12	0	2	0	× 10, 50, 100 wheel damping
13	0	2	0	× 10, 50, 100 wheel damping, $\lambda = 0.1$

Nominal parameters

A right-hand Class 158 wheel; $N_0 = 62$ kN, $V_0 = 10$ m/s, $a = 5$ mm, $b = 5$ mm, $\mu_0 = 0.3$, $\lambda = 0.3$, $\kappa = 0.005$, the nominal wheel/rail contact positions and angle: $l_y^w = l_z^w = 0$, $l_y^r = l_z^r = 0$, $\delta = 0^\circ$.

5.7.1.1 Friction

Figure 5-11 shows the friction curves used in the case study. These are calculated using FASTSIM, and are plotted after normalisation by the Coulomb friction $\mu_0 N_0$. The friction curves with different falling slope are presented in Figure 5-11(a). The coefficients in the falling function are assumed to be $\kappa = 0.005$, $\lambda = 0.1, 0.3, 0.5$. In Figure 5-11(b), the curves of lateral friction with respect to the lateral creepage are shown for various values of the steady-state longitudinal creepage. The falling zone of the friction curve is attenuated or even eliminated if the longitudinal creepage is large enough. Figure 5-11(c) shows the effect of a large steady-state spin on the lateral

---

[7] Only parameters that are different from the nominal ones are listed.

friction. The large spin can attenuate the falling zone in the same way as the longitudinal creepage. As discussed in Appendix A, the resultant force produced by a spin is in the lateral direction. This additional lateral friction can offset the lateral friction curve in terms of the lateral creepage, making the lateral friction curve asymmetric about the axis of zero creepage. Hence, either a longitudinal creepage or a large enough spin may change the friction characteristics in the lateral direction. A similar phenomenon can be found in the longitudinal friction behaviour. In the time-domain calculations, the friction forces (and spin moment) are obtained by using FASTSIM at each step of the simulation, with the corresponding longitudinal, lateral and spin creepages.

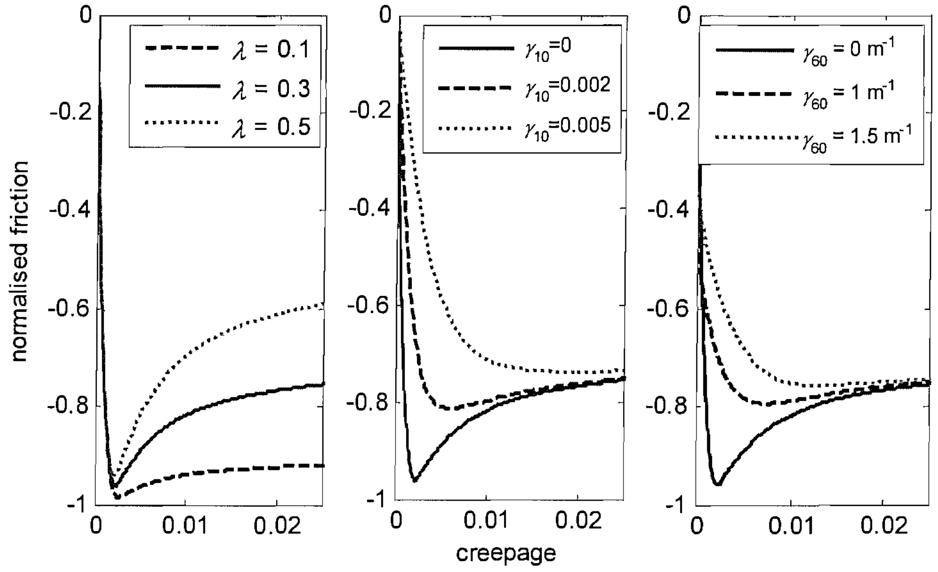

(a) (b) (c)

Figure 5-11 Friction force (normalised by the Coulomb friction) with respect to the creepage. (a) Resultant friction with respect to the resultant creepage, with different falling ratios and without spin; (b) lateral friction with respect to the lateral creepage, with falling ratio λ = 0.3, different steady-state longitudinal creepages and without spin; (c) lateral friction with respect to the lateral creepage, with falling ratio λ = 0.3, different steady-state spin.

5.7.1.2 Dynamic properties of wheel and rail at the nominal contact

The rail (track) system is a standard UIC 60 rail with a pad of moderate stiffness. The parameters of the track system are provided in Table E-1, Appendix E. The vehicle is a Class 158 DMU with parameters provided in Table D-1, Appendix D. The wheel is the

Class 158 wheel. The significant modes below 5000 Hz are listed in Table H-1, Appendix H, with 27 modes included in the calculations. The wheel and rail mobilities at the nominal contact position are shown in Figure 5-12 to Figure 5-15, respectively. In the vertical direction, the mobility of the vertical contact spring is included in the model. The stiffness of the vertical contact spring is taken as $k_H = 1.50 \times 10^9$ N/m. The most significant modes in each direction are identified in the corresponding mobility curve. The 'rigid' modes are the lowest vibration modes in the wheel, approximately determined by the inertia of wheel and the stiffness and damper of the vehicle suspension.

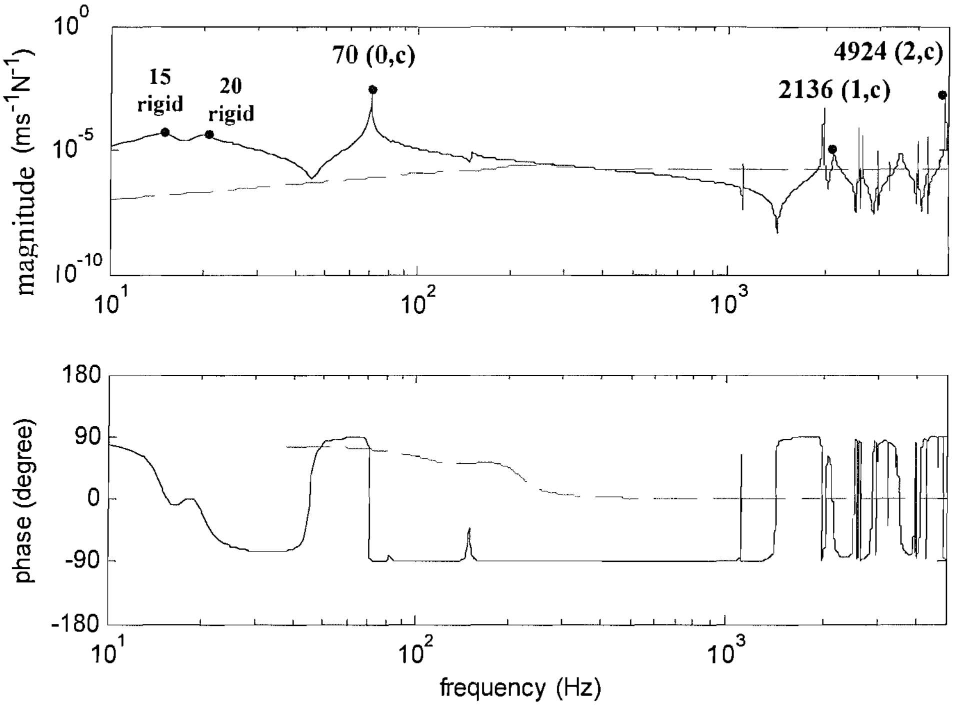

Figure 5-12 Longitudinal mobilities of the wheel and rail at the nominal contact point, —— wheel, --- — rail. Natural frequencies (in Hz) and mode identification of predominant modes are indicated .

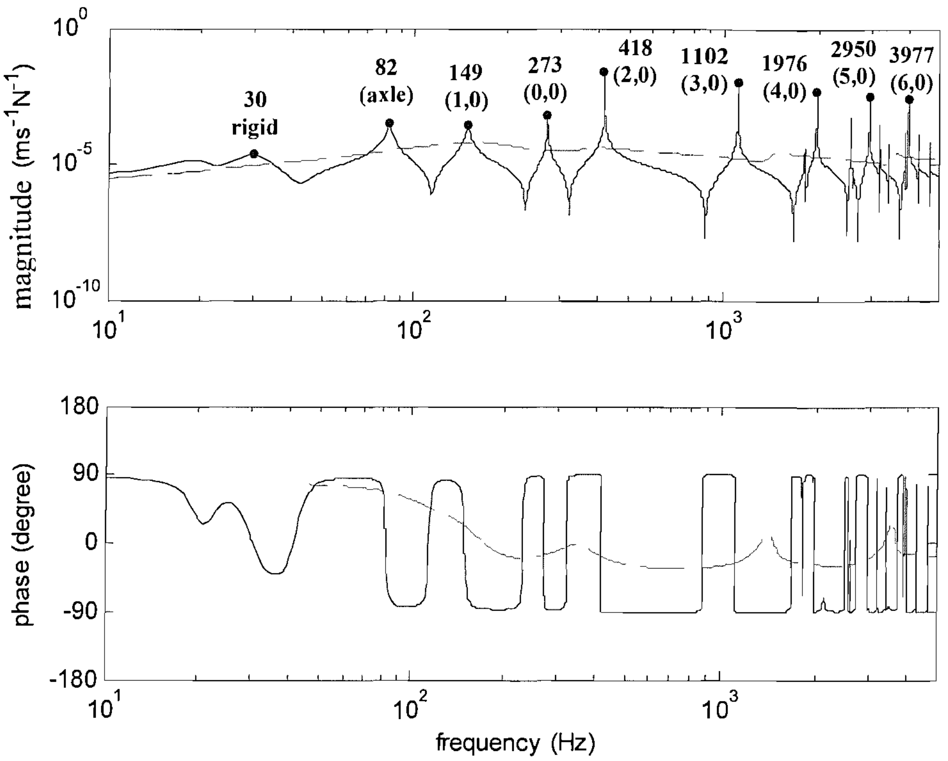

Figure 5-13 Lateral mobilities of the wheel and rail at the nominal wheel/rail contact point, —— wheel, — — rail. Natural frequencies (in Hz) and mode identification of predominant modes are indicated.

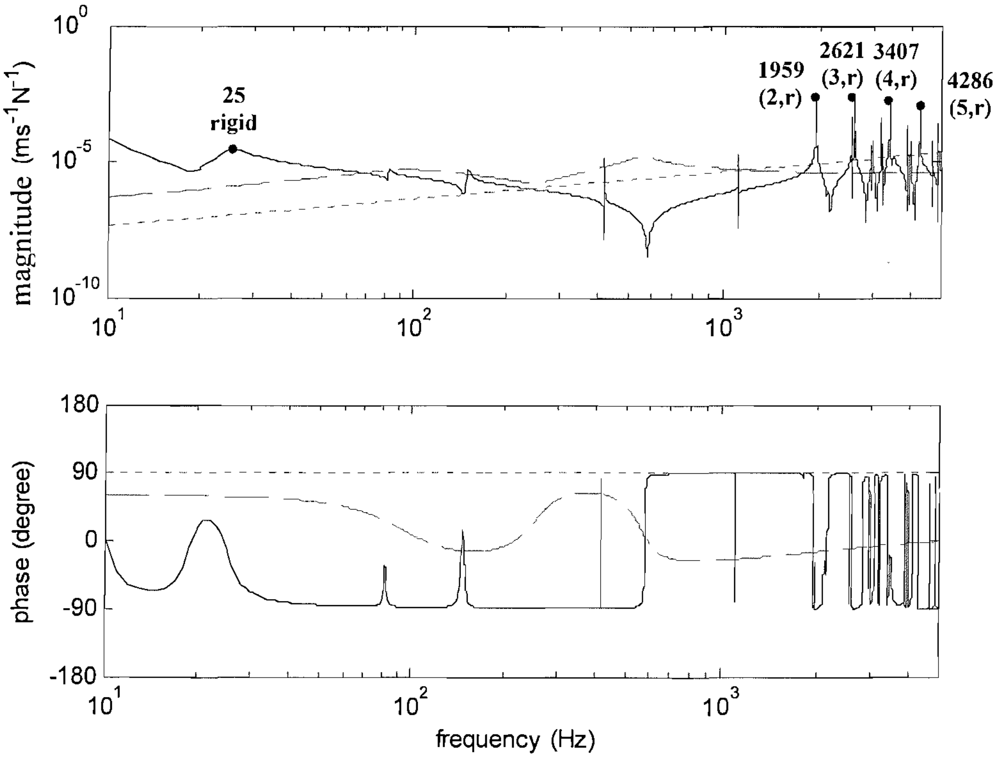

Figure 5-14 Vertical mobilities of the wheel, rail and contact spring at the nominal contact point, —— wheel, — — rail, ----- contact spring. Natural frequencies (in Hz) and mode identification of predominant modes are indicated.

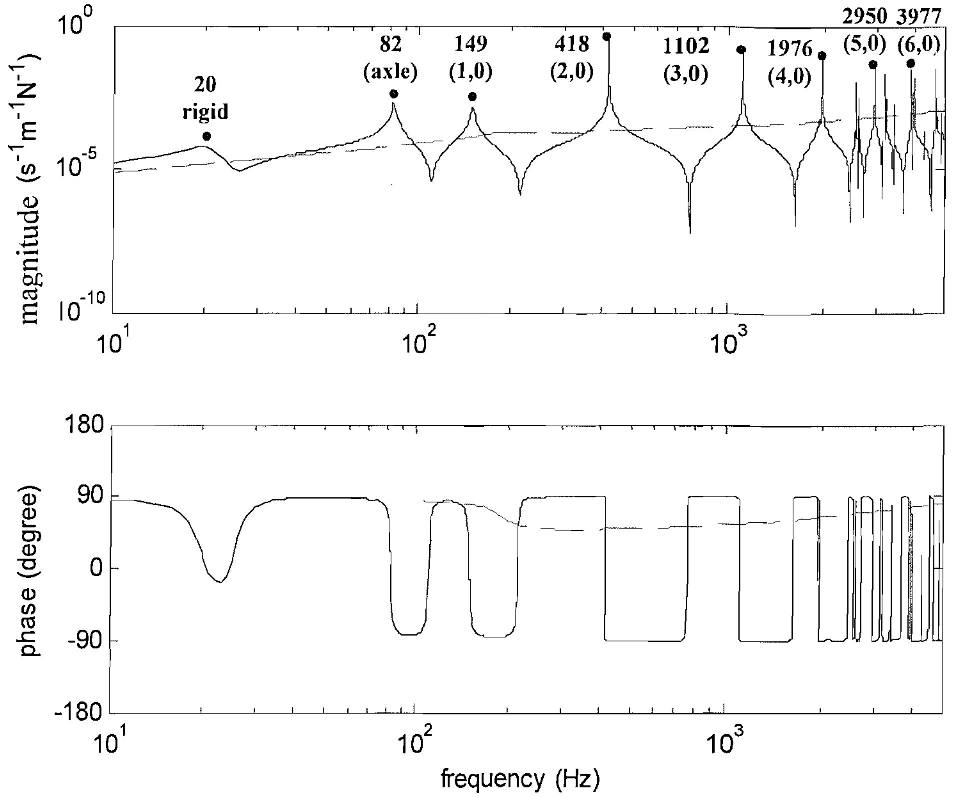

Figure 5-15 Spin mobilities of the wheel and rail at the nominal contact point, —— wheel, — — rail. Natural frequencies (in Hz) and mode identification of predominant modes are indicated.

5.7.1.3 Dynamic properties of wheel and rail at the flange contact position

For a curving bogied vehicle, some wheel/rail contact positions are far from the nominal position and with a large contact angle at the flange. In Case (11), flange contact takes place at the right-hand wheel. Consequently, the wheel and rail contact positions shift from the nominal contact point with distances of $l_y^w = l_y^r = -30$ mm, and the contact plane between them rotates by a contact angle of $\delta = -45^\circ$. In the new contact frame, the mobilities of wheel and rail can be transformed from those at the nominal position by using a rigid transformation. In Figure 5-16, the transformed wheel mobilities in the transverse and normal directions are compared with corresponding mobilities at the nominal position. Due to the rotation of the contact plane, the lateral resonances are not as flexible at the flange as at the nominal contact position. Furthermore, the lateral resonances can also be found in the normal mobility, making the wheel more flexible in this direction. Similar analyses can be applied for the rail mobilities, see Figure 5-17.

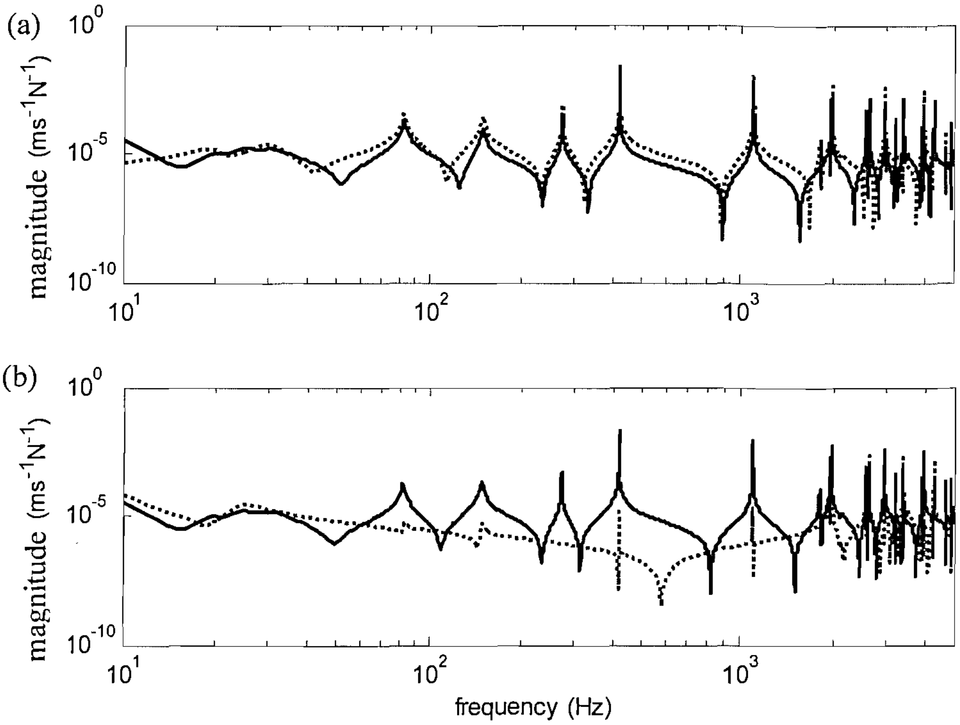

Figure 5-16 Comparison of the wheel mobilities at different contact positions, —— at the flange contact position, ······ at the nominal contact position, (a) the lateral (transverse) mobility, (b) the vertical (normal) mobility.

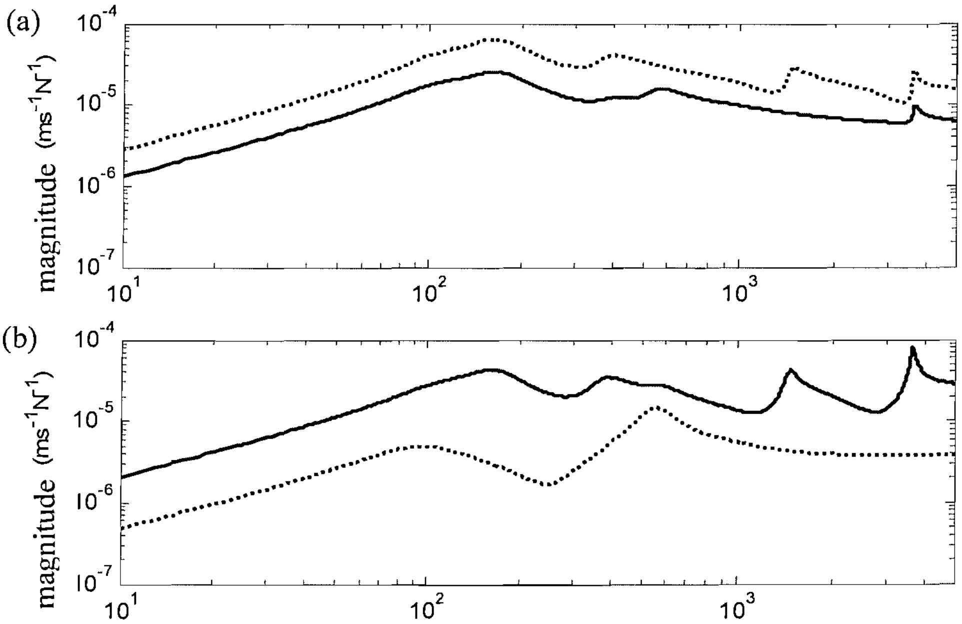

Figure 5-17 Comparison of the mobilities of the rail at different contact positions, —— at the flange contact position, ······ at the nominal contact position, (a) the lateral (transverse) mobility, (b) the vertical (normal) mobility.

5.7.2 Squeal prediction for an example case

Case (1), with a large steady-state lateral creepage $\gamma_{20} = 0.02$, is chosen as an example to show the application of alternative squeal prediction methods. When a bogied vehicle negotiates a tight right-hand curve, the conditions of the right-hand wheel of the leading wheelset are very similar to Case (1). This leading inner wheel is normally accepted as one of the main sources of squeal on curves.

5.7.2.1 Time-domain calculation

The time-domain integration of the self-excited vibration loop, as shown in Figure 5-5, can provide steady-state (or limit-cycle) responses of wheel and rail after about 1 second. For the ease of acoustic calculations, the wheel and rail vibration is evaluated in the reference frame of the wheelset, not the local contact frame (in which the stick-slip motion takes place). However, if the contact angle is small, which is the case at the nominal contact position, the coordinates in the contact frame are consistent with those in the reference frame. In Figure 5-18 and Figure 5-19, the longitudinal and lateral quasi-steady responses of wheel and rail are shown in terms of (a) their time histories and (b) the corresponding spectra evaluated over a period of 0.5 s, using a rectangular FFT (fast Fourier transform) window over 0.25 s (frequency resolution 4 Hz). In the time histories, the dynamic velocities of the wheel and rail are normalised by the speed of vehicle V_0, giving v_i^w / V_0 and v_i^r / V_0. The total sliding velocity is also shown, normalised by V_0, giving $v_{i,tot}^s = \gamma_{i0} + (v_i^r - v_i^w) / V_0$, $i = 1,2$.

The wheel response in the lateral direction is much greater than that in the longitudinal direction. The longitudinal responses are coupled with the lateral responses at the lateral flexible mode of wheel. The maximum response actually occurs at 1098 Hz (identified in the spectrum with frequency resolution as high as 1 Hz), not exactly at the natural frequency of (3,0) mode, which is 1102 Hz. In the lateral response of the wheel, some small resonances can still be identified corresponding to the (4,0), (5,0) and (6,0) flexible modes, but these are much smaller than the harmonics of the (3,0) mode. The 'slip' motion can be clearly seen in the time-domain responses, taking place at the dominant frequency of the (3,0) mode, as shown in Figure 5-19(a).

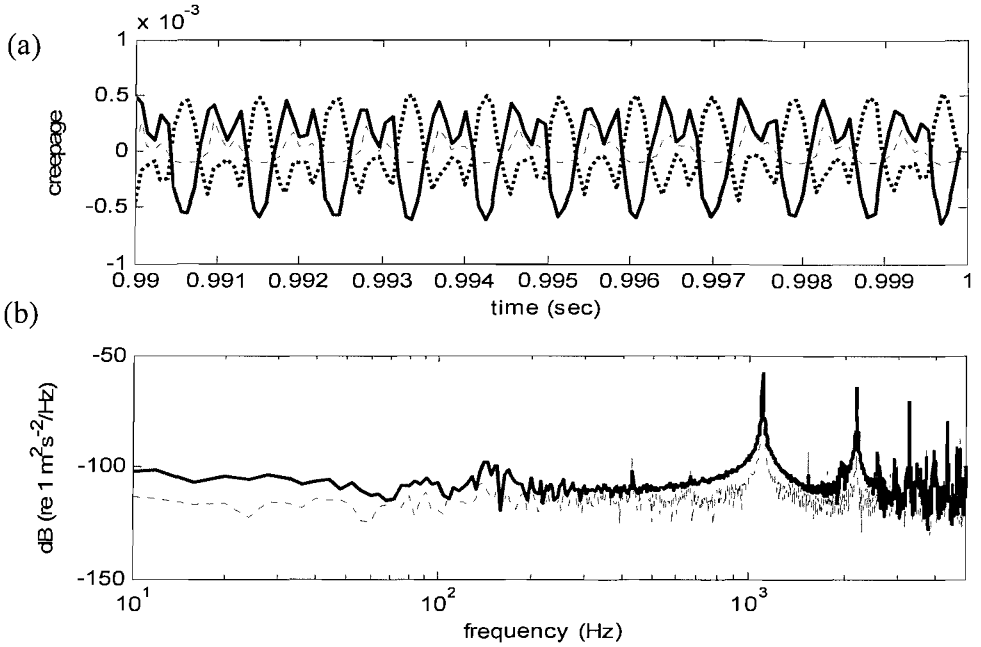

Figure 5-18 Case (1), γ_{20} = 0.02. Longitudinal responses of the wheel and rail at the contact position, (a) longitudinal dynamic velocities of the wheel, rail and sliding velocity between the wheel and rail, normalised by the vehicle speed V_0, —— wheel, ------ rail, ······ sliding; (b) spectra of the longitudinal responses of the wheel and rail, —— wheel, ------ rail.

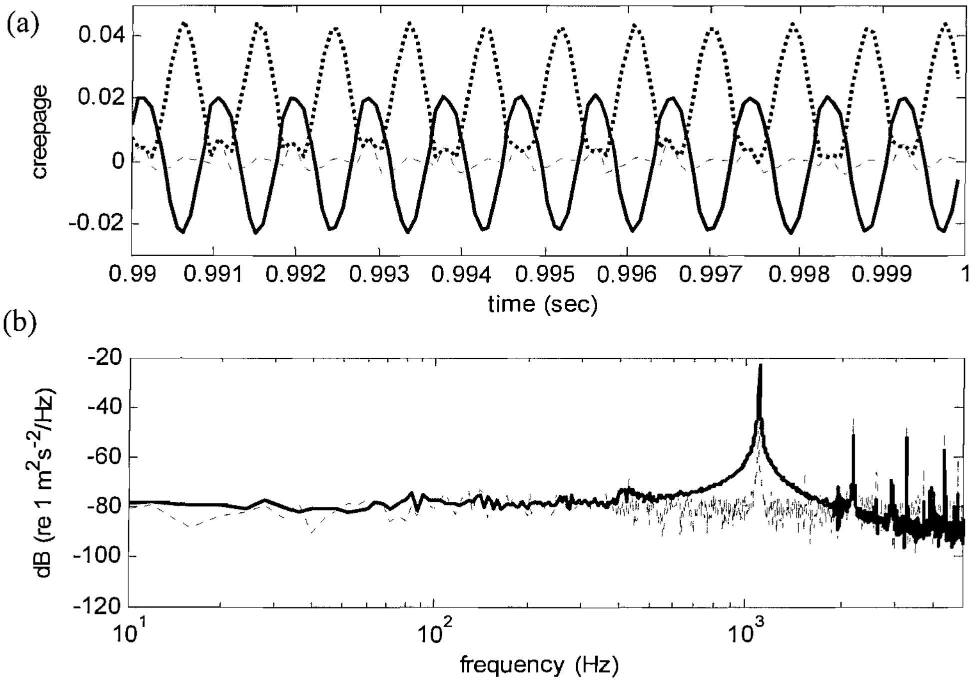

Figure 5-19 Case (1), γ_{20} = 0.02. Lateral responses of the wheel and rail at the contact position, (a) lateral dynamic velocities of the wheel, rail and sliding velocity between the wheel and rail, normalised by the vehicle speed V_0, —— wheel, ------ rail, ······ sliding; (b) spectra of the lateral responses of the wheel and rail, —— wheel, ------ rail.

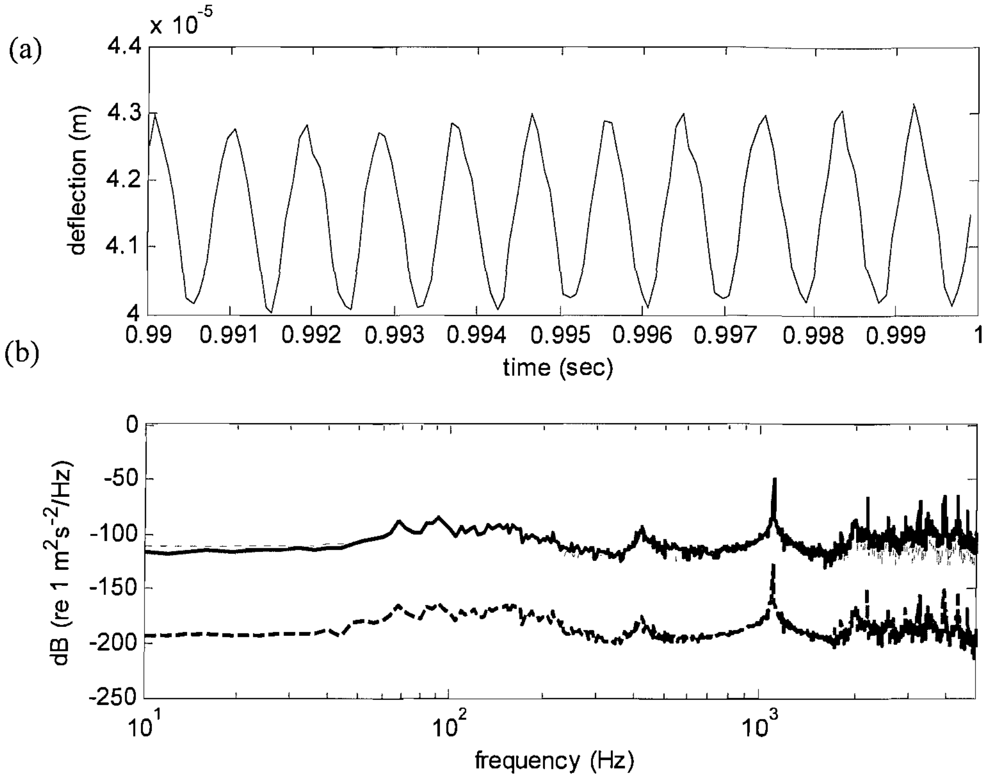

Figure 5-20 Case (1), γ_{20} = 0.02. Vertical responses of the wheel and rail at the contact position, (a) vertical deflection between the wheel and rail; (b) spectra of vertical responses of the wheel and rail, —— wheel, ------ rail, - - - deflection between the wheel and rail.

The 'vertical' responses (normal to the contact plane) are shown in Figure 5-20. The vertical deflection between the wheel and rail produces a fluctuating normal force. The vertical responses of the wheel and rail are coupled with the lateral responses, so they also contain the squeal mode at 1098 Hz. The amplitudes of wheel and rail responses are almost equal at the dominant frequency of 1098 Hz, resulting in only a small vertical deflection between the wheel and rail, as shown in Figure 5-20(a).

5.7.2.2 Stability analysis

By using the stability analysis, it is possible to predict unstable modes without a time consuming calculation. The stability analysis in the frequency domain can be graphically shown in the Nyquist contour and the Bode plot. Since the Bode plot includes the frequency information of unstable modes, it is a more useful representation. Alternatively, because the wheel is much more important than the rail in the squeal prediction, the stability of the wheel modes can be analysed by calculating the roots of the closed-loop characteristic function, using Eq.(5.90), assuming only lateral (or longitudinal) and vertical motions.

Figure 5-21 shows the results of the stability analysis for Case (1). The unstable frequencies below 5000 Hz are represented in both the Nyquist contour and the modulus graph of Bode plot, and unstable frequencies are identified by a '*'. It can be found that these unstable frequencies are related to the wheel lateral modes (i,0), $i = 0,\cdots,6$. In Figure 5-21(b), the unstable mode with the maximum loop gain is the (2,0) mode at 418 Hz. However, the time-domain simulation indicates that the dominant mode is actually the (3,0) mode at 1102 Hz, as shown in Figure 5-19.

These unstable modes are also predicted by evaluating the roots of the closed-loop characteristic function, as shown in Figure 5-22. Compared with the results of the frequency-domain stability analysis, more modes are considered unstable in Figure 5-22, e.g. the axle mode at 82 Hz. In this case the (3,0) mode is identified as having root with the largest positive real component.

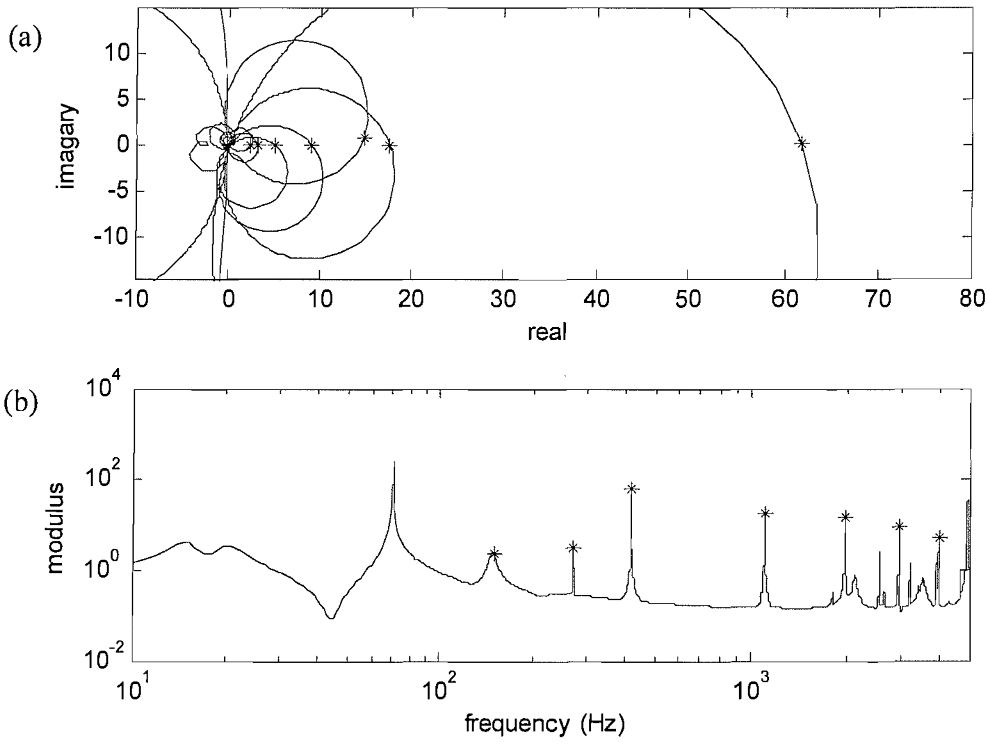

Figure 5-21 Case (1), γ_{20} = 0.02. Nyquist stability analysis, (a) Nyquist contour of eigenloci, * unstable modes; (b) modulus of the Bode diagram of eigenloci, * unstable modes.

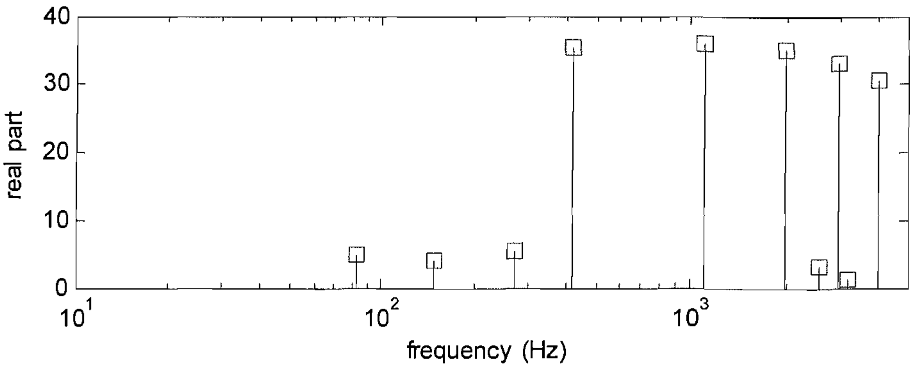

Figure 5-22 Case (1), γ_{20} = 0.02. Closed-loop roots of the wheel under only lateral forces, □ roots with positive real components.

5.7.2.3 Noise radiation

The acoustic radiation of the wheel can be calculated using the method described in Appendix G, which is based on an engineering method introduced by Thompson and Jones [62]. In calculating the sound pressure, the wheel is assumed a point source and the directivity of sound radiation is not considered here. The sound pressure level (SPL) is evaluated at a position 7.5 metres from the sound source. The radiation from the rail is neglected.

The noise radiation of Case (1) is shown in Figure 5-23. The lateral response at the dominant frequency of 1098 Hz determines the total SPL. The A-weighted and un-weighted sound pressure levels are virtually identical, as the A-weighting function has no effect on the 1 kHz band. In the following cases, the A-weighted SPL is used to represent the squeal level, as this is closer to the human perception of sound than un-weighted SPL.

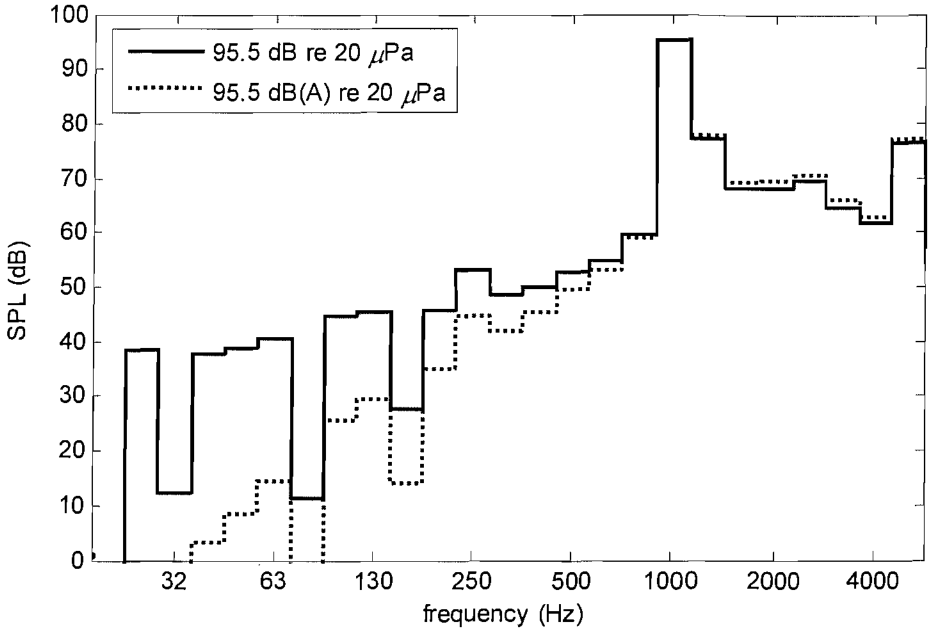

Figure 5-23 Case (1), γ_{20} = 0.02. Noise radiation from the wheel, —— SPL, ······ A-weighted SPL.

5.7.3 Steady-state creepages

The steady-state creepages are determined by the steady-state curving behaviour. This will be discussed in Chapter 7. The fundamental curve squeal problem can be considered in terms of one direction of steady-state creepage being dominant and other directions of creepage having negligible influence. Cases (1) to (4), with only lateral or longitudinal steady-state creepages, are used to simulate such conditions. Under a more general condition, one dominant steady-state creepage may accompany steady-state creepages in other directions. To investigate such conditions, Cases (5) to (7), with a dominant lateral steady-state creepage as well as another direction of steady-state creepage, are discussed.

5.7.3.1 Lateral steady-state creepage

Case (2) has a smaller steady-state creepage $\gamma_{20} = 0.005$ than Case (1). Figure 5-24 shows a clear stick-slip motion between the wheel and rail in the lateral direction, with a fundamental frequency at 140 Hz, corresponding to the (1,0) mode. At this fundamental frequency, the wheel and rail responses are almost at the same level. The wheel response at the first two harmonics is also large; these correspond closely to the (0,0) mode and the (2,0) mode. The amplitude of wheel lateral vibration is quite small and the vibration energy concentrated at lower frequencies, so that the A-weighted SPL is only 78 dB, see Figure 5-25. This is 18 dB lower than that of Case (1). Therefore, this noise may not be perceptible because the wheel/rail rolling noise in this frequency band may have similar or even higher noise levels.

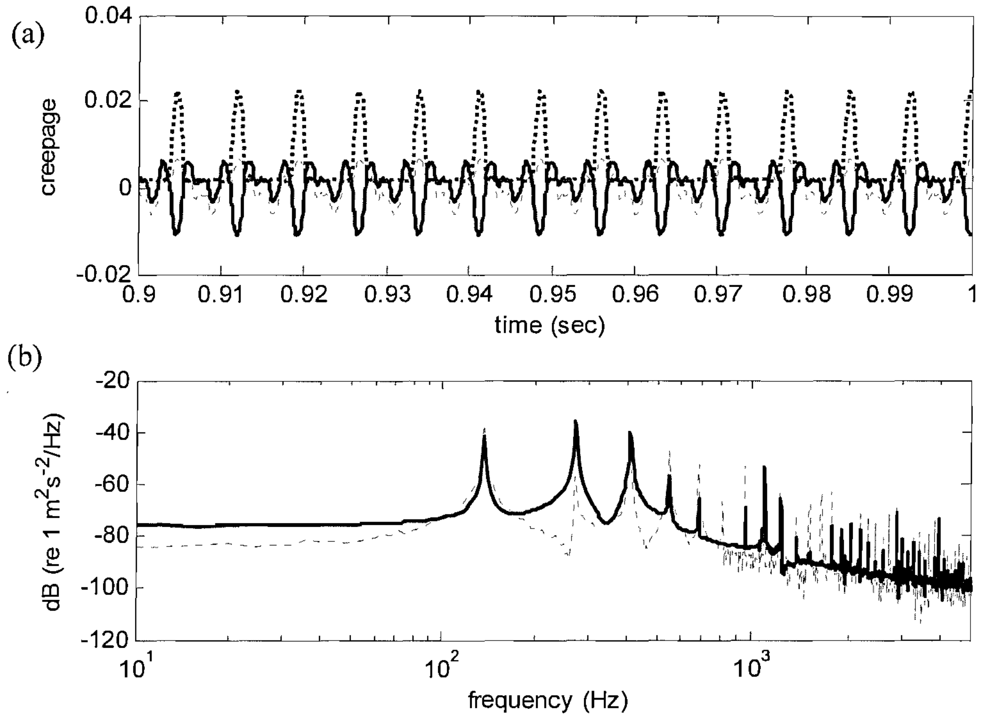

Figure 5-24 Case (2), $\gamma_{20} = 0.005$. Lateral responses of the wheel and rail at the contact position, (a) lateral dynamic velocities, normalised by V_0, —— wheel, ------ rail, ······ sliding; (b) spectra of the lateral responses, —— wheel, ------ rail.

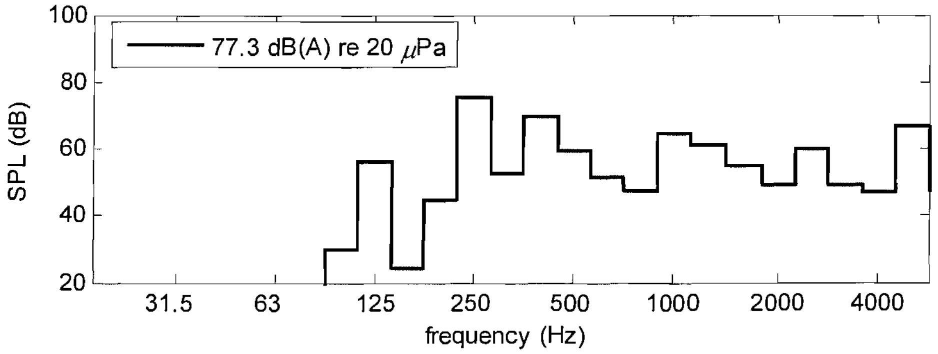

Figure 5-25 Case (2), $\gamma_{20} = 0.005$. Noise radiation from the wheel: A-weighted SPL in dB.

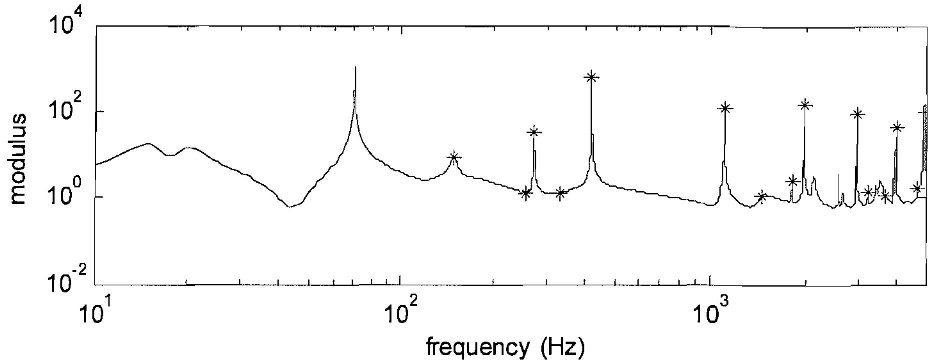

Figure 5-26 Case (2), γ_{20} = 0.005. Nyquist stability analysis: modulus of the Bode diagram of eigenloci, * unstable modes.

The stability analysis, shown in Figure 5-26, can predict the unstable modes. The fundamental frequency in Figure 5-24 is at the lowest unstable mode but not at the unstable mode with the largest loop gain. Note that the stability analysis suggests a greater instability (in mode (2,0)) than the higher creepage Case (1), see Figure 5-21. This is due to the higher slope of the friction curve close to the turning point. However, this is not reflected in the time-domain results.

5.7.3.2 Longitudinal steady-state creepage

In Cases (3) and (4), only longitudinal steady-state creepages are present. If the steady-state creepage is large, as in Case (3) with $\gamma_{10} = 0.02$, self-excited vibration may take place at the (2,c) mode, 4924 Hz, as shown in Figure 5-27. The corresponding noise radiation is quite high, about 87 dB(A). However, if the steady-state creepage is small, as in Case (4) with $\gamma_{10} = 0.005$, stick-slip motion may take place at the low frequency (0,c) mode at 70 Hz, as shown in Figure 5-28. The noise level of Case (4) is 70 dB(A), which is much lower than that of Case (3), but is still dominated by the (2,c) mode. An important point to induce is that the argument of Rudd [7] for discounting longitudinal creepage as a course of curve squeal is fallacious.

The Nyquist stability analyses of Cases (3) and (4) have similar graphs: both with two unstable circumferential modes, (0,c) and (2,c), but with different loop gains. These unstable modes are also predicted in the roots of the closed loop of the wheel system. The stability results of Case (4) are shown in Figure 5-29.

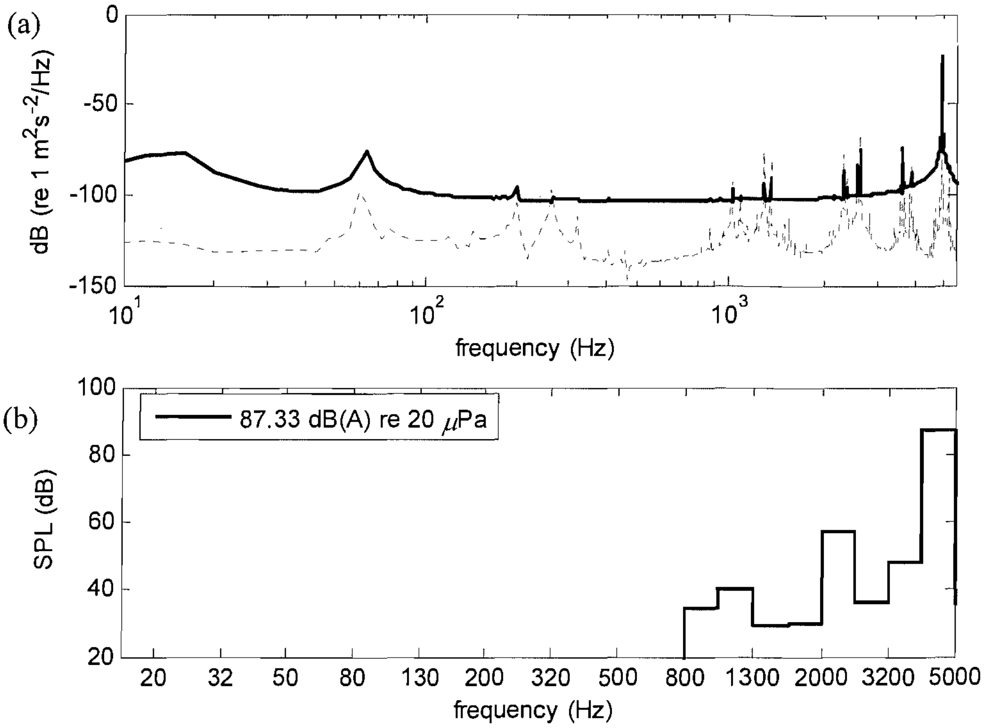

Figure 5-27 Case (3), γ_{10} = 0.02. (a) Spectra of the longitudinal responses at the contact position, —— wheel, ------ rail; (b) noise radiation of the wheel: A-weighted SPL in dB.

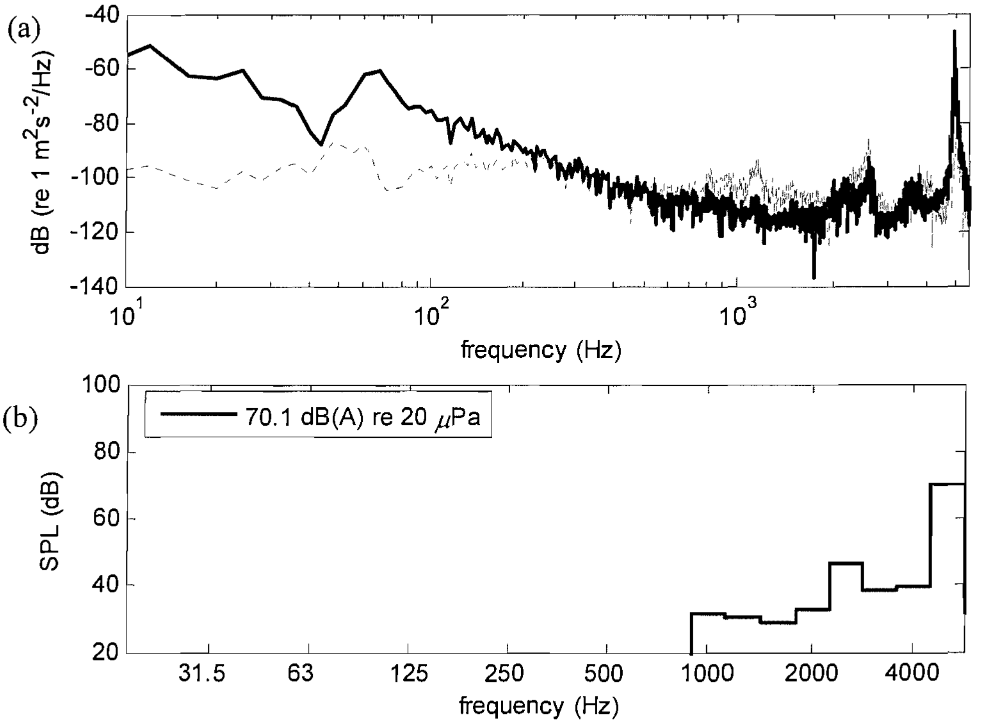

Figure 5-28 Case (4), γ_{10} = 0.005. (a) Spectra of the longitudinal responses of wheel and rail at the contact position, —— wheel, ------ rail; (b) noise radiation of the wheel: A-weighted SPL in dB.

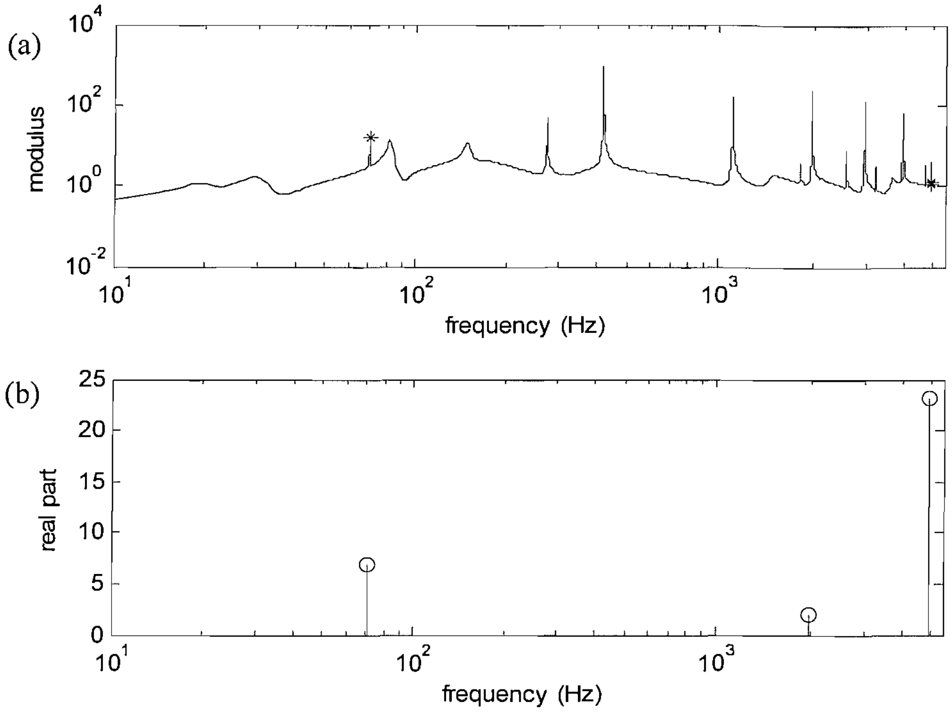

Figure 5-29 Case (4), γ_{10} = 0.005. Stability analysis, (a) Nyquist stability analysis, shown in the modulus of Bode diagram of eigenloci, * unstable modes; (b) closed-loop roots of the wheel for only longitudinal forces, ○ roots with positive real components.

5.7.3.3 Effects of longitudinal creepage together with lateral creepage

Case (5) has a large steady-state lateral creepage $\gamma_{20} = 0.02$, accompanied by a small steady-state longitudinal creepage, $\gamma_{10} = 0.005$. According to the friction curve shown in Figure 5-11(b), this longitudinal creepage can reduce the slope of the lateral friction and even remove the falling tendency at the steady-state point $\gamma_{20} = 0.02$. However, the longitudinal creepage in vibration is not always equal to this steady-state value. If the longitudinal creepage is a bit smaller due to some fluctuation, the falling properties of the friction force still exist in the lateral direction; consequently, the unstable vibration may start to develop. In Figure 5-30, the development of unstable vibration can be seen to be very slow, because the falling slope in the lateral friction curve is small. In practice, this development process may be interrupted by changes in the curving conditions, producing intermittent curve squeal. The stability analysis in Figure 5-31 shows that the Nyquist stability analysis can predict the unstable modes but no root in either the longitudinal or the lateral closed loop has positive real component. This is due to the calculation of roots has not included the coupling between the lateral and longitudinal forces.

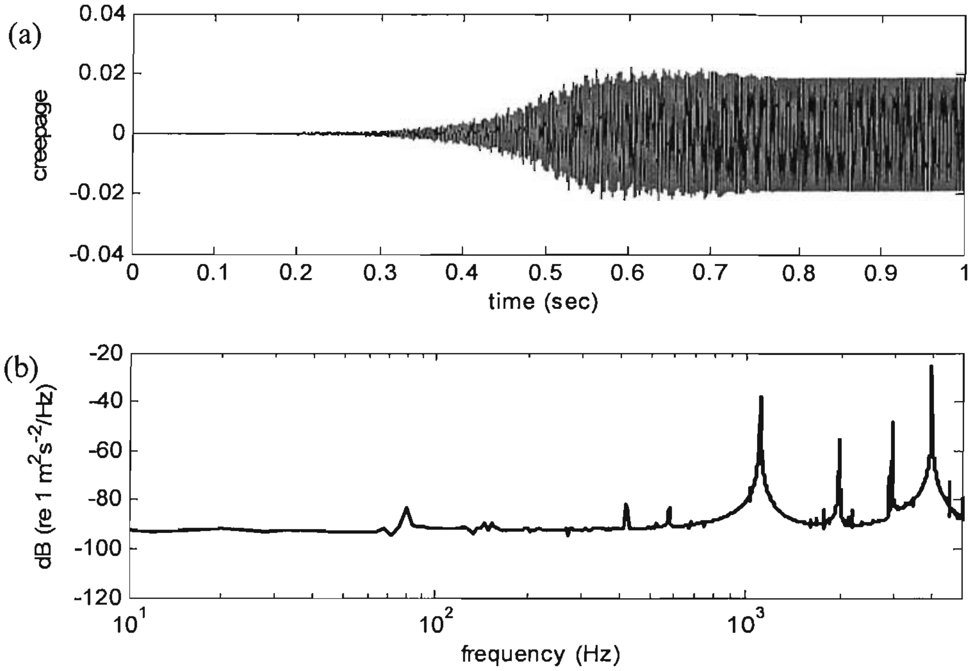

Figure 5-30 Case (5), γ_{10} = 0.005 and γ_{20} = 0.02. (a) Time histories of the lateral response of the wheel at the contact position; (b) spectra of the lateral response of the wheel.

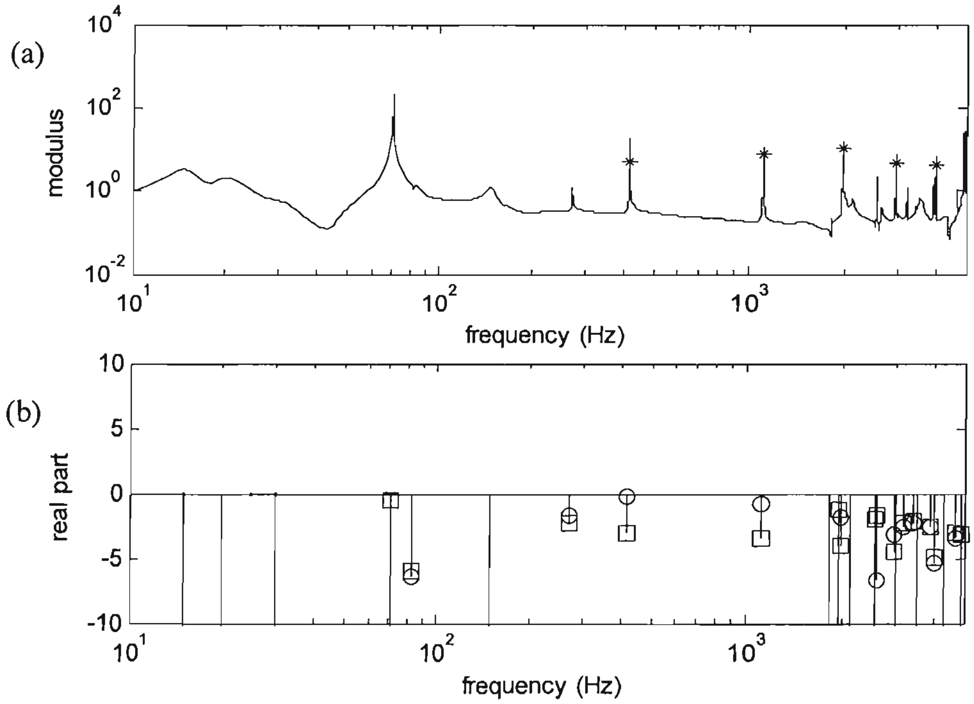

Figure 5-31 Case (5), γ_{10} = 0.005 and γ_{20} = 0.02. Stability analysis, (a) modulus of the Bode diagram of eigenloci, * unstable modes; (b) closed-loop roots of the wheel with positive real components, ○ in the longitudinal direction, □ in the lateral direction.

In Case (6), the small longitudinal creepage is combined with a smaller lateral steady-state creepage, $\gamma_{10} = \gamma_{20} = 0.005$. In Figure 5-32, the Nyquist stability analysis shows that the system is stable. However, in the time-domain simulation, see Figure 5-33, unstable vibration occurs at the (0,c) mode of 70 Hz, in both the longitudinal and the lateral directions. No high-frequency flexible mode is excited. Thus, the noise radiation is very low, even though the system is unstable.

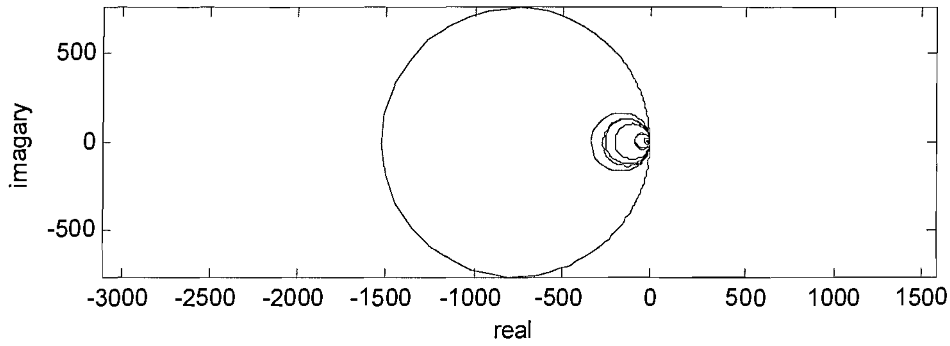

Figure 5-32 Case (6), $\gamma_{10} = \gamma_{20} = 0.005$. Nyquist contour of eigenloci.

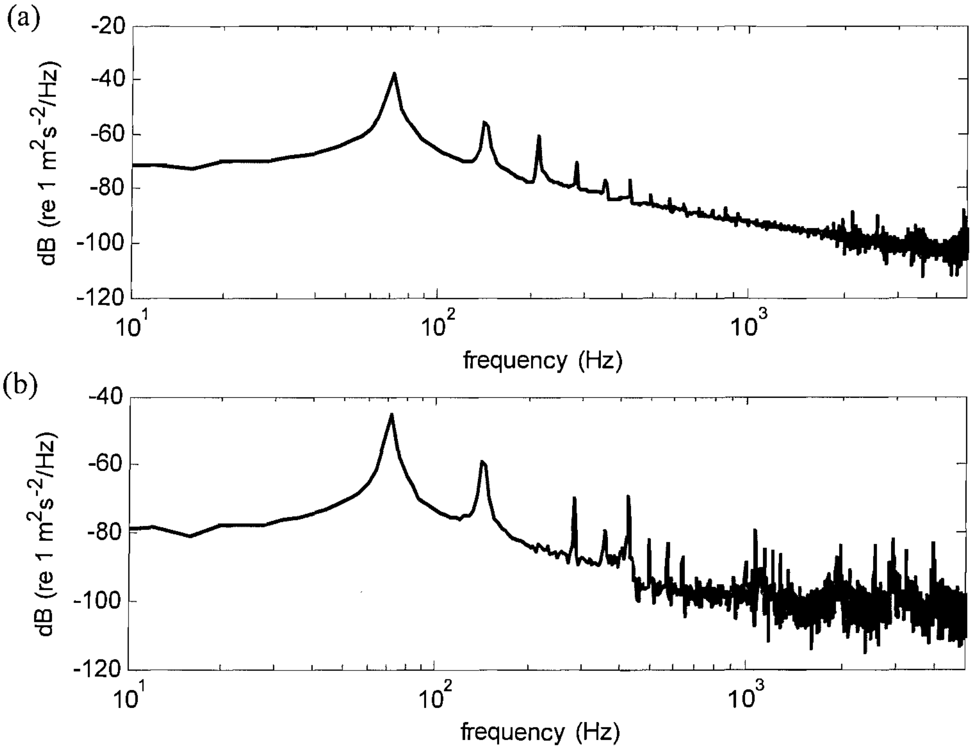

Figure 5-33 Case (6), $\gamma_{10} = \gamma_{20} = 0.005$. (a) Spectrum of the longitudinal response of the wheel; (b) spectrum of the lateral response of wheel.

5.7.3.4 Effects of spin combined with lateral creepage

According to the friction curves shown in Figure 5-11(c), a large steady-state spin creepage will reduce the slope in the falling zone of the lateral creepage-friction curve. In Figure 5-34(b), the stability analysis of Case (7), with $\gamma_{20} = 0.02$ and $\gamma_{60} = 1.5\ \mathrm{m}^{-1}$, indicates fewer unstable modes than Case (1), see Figure 5-21. The unstable (3,0) mode can still develop the large amplitude vibration, producing the squeal noise as loud as 92 dB(A), but it develops more slowly than in Case (1). If the steady-state spin is large enough, e.g. $\gamma_{60} > 2\ \mathrm{m}^{-1}$, the simulation results indicate that the system is stable and the squeal will not occur [8].

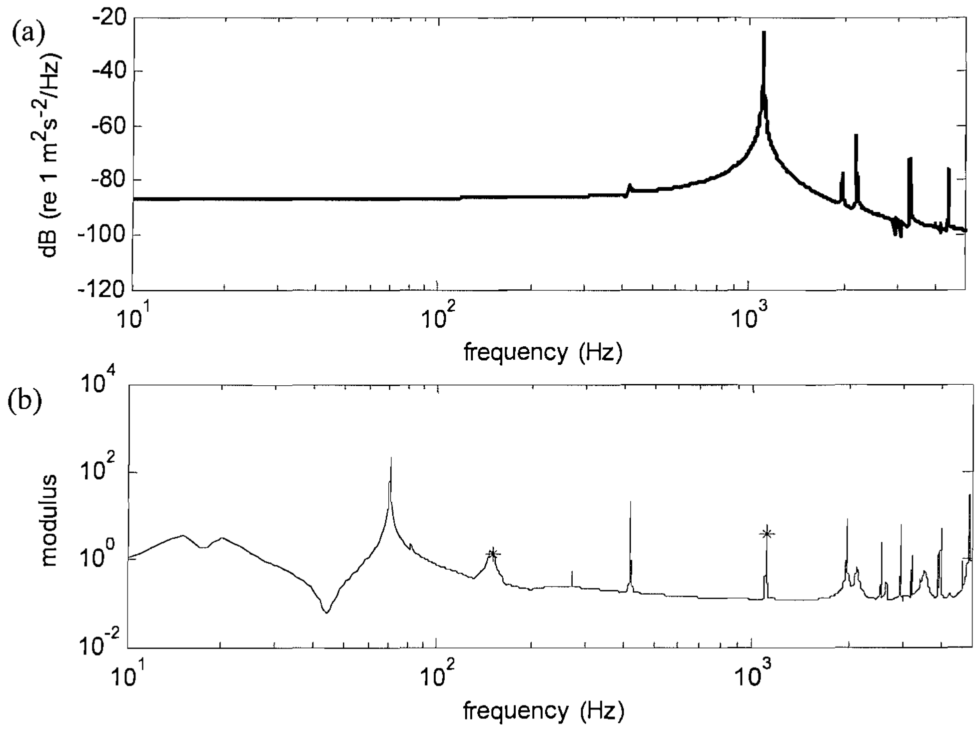

Figure 5-34 Case (7), γ_{20} = 0.02 and γ_{60} = 1.5 m^{-1}. (a) Spectra of the lateral responses of the wheel; (b) stability analysis: modulus of the Bode diagram of eigenloci, * unstable modes.

5.7.3.5 Sensitive parameters

The time-domain calculation is very sensitive to some modal parameters, e.g. modeshapes. Slight changes (e.g. 5%) in the modeshapes of flexible modes may shift the dominant frequency.

---

[8] Note that, in practice, large spin is associated with a large contact angle and contact location at the flange. However, this effect is not included in Case (7), see Case (11) below.

5.7.4 Wheel/rail contact position and contact angle

The wheel/rail contact in Cases (1) to (7) is assumed to be located at the nominal contact position with zero contact angles. However, the wheel/rail contact in a curve may shift a significant distance from the nominal contact. If the wheel/rail contact is in the flange zone, the contact angle will be large. The variances of contact position and contact angle may significantly change the wheel/rail dynamic properties (e.g. modeshapes) at the contact (see Figure 5-16), and consequently, the characteristics of squeal.

5.7.4.1 Contact position

Cases (8) and (9) are used to investigate the influence of changing the contact position. In Case (8) the wheel contact position is offset away from the flange to a position 30 mm right of the nominal contact, while in Case (9) the wheel contact position is offset towards the flange, to a position 30 mm to the left of the nominal contact, as shown in Figure 5-35. In both cases, the rail contact positions are assumed to remain at the nominal contact point, and the contact angles are assumed zero.

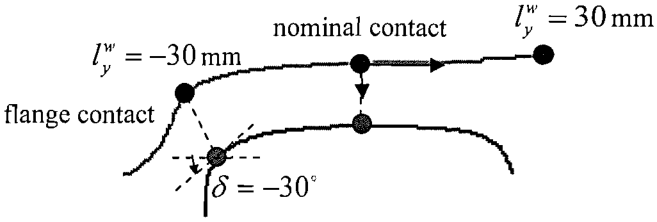

Figure 5-35 Schematic diagram of the different contact positions in a right-hand wheel.

The lateral responses of wheel and the Nyquist stability analyses for Cases (8) and (9) are shown in Figure 5-36 and Figure 5-37, respectively. Compared with the corresponding results for Case (1), the significant offset of the wheel contact position can change the dominant squeal frequency. The offset away from the flange induces a shift of dominant frequency to a higher mode (6,0) at 3977 Hz, while the offset towards the flange induces a shift of dominant frequency to a lower mode (2,0) at 418 Hz. If the offset distance is small in these two cases, e.g. less than 10 mm, the squeal prediction results are the same as those of Case (1). The offset of contact point on the rail has also been considered but was found to have no obvious influence on these two cases, but it may play an important role under other conditions.

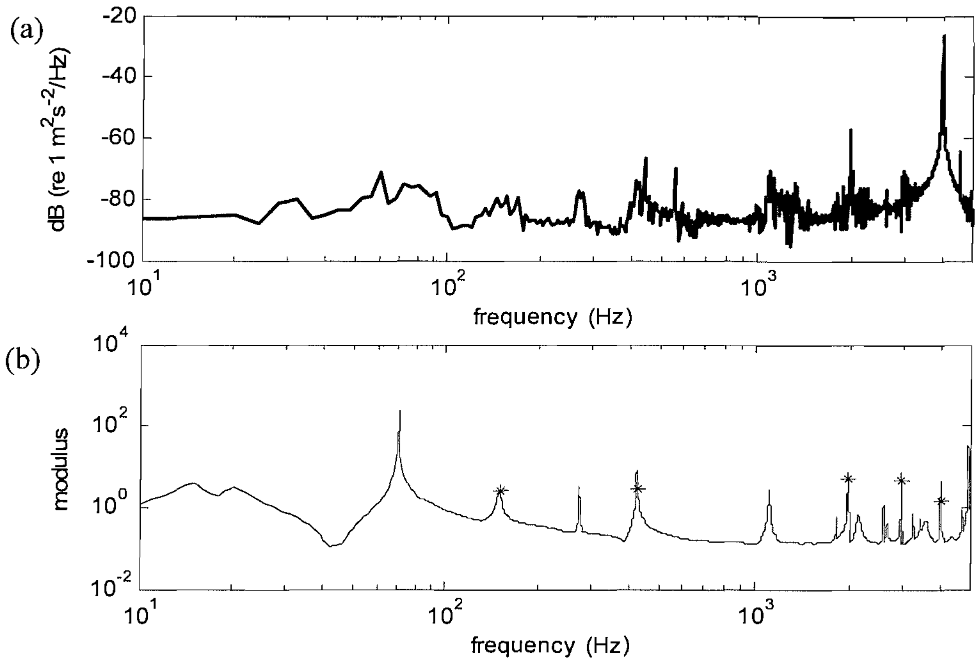

Figure 5-36 Case (8), γ_{20} = 0.02 and l_y^w = 30 mm. (a) Spectra of the lateral responses of the wheel; (b) Nyquist stability analysis: modulus of the Bode diagram of eigenloci, * unstable modes.

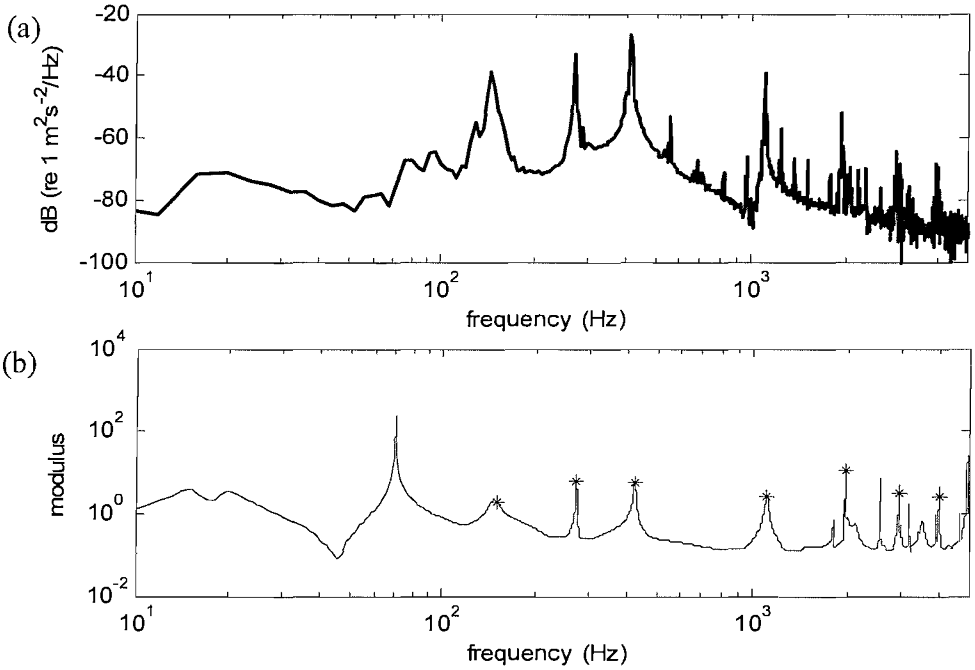

Figure 5-37 Case (9), γ_{20} = 0.02 and l_y^w = -30 mm. (a) Spectra of the lateral responses of the wheel; (b) Nyquist stability analysis: modulus of the Bode diagram of eigenloci, * unstable modes.

5.7.4.2 Contact angle

A large contact angle occurs when the contact position is close to the wheel root (indicated in Figure 3-2). For the right-hand wheel, only a negative contact angle is meaningful, see Figure 5-35. In Case (10), a contact angle $\delta = -30^\circ$ is present with a steady-state lateral creepage $\gamma_{20} = 0.02$, but no spin included. The contact position is not offset laterally. The lateral response shown in Figure 5-38 indicates that squeal still occurs but the unstable vibration develops very slowly. The Nyquist stability analysis predicts only three unstable modes with values just over the critical value 1, as shown in Figure 5-39. This is because the transverse mobility in the rotated contact plane is less flexible than the lateral mobility of Case (1). If the contact angle increases, for example $|\delta| \geq 45^\circ$, the squeal can be eliminated in this case. If the contact angle is quite small, for example $|\delta| < 10^\circ$, the contact angle has a negligible effect on the generation of squeal.

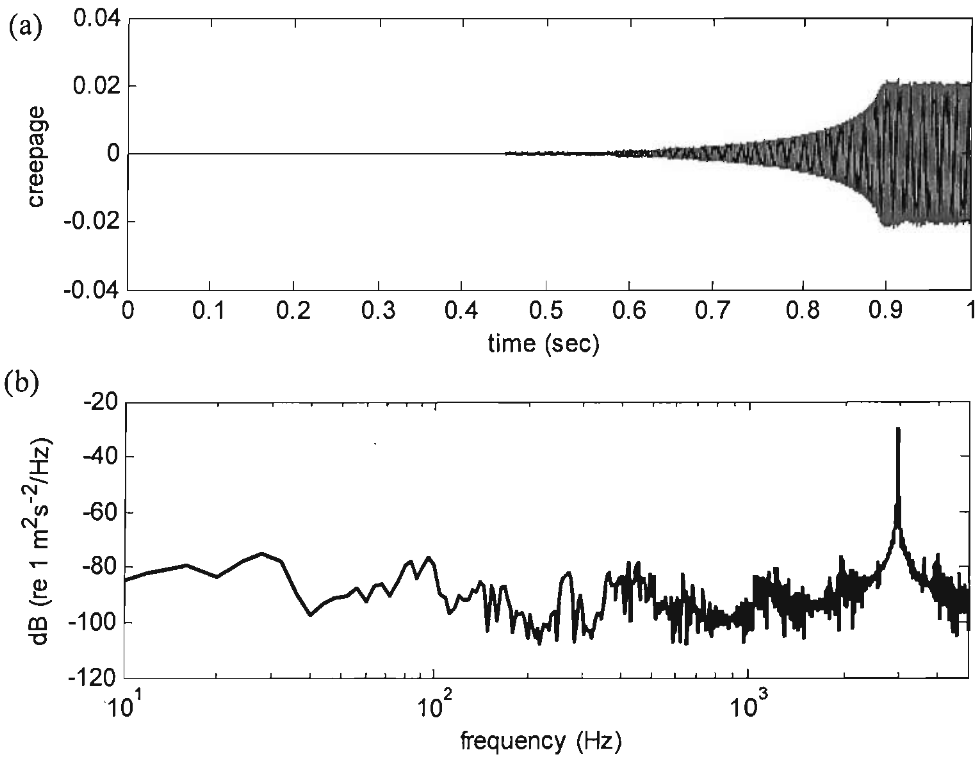

Figure 5-38 Case (10), γ_{20} = 0.02 and δ = -30°. (a) Time history of lateral response of the wheel at the contact position; (b) spectra of the lateral response of the wheel.

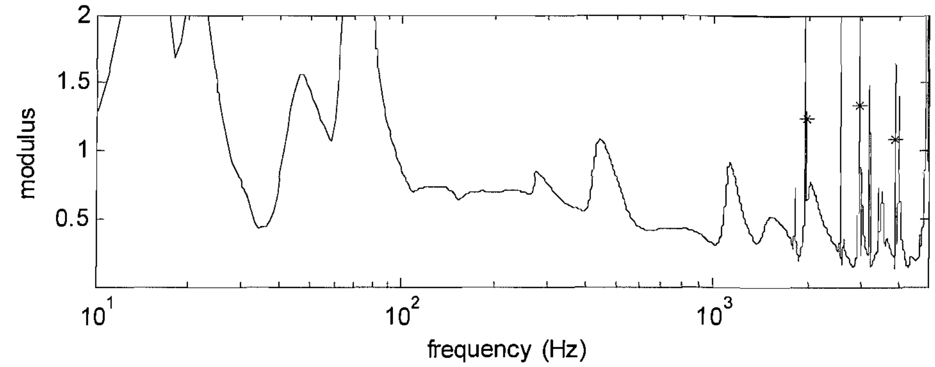

Figure 5-39 Case (10), γ_{20} = 0.02 and δ = -30°. Nyquist stability analysis: modulus of the Bode diagram of eigenloci, * unstable modes.

5.7.4.3 Flange contact

The flange contact of the right-hand wheel is introduced in Case (11). Case (11) has a large steady-state lateral creepage $\gamma_{20} = 0.02$ and a large spin, $\gamma_{60} = 1.5$ m^{-1}. The wheel/rail contact positions are shifted from the nominal position with distances $l_y^w = l_y^r = -30$ mm , and the contact angle is $\delta = -30^\circ$. According to the previous analyses, both flange contact and large spin can decrease the possibility of squeal occurrence. The time-domain simulation shows that the system in Case (11) is stable. Figure 5-40 provides the Nyquist stability analysis result. All modes are stable.

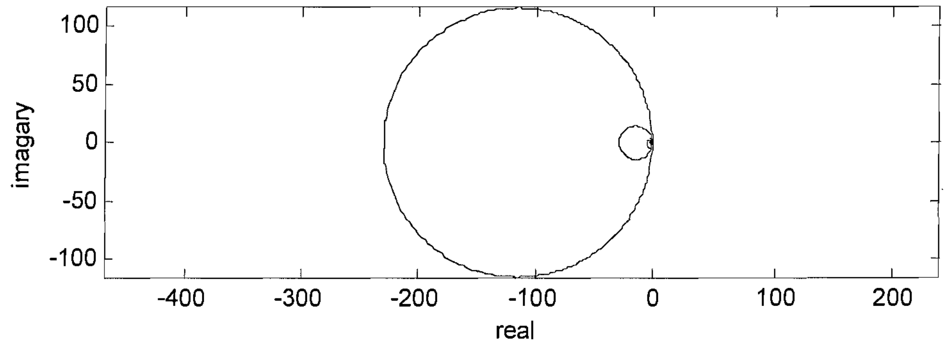

Figure 5-40 Case (11), γ_{20} = 0.02, γ_{60} = 1.5 m^{-1} and δ = -30°. Nyquist contour of eigenloci.

5.7.5 Generic study of curve squeal control methods

The conventional control methods for curve squeal include damping treatments on the wheel and friction modification at wheel/rail contact position. In this squeal model, damping treatments can be simulated by adjusting the damping ratio of the flexible wheel modes; the axle and rigid modes are not affected. Friction modification can be simulated by adjusting the coefficients in the friction function, especially the falling ratio.

5.7.5.1 Damping control

Case (12) has the same conditions as Case (1), except that the wheel damping is multiplied by factors of 10, 50 and 100. Since the original values of wheel damping ratio, apart from the rigid modes, are in a range from 0.01 to 0.0001, to avoid impractical damping treatment, an upper-limit value of damping ratio is set to be 0.01. Figure 5-41 shows the stability analysis results for different factors of damping increment. The damping treatment can cause unstable wheel modes to become stable. The more damping is applied to the wheel, the fewer unstable modes will exist. However, if only one unstable mode exists, the self-excited vibration may still develop at this mode. The spectrum of lateral wheel response, and therefore the noise radiation are similar for these cases with different wheel damping increments, see Figure 5-42. Compared with the spectrum in Case (1), after applying the damping treatment, the dominant frequency will shift from the (3,0) mode at 1102 Hz to the (2,0) mode at 418 Hz. This results in a decrease of the SPL. In this case, if the factor of damping increment can be as large as 120, no unstable mode will exist; consequently, squeal can be eliminated. However, this will make the damping ratio of flexible modes higher than the assumed upper limit of 0.01.

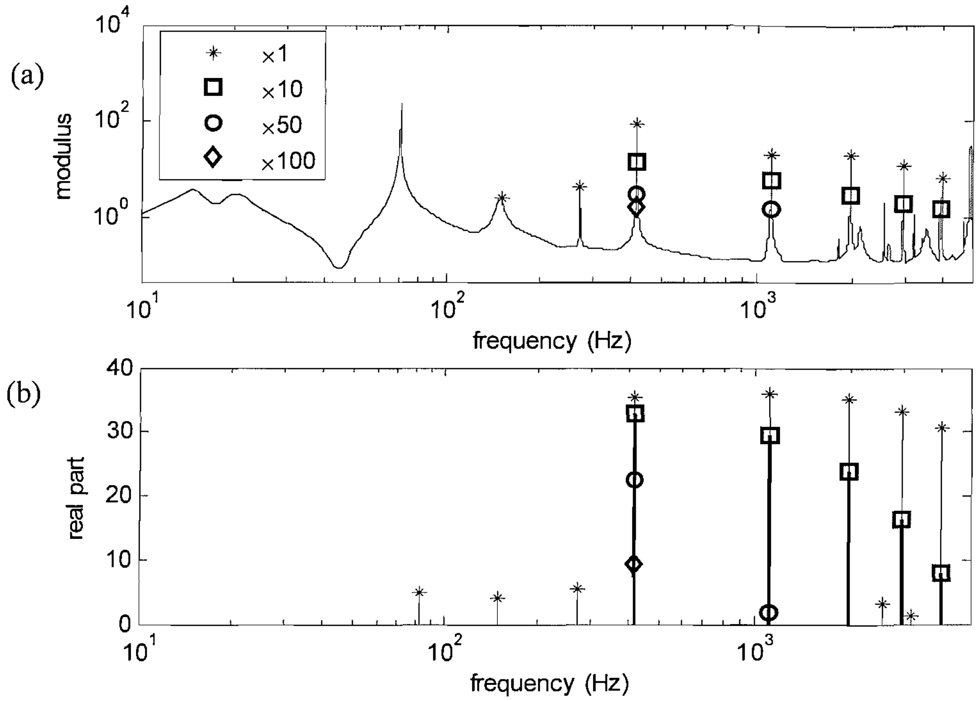

Figure 5-41 Case (12), γ_{20} = 0.02 and λ = 0.3, wheel damping increased by factors of 1, 10, 50 and 100. Stability analysis for wheel damping treatment: (a) modulus of the Bode diagram of eigenloci; (b) real components of the closed-loop roots of the wheel for only lateral forces.

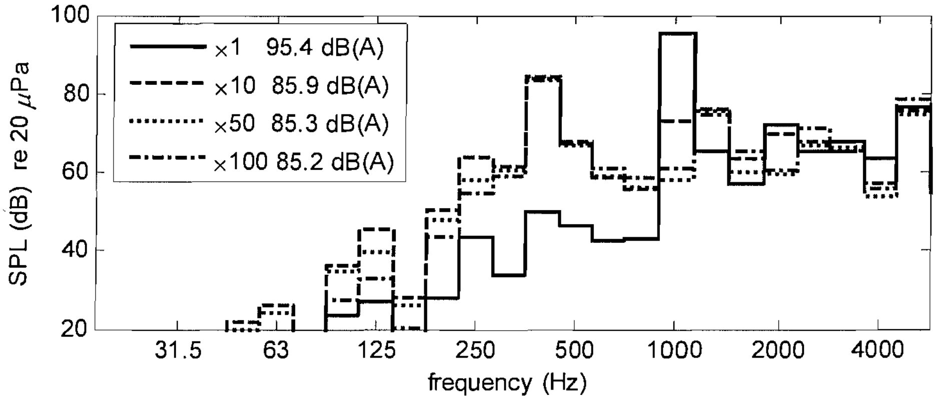

Figure 5-42 Case (12), γ_{20} = 0.02 and λ = 0.3. Noise radiation of the wheel, A-weighted SPL in dB, after the wheel damping is increased by factors of 1, 10, 50 and 100.

5.7.5.2 Friction modification

In Case (13), the falling ratio of the friction function is set to be a small value $\lambda = 0.1$. This leads to less damping being required to control squeal than in Case (12), as shown in Figure 5-43. If the damping is increased by 50 times, the system is almost stable and the amplitude of unstable vibration increases very slowly. Unlike Case (12), the squeal in Case (13) occurs in the (3,0) mode and the noise level in steady state is still as high as

95 dB(A) if the wheel damping is increased by a factor of 10, as shown in Figure 5-44. If the friction modification can eliminate the falling friction characteristic completely, i.e. $\lambda \to 0$, squeal will not occur.

Compared with the falling ratio, Coulomb friction coefficient has little influence on the squeal prediction results.

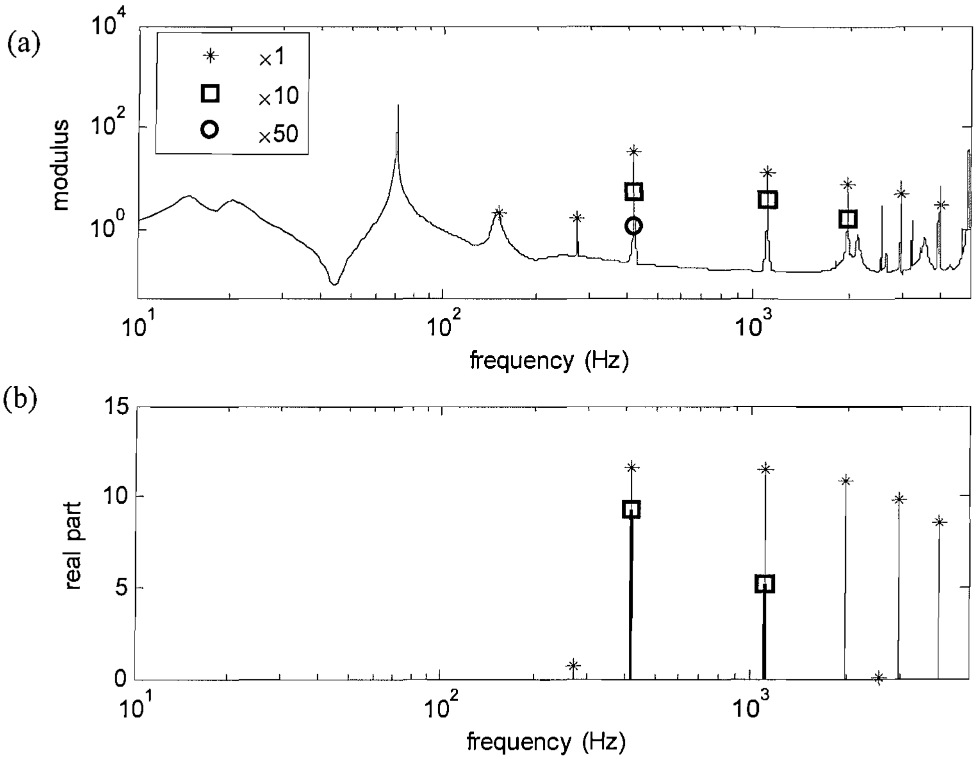

Figure 5-43 Case (13), γ_{20} = 0.02 and λ = 0.1, wheel damping increased by factors of 1, 10 and 50. Stability analysis for reduced falling friction: (a) modulus of the Bode diagram of eigenloci; (b) real components of the closed-loop roots of the wheel for only lateral forces.

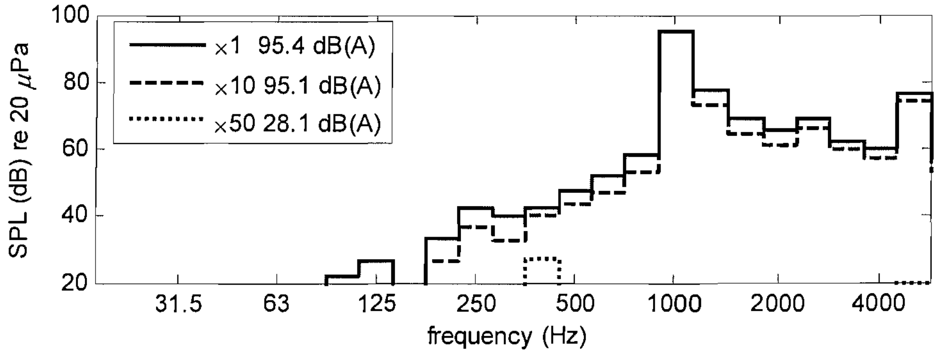

Figure 5-44 Case (13), γ_{20} = 0.02 and λ = 0.1. Noise radiation of the wheel, A-weighted SPL in dB, after the wheel damping is increased by factors of 1, 10 and 50.

5.7.6 Discussion

5.7.6.1 Parameters

The most important parameters involved in the squeal analysis are the steady-state creepages, dynamic properties of the wheel, and the friction characteristic. These parameters determine whether the squeal occurs and if it occurs, how high is the level. Since the steady-state creepages are determined by the curving behaviour and the wheel dynamic properties are also related to the contact positions during curving, the conditions determining the steady-state curving behaviour are also important, e.g. the curve radius, track cant angle, vehicle speed, wheel/rail profiles, Coulomb friction and vehicle suspension properties. Although the rail has a limited influence on the squeal, it forms the stick-slip motion with wheel. If the fundamental frequency of the stick-slip motion is low, the rail may have responses as large as the wheel. The Hertz contact spring produces the vertical fluctuating force in the contact patch. This vertical force is strongly coupled with the lateral force if a large contact angle exists. Under these conditions, including or neglecting the rail and/or contact spring can result in different squeal prediction results, especially in the time-domain simulation results. The time-domain squeal results, e.g. the dominant mode, are very sensitive to the modeshapes, sometimes the damping ratio, of the flexible modes. This is the reason why the dominant frequency predicted in the time-domain calculation will be shifted after some changes in the wheel/rail contact positions or wheel damping. In the simulations, the squeal prediction results are found not to be sensitive to the sign of creepages. Because the structural dynamics of a pair of wheels (left- and right-hand wheels) in a wheelset are in the form of mirror symmetry, appropriate sign changes need to be made to the contact position and angle when considering a left-hand wheel.

5.7.6.2 Stability analysis

The Nyquist stability analysis can predict unstable modes under steady-state conditions. The squeal may occur at one of these unstable modes. Although the quasi-steady conditions will vary during the development of squeal, especially the non-linear friction forces, the effectiveness of the stability analysis is acceptable according to the cases considered. If the nonlinearity in the friction is limited, for example, with a large steady-state creepage dominant in one direction, the Nyquist stability analysis can effectively indicate the unstable modes. On the other hand, if the steady-state creepages are small, i.e. close to the saturation zone, or if there is no single dominant creepage, the Nyquist stability criterion may give different results from the time-domain simulations. Fortunately, as the squeal usually occurs under large steady-state creepages, the Nyquist stability analysis can be considered as a useful method for squeal prediction.

It is meaningful to predict the dominant squeal mode using stability analysis. The dominant mode is one of the unstable modes, which has the largest increment gain in the self-excited vibration. As discussed in Section 5.5, an unstable mode possessing a large mass-normalised modeshape and small damping is a likely candidate for the dominant squeal mode. The generalised Nyquist stability analysis uses the eigenloci to judge the stability of the MIMO squeal model. Strictly speaking, the eigenvalues of the open-loop matrix do not correspond to the increment gain. According to the cases considered, the unstable modes with the largest eigenvalue of open loop gain may not be the dominant squeal mode, but the dominant squeal mode is one of the modes with large eigenvalues. Actually, during the complex process included in the stick-slip motion, other factors, besides the modeshapes and structural damping, may influence which mode can finally develop to be the dominant one. In the application of squeal control, because the stability results are not as sensitive as the calculation of the dominant mode, the eigenvalue can be considered as an instability scale indicating how difficult it is to control the squeal.

5.7.6.3 Flange contact

The flange contact condition is the most complex condition in the squeal analysis. Three possible creepages are involved, with large lateral creepage, large spin and small longitudinal creepage. The contact position is located at the wheel root and the contact plane is inclined relative to the wheel axis with a large contact angle. According to the parametric study, all these factors tend to reduce or eliminate the generation of squeal. However, due to the coupling between the longitudinal, lateral and vertical motions, squeal may still happen after very slow development from a small fluctuation. This process is easily interrupted by some changes in the conditions.

5.7.6.4 Squeal control

Although all the important parameters involved in the squeal generation can be selected to control the squeal, damping treatments added to the wheel and friction modification are two of the most widely used practical methods. The stability analysis is useful in studying the squeal control methods. It is found that only by stabilising all the possible unstable modes is the squeal control successful. Noise levels are not necessarily reduced if unstable modes still exist.

5.8 Summary

A general self-excited vibration loop has been presented, which can be used to investigate the squeal phenomenon in both the time domain and the frequency domain. The time-domain stability analysis of the closed loop shows that a wheel mode possessing a large mass-normalised modeshape and small damping is likely to be the dominant squeal mode. The frequency-domain stability analysis, i.e. general Nyquist stability analysis, has been validated by comparisons with the time-domain squeal results. The frequency-domain stability analysis can effectively indicate the unstable modes if the nonlinearity in the friction is limited which is the case for large creepages. The parametric study shows that the steady-state creepages, dynamic properties of the wheel, and the friction characteristic are the most important parameters that determine whether the squeal occurs and if it occurs, at what level.

6. SQUEAL EXPERIMENTS ON A TWIN-DISC RIG

6.1 Introduction

In the light of the previous theoretical work, the phenomenon of curve squeal is seen to be related to many factors, e.g. steady-state curving behaviour of the vehicle, dynamic properties of the wheel and rail, and non-linear creepage-dependent friction forces. For the purpose of investigating the squeal phenomenon and validating the squeal prediction model, a twin-disc rig was constructed by the Rail Technology Unit, Manchester Metropolitan University (MMU) [63]. Measurements with this rig were conducted by the author jointly with personnel from MMU in the period from March 2006 to June 2006, as part of a project supported by Rail Research UK. The detailed descriptions of the twin-disc rig and the test method developed can be found in the paper [63]. This Chapter shows a comparison of the measurement data with the rolling friction and wheel/rail squeal models presented in this thesis.

With this rig, the normal load and the (quasi-steady) lateral forces acting on the discs due to varying amounts of lateral creepage can be measured in a controlled environment, as well as the acoustic and vibration responses of discs. The analysis of experimental results presented here is focused on finding: (1) the relationship between the squeal and frictional characteristics, (2) the effects of the dynamic behaviour of the wheel and rail discs on squeal, (3) evidence for the squeal mechanisms assumed in the theoretical models, i.e. stick-slip motion and self-excited vibration, (4) validation of the theoretical model.

6.2 Twin-disc rig

6.2.1 Experimental set up

Figure 6-1 shows the twin-disc rig [63]. The main components of the rig are a steel frame, wheel and rail discs, a vertical loading device (using a hydro-jack), a drive motor for turning the wheel disc, and an adjusting unit for yawing and moving the rail disc laterally. Figure 6-2 presents a schematic diagram, showing the reference frame on the rail disc.

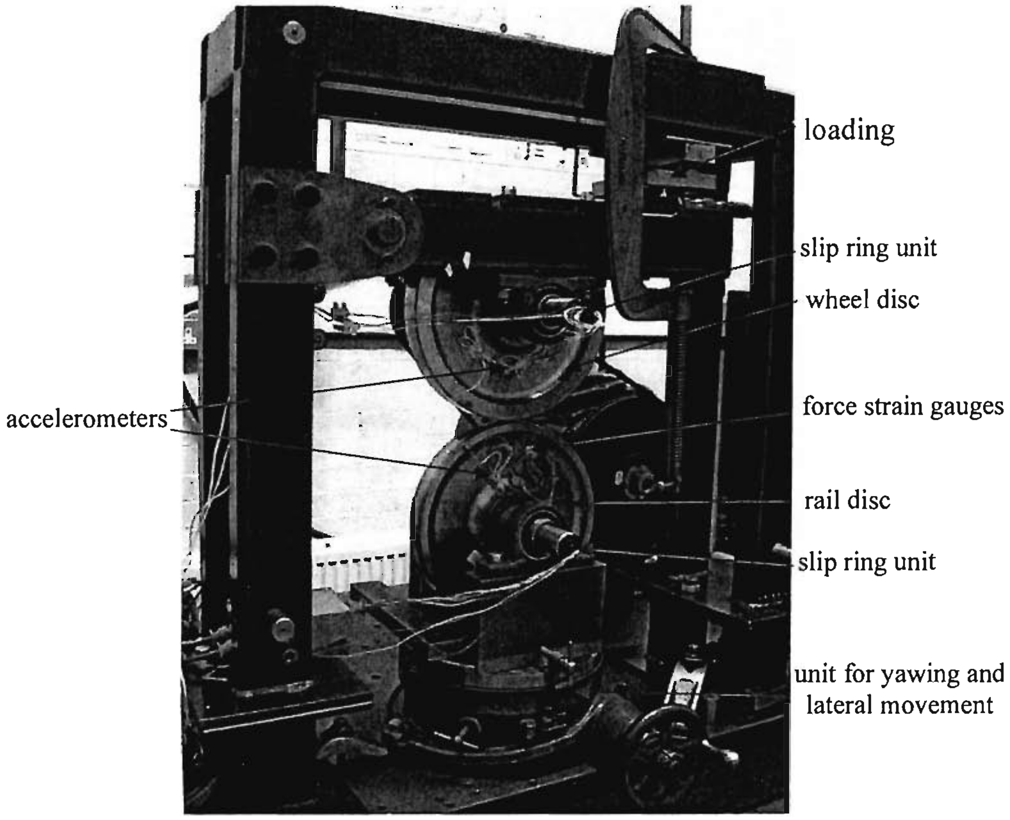

Figure 6-1 Twin-disc rig.

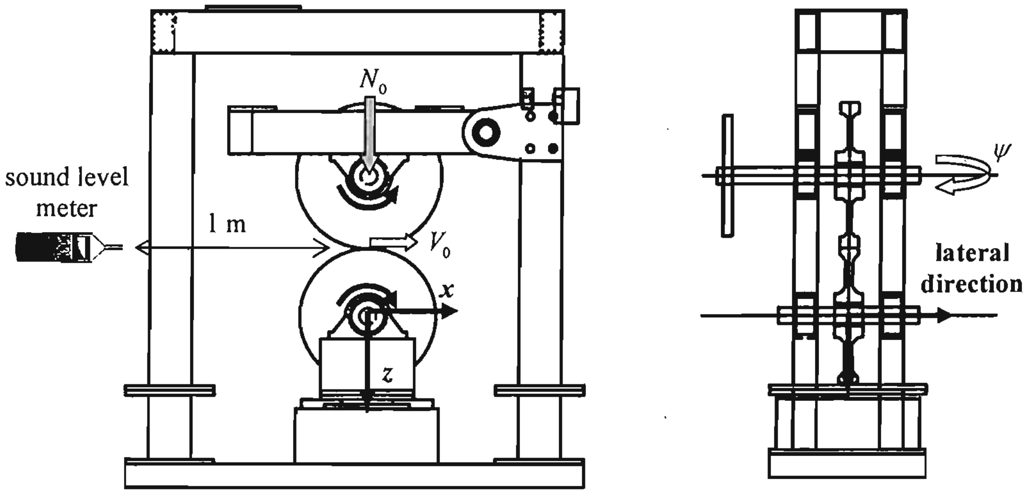

Figure 6-2 Schematic diagram of the twin-disc rig.

The diameters of wheel and rail discs are 310 mm and 290 mm, respectively. The rail disc is damped by the addition of damping material on both sides, in order to reduce the possibility of the rail disc squealing rather than the wheel disc squeal. Furthermore, the tread of the wheel disc has a flat cylindrical profile, while that of the rail disc is profiled with a transverse radius of 100 mm, which allows a 'point' contact between them to simulate the actual wheel/rail contact condition. The web and tyre of the wheel disc roughly represent a locomotive wheel (Class 91) at scale 1:3, although there is no flange. The web of the rail disc is flat for ease of application of strain gauges, which are mounted on the web for the measurement of contact forces between the two discs.

An inverter motor drives the wheel disc, while the rail disc is free to rotate. When the rig is working for experiments, a vertical load is applied on the wheel disc to keep it in contact with the rail disc. If a significant yaw angle ψ is introduced between the rail and wheel discs by adjusting the rail-disc angle, the wheel disc will keep sliding laterally on the rail disc. Thus, unstable lateral friction forces may lead to large responses of both discs, and consequently the occurrence of squeal.

The adjustable parameters in the experiment are the normal load N_0 (about 2 to 4 kN), rotating speed of the wheel disc V_0 (about 1 to 5 m/s), yaw angle ψ (from -3° to 3°), lateral offset of the rail disc (between -30 mm and 30 mm), and friction condition (i.e. dry and clean, lubricated and watered).

6.2.2 Measurement system

Definitions of velocities and forces in the measurement system are shown in Figure 6-3.

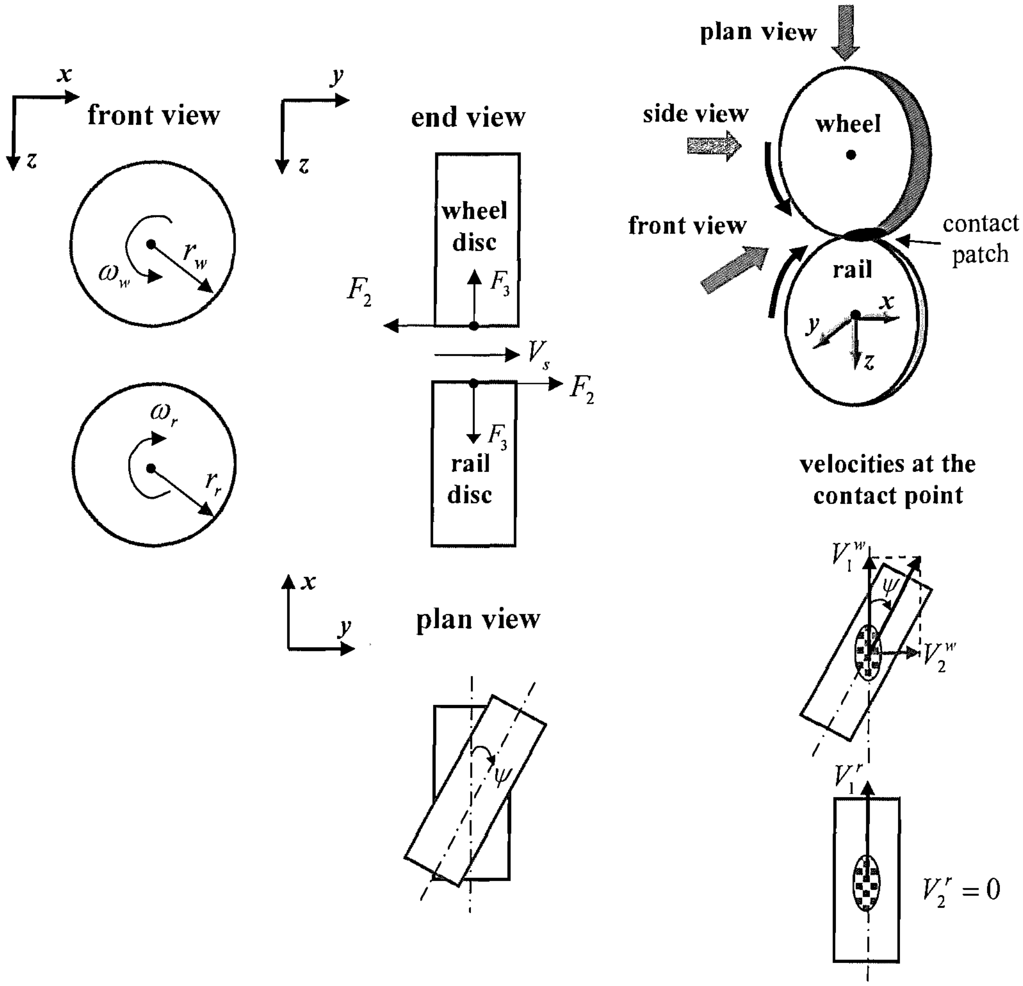

Figure 6-3 Definitions of velocities and forces in the measurement system.

The mean rolling speed of the wheel and rail discs at the contact patch is

$$V_0 = \frac{r_r\omega_r + r_w\omega_w}{2} \approx r_w\omega_w, \tag{6.1}$$

where $\omega_r > 0$, $\omega_w > 0$ are the angular speeds of the wheel and rail discs, and $r_r = 145$ mm, $r_w = 155$ mm are the radii of the wheel and rail discs. Assuming no slip occurs between the discs in the longitudinal direction, the steady-state longitudinal creepage can be taken to be zero:

$$\gamma_{10} = \frac{V_1^r - V_1^w}{V_0} = 0\,. \tag{6.2}$$

The steady-state lateral creepage is determined by the yaw angle ψ between the rail and wheel discs:

$$\gamma_{20} = \frac{V_2^r - V_2^w}{V_0} = \frac{0 - V_0 \sin\psi}{V_0} = -\sin\psi \approx -\psi . \tag{6.3}$$

As the contact plane is perpendicular to the vertical axis in this rig, assuming perfect vertical alignment of the rollers, the spin effect can be neglected. Hence, the non-dimensional friction force can be obtained as

$$\mu(\gamma_{20}) = \frac{F_2}{F_3}, \tag{6.4}$$

where F_2 is the lateral friction force acting on the rail disc, and F_3 is the normal contact force between the wheel and rail discs. These two forces are measured by 8 strain gauges mounted on rail disc web, as shown in Figure 6-4(a), the signals from which were recorded via slip ring units. Two symmetrically positioned strain gauges can form a couple as follows: (SG1, SG4) and (SG2, SG3) on the left side of the rail disc, (SG5, SG8) and (SG6, SG7) on the right side of the rail disc. Each pair of strain gauges can be integrated into a half bridge circuit, see Figure 6-4(b).

When the rail disc rotates to the position where the strain gauges and the normal force are distributed in line, the relationship between the surface strain and the lateral and vertical forces can be schematically represented as in Figure 6-4(c). The strain gauge pairs (SG1 and SG4) and (SG5 and SG8) are chosen to measure the normal contact force. Because the lateral force will bend the disc and give an opposite influence on the two sides, the influence of the lateral force can be counteracted by averaging the measurement results from (SG1 and SG4) and (SG5 and SG8). Similar analysis can be applied for the measurement of lateral force. The lateral force can be obtained by measuring using strain gauge pairs (SG2 and SG3) and (SG6 and SG7). The influence of the normal force can be eliminated by subtracting one from the other. The positions of the strain gauges on the disc were chosen using FE analysis [63]. The measurement of contact forces via the strain gauges is only valid when the strain gauges and the normal forces are in line vertically, which means there are two opportunities to measure these contact forces in one disc revolution.

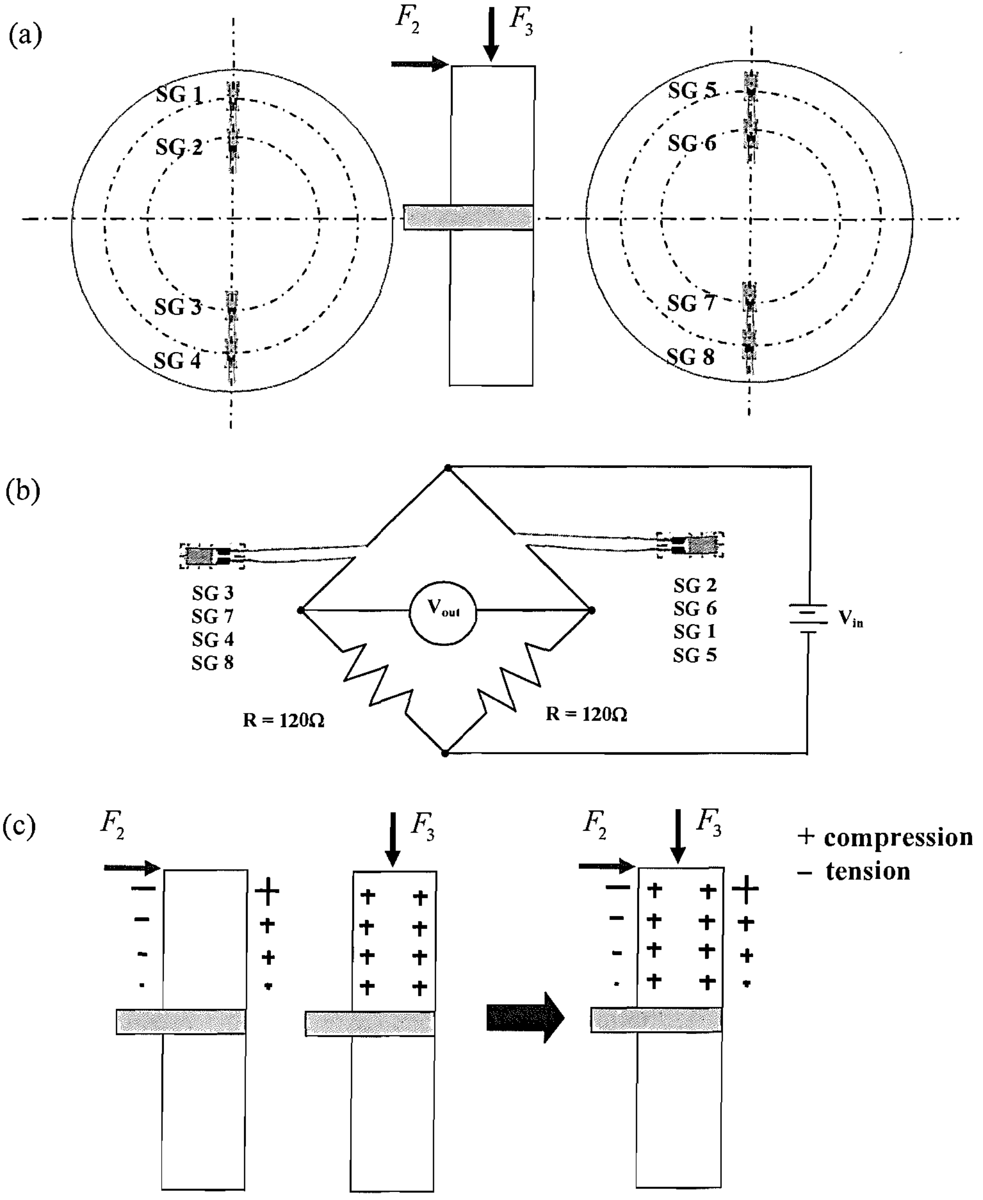

Figure 6-4 Measurement system for contact forces: (a) strain gauges on the rail disc; (b) half bridge circuit; (c) relationship between the surface strain and the lateral and vertical forces.

An example result from the measurement of the contact forces and the calculation of the friction coefficient is shown in Figure 6-5. The measured contact forces fluctuate according to the rotation of the rail disc, which has a rotating cycle of about 0.28 s, as shown in Figure 6-5(a). The vertical force reaches its peak value when the strain gauges are in line with the normal contact force. The instantaneous friction coefficient can be calculated from the lateral and vertical contact forces measured at that point. In each revolution of the rail disc, the instantaneous friction coefficient can be calculated twice when the vertical force reaches its peak. The friction coefficient in Figure 6-5(b) is the averaged value in each revolution of the rail disc.

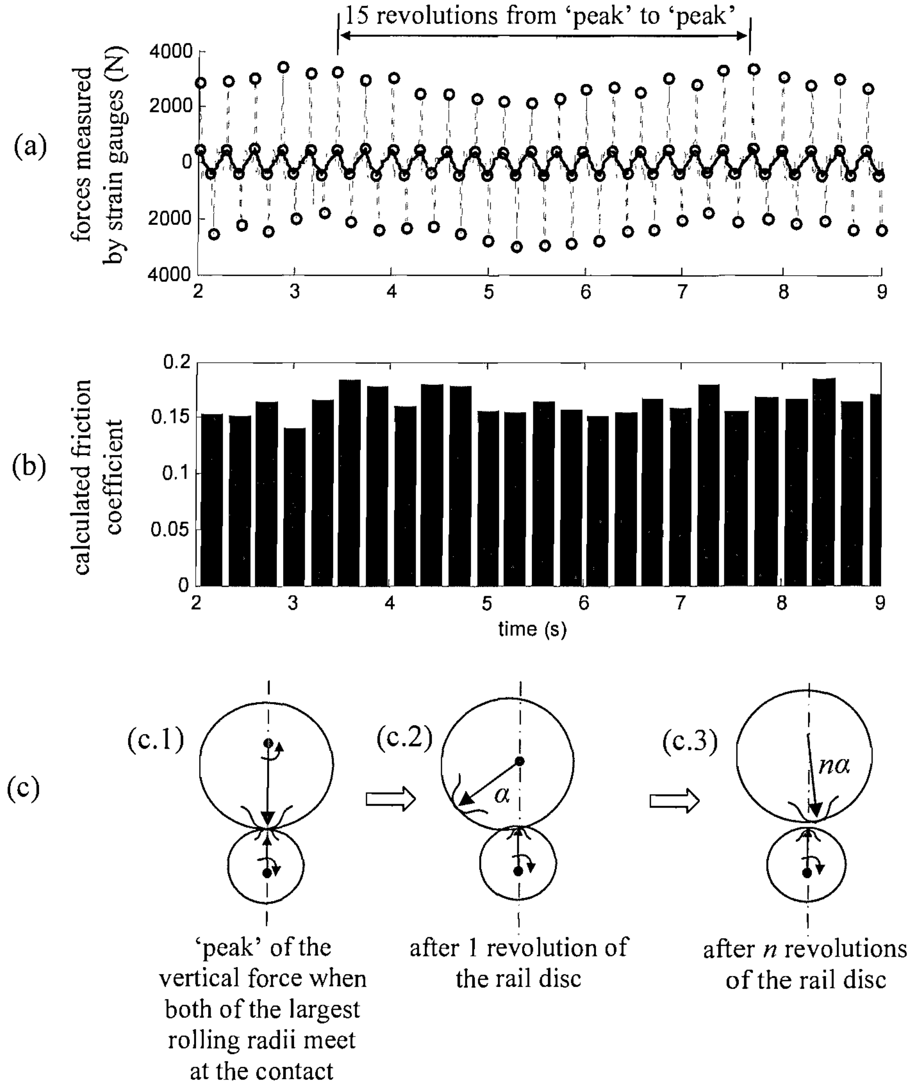

Figure 6-5 Measurements of contact forces and friction coefficient: (a) contact forces, ----- vertical contact force F_3, —— lateral friction force F_2; (b) friction coefficient calculated by the vertical contact force at its peak and its corresponding lateral friction force; (c) fluctuation of the measured vertical force due to eccentricity of the discs.

The vertical force is not a constant value but fluctuates at a low frequency. The peaks in the measured vertical force take place when the wheel and rail discs contact each other at the positions where both have their largest rolling radii[9], as shown in Figure 6-5(c.1). As the wheel/rail discs have the same linear speeds at the contact but different rotational speeds due to their different nominal rolling radii ($r_w = 155$ mm $> r_r = 145$ mm), after n revolutions of the rail disc, the wheel disc will lag by a whole revolution, giving

$$\begin{aligned} & n\left[(2\pi r_w - 2\pi r_r)/(2\pi r_w)\right] = 1 \\ & \rightarrow n = \frac{r_w}{r_w - r_r} = \frac{155}{155-145} = 15.5 \end{aligned} . \tag{6.5}$$

Hence, the local 'peak' of the measured vertical force will take place in every 15 or 16 revolutions of the rail disc, as shown in Figure 6-5(a).

Besides the measurement of contact forces and friction forces, the vibration responses of the wheel and rail discs are detected by two accelerometers mounted on each web surface, at positions close to the edges of discs. These signals were passed through slip ring units on the axle of each disc.

The acoustic radiation was measured by a sound level meter positioned about 1 m from the rig, pointed horizontally at the wheel/rail contact position and inclined to the disc planes with an angle of about 30°. The sound level meter provides an A-weighted overall sound pressure signal, which was recorded along with the disc vibration for subsequent analysis. The acoustic measurement condition is not ideal as it is limited to a single position and is influenced by background noise from the motor. However, the measurement results are still useful for studying the relationship between the squealing noise and the vibration of the discs.

6.3 Experimental results and discussion

The experiments performed include the measurements of the modal properties of the discs at the contact position, measurements of the friction coefficients with respect to

---

[9] The eccentricities of the two discs were measured and found to be 0.03 mm for the rail disc and 0.1 mm for the wheel disc [63].

the amount of lateral creepage and the dynamic responses of the discs in terms of the excitation of friction forces.

6.3.1 Modal properties of discs

The modal properties of discs are important in determining the possible squeal modes and squeal level. The wheel and rail discs have been modelled using FE analysis, which can provide the modal parameters of their significant modes. But the modal damping ratio in the FE model was initially set to an approximation based on experience of damping values in railway wheels [64]. The FE models need to be verified and adjusted according to measurements. These adjusted modal parameters are used in the squeal models.

In the squeal analysis of the twin-disc rig, the lateral dynamic properties of the discs are most important. These were measured by using hammer impact tests. In this method, an instrumental hammer is used to impact on a structure to excite its vibration. The vibration is measured by an accelerometer mounted on the structure. The frequency response function (FRF) between the force applied by the hammer (the reference signal in the FRF) and the acceleration of the structure is named ‘accelerance’. Mobility, the FRF between the force and the velocity of the structure, can be calculated in the frequency domain from the accelerance. If the impact is located at the same position as that of the accelerometer, the corresponding mobility is named the ‘point’ mobility.

When carrying out the mobility measurements for the discs, each disc was installed on its axle but not freely suspended in space. This makes the measurement condition of the mobility close to that of the subsequent squeal measurements. Three measurement positions were evenly distributed (with 120° angular interval) around one side of the tyre. These were located as near as possible to the edge (considered as the contact position) in the axial direction. The dynamic response of the disc is measured using a piezoelectric accelerometer (PCB 352C22), with a frequency range higher than 10 kHz and negligible small mass. The hammer (PCB 086D80) is light and installed with a steel tip, with dynamic range as high as 12 kHz (under appropriate conditions). The analyser used was a SignalCalc Dynamic Signal Analyser, a product of Data Physics. The parameters chosen for the FFT analysis are as follows: a sampling frequency of 56 kHz, no weighting window (rectangular window), a frequency resolution of 0.78 Hz and averaging of 4 FRF samples. The modal parameters at most significant resonances, i.e. natural frequency and damping coefficient, are identified using the circle-fit method [65].

Since the measurement results from the three positions on each disc are similar, the wheel lateral mobility measured at one of the positions is shown in Figure 6-6. The measured mobilities have poor coherence below 1 kHz, where the motions of each disc are coupled to those of the corresponding axle and its suspension. In the wheel lateral mobility curve, the main resonances in the lateral direction are labelled with their corresponding modes (n,m). Since the largest response of the zero-nodal-circle modes takes place at the edge, all the largest peaks shown in Figure 6-6 correspond to these modes. However, the modes (0,0) and (1,0) (with zero and one nodal diameters) cannot be clearly identified in the measurement results. A possible reason is that the motion of these two modes is coupled with that of the axle, and is consequently damped by the axle bearings.

The modal parameters obtained using FE analysis must be adjusted according to the measurements. In Figure 6-7, the mobility curves of the wheel disc obtained using both original and adjusted modal parameters are compared with the measured results. The original and adjusted modal parameters of the main resonances of the wheel disc are listed in Table 6-1. The natural frequencies of these modes are adjusted by only 1%. The modeshapes have been adjusted by changing the modal mass. The modal damping ratio of the wheel disc is slightly higher than the nominal values. Figure 6-8 provides an example of identifying the damping ratio at the (2,0) mode using the circle-fit method.

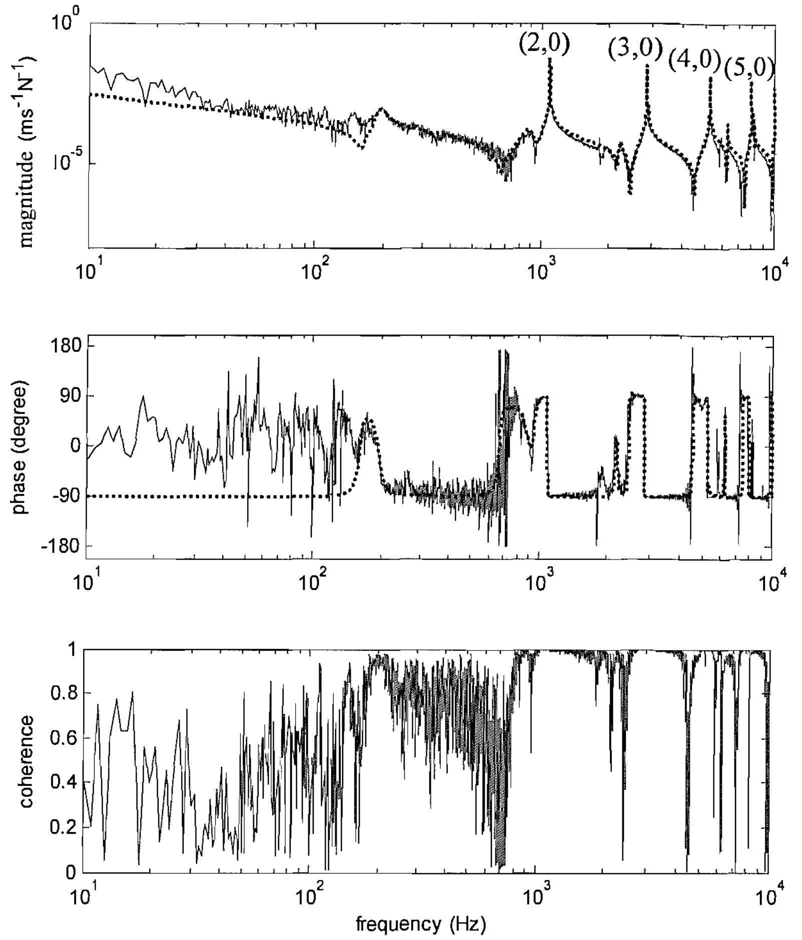

Figure 6-6 Lateral mobility of the wheel disc at the position close to the edge: (2,0) mode at 1094 Hz, (3,0) mode at 2874 Hz, (4,0) mode at 5283 Hz, and (5,0) mode at 7983 Hz. —— measurement result, ------ adjusted FE analysis result.

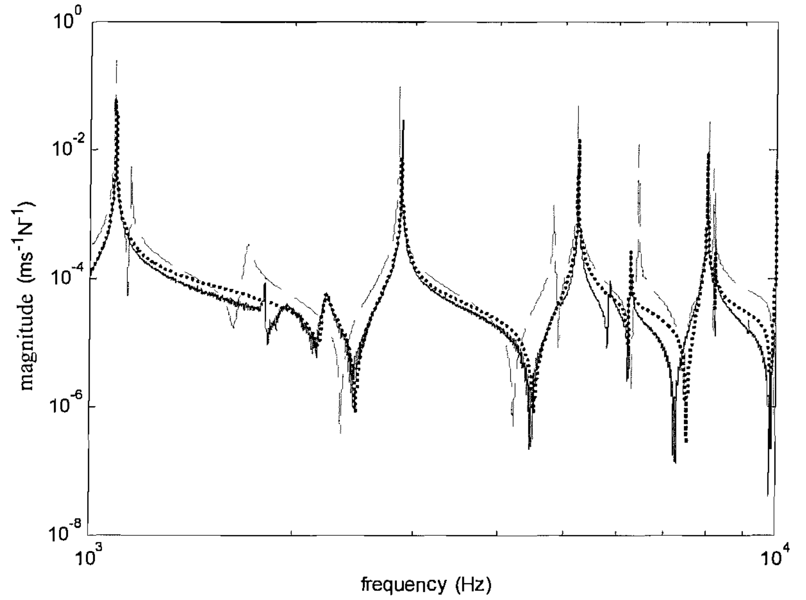

Figure 6-7 Comparison of the measured and predicted lateral wheel mobilities (only show the magnitude): —— measurement, — — FE analysis result before adjustment, ------ FE analysis result after adjustment.

Table 6-1 Modal parameters of the predominant lateral modes of the wheel disc below 10 kHz

mode (n,m)[10]	frequency f_i / [Hz]		damping ratio ζ_i / [–]		modal mass m_i / [kg]		lateral modeshape ϕ_2 / [–]
	original	adjusted	original	adjusted	original	adjusted	
(2,0)	1089	1094	0.0001	0.0003	0.5	0.7	0.4092
(3,0)	2851	2874	0.0001	0.0002	0.5	0.8	0.4180
(4,0)	5223	5238	0.0001	0.0002	0.5	1.0	0.4233
(5,0)	8032	7983	0.0001	0.0002	0.5	1.0	0.4280

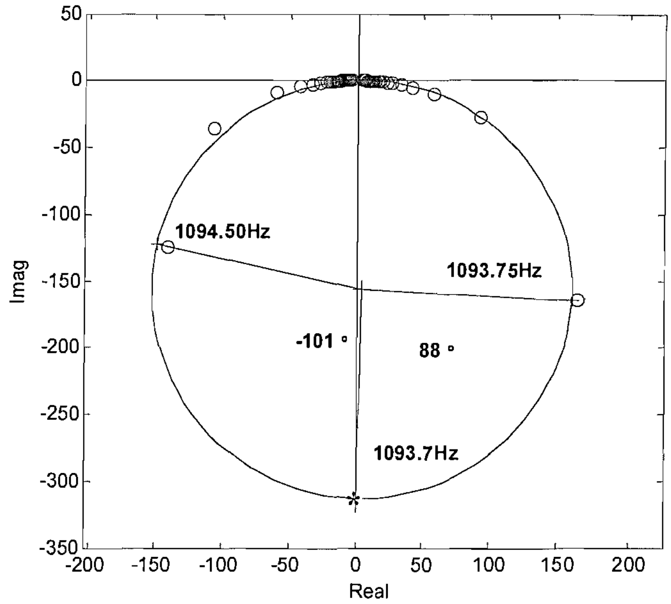

Figure 6-8 Modal damping ratio calculation for the wheel mode (2,0), using the circle-fit method: ○ measured points in the FRF, * resonance peak determined by circle fit.

The measured and adjusted lateral mobilities of the rail disc are shown in Figure 6-9. The mobility curves of the rail disc obtained using both original and adjusted modal parameters are compared with the measured results in Figure 6-10. Similar analysis for the mobility of the wheel disc can be applied to the rail disc. In Table 6-2, the original and adjusted modal parameters of the main resonances of the rail disc are listed. The natural frequencies of these modes are adjusted by about 5%, larger than the adjustments in the wheel disc. The modeshapes are adjusted by changing the modal mass. Due to the added damping treatment, the modal damping of the rail disc is about 5 times higher than that of the wheel disc.

---

[10] *n* Number of nodal diameters on the disc plane; *m* number of nodal circles on the disc plane.

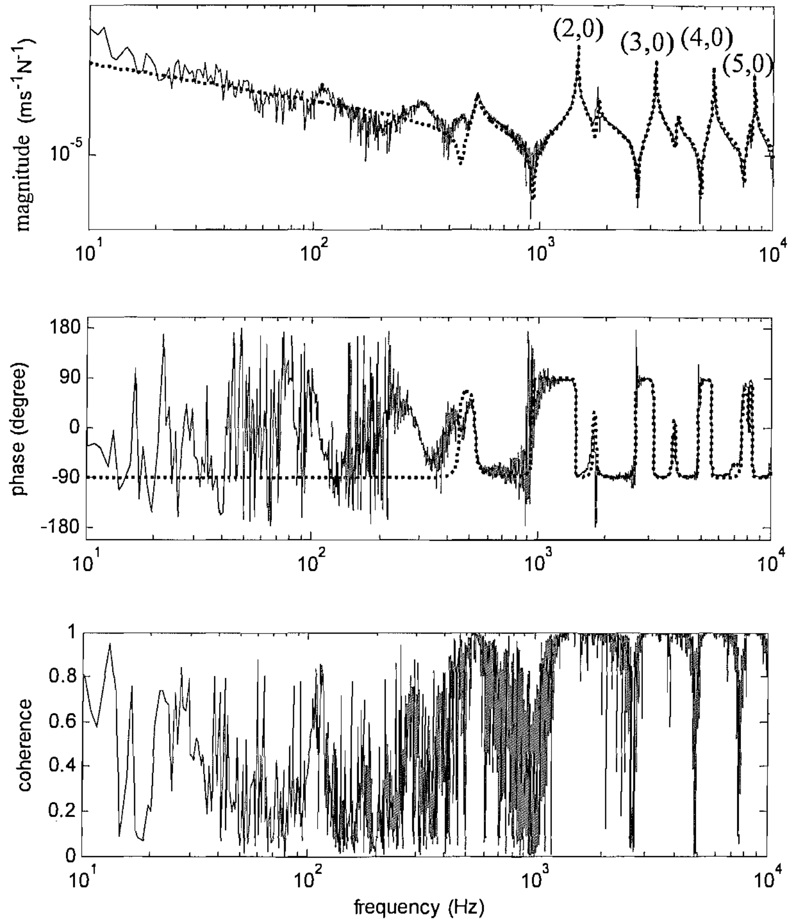

Figure 6-9 Lateral mobilities of the rail disc at the position close to the edge: (2,0) mode at 1460 Hz, (3,0) mode at 3143 Hz, (4,0) mode at 5533 Hz, and (5,0) mode at 8500 Hz. —— measurement result, ------ adjusted FE analysis result.

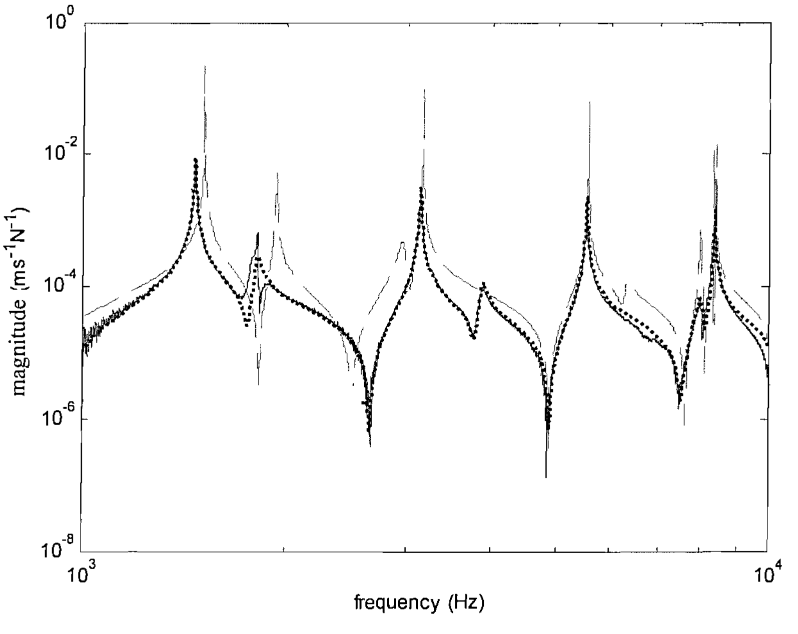

Figure 6-10 Comparison of the measured and predicted lateral rail mobilities (only show the magnitude): —— measurement, — — FE analysis result before adjustment, ------ FE analysis result after adjustment.

Table 6-2 Modal parameters of the predominant lateral modes of the rail disc below 10 kHz

mode (n,m)	frequency f_i / [Hz]		damping ratio ζ_i / [-]		modal mass m_i / [kg]		lateral modeshape ϕ_2 / [-]
	original	adjusted	original	adjusted	original	adjusted	
(2,0)	1512	1460	0.0001	0.0016	0.5	0.8	0.4601
(3,0)	2969	3143	0.0001	0.0017	0.5	1.0	0.4698
(4,0)	5558	5533	0.0001	0.0016	0.5	0.9	0.4765
(5,0)	8415	8500	0.0001	0.0013	0.5	0.4	0.2725

6.3.2 Friction coefficient

The friction coefficients were measured with the following nominal parameters: a normal load of 2.2 kN, a nominal wheel disc speed of 20 rad/s and a nominal rail disc speed of 21.4 rad/s (with a rolling velocity 3.1 m/s) and no relative lateral offset between the wheel and rail. In each measurement series, the yaw angle is varied from negative to positive angles to produce the corresponding lateral creepage. For each yaw angle, the quasi-steady lateral friction force was measured and calculated using the method shown in Figure 6-5. In general, the rig (frame) was found to be stable with no undesirable oscillation up to the yaw angle of $\pm 2^\circ$, or $\gamma_{20} = \mp 0.035$ (see Eq.(6.3)). Hence, the measurements were usually performed in this range of yaw angle. Results are mostly presented for a slightly narrower range of $\pm 1.43^\circ$, or $\gamma_{20} = \mp 0.025$.

Prior to each test step with a specified yaw angle, the running surfaces of both discs were first abraded with fine emery paper and then wiped dry with tissue and cleaned with degreaser. Having set up the required rolling contact condition, the inverter motor was started and a run-in period under load was allowed to ensure steady-state conditions before data acquisition was commenced. At least 10 seconds of data were recorded in each test step. This duration is increased where transient conditions were also of interest, such as the period from non-squealing to squealing. The relatively short recording time was necessary to avoid the build up of wear debris on the running surfaces. This appeared to be appreciable at large yaw angles and large normal loads under dry contact conditions. By wiping the rollers between each test step, the amount of debris on the surfaces remained relatively constant.

Three different surface conditions, dry, watered and lubricated, are considered. In the dry condition, the conditions of the rolling surfaces satisfy those required in the rolling contact theories, e.g. Hertz contact. The surfaces are smooth and clean, without water, grease or significant wear debris. The measured friction coefficients under the dry condition are shown in Figure 6-11.

In the watered condition, the rolling surfaces of discs were prepared in the dry condition before each test step. When the discs started to run, water was wiped onto the contact surfaces with a brush. After about two revolutions, when a little water was almost evenly covering the contact surfaces, the action of adding water was stopped. The experimental results of friction coefficients under the watered condition are shown in Figure 6-12.

In the lubricated condition, the rolling surfaces of the discs were again prepared in the dry condition before each test step. When the discs started to run, machining lubricant (this has a viscosity similar to vegetable cooking oil) was wiped onto the contact surfaces with a brush during the first two revolutions. The experimental results of friction coefficients under the lubricated condition are shown in Figure 6-13.

For each creepage in a curve of friction coefficient, the measured friction coefficient is only a quasi-steady value due to fluctuations of some parameters, e.g. the normal load, so that an error bar representing its standard deviation is provided as well as its averaged value. The sound radiation is measured simultaneously with the measurement of friction coefficient. This provides an indicator of whether squeal is taking place.

It should be noted that the friction coefficients measured here may not represent those for a constant creepage for the following reason. In this twin-disc rig, a steady-state lateral creepage is imposed by setting a constant yaw angle between wheel and rail discs. If the discs are rotating in a quasi-steady condition, which means the lateral dynamic responses of discs should be very small compared with this nominal lateral creepage, the measured friction coefficient can be considered as that applying at this creepage.

However, since the rig is primarily built for squeal measurements, the discs may have large vibration amplitudes for some large yaw angles. If the amplitudes of lateral responses of the discs are of a similar order to the nominal steady-state lateral creepage, the measured friction coefficient is no longer that applying at this creepage, but represents an averaged result under this measurement condition.

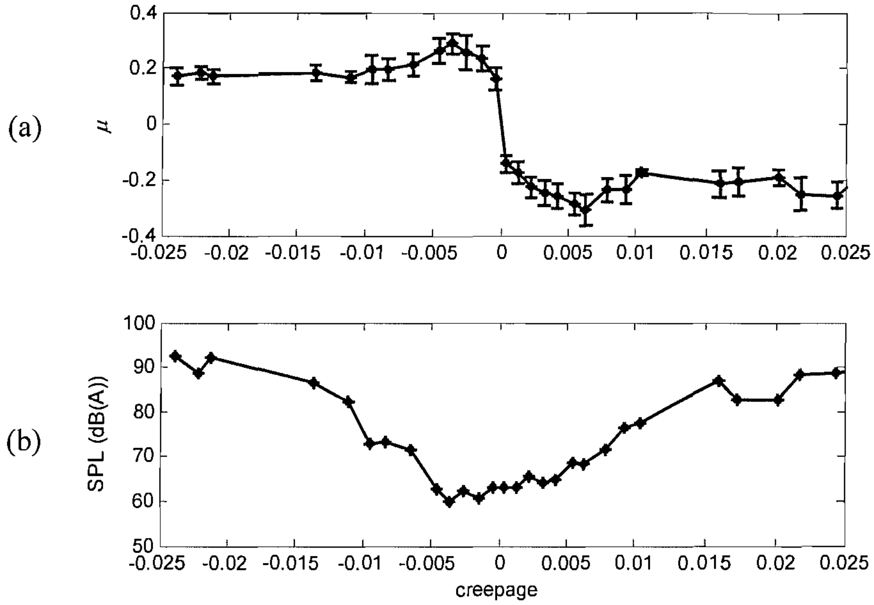

Figure 6-11 Friction coefficients measured under the dry surface condition, with a normal load 2.2 kN and a rolling speed 3.1 m/s: (a) friction coefficient; (b) sound pressure level.

For the results shown in Figure 6-11, the contact surfaces of the wheel and rail discs are kept dry and clean. The curve of friction coefficients is almost symmetrical about the zero creepage, although the measurement errors of the friction coefficients for positive creepage are a bit larger than those for negative creepage. In the curve with positive creepage, the transition from adhering friction (where the friction coefficients increase with the increment of creepages) to sliding friction (where the friction coefficients remain constant) takes place at about $\gamma_{20} = 0.007$. Then a region of falling friction follows until a roughly constant value of friction is reached at about $\gamma_{20} = 0.012$. Clearly the noise level increases quickly in this falling region, from 70 dB(A) to 85 dB(A), and then remains at a high value of about 90 dB(A) for large sliding creepages. According to the variation in friction coefficient and corresponding noise radiation, three zones can be identified: (1) adhering zone, no squeal with sound pressure level (SPL) less than 70 dB(A); (2) falling zone, noise increasing from 70 dB(A) to 85 dB(A); and (3) sliding zone, squeal with SPL greater than 85 dB(A).

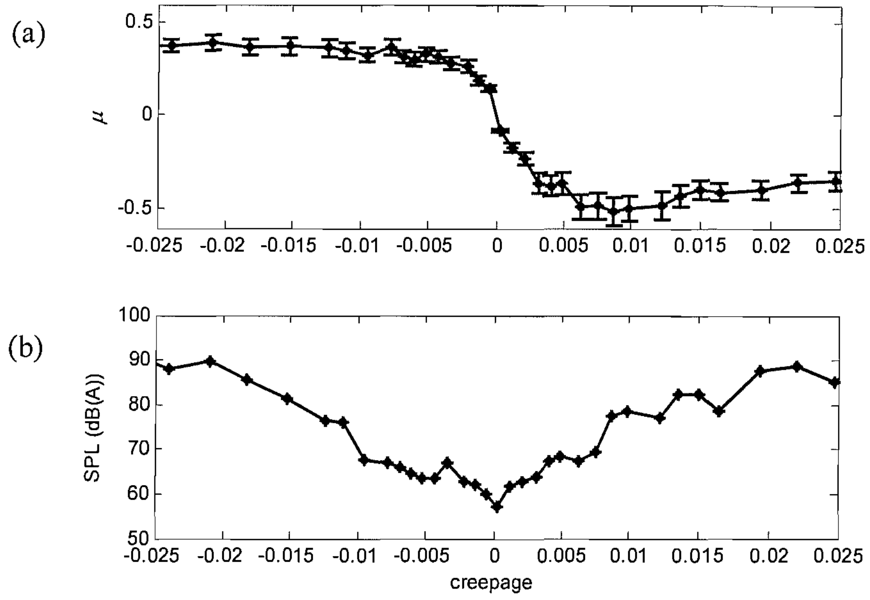

Figure 6-12 Friction coefficients measured under the watered surface condition, with a normal load 2.2 kN and a rolling speed 3.1 m/s: (a) friction coefficient; (b) sound pressure level.

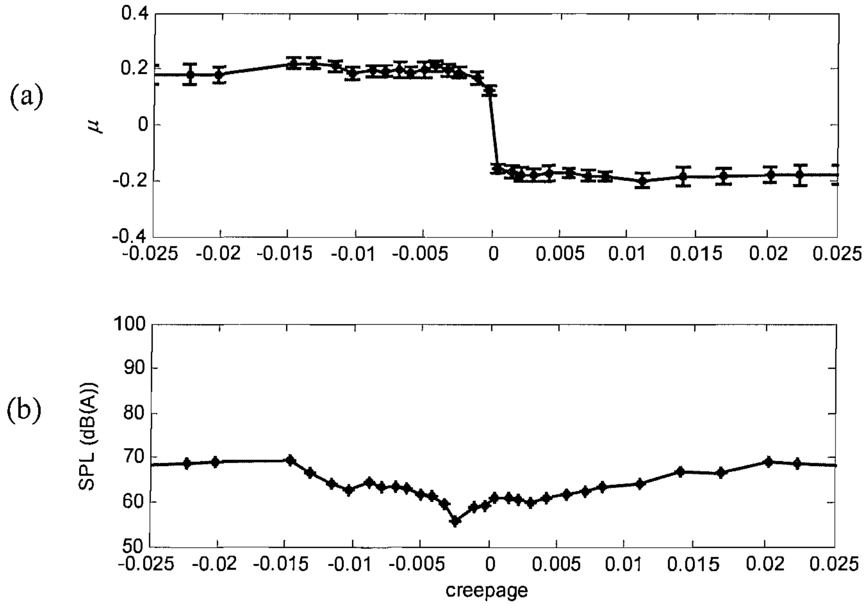

Figure 6-13 Friction coefficients measured under the lubricated surface condition, with a normal load 2.2 kN and a rolling speed 3.1 m/s: (a) friction coefficient; (b) sound pressure level.

Similar analysis can be applied to the two other cases, watered and lubricated. In the lubricated case, the sound levels are much lower and although they increases with increasing yaw angle, squeal is eliminated. Surprisingly, the water case does not eliminate or significantly reduce squeal.

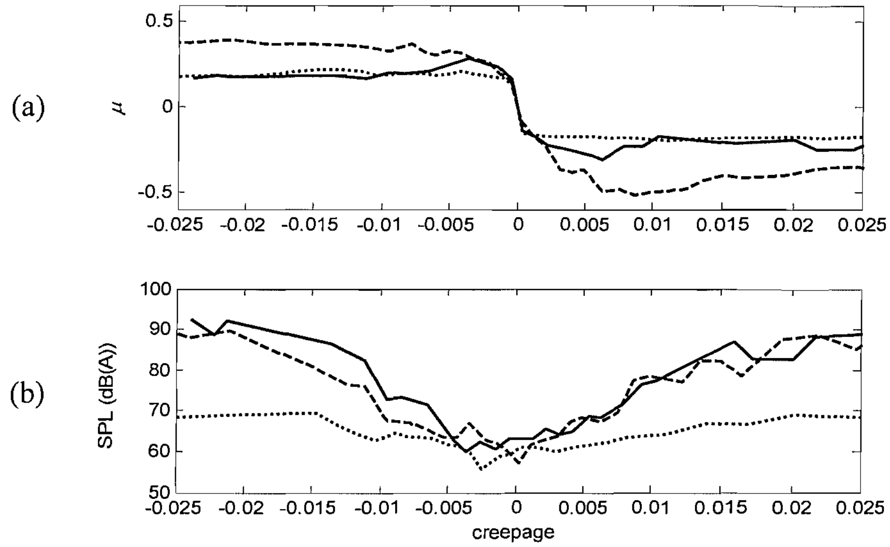

Figure 6-14 Comparison of the friction coefficient curves measured under different contact conditions, all with a normal load 2.2 kN and a rolling speed 3.1 m/s: (a) friction coefficients under the following contact conditions, —— dry and clean, ------ watered, ······ lubricated; (b) sound pressure level under the following contact conditions, —— dry and clean, ------ watered, ······ lubricated.

To investigate the possible relationships between the frictional characteristics and squeal phenomenon, all three cases are compared in Figure 6-14. The friction curves of all three cases are the same for very small creepages in the zone, $\gamma_{20} \leq 0.001$, as shown in Figure 6-14(a). When creepages increase from 0.001 to 0.015, all these friction curves gradually change from adhering to sliding at different rates. The lubricated case saturates at a small creepage of 0.001 and directly turns to sliding without a falling zone. The watered case starts to saturate at a creepage as large as 0.008 and has a much higher friction in the saturated region. In the saturated and falling friction zones, surface conditions are clearly important.

It was observed that the watered surface was normally a bit 'stickier' than the dry one, and exhibited considerable wear after rolling for a while. Similarly the dry one was 'stickier' than the lubricated one. This 'stickiness' may be associated with wear debris. Although the complex mechanisms behind these phenomena cannot be explained theoretically, the falling friction force after saturation found here is consistent with earlier findings [32][39].

Compared with the other two cases, the watered case is less symmetric about zero creepage. This is probably due to variations in the amount of water added on the surfaces. In Figure 6-14(b), the wheel and/or rail discs squeal under the dry and watered conditions but do not squeal under the lubricated condition. The squeal noise intensity is similar in dry and watered cases at the same creepages despite differences in the friction curve. The squeal intensity is related more to the creepage than details of the friction.

In practice, it is known that railway curve squeal will be reduced or eliminated in a rainy climate, with watered rails [66]. Koch [23] also found the watered contact surface can eliminate the occurrence of squeal in a 1/4 scale test rig. However, this phenomenon is not found on the twin-disc rig. But this may be due to the fact that the rail disc is a small finite system whereas a rail has infinite length (wheel running over a given point only once). In such circumstances, the building of wear debris will be much less significant.

6.3.3 Dynamic response

The squeal generated in the twin-disc rig is a quasi-steady phenomenon. The dynamic responses, including lateral vibration velocity of the discs and noise radiation, can be analysed in terms of their spectra. These are given here in terms of power spectral density (PSD), with the frequency resolution 1 Hz and the measurement time greater than 4 seconds. Two cases are presented: case (1) shown in Figure 6-15 and case (2) shown in Figure 6-16, with different creepages, both corresponding to dry and clean contact surfaces.

shown in Figure 6-16, with different creepages, both corresponding to dry and clean contact surfaces.

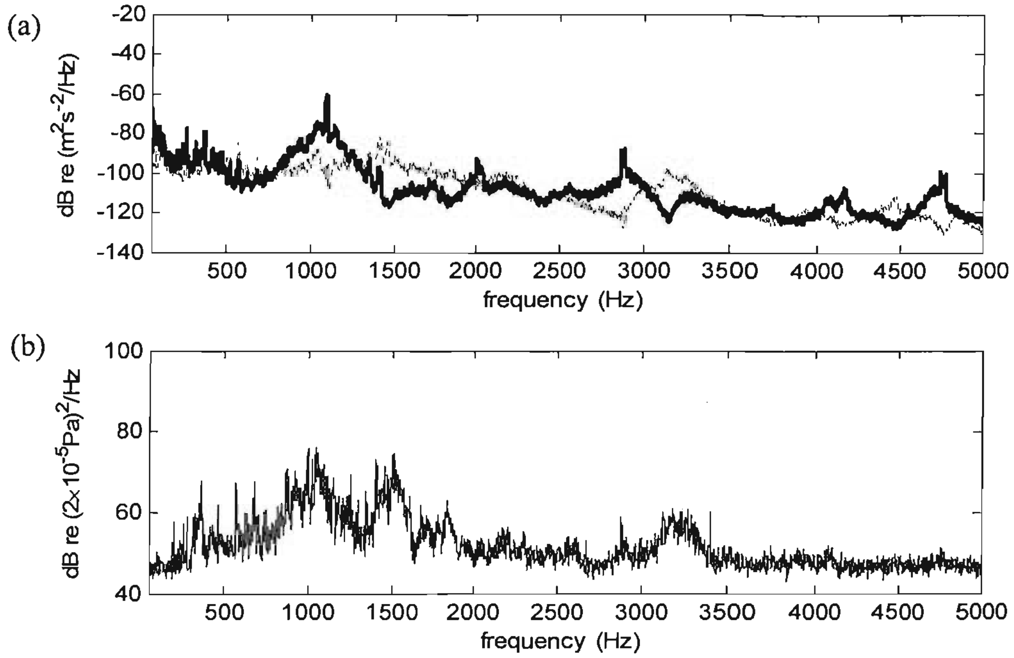

Figure 6-15 Dynamic responses at the lateral creepage γ_{20} = 0.005, under the dry contact surface, with a normal load 2.2 kN, a rolling speed 3.1 m/s and 70 dB(A) SPL; (a) spectrum of amplitude of velocities of the wheel and rail discs, —— wheel, ······ rail; (b) A-weighted sound pressure level measured at 1 m from the rig.

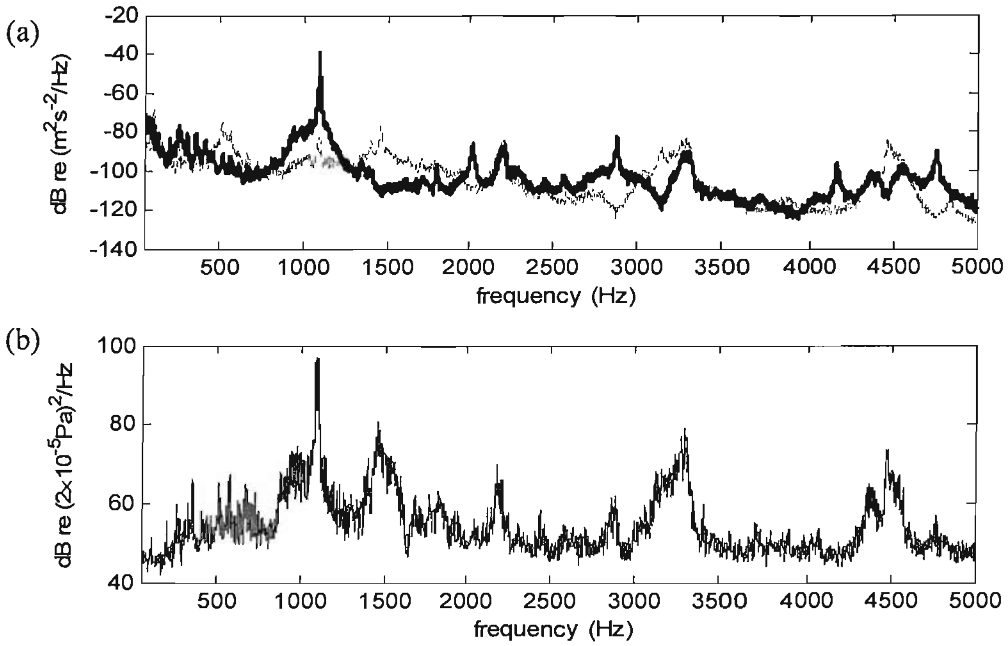

Figure 6-16 Dynamic responses at the lateral creepage γ_{20} = 0.02, under the dry contact surface, with a normal load 2.2 kN, a rolling speed 3.1 m/s and 86 dB(A) SPL; (a) spectrum of the amplitude of velocities of the wheel and rail discs, —— wheel, ······ rail; (b) A-weighted sound pressure level measured at 1 m from the rig.

In case (1) squeal does not occur and the dynamic responses are smaller, whereas in case (2) squeal occurs with much larger dynamic responses at a frequency of 1094 Hz. This gives the largest wheel response and consequently a distinctive peak in the noise radiation.

To investigate the relationships between the wheel and rail responses with respect to lateral creepages, a spectrum map is presented in Figure 6-17. The vibration of each disc and noise radiation are plotted with respect to the lateral creepage for dry contact surfaces. The corresponding friction curve can be found in Figure 6-11.

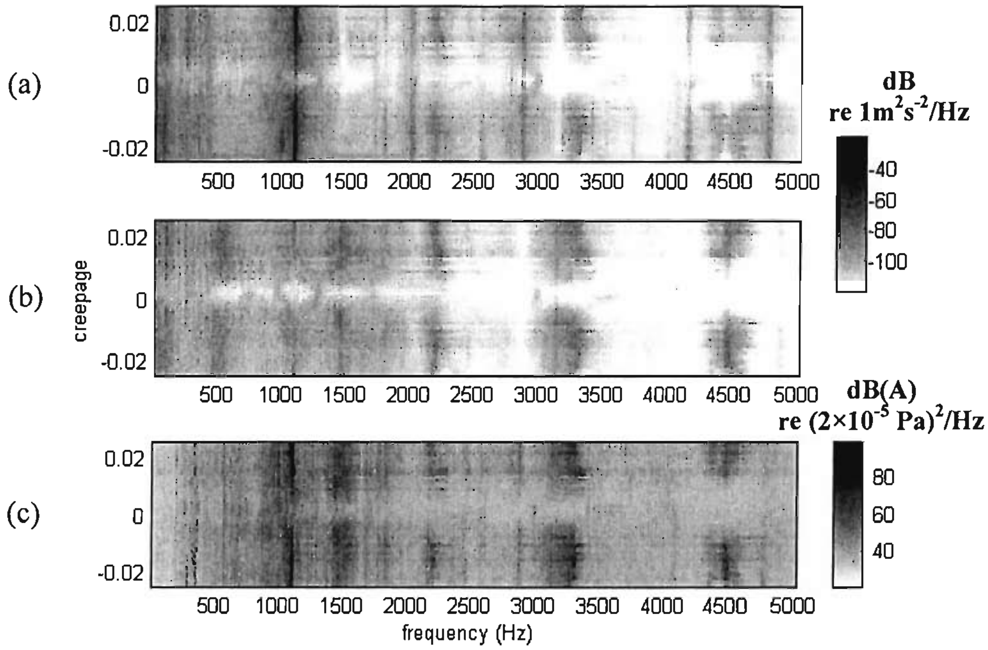

Figure 6-17 Spectra of velocity response of the wheel and rail discs and their noise radiation with respect to lateral creepages, [-0.025, 0.025], dry contact surface, with a normal load 2.2 kN and a rolling speed 3.1 m/s: (a) velocity spectrum of the wheel disc; (b) velocity spectrum of the rail disc; (c) A-weighted sound pressure level.

In the response of the wheel disc, Figure 6-17(a), as the creepage is increased from zero to about 0.01, the vibration amplitude at the dominant mode, 1094 Hz, increases significantly. Some higher harmonics of the dominant frequency are observed at 2200 Hz and 3300 Hz. Another distinct mode is the (3,0) mode seen at about 2874 Hz. The responses below 500 Hz are not negligible, and increase as the creepage increases, but their contribution to the total noise radiation can be ignored due to their low acoustic radiation ratios and the A-weighting applied in the current acoustic measurements.

The response of the rail disc is much lower than that of the wheel disc, as shown in Figure 6-17(b). The visible resonances are the (2,0) mode at 1460 Hz and the (3,0) mode at 3143 Hz. Other large responses are related to the vibration of the wheel disc, i.e. responses around the dominant frequency of 1094 Hz and its higher harmonics, about 2200 Hz, 3300 Hz and 4400 Hz. This shows that the lateral friction force, which drives the rail disc in the lateral direction, must have high frequency oscillations with a fundamental frequency at the dominant frequency. Furthermore, the self-excited vibration can only be established at this dominant frequency. According to the analyses of the vibration responses, the main noise radiation is at the dominant frequency and its high frequency harmonics as well as the other flexible modes identified above, as shown in Figure 6-17(c).

The results of the other two contact conditions, watered and lubricated, are shown in Figure 6-18 and Figure 6-19. Since the results at negative creepages are symmetric to those at positive creepages, only the results for positive creepages are shown.

The responses of the watered case are similar to those of the dry case, both of which squeal. There are two differences between them: one is that in the watered case, the rail disc mode at 526 Hz has quite a large response for creepages up to 0.015; the other is that the watered case has larger responses than those of the dry case for creepages up to 0.010. No explanation can be offered for these differences.

The lubricated case does not squeal even for large creepages. The significant responses of the wheel and rail discs are all located at their own modes. It seems the lateral friction forces evenly excite all wheel and rail modes, as they are excited by roughness in contact. No self-excited vibration appears to exist between the friction force and responses of the contacting bodies, and no dominant frequency with its harmonics is found in the dynamic responses.

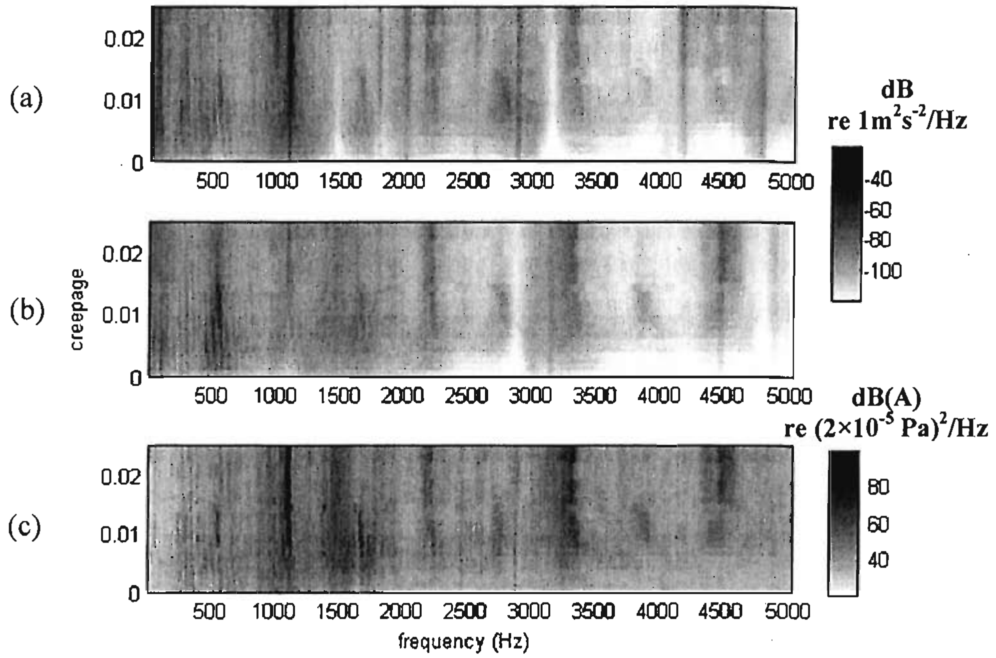

Figure 6-18 Spectra of velocity response of the wheel and rail discs and their noise radiation with respect to lateral creepages, [0, 0.025], watered contact surface, with a normal load 2.2 kN and a rolling speed 3.1 m/s: (a) velocity spectrum of the wheel disc; (b) velocity spectrum of the rail disc; (c) A-weighted sound pressure level.

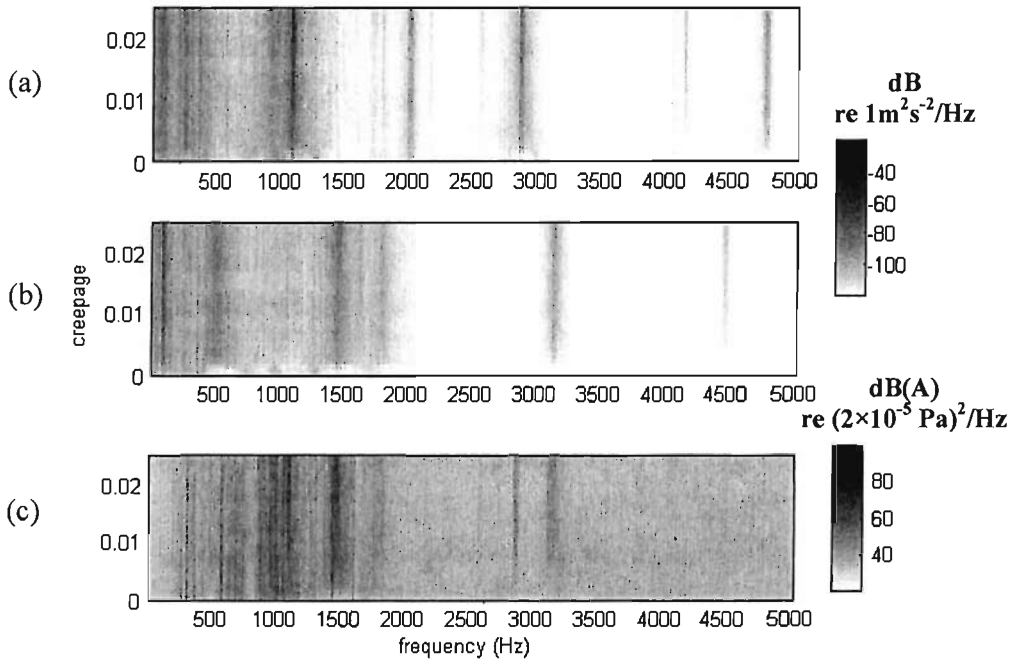

Figure 6-19 Spectra of velocity response of the wheel and rail discs and their noise radiation with respect to lateral creepages, [0, 0.025], lubricated contact surface, with a normal load 2.2 kN and a rolling speed 3.1 m/s: (a) velocity spectrum of the wheel disc; (b) velocity spectrum of the rail disc; (c) A-weighted sound pressure level.

6.3.4 Summary of observations in the experiments on the twin-disc rig

Squeal noise has been shown to be associated with a falling zone in the friction curve. If there is no obvious falling zone in the friction curve, as in the lubricated case, no squeal is generated even for large lateral creepages. Although the possibility of squeal depends on this falling zone, the amplitude of squeal has no obvious relationship with it.

The dominant frequency plays an important role in the dynamic responses. In the experiments with the same wheel and rail discs, the dominant frequency was always found to be 1094 Hz, the (2,0) mode of the wheel disc, which has the largest mass-normalised lateral mode shape of all wheel modes and a smaller damping ratio than any rail disc modes. The response at this dominant frequency is much larger than at any other mode indicating that self-excited vibration takes place at this frequency.

Peaks in the noise radiation are all related to the vibration resonances of the discs; the dominant frequency, its higher harmonics and other flexible modes are found. No obvious frequency shift is found in the vibration responses.

6.4 Validation of the squeal model

The wheel/rail squeal model described in Chapter 5 can be partly validated using the experimental results on the twin-disc rig.

6.4.1 Friction curve

The friction curve used in the validation is based on the one measured under the dry and clean condition, as shown in Figure 6-11. For convenience of simulation, the measured friction curve is fitted approximately by the theoretical friction model (see Eq.(2.28)) with the following coefficients: $\mu_0 = 0.3$, $\kappa = 0.005$ and $\lambda = 0.3$, see Figure 6-20(a). It can be found that the measured and theoretical friction curves agree in the adhering and falling zones, but agree less well in the saturation region.

The friction curve measured under the watered contact surface condition can only be fitted approximately by the theoretical friction model at positive creepages, with the coefficients: $\mu_0 = 0.6$, $\kappa = 0.005$ and $\lambda = 0.4$, as shown in Figure 6-20(b). The measurement results at negative creepages differ from those at positive creepage, because no falling friction is found at large creepages. It is therefore not possible to fit the current friction model to these results. In the following simulation, only the measurement cases at positive creepages are used to validate the squeal model. For the positive creepages, the difference in the adhering region is quite large. In the theoretical friction model, FASTSIM is used to calculate the friction in the adhering region. As discussed in Appendix A, FASTSIM is based on the Hertz contact which is applied to clean contact surfaces. Therefore, this theoretical friction model can only represent the friction characteristics under the clean and dry contact surfaces.

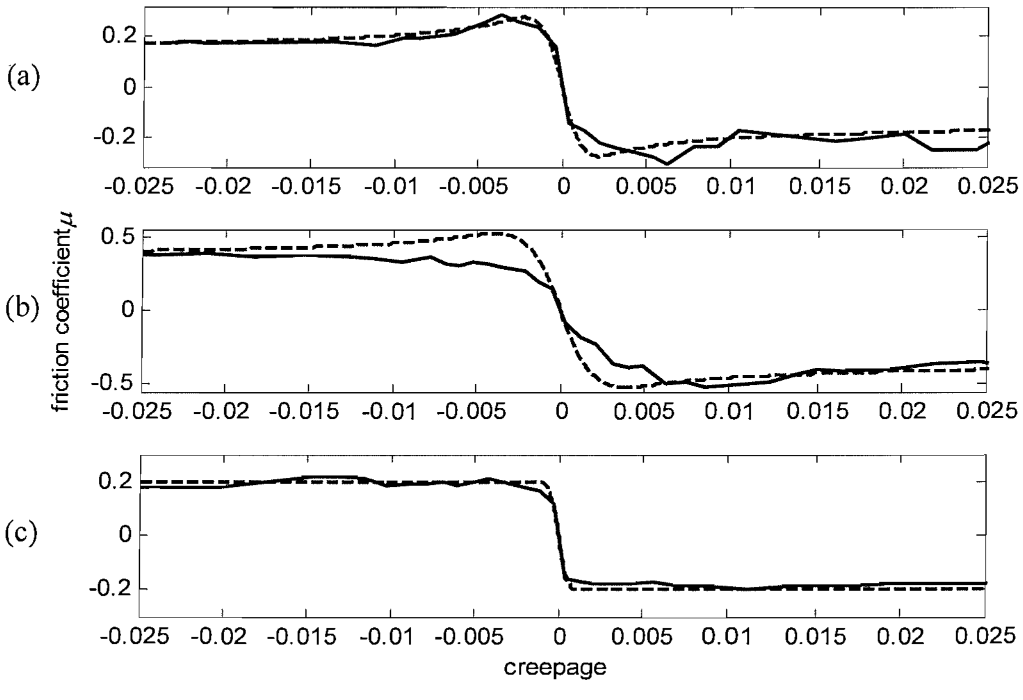

Figure 6-20 Comparison of the measured and theoretical friction curves, with a normal load 2.2 kN and a rolling speed 3.1 m/s: (a) dry contact condition, —— measured, ------ theoretical, (b) watered contact condition, —— measured, ------ theoretical, (c) lubricated contact condition, —— measured, ------ theoretical.

The friction curve, measured under the lubricated contact surface condition, is well approximated by the theoretical friction model with coefficients, $\mu_0 = 0.2$ and $\lambda = 0$, as shown in Figure 6-20(c). However, according to the squeal mechanism assumed in the current squeal model, the lubricated case, without falling slope at large creepages, will not generate squeal. The validation will therefore only consider the dry and clean friction curve.

6.4.2 Vibration of discs

The squeal model simulation of the twin-disc rig adopts the modal parameters of the wheel and rail discs given in Table 6-1 and Table 6-2. To represent the low-frequency dynamics of axle-mounted discs, the rigid modes of the wheel and rail discs are assumed and included in the simulation. The wheel rigid mode has a natural frequency of 25 Hz, mass of 12 kg, modeshape amplitude of 1, and damping ratio of 0.7. The rail disc rigid mode has a natural frequency of 30 Hz, mass of 10 kg, modeshape of 1, and damping ratio of 0.7.

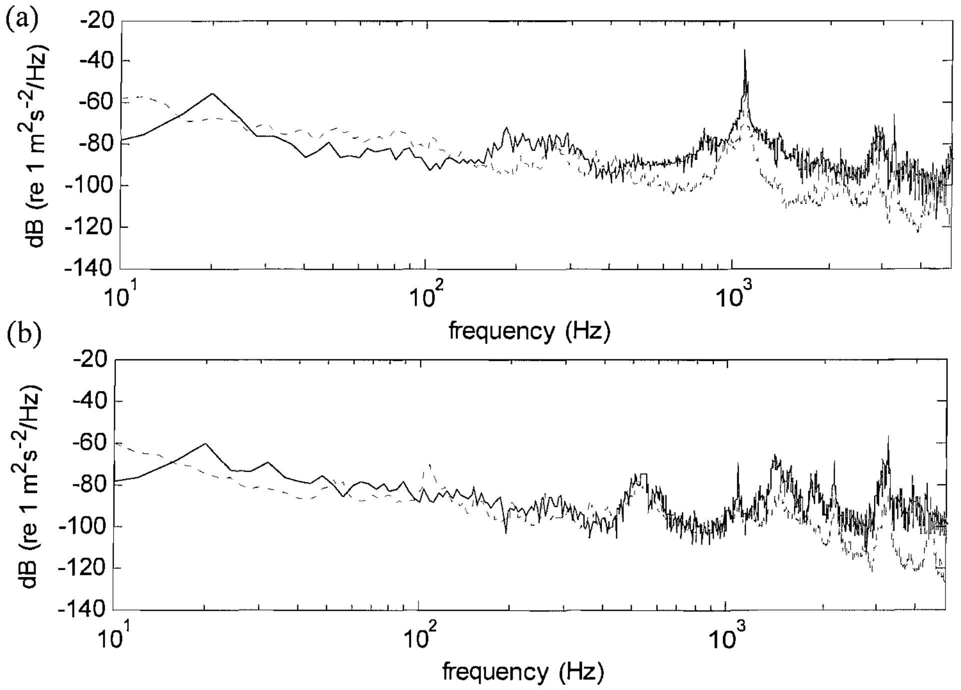

Figure 6-21 Comparison of the simulation and measurement results of lateral responses of the wheel and rail discs, under γ_{20} = 0.02, dry contact surface, a normal load 2.2 kN and a rolling speed 3.1 m/s: (a) wheel responses, —— simulation, ······ measurement; (b) rail responses, —— simulation, ······ measurement.

In Figure 6-21, the lateral responses from the simulation are compared with corresponding measured responses. The squeal conditions are for a large steady-state lateral creepage $\gamma_{20} = 0.02$, with normal load 2.2 kN and rolling speed 3.1 m/s. For the lateral response of the wheel disc, as shown in Figure 6-21(a), the simulation results are close to the measured results. The dominant frequency of 1094 Hz at the (2,0) mode is predicted correctly in the simulation. The difference in response amplitude at this dominant frequency is only about 3 dB. However, although peaks in the responses are predicted at other distinct modes, the differences of amplitude at these modes are quite large, especially for the high-frequency modes. This amplitude difference can also be found in the rail responses, as shown in Figure 6-21(b).

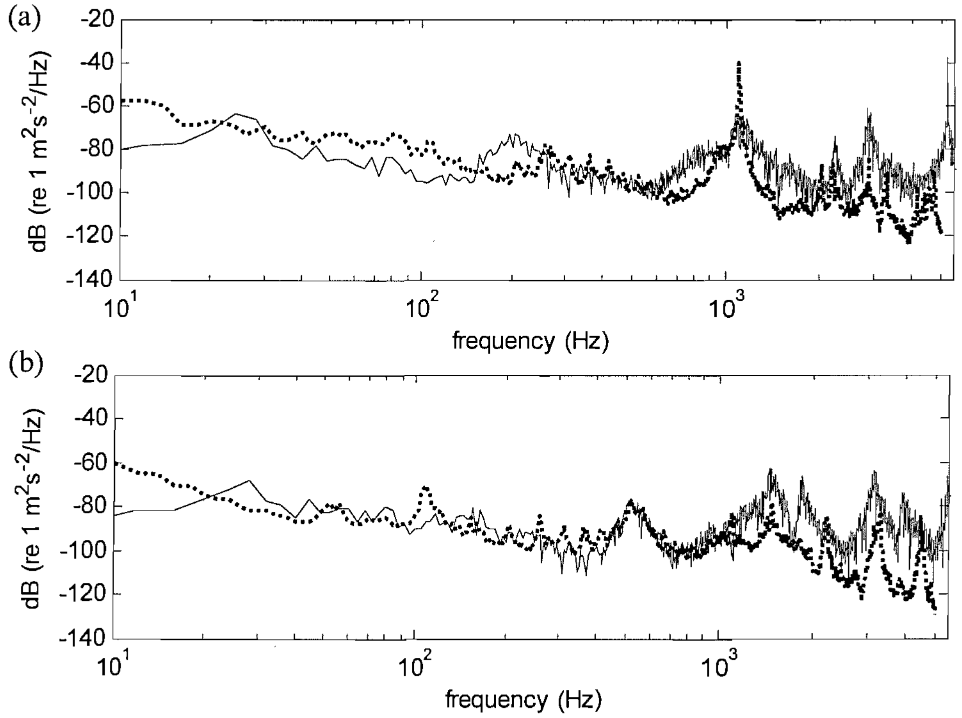

Figure 6-22 Comparison of the simulation (using the modal parameters without the adjustment of the modal masses) and measurement results of lateral responses of the wheel and rail discs, under γ_{20} = 0.02, dry contact surface, a normal load 2.2 kN and a rolling speed 3.1 m/s: (a) wheel responses, —— simulation, ······ measurement; (b) rail responses, —— simulation, ······ measurement.

The modeshapes of the flexible modes of the wheel and rail discs are sensitive to the squeal prediction results. Figure 6-22 shows the prediction results using the original modal masses (but other modal parameters are adjusted), as given in Table 6-1 and

Table 6-2. The predicted dominant resonance is changed to be the (4,0) mode at 5238 Hz, which is not consistent with the measured dominant resonance at the (2,0) mode.

6.4.3 Acoustic radiation

The curves of sound pressure level from simulation and measurement results are compared in Figure 6-23. The original data of measured sound pressure is A-weighted. In order to show the difference at low-frequency bands, the A-weighting has been removed from the measured sound pressure before applying the comparison.

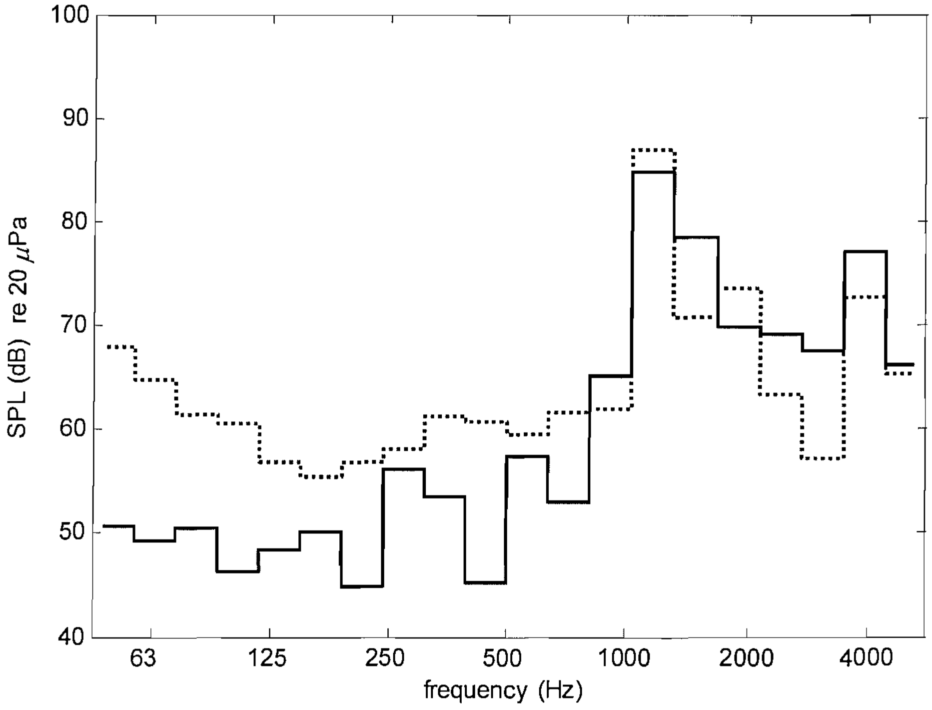

Figure 6-23 Comparison of the simulation and measurement results of sound pressure level, under $\gamma_{20} = 0.02$, dry contact surface, with a normal load 2.2 kN and a rolling speed 3.1 m/s: —— simulation, 86 dB, ······ measurement, 88 dB.

The low-frequency band of measured noise includes the background noise, about 60 dB. Since this background noise does not radiate from the vibrating discs, the difference of sound pressure between the measurement and simulation is much larger than that for the vibration in the frequency range below 500 Hz. The total sound pressure levels for measurement and simulation are 88 dB and 86 dB, respectively. The difference mainly reflects that found in the vibration amplitudes at the dominant frequency of 1094 Hz.

6.4.4 Stability analysis

The stability analysis for squeal prediction can be applied to the twin-disc rig. Since the dynamic properties of the wheel and rail discs are both described by FE models, the roots of the closed feedback loop can include both the wheel and rail modes. Hence, the stability analysis of the closed-loop roots gives similar results to the Nyquist stability analysis, as shown in Figure 6-24.

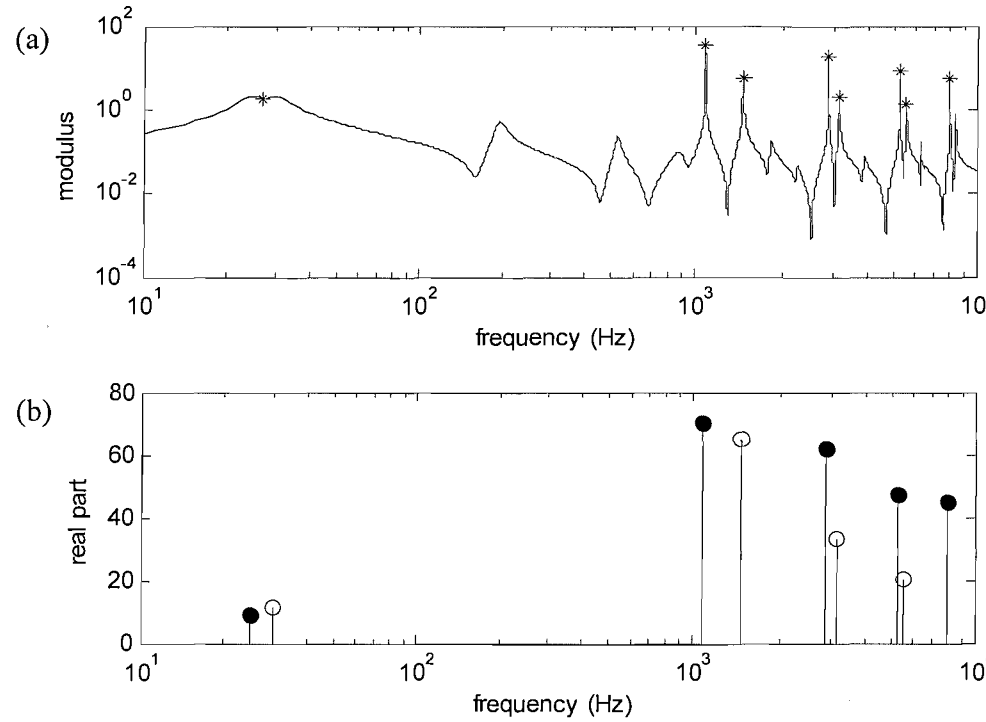

Figure 6-24 Stability analysis on the twin-disc rig, under $\gamma_{20} = 0.02$, dry contact surface, with a normal load 2.2 kN and a rolling speed 3.1 m/s, (a) —— modulus of Bode diagram of eigenloci, * unstable modes, (b) real component of closed-loop roots of the wheel and rail under lateral forces, • wheel modes, ○ rail modes.

6.4.5 Results for smaller creepages

If the steady-state creepage is in the region where the friction curve cannot be fitted very well by the theoretical model, as shown in Figure 6-20(a), the simulation results may show a great difference from the measurement results. For example: Figure 6-25 and Figure 6-26 show a case with steady-state lateral creepage $\gamma_{20} = 0.005$. However, this case is not a typical squeal case in the experiments.

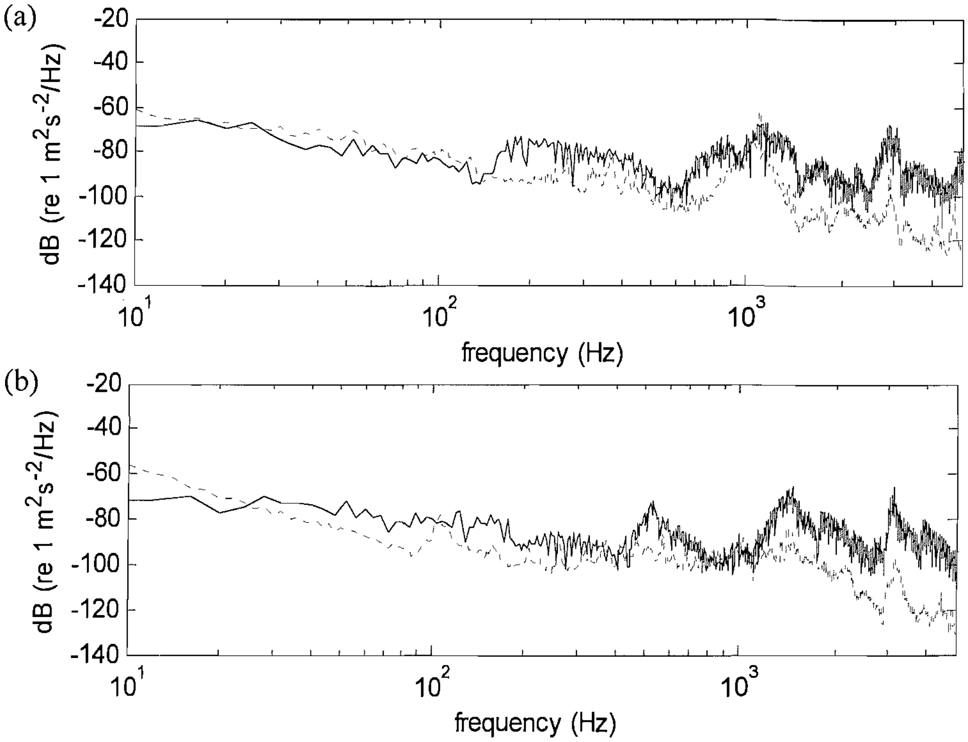

Figure 6-25 Comparison of the simulation and measurement results of the lateral responses of the wheel and rail discs, under γ_{20} = 0.005, dry contact surface, with a normal load 2.2 kN and a rolling speed 3.1 m/s: (a) wheel responses, —— simulation, ······ measurement; (b) rail responses, —— simulation, ······ measurement.

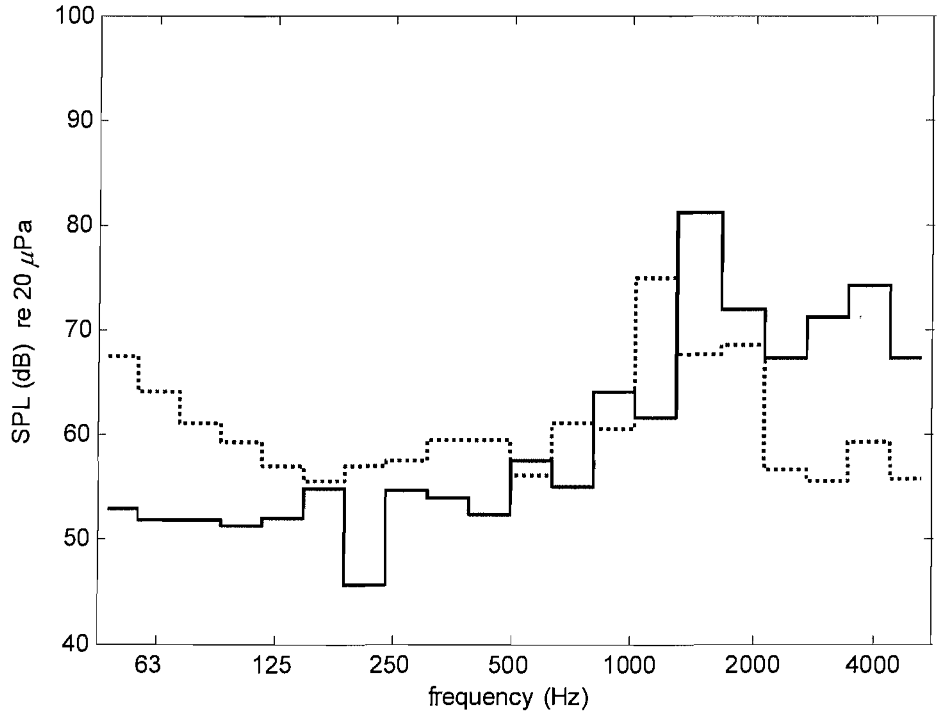

Figure 6-26 Comparison of the simulation and measurement results of sound pressure level, under γ_{20} = 0.005, dry contact surface, with a normal load 2.2 kN and a rolling speed 3.1 m/s: —— simulation, 83 dB, ······ measurement, 76 dB.

6.5 Summary

According to the experimental results measured under controllable conditions, the falling friction is closely related to the self-excited vibration and hence the occurrence of squeal. The self-excited vibration normally takes place at one of the flexible lateral modes of the rolling discs (usually the wheel disc). The larger the lateral steady-state creepage, the greater the intensity of squeal noise, especially at the creepages where the friction just starts to fall. Based on the comparisons of squeal results measured under dry and watered surface conditions, it seems that the detailed information of friction curves, e.g. the value of falling slope, does not play an important role in the squeal intensity.

The measurements of friction curve under watered condition were anomalous. This is possibly due to relatively significant changes of the measurement conditions during each measurement of the friction curve, e.g. the amount of water and the quick build-up of wear debris.

Squeal can be controlled using friction modification, e.g. lubricating contact surfaces. Another squeal method, the damping treatment on the wheel disc, has not been investigated on the twin-disc rig. This should be done in the future.

Although the evidence for the squeal mechanism assumed in this theoretical model, i.e. stick-slip motion, cannot be identified explicitly from the measured results, the validation of the theoretical model is successful. By using the measured friction curves and adjusted modal parameters of the discs, the unstable vibration and subsequent squeal radiation can be predicted by the theoretical model.

The effects of large spin and a lateral creepage together with a longitudinal one can also be studied on a revised twin-disc rig. If the rail disc is replaced by a moving belt, by adjusting the angle of the contact plane on the belt, large spin can be obtained. If the speed of the moving belt can be adjusted, longitudinal creepage can be produced.

7. APPLICATION OF THE MODEL TO CURVE SQUEAL PREDICTION

7.1 Introduction

In order to predict the occurrence of curve squeal, the steady-state curving behaviour of a typical UK passenger vehicle, the Class 158 DMU, on various tight curves has been predicted using the vehicle dynamics program described in Chapter 3. Once the vehicle behaviour has been determined, the curve squeal calculation can be applied for all four wheel/rail contacts in a bogie. The effectiveness of traditional control methods for the curve squeal, i.e. wheel damping treatment and friction modification, is also investigated.

7.2 Curving behaviour

The steady-state curving behaviour of the Class 158 DMU vehicle has been simulated using a dedicated program discussed in Chapter 3. This treats the vehicle dynamics with a limited number of DOF. Typical wheel and rail profiles are adopted in the simulation, with contact results provided in Section 3.2. The steady-state curving parameters for the squeal prediction are given in Table 7-1 and Table 7-2, with the Coulomb friction coefficient set to $\mu_0 = 0.3$ and $\mu_0 = 0.4$, respectively.

All these cases, except the case with vehicle speed of 10 m/s on a curve of radius 150 m, are chosen to represent curving without cant deficiency. The four wheel/rail contacts in a bogie are investigated. The important curving parameters for the squeal prediction, obtained from the vehicle dynamics calculations, are as follows: (1) the steady-state creepages γ_1^*, γ_2^* and γ_6^*, which are defined in the vehicle dynamics calculation with opposite sign to those defined in the squeal model; (2) the steady-state normal contact force N_0; (4) the semi-axes of the contact patch a, b; (3) the contact angle δ between the wheel and rail; (5) the contact position in the wheel coordinates l_x^w, l_y^w; (6) the contact position in the rail coordinates l_x^r, l_y^r.

Table 7-1 Steady-state curving behaviour, with the Coulomb friction coefficient $\mu_0 = 0.3$.

R_0 [m] V_0 [ms^{-1}] ϕ_0 [°]	wheel	γ_1^* [%]	γ_2^* [%]	γ_6^* [m^{-1}]	N_0 [kN]	a, b [mm]	δ [°]	l_x^w, l_y^w [mm]	l_x^r, l_y^r [mm]
150 6 1.4	leading outer	-0.3	1.9	1.5	64	8.0, 1.1	39	35, 6.2	35, 5.5
	leading inner	0.3	1.5	0.0	59	5.5, 5.3	-0.8	12, -0.3	-3.5, 0.0
	trailing outer	0.9	-0.2	0.0	62	5.7, 5.1	0.9	-12, -0.3	4.3, 0.0
	trailing inner	-0.9	-0.2	-0.6	61	6.9, 2.4	-16	-27, 2.9	-27, 2.5
150 10 1.4	leading outer	-0.3	2.0	1.6	69	8.1, 1.1	43	36, 7.2	35, 6.1
	leading inner	0.3	1.5	0.0	58	5.8, 5.3	-0.8	12, -0.3	-3.2, 0.0
	trailing outer	0.8	-0.2	0.0	59	5.6, 5.1	1.3	-12, -0.3	4.3, 0.0
	trailing inner	-0.8	-0.2	-0.4	64	6.6, 3.1	-9.1	-22, 2.1	-23, 2.1
200 8 2	leading outer	-0.4	1.6	1.4	65	8.0, 1.1	38	34, 6.1	34, 5.4
	leading inner	0.4	1.2	0.0	59	5.5, 5.2	-0.9	12, -0.3	-3.2, 0.0
	trailing outer	0.6	0.0	0.0	57	5.5, 5.0	1.0	-10, -0.3	3.7, 0.0
	trailing inner	-0.6	0.0	-0.4	66	6.5, 3.5	-8.6	-21, 1.7	-21, 1.3
300 12 2.8	leading outer	-0.5	1.0	1.3	67	8.1, 1.2	34	34, 5.6	33, 5.0
	leading inner	0.5	0.8	0.0	58	5.6, 5.0	-0.9	12, -0.3	-3.3, 0.0
	trailing outer	0.3	0.0	0.1	62	6.0, 4.2	1.6	-3.4, -0.1	6.2, 0.1
	trailing inner	-0.3	0.0	-0.1	61	6.0, 4.0	-3.3	-6.5, 0.3	-11, 0.3

Table 7-2 Steady-state curving behaviour, with the Coulomb friction coefficient $\mu_0 = 0.4$.

R_0 [m] V_0 [ms^{-1}] ϕ_0 [°]	wheel	γ_1^* [%]	γ_2^* [%]	γ_6^* [m^{-1}]	N_0 [kN]	a, b [mm]	δ [°]	l_x^w, l_y^w [mm]	l_x^r, l_y^r [mm]
150 6 1.4	leading outer	-0.5	2.3	1.8	69	8.1, 1.3	49	37, 7.9	36, 6.8
	leading inner	0.5	1.4	0.0	58	5.3, 5.6	-0.8	13, -0.3	-2.8, 0.0
	trailing outer	0.9	-0.2	0.0	59	5.6, 5.1	1.0	-12, -0.3	3.5, 0.0
	trailing inner	-0.9	-0.2	-0.7	64	7.1, 2.3	-18	-27, 3.3	-27, 2.9
150 10 1.4	leading outer	-0.4	2.4	1.9	72	7.8, 1.9	52	37, 8.6	36, 7.4
	leading inner	0.6	1.4	0.0	57	5.4, 5.2	-0.7	13, -0.3	-2.7, 0.0
	trailing outer	0.8	-0.2	0.0	59	5.6, 5.1	1.0	-11, -0.3	3.7, 0.0
	trailing inner	-0.8	-0.2	-0.5	64	6.8, 2.9	-9.1	-24, 2.2	-23, 1.8
200 8 2	leading outer	-0.5	1.8	1.7	65	8.0, 1.1	46	36, 7.3	35, 6.3
	leading inner	0.5	1.2	0.0	59	5.3, 6.0	-0.8	13, -0.3	-2.9, 0.0
	trailing outer	0.6	0.0	0.0	57	5.5, 5.0	1.0	-10, -0.3	3.8, 0.0
	trailing inner	-0.6	0.0	-0.3	65	6.3, 3.8	-8.1	-20, 1.5	-20, 1.2
300 12 2.8	leading outer	-0.5	1.0	1.5	65	8.0, 1.1	41	35, 6.5	34, 5.7
	leading inner	0.5	0.8	0.0	58	5.4, 5.6	-0.8	12, -0.3	-3.0, 0.0
	trailing outer	0.3	0.0	0.1	62	6.0, 4.2	1.6	-3.4, 0.0	6.2, 0.1
	trailing inner	-0.3	0.0	-0.1	61	6.0, 4.0	-3.3	-6.5, 0.3	-11, 0.3

Due to the tight curve radii in all these cases, the contact of the leading outer wheel is located in the flange area, giving a large spin as well as a large steady-state lateral creepage. The contact position of the leading inner wheel is far from the flange, with a large lateral creepage but without spin. For the trailing wheelset, the lateral creepages of both inner and outer wheel/rail contacts are small, but the longitudinal creepages are quite large and increase as the curve radius reduces. If the curve radius is extremely tight, the contact of the trailing inner wheel is close to the flange but the contact angle is not large. All four wheel/rail contacts shift from the nominal contact positions to varying extents. The main effect of increasing the friction coefficient is to increase the contact angle and the lateral creepage on the leading outer wheel.

The cases considered in Section 5.7 show that the steady-state creepages and contact angle are the most important parameters from the curving behaviour in the curve squeal prediction. According to the curving results given in Table 7-1 and Table 7-2, the steady-state creepages in curves are mainly determined by the following curving parameters: the curve radius, the train speed and the Coulomb friction coefficient. Changes in the curving conditions may affect one or two of the steady-state creepages to some extent. The relations between these curving conditions and the steady-state creepages are summarised in Table 7-3.

Table 7-3 Relations between the steady-state creepages and curving conditions.

curving conditions	wheelset			wheel			
		lateral movement	yaw		$\lvert\gamma_1^*\rvert$	$\lvert\gamma_2^*\rvert$	$\lvert\gamma_6^*\rvert, \lvert\delta\rvert$
tighter curve: $R_0 \downarrow$	leading	outward in the curve	↑	outer	—	↑	↑
				inner	—	↑	—
	trailing	inward in the curve	↑	outer	↑	—	—
				inner	↑	—	↑
greater cant deficiency: (train speed $V_0 \uparrow$, with fixed cant angle)	leading	outward in the curve	—	outer	—	↑	↑
				inner	—	—	—
	trailing	outward in the curve	—	outer	↓	—	—
				inner	↑	—	↓
higher friction: $\mu_0 \uparrow$	leading	outward in the curve	—	outer	—	↑	↑
				inner	—	—	—
	trailing	—	—	outer	—	—	—
				inner	—	—	—

↑ increased; ↑ reduced; — little change.

7.3 Squeal prediction

7.3.1 Parameters

The squeal prediction has been applied to each curving case shown in Table 7-1 and Table 7-2. The dynamic properties of a Class 158 wheel can be found in Appendix H. The predictions are based on 5 rigid modes and 22 selected flexible modes below 5000 Hz . Since the modal model represents a right-hand wheel, some necessary transform will be applied before using the modal parameters for a right-hand wheel. The dynamic properties of the track and the equivalent systems can be found in Appendix L. The friction model is introduced in Section 2.4. The creep-force relation adopted in the simulation is calculated by FASTSIM, with falling friction introduced for large creepages from Eq.(2.28). The creep-friction relationship in one direction, e.g. the lateral, may be influenced by the creep in other directions, e.g. the longitudinal creepage and large spin. In the following simulations, the coefficients in the falling friction function are $\lambda = 0.3$ and $\kappa = 0.005$, representing a typical falling slope (see Figure 5-11). The squeal is evaluated in terms of the A-weighted sound pressure level at 7.5 m from the squealing wheel.

7.3.2 Squeal prediction for a bogie

One of the curving cases in Table 7-1 is adopted as an example to show the squeal prediction applied on all four wheel/rail contacts in a bogie. The curving conditions in this case are $\mu_0 = 0.3$, $V_0 = 10\,\mathrm{m/s}$ and $R_0 = 150\,\mathrm{m}$.

Because of the large lateral steady-state creepages at the leading outer and inner wheel/rail contacts, they will produce squeal with a level of 93 dB(A) at one of the lateral flexible modes, as shown in Figure 7-1. According to the stability analysis, the outer contact has fewer unstable modes with much smaller unstable eigenvalues than the inner one. This is because the outer contact is in the flange zone, with a large contact angle and a large spin. Therefore, the outer wheel is much easier to control than the inner one.

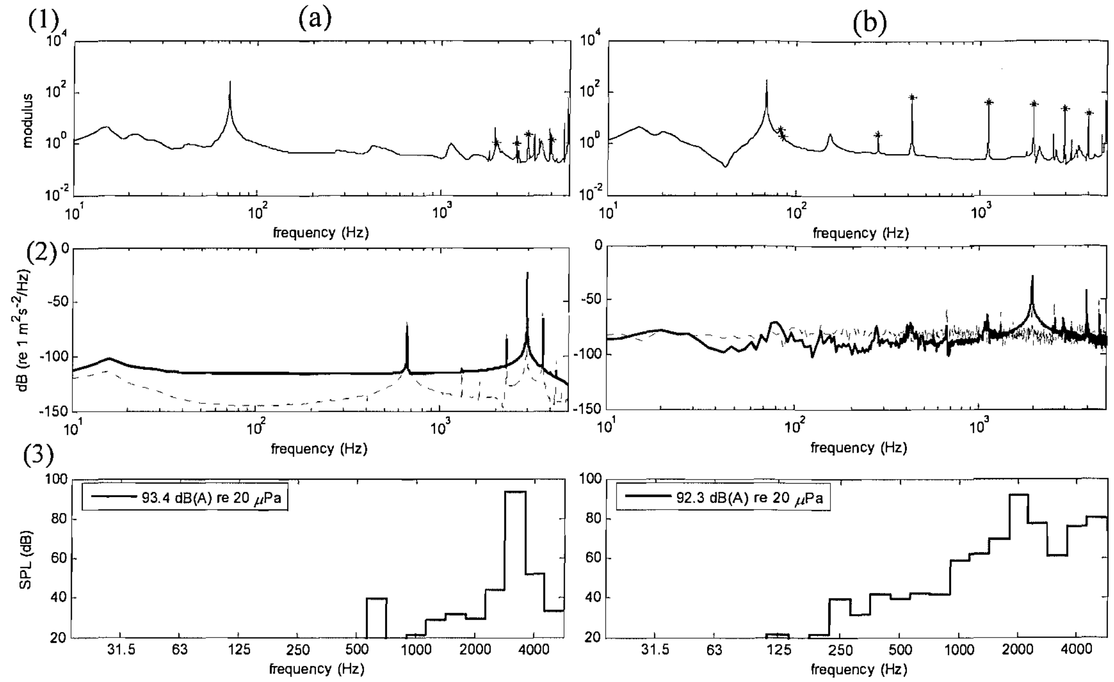

Figure 7-1 Squeal prediction for the leading outer (a) and inner (b) wheels in a bogie of the Class 158 DMU vehicle, running at 10 m/s on the curve with 150 m curve radius for a Coulomb friction coefficient 0.3: (1) Nyquist stability analysis: modulus of the Bode diagram of eigenloci, * unstable modes; (2) spectra of the lateral wheel and rail velocities at the contact position, — wheel, – – – rail; (3) A-weighted SPL of wheel at 7.5 m from the source.

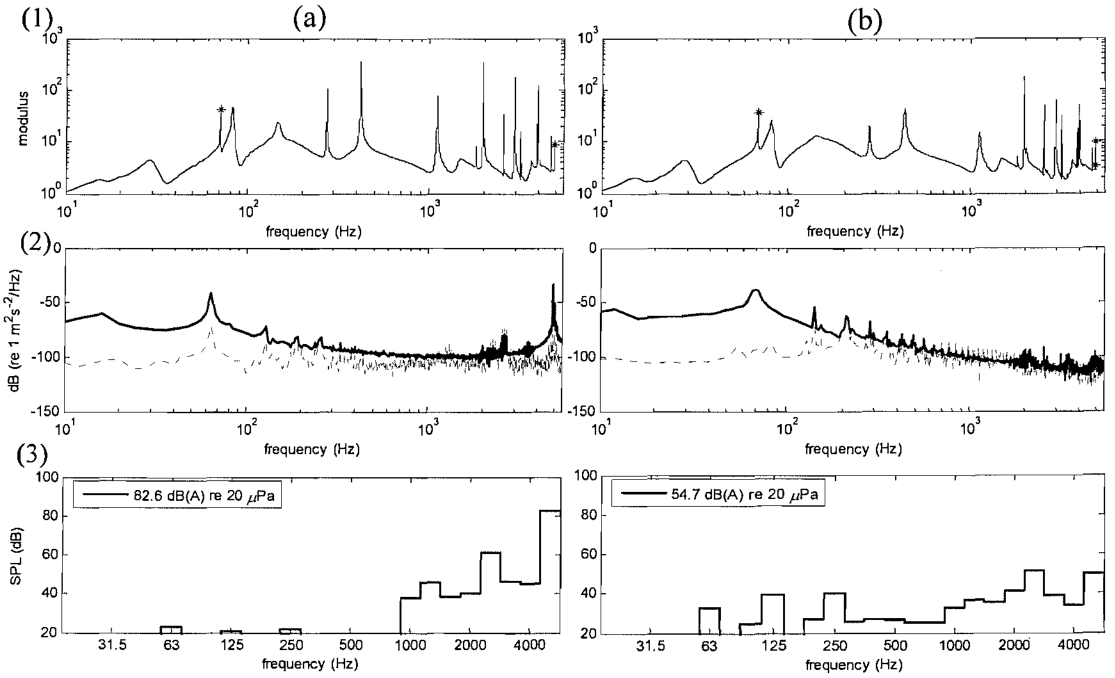

Figure 7-2 Squeal prediction for the trailing outer (a) and inner (b) wheels in a bogie of the Class 158 DMU vehicle, running at 10 m/s on the curve with 150 m curve radius for a Coulomb friction coefficient 0.3: (1) Nyquist stability analysis: modulus of the Bode diagram of eigenloci, * unstable modes; (2) spectra of the longitudinal wheel and rail velocities at the contact position, — wheel, – – – rail; (3) A-weighted SPL of wheel at 7.5 m from the source.

Both contacts at the trailing wheelset have large longitudinal creepages but small lateral creepages, which means the possible unstable modes are in the longitudinal direction, as shown in Figure 7-2. However, whether it can be considered as squeal or not is determined by the frequency at which the unstable vibration takes place. The time-domain simulation shows that the trailing outer wheel squeals with quite low intensity, while the trailing inner wheel does not.

Considering the sensitivity in the squeal calculation, the prediction results for one curving case are not sufficient to draw general conclusions. It is useful to investigate the squeal under a set of curving conditions and obtain the relations between the squeal and curving conditions.

7.3.3 Squeal prediction under different curving conditions

Table 7-4 gives the dominant squealing mode and sound pressure level for all four wheel/rail contacts in a Class 158 bogie, under the different curving conditions provided in Table 7-1 and Table 7-2. The shaded results are considered as squeal, normally with an A-weighted SPL higher than 80 dB.

Under almost all the curving conditions considered, the leading wheels are prone to squeal at one of the lateral flexible modes, because they have large lateral steady-state creepages. For the squealing cases, larger steady-state lateral creepages tend to produce higher squeal intensities. However, there are some exceptions. One exception can be found at the leading outer wheel under the conditions: $\mu_0 = 0.4$, $R_0 = 150\,\text{m}$, $V_0 = 6\,\text{m/s}$ and $V_0 = 10\,\text{m/s}$. Due to the tight curve and the high Coulomb friction, from Table 7-2, the contact angle and the spin at this wheel may be large enough to eliminate the occurrence of squeal. The other exception happens at the leading inner wheel under quite large curving radius, $R_0 = 300$ m. As the curve radius increases, there is a tendency for the steady-state lateral creepage to reduce but the steady-state longitudinal creepage increases somewhat. If both longitudinal and lateral steady-state creepages are small, the unstable vibration may occur at the axle mode, which does not appear as squeal.

Table 7-4 Squeal prediction results for a bogie of Class 158 DMU vehicle on different curves.

R_0 [m] V_0 [ms^{-1}] ϕ_0 [°]	wheel	$\mu_0 = 0.3$			$\mu_0 = 0.4$		
		squeal frequency [Hz]	dominant mode	SPL [dB(A)]	squeal frequency [Hz]	dominant mode	SPL [dB(A)]
150 6 1.4	leading outer	2950	(5,0)	90	—	—	—
	leading inner	1976	(4,0)	90	1976	(4,0)	90
	trailing outer	70	(0,c)	56	4924	(2,c)	73
	trailing inner	70	(0,c)	52	70	(0,c)	69
150 10 1.4	leading outer	2950	(5,0)	93	—	—	—
	leading inner	1976	(4,0)	92	1976	(4,0)	96
	trailing outer	70	(0,c)	51	70	(0,c)	53
	trailing inner	70	(0,c)	53	70	(0,c)	53
200 8 2	leading outer	1976	(4,0)	88	1976	(4,0)	89
	leading inner	1976	(4,0)	92	1976	(4,0)	92
	trailing outer	70	(0,c)	68	—	—	—
	trailing inner	70	(0,c)	68	—	—	—
300 12 2.8	leading outer	1976	(4,0)	89	1976	(4,0)	86
	leading inner	82	axle	67	82	axle	69
	trailing outer	—	—	—	—	—	—
	trailing inner	—	—	—	—	—	—

Squeal hardly occurs at the wheels of the trailing wheelset, although they may have unstable vibration at the lower longitudinal modes. For large curve radii, e.g. $R_0 = 300$ m, the steady-state longitudinal creepages are quite small and the trailing wheels are stable.

7.4 Damping treatments on the wheel

The effectiveness of damping treatments on the wheel is simulated by increasing the damping of the wheel by a factor 10 and 50, respectively. The squeal prediction results are given in Table 7-5. The curving conditions are calculated for the Coulomb friction coefficient $\mu_0 = 0.3$.

The simulation results show that the light damping treatment, increasing the damping by a factor of 10, can eliminate the squeal at the leading outer wheels and trailing wheels in some situations. Since the original values of wheel damping are assumed approximately according to previous measurements, the results of the light damping treatment can be considered as representing the sensitivity of the squeal prediction results, especially for the flange contact cases.

Table 7-5 Squeal prediction after the wheel damping treatments, $\mu_0 = 0.3$.

R_0 [m] V_0 [ms^{-1}] ϕ_0 [°]	wheel	wheel damping ×10			wheel damping ×50		
		squeal frequency [Hz]	dominant mode	SPL [dB(A)]	squeal frequency [Hz]	dominant mode	SPL [dB(A)]
150 6 1.4	leading outer	2950	(5,0)	89	—	—	—
	leading inner	1976	(4,0)	89	418	(2,0)	80
	trailing outer	70	(0,c)	45	70	(0,c)	43
	trailing inner	70	(0,c)	49	70	(0,c)	42
150 10 1.4	leading outer	—	—	—	—	—	—
	leading inner	1976	(4,0)	92	82	axle	75
	trailing outer	70	(0,c)	47	70	—	—
	trailing inner	70	(0,c)	49	70	—	—
200 8 2	leading outer	1976	(4,0)	88	—	—	—
	leading inner	1976	(4,0)	92	82	axle	75
	trailing outer	70	(0,c)	40	70	(0,c)	39
	trailing inner	70	(0,c)	43	70	(0,c)	41
300 12 2.8	leading outer	1976	(4,0)	89	—	—	—
	leading inner	82	axle	65	82	axle	60
	trailing outer	—	—	—	—	—	—
	trailing inner	—	—	—	—	—	—

A higher damping treatment, represented by a factor of 50, can effectively control the squeal for larger curve radii. However, the squeal at the leading inner wheel is the most difficult to control. Adopting only the method of damping treatment may fail to control the squeal occurrence at the leading inner wheel on tight curves. If the damping treatment cannot stabilise the wheel and eliminate the squeal, the intensity of squeal noise may not decrease significantly, see Table 7-5. One exception is where the damping treatment does not eliminate the squeal but shifts the dominant squealing mode to one that has a lower acoustic radiation ratio.

7.5 Friction modification

Friction modification is another practical squeal control method. The experiments on the twin-disc rig showed that the lubrication of the contact surface can reduce the falling slope at large creepages as well as the Coulomb friction coefficient.

As indicated in Section 5.7, Coulomb friction coefficient is not directly related to the squeal occurrence. However, since the curving behaviour is sensitive to the Coulomb friction coefficient (see Table 7-4), it may play a role on the curve squeal under some conditions.

Table 7-6 Effects of the friction modification on the squeal predictions, $\mu_0 = 0.3$.

R_0 [m] V_0 [ms^{-1}] ϕ_0 [°]	wheel	$\lambda = 0.3$			$\lambda = 0.1$		
		squeal frequency [Hz]	dominant mode	SPL [dB(A)]	squeal frequency [Hz]	dominant mode	SPL [dB(A)]
150 6 1.4	leading outer	2950	(5,0)	90	2950	(5,0)	87
	leading inner	1976	(4,0)	90	1976	(4,0)	87
	trailing outer	70	(0,c)	56	4924	(2,c)	78
	trailing inner	70	(0,c)	52	70	(0,c)	73
150 10 1.4	leading outer	2950	(5,0)	93	—	—	—
	leading inner	1976	(4,0)	92	1976	(4,0)	91
	trailing outer	70	(0,c)	51	4924	(2,c)	83
	trailing inner	70	(0,c)	53	4924	(2,c)	80
200 8 2	leading outer	1976	(4,0)	88	—	—	—
	leading inner	1976	(4,0)	92	1976	(4,0)	89
	trailing outer	70	(0,c)	68	70	(0,c)	73
	trailing inner	70	(0,c)	68	70	(0,c)	71
300 12 2.8	leading outer	1976	(4,0)	89	—	—	—
	leading inner	82	axle	67	82	axle	67
	trailing outer	—	—	—	—	—	—
	trailing inner	—	—	—	—	—	—

The modification of the falling ratio of the friction law is directly related to the squeal prediction results. According to the curve squeal mechanism adopted in this theoretical model, if there is no falling region, setting $\lambda = 0$ in the simulation, squeal will not occur under any circumstances. To show the effects of varying the falling ratio, a small non-zero falling ratio $\lambda = 0.1$ is selected. Table 7-6 presents comparisons between the squeal prediction results using $\lambda = 0.3$ and $\lambda = 0.1$ under the same curving conditions with $\mu_0 = 0.3$, as provided in Table 7-1.

From the comparisons, the smaller falling ratio stabilises the leading outer wheels, because the large spin in the flange contact may eliminate the falling friction. It is interesting that the trailing wheels will have unstable vibration at the higher longitudinal mode (2,c) but not the lower longitudinal mode (0,c), if the falling ratio is smaller. The higher mode provides larger acoustic radiation ratio and consequently generates a higher sound level.

7.6 Summary

The squeal prediction using the parameters obtained from curving behaviour shows that squeal is prone to occur at the leading wheels of a bogie, mainly due to the large lateral steady-state creepage. The leading outer wheel in the flange contact has less possibility for squeal than the leading inner one. The trailing wheels with large longitudinal steady-state creepage may squeal if the dominant mode of self-excited vibration is at a high-frequency mode. Both damping treatments and friction modification can be used to control the squeal, but will not always be effective.

8. CONCLUSIONS AND FURTHER WORK

Railway curve squeal noise, caused by unstable high frequency vibration of wheels during curving, is a high-pitched and high-intensity noise. Although a lot of research work on curve squeal has been carried out for more than 40 years, some problems in this area still remain to be solved. From a viewpoint of academic research, the mechanisms of curve squeal and the relations between the many parameters involved in the squeal model are of interest. In addition, as an engineering problem, any practical methods that can effectively control the curve squeal need to be investigated. All these requirements can be reached if a general curve squeal model is established. This model should be built based on solid evidence of the squeal mechanism, considering the curving behaviour of vehicles and providing engineering-friendly approaches for the squeal prediction and control. This is the original motivation for the work presented in this thesis.

It is useful to summarise briefly the main outcomes of the thesis. Some suggestions are then made for possible further work.

8.1 Outcomes

8.1.1 Mechanism of curve squeal

The mechanism of curve squeal is considered in this thesis as 'stick-slip' self-excited vibration induced by a decreasing friction coefficient at large creepages. The experimental results measured on the twin-disc rig indicate that the falling friction at large creepages indeed occurs and has intimate relations with the self-excited vibration and hence the occurrence of squeal. In the experiments, the self-excited vibration normally commences at the steady creepages where the friction coefficient curve just starts to fall. If this falling zone is eliminated by lubricating the contact surfaces, the discs are stable at any steady creepage. The theoretical model, based on the 'stick-slip' mechanism, can predict the unstable vibration and squeal radiation, by using the measured falling friction curves and adjusted modal parameters of the discs. Although no direct evidence has been found to support the assumption of stick-slip motion, this mechanism, up to now, is undoubtedly the most appropriate mechanism for the curve squeal analysis. Excellent agreement between predicted and measured vibration amplitudes supports this conclusion.

For an obvious stick-slip motion, a ‘stick’ process and a ‘slip’ process, normally represented in the time domain, can be easily identified in each cycle of limit-cycle sliding velocity. However, according to the simulation results, if the unstable vibration between the wheel and rail can produce squeal, the ‘stick’ process in sliding is difficult to identify in the time domain, whereas the ‘slip’ process in the sliding is significant. If the ‘stick’ process is obvious in the steady responses, the vibration normally takes place at lower frequency wheel/rail modes with smaller amplitudes, and therefore, squeal does not occur. Since the obvious stick-slip motion normally takes place in a low frequency range, it is not usually considered to be a squeal mechanism. It is shown that curve squeal can be simulated using the stick-slip mechanism, in which the motion is dominated by the slip component.

8.1.2 Characteristics of friction

In the friction model for the purpose of squeal analysis, the relations are required between the sliding velocities and friction coefficients, covering the whole range from adhering to sliding.

To represent the adhering friction in the presence of longitudinal and lateral creepages and a large spin, Kalker’s FASTSIM algorithm is adopted. The main limitation in this friction model, as with other conventional rolling friction models, is that it is normally restricted to the conditions of steady rolling. However, in the time-domain squeal simulation, this steady rolling friction model has been directly applied for the unsteady cases.

Since the wheel/rail squeal is mainly related to the 'slip' process in the wheel/rail motion, for the squeal analysis, the frictional characteristics in sliding are more important than those in adhering. Unfortunately, no appropriate theoretical friction model in terms of sliding is available. In this thesis, the falling friction at large creepages is realised by weighting the results of FASTSIM with a heuristic falling function. The coefficients in the falling function rely on the experimental results. However, the experimental results measured on the twin-disc rig can only represent the steady-state properties of the friction. Therefore, the complex dynamic properties of the friction cannot be included in the current squeal model.

8.1.3 Wheel/rail squeal model

The wheel/rail squeal model considers the wheel/rail dynamics at the contact, including all the important DOF. Based on a feedback loop between the wheel/rail responses and contact forces, wheel/rail squeal has been predicted in both the time domain and the frequency domain.

The stability analysis in the frequency domain cannot include the non-linear effects in the friction. From comparisons with the time-domain results, it is shown that the stability analysis can effectively predict the possible unstable modes if the nonlinearities of friction around the steady-state creepages are limited. This occurs, for example, if there is only one significant steady-state creepage. If the creepage is near the transition between adhering and sliding, the stability analysis tends to over-estimate the likelihood of squeal.

The time-domain simulation can include the nonlinearities of friction and predict the squeal intensity as well as the possible unstable modes. However, the time-domain simulation is sensitive to the modal parameters in the wheel system, in particular, the modeshapes. This can lead to a shift of the dominant squeal frequency if the modeshapes of those flexible modes are slightly changed under some conditions. These effects of changing modal parameters have not been validated in experiments.

8.1.4 Vehicle dynamics and wheel/rail squeal

The intimate relations between the curving behaviour and the occurrence of squeal are clear. In this thesis attention has been given to connecting the theoretical wheel/rail squeal model with a steady-state curving calculation with necessary DOF. According to the simulations in the case study and the application, the most important parameters of curving behaviour are the steady-state creepages and spin.

For a conventional bogied vehicle in a curve with a small curve radius, the wheels in the leading wheelset normally have large lateral creepages, making the two wheels prone to squeal. However, the outer wheel is in contact in the flange region and may not squeal due to the presence of large spin and the large contact angle at the flange.

The wheels in the trailing wheelset normally have very small lateral creepages but may have large longitudinal creepages if the curve is very sharp. The large longitudinal creepages may lead to the unstable vibration of the wheels in the longitudinal direction, which may in some circumstances be audible as squeal.

Besides the steady-state creepages, the wheel/rail contact position is also important. Therefore, for a particular vehicle, some parameters of the curving conditions, i.e. curve radius, vehicle speed, wheel/rail profiles and Coulomb friction coefficient, can determine the steady-state creepages and wheel/rail contact positions, and consequently, the occurrence of squeal. If the suspensions of the vehicle can be changed to decrease the lateral creepages at the leading wheelset, this can also lessen the occurrence of squeal on curves. However, this has not been investigated here.

8.1.5 Curve squeal control

Two conventional squeal control methods are discussed in this thesis. The effects of the friction modification have been realised on the twin-disc rig by lubricating the contact surfaces. According to the squeal mechanism assumed, the friction modification decreases the negative damping effect of falling friction in the sliding region, while the wheel damping treatment increases the structural damping of the flexible wheel modes to overcome the negative damping effect of falling friction. Hence, using either control method, it is possible to stabilise the wheel vibration and control the squeal. Under some conditions, these two methods should be combined together to successfully control the curve squeal.

Besides these two conventional methods, some sensitive parameters in the wheel/rail squeal model and steady-state curving may be controllable. The effectiveness and engineering feasibility of using these parameters have not been discussed in this thesis.

8.2 Suggestions for further work

8.2.1 Wheel/rail squeal experiments

The current twin-disc rig can provide useful information about the relationship between the friction and the squeal noise. Based on the measurement results on the twin-disc rig, the squeal model in this thesis has been partly validated. However, more experiments can be carried out on the current rig to investigate wheel/rail squeal. Additionally, some important assumptions related to the mechanism of squeal, i.e. stick-slip motion and velocity-dependent friction forces, still require more evidence to verify the model. New findings from the experimental results can help understand the squeal phenomenon and therefore improve the wheel/rail squeal model.

Experiments on the damping control should be carried out. This requires good damping materials and an appropriate method for attaching the damping material. In the squeal model, the squeal prediction is particularly sensitive to some modal parameters of the discs, i.e. modeshape and modal damping ratio. This could be investigated using more wheel and rail discs with different modal properties. The effects of large spin and a lateral creepage together with a longitudinal one could also be studied on a revised twin-disc rig [39]. The friction curves shown in this thesis were measured under one rolling speed. As the saturation region in the friction curve is related to the rolling speed, the friction curves should also be measured under different rolling speeds.

Further experimental investigation is required related to the mechanism of wheel/rail squeal and velocity-dependent friction forces. To implement this investigation, some necessary improvements are required on the current twin-disc rig. In the current rig, the lateral friction force and vibration at the contact can only be measured at two instantaneous times during each revolution of the rail disc. Since the stick-slip motion should be observed in a continuous period, the strain gauges and the accelerometers should ideally be fixed at the contact position, not rotate with the rail and wheel discs, but this is not practical. A better method for force measurement is therefore needed. The acceleration of the squealing wheel disc at the contact position could be measured by a laser vibrometer. With these improvements on the twin-disc rig, measurements of the velocity-dependent friction forces may be possible.

With these new experimental results, the current squeal model can be further validated.

8.2.2 Wheel/rail squeal model

In the current wheel/rail squeal model, some components have been simplified or even omitted. For example, the tangential contact springs are not included in the time-domain model; the vertical contact spring is simplified to be a linear one; the cross-mobilities of the track are ignored in the time-domain simulations. These components may play important roles, so that they should be considered and implemented in the future. Since the current model simulates squeal under a steady-state curving behaviour, it could be extended to treat unsteady curving conditions. Two-point wheel/rail contact may also be important at the wheel flange.

8.2.3 Vehicle dynamics

The vehicle dynamic package could be improved to calculate transient curving behaviour. To reach this purpose, extra DOF are required in the vehicle dynamics model.

The effects of two-point contacts in the flange region could be considered in the new vehicle model. It would be valuable to use the model to study systematically the influence of changing bogie parameters or wheel/rail profiles on the occurrence of curve squeal.

APPENDIX A. REVIEW ON THE WHEEL/RAIL ROLLING CONTACT

A.1 Hertz contact

The widely adopted formulae of wheel/rail rolling contact are based on the classic Hertzian contact theory, which was published by Heinrich Hertz in 1881 [33] and translated into English in 1896 [34]. His research, originating from the contact problem of two optical lens, showed that an ellipsoidal distribution of contact pressure would produce elastic displacements in the two contact bodies. In the Hertz contact, as shown in Figure A-1, the semi-axes of the contact ellipse a, b and the distribution of normal contact stress $p(x,y)$ are determined by the normal load and the principal curvatures (the maximum and minimum curvatures in all possible planes including the normal vector) of the two contacting bodies. Due to the importance of Hertz theory in rolling contact mechanics, the theory is restated in Appendix B.

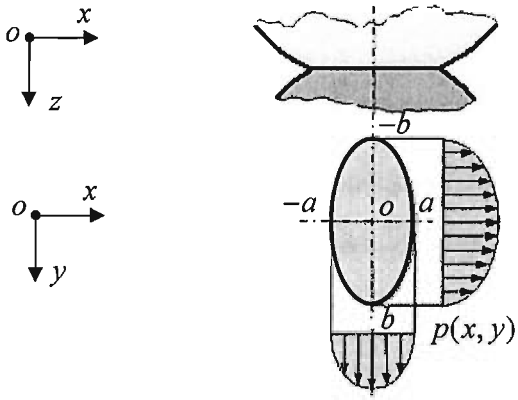

Figure A-1 Schematic diagram of the Hertzian contact.

The Hertz theory is restricted to frictionless surfaces and is based on a half-space assumption (infinite elastic body bounded by the contact surfaces). The wheel and rail contact is normally considered as a good example of Hertz contact. Nevertheless, the rolling action of the driving wheels under traction will produce adhering forces in the contact area, which drive the vehicle forward. Both driven and undriven wheels may be partly, or even wholly, sliding on the rail to provide steering or braking forces. Hence, the normal and tangential forces in the contact area are coupled to each other, making the stress distributions more complex.

A.2 Carter's two-dimensional theory

The first theoretical wheel/rail contact model based on the Hertz theory is Carter's two-dimensional model from 1926 [67]. He assumed that the contact area can be approximated in shape by a uniform strip transverse to the rail, which will be flattened with use. This is close to the case of a Hertzian contact ellipse with axes $b >> a$, as shown in Figure A-2(a). The distribution of normal stress near the origin O is the same as that of a cylinder rolling on a flat plane. Ignoring the boundary effects in the y-direction, the normal stress distribution is $p(x)$ and the corresponding traction is $q(x)$. Since only longitudinal creepage γ_1 is considered, it is a two-dimensional problem.

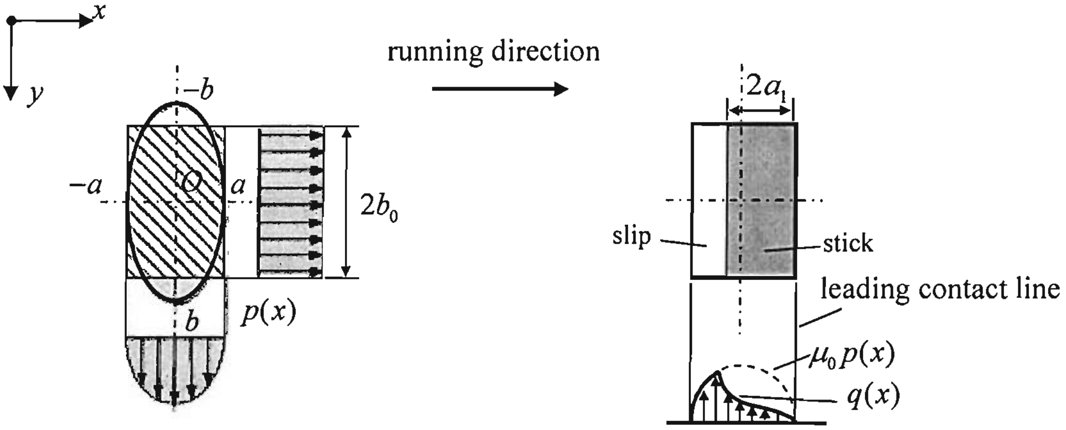

(a) (b)

Figure A-2 Distribution of the normal and tangential stresses of the Carter's two-dimensional model: (a) normal stress distribution, (b) stick and slip zone in the contact area and corresponding distribution of tangential stresses.

In the rolling contact problem, a 'stick' region may exist in the contact area, where two incident particles in the corresponding contact surfaces will move together. The resultant tangential elastic stress at such a 'stick' position must not exceed its limiting value

$$|q(x,y)| \le \mu_0 p(x,y), \tag{A.1}$$

where $p(x,y)$ is the normal stress, and μ_0 is the Coulomb friction coefficient.

On the other hand, the 'slip' region in the contact area has a resultant tangential stress with the limiting value

$$|q(x,y)| = \mu_0 p(x,y). \tag{A.2}$$

Carter expected the contact area to be divided into zones of 'slip' and 'stick', as shown in Figure A-2(b). In the stick zone, the tangential stress q is less than the limiting traction $\mu_0 p$ given by the dashed curve. In the slip zone, the tangential stress q is determined by the corresponding limiting value $\mu_0 p$. Carter pointed out that the stick zone should start from the leading edge of the contact area and the possible slip zone should be at the trailing edge. He gave an equation to express the boundary of the stick zone a_1 in terms of the creepage γ_1. Consequently the tangential force Q_1 can be calculated with respect to the creepage γ_1.

However, three-dimensional bodies in rolling contact, e.g. the wheel and rail, may be simultaneously subjected to the lateral creepage γ_2, and spin creepage γ_6 as well as the longitudinal one γ_1. This should be solved using three-dimensional rolling contact theory.

A.3 Johnson's three-dimensional theory without spin – V-J formula

Johnson analysed the three-dimensional rolling contact problem, with the size of contact area and the distribution of normal stress based on the Hertzian theory. The difficulty in the three-dimensional model for partial slip is how to determine the 'stick' and 'slip' zones in the contact ellipse. Johnson [68] assumed that the stick zone was an ellipse touching the contact ellipse at the leading point $(a,0)$, with a shape similar to that of the contact ellipse, as shown in Figure A-3. However, this assumption of an elliptical stick region is incorrect. Haines and Ollerton in 1963 [69] showed that the stick region to be roughly 'lemon' shaped via the observation of the contact ellipse between photo-elastic models. One edge coincides with the leading edge of the contact ellipse and the boundary with the slip zone is a reflection of the leading edge, as shown in Figure A-3.

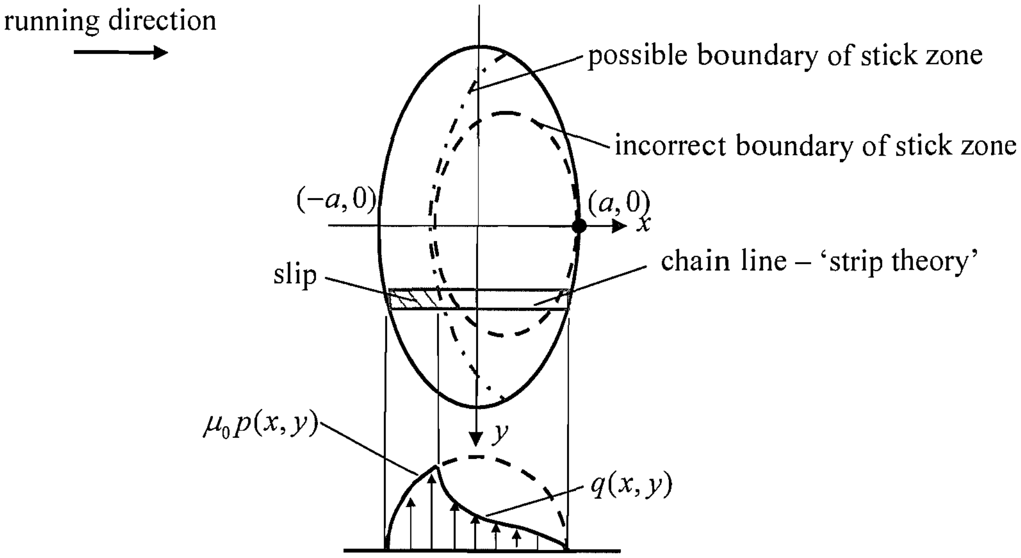

Figure A-3 Boundary of the stick zone in the three-dimensional contact problem.

Although Johnson's assumption of the stick boundary is not practical, it has the merit of giving simple expressions for the relationship between the traction and creep. The analytical formula related to this theory, provided by Vermeulen and Johnson in 1964 [70], is still valuable. This V-J formula gives a non-linear creep-force relationship without spin effect for partial slip, with saturation of the friction coefficient for total slip in the contact area

$$\begin{aligned} Q &= -\mu_0 P\left[1-\left(1-\frac{\xi}{3}\right)^3\right] \\ &= -\mu_0 P\left[\xi-\frac{\xi^2}{3}+\frac{\xi^3}{27}\right], \qquad \xi \le 3 \end{aligned} \tag{A.3}$$

and

$$Q = -\mu_0 P, \qquad \xi > 3 \tag{A.4}$$

where the reduced creepage is

$$\xi = \left(\xi_1^2 + \xi_2^2\right)^{1/2}, \tag{A.5}$$

where

$$\xi_1 = \frac{abGC_{11}}{\mu_0 P}\gamma_1, \quad \xi_2 = \frac{abGC_{22}}{\mu_0 P}\gamma_2. \tag{A.6}$$

The two contacting bodies should have quasi-identical material with shear modulus

$$G_1 = G_2 = G. \tag{A.7}$$

C_{ij} are creep coefficients, as given by Kalker [71]. This is a widely accepted approach.

If the creepage is very small (before saturation), using a Taylor series expansion at the point $\gamma_1 = \gamma_2 = 0$ and keeping only the first derivatives, the linear tangential forces of Johnson, Q_1^J and Q_2^J, can be obtained from Eq.(A.3):

$$Q_1^J = -\mu_0 P\xi_1 = -abGC_{11}\gamma_1, \tag{A.8}$$

and

$$Q_2^J = -\mu_0 P\xi_2 = -abGC_{22}\gamma_2. \tag{A.9}$$

Johnson also studied the spin effect [72] and found that pure spin will contribute a resultant lateral tangential force as well as a moment about the normal.

A.4 Kalker's three-dimensional exact theory

Kalker's full numerical solution of the general three-dimensional case was given in his thesis of 1967 [73]. This method can accept any combination of creepage and spin, from small values up to full sliding, for a wide range of contact ellipses. The limitation of stick boundary in Johnson's model is avoided in Kalker's model by using a 'strip theory' originally proposed by Haines and Ollerton in 1963 [69]. In their method, the contact area is divided into thin strips parallel to the rolling direction x-axis, as shown in

Figure A-3. Kalker combined the separate conditions of stick and slip into a single condition which is satisfied approximately throughout the contact area. The computational method itself determines the regions of stick and slip within the contact area. Detailed information about his exact theory, with a state-of-the-art review of rolling contact mechanics up to the end of 1980s, can be found in his book of 1990 [71].

For small creepages and spin before saturation ('stick' within the whole contact area), Kalker provided a linear theory, giving linear relationships between the linear tangential forces (and the spin moment) and all possible creepages (and spin):

$$Q_1^L = -GabC_{11}\gamma_1, \qquad \text{(A.10)}$$

$$Q_2^L = -\left(GabC_{22}\gamma_2 + G(ab)^{3/2}C_{23}\gamma_6\right), \qquad \text{(A.11)}$$

and

$$M^L = -\left(G(ab)^{3/2}C_{32}\gamma_2 + G(ab)^2 C_{33}\gamma_6\right),\ C_{32} = -C_{23}. \qquad \text{(A.12)}$$

where the creep coefficients C_{ij} are obtained from his exact theory. In his thesis [73] these creep coefficients were tabulated and these have been widely adopted in applications related with wheel/rail contact. If the spin effect is ignored in Kalker's linear theory, the longitudinal and lateral tangential forces given in Eq.(A.10) and Eq.(A.11) are the same as those of Johnson, as given in Eq.(A.8) and Eq.(A.9).

For general cases, Kalker produced two programs, called DUVOROL (in 1978) and CONTACT (in 1982). Both are based on his three-dimensional exact theory. DUVOROL can solve the problem of steady-state rolling in a Hertz contact. Its successor, CONTACT, can also calculate non-Hertzian contact areas and transient problems [71].

A.5 Kalker's simplified theory – FASTSIM algorithm

Kalker's exact theory maintains the elastic relationship between stresses and strains in the elastic half space, which means the strain at any point in the contact surfaces depends upon the distribution of stress throughout the whole contact. Hence, the computational time of programs based on the complete theory is unacceptable for some applications involving iterative calculation of rolling contact. Subsequently Kalker offered an approximate solution for faster computation, the FASTSIM algorithm [36], which is based on the 'simplified theory' introduced by Kalker in 1973 [37].

Compared with the exact theory, the simplified theory assumes a local surface deformation corresponding to a local force and their relationship can be represented by a linear spring with flexibility L. A quantitative agreement with the exact theory of rolling contact is possible by the proper choice of the flexibility parameter L, which depends on the creep coefficient C_{ij} of the linear theory and the creepages and spin. The accuracy of the simplified theory is at least 85% according to the introduction in Kalker's book [71].

In the FASTSIM algorithm, the elliptical contact area is divided into independent longitudinal parallel strips. Each strip is divided into the same number of elements. The traction is then calculated in each element, beginning from the one at the leading edge, from element to element. More details of FASTSIM algorithm are given in Appendix C.

A.6 Shen-Hedrick-Elkins formulation for small spin

Kalker's exact theory and simplified theory are appropriate for numerical calculation of rolling contact. In some circumstances, however, an analytical rolling contact model is necessary. If the creepages and spin are small (before saturation), Kalker's linear formula, as given in Eq.(A.10) to Eq.(A.12), is sufficient. If the creepages are in the saturated zone but no spin is involved, the non-linear V-J formula, as given in Eq.(A.3), can be adopted. Alternatively, if the spin exists but its value is small, as applies for the general case of wheel and rail contacting on the tread, the formulation developed by Shen, Hedrick and Elkins [38] can be applied. The Shen-Hedrick-Elkins formula is improved from the V-J formula by including the spin effect. The process is introduced as follows.

If the tangential forces Q_1^J, Q_2^J given in Johnson's linear formula were equal to the corresponding tangential forces Q_1^L, Q_2^L given in Kalker's linear formula, new reduced longitudinal and lateral creepages s_1, s_2 can be obtained. The new longitudinal one s_1 is the same as that of Johnson ξ_1:

$$\xi_1 = s_1 = \frac{abGC_{11}}{\mu_0 P}\gamma_1, \tag{A.13}$$

while the new lateral one s_2 includes an additional spin effect compared with that of Johnson ξ_2:

$$\xi_2 \neq s_2 = \frac{abGC_{22}}{\mu_0 P}\gamma_2 + \frac{(ab)^{3/2}GC_{23}}{\mu_0 P}\gamma_6 . \tag{A.14}$$

Substituting the new resultant reduced creepage $s = (s_1^2 + s_2^2)^{1/2}$ for ξ, Eq.(A.3) can be rewritten to be

$$Q^S = -\mu_0 P\left[s - \frac{s^2}{3} + \frac{s^3}{27}\right], \quad s \le 3 \tag{A.15}$$

The new resultant force Q^S includes the effect of saturation while Kalker's linear resultant force $Q^L = \left((Q_1^L)^2 + (Q_2^L)^2\right)^{1/2}$ does not, so that a discount ratio can be obtained by comparing them:

$$\varepsilon = \left|\frac{Q^S}{Q^L}\right| . \tag{A.16}$$

Then the saturated tangential forces and spin moment can be obtained by discounting Kalker's linear ones

$$Q_1^S = \varepsilon Q_1^L , \tag{A.17}$$

$$Q_2^S = \varepsilon Q_2^L, \qquad \text{(A.18)}$$

and

$$M^S = \varepsilon M^L. \qquad \text{(A.19)}$$

After comparing the creep-force line from V-J and Shen-Hedrick-Elkins for pure creepages (without spin), Kalker pointed out that *the latter improves the original V-J line, to the extent that it can be taken as the standard for pure creepage* [71]. By comparing with CONTACT for the case including spin, he concluded that *Shen-Hedrick-Elkins may be used in non-flanging railway theory as a substitute for Hertzian simplified theory* [71].

A.7 Conclusions

The main rolling contact theories for wheel/rail applications have been reviewed. Most of these theories are based on the assumption of Hertz contact, with an elliptic contact area and an ellipsoidal distribution of normal stress. For general applications of wheel/rail contact, three-dimensional rolling contact theory is required. In the cases considering small creepages and spin, Kalker's linear theory is important, which is also the root of many other analyses, i.e. the simplified theory and Shen-Hedrick-Elkins formula. If spin exists but is not very large, i.e. non-flange wheel/rail contact, Shen-Hedrick-Elkins' analytical formula, improved from Vermeulen and Johnson's no-spin theory, can be used, which covers saturation at large creepages as well as the linear zone for small creepages and spin. For a general case, especially with large spin and non-Hertzian contact, the program CONTACT based on Kalker's exact theory can be applied. If computation time is a concern, another program, FASTSIM, based on Kalker's simplified theory can provide good computation speed with small cost in terms of accuracy.

APPENDIX B. HERTZIAN CONTACT THEORY

When two non-conforming solids are brought into contact they touch initially at a single point (or along a line), as shown in Figure B-1. Under the action of the lightest load, they deform in the vicinity of their point of first contact. Consequently, they touch over an area, which is finite and small compared with the dimensions of the two bodies. In this contact area, there are relations between the normal contact force, topographic shape of the contact area, and the magnitude and distribution of normal stress, which are formulated by Hertzian contact theory. This theory is based on the linearly elastic relation between the stress and small deformation of contact bodies.

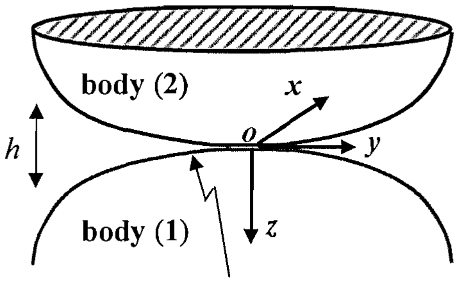

Figure B-1 Schematic diagram of the non-conforming Hertzian contact before deformation.

B.1 Topographic shape of the contact area

In the system frame $oxyz$, the origin is chosen at the initial contact point o, and the z-axis is along the normal vector of contact plane and pointing into contact body (1). The contact surfaces are represented in their local coordinates ox_iy_iz, (z-axis chosen according to that of the system coordinates) by

$$z_i = f_i(x_i, y_i) \quad i = 1,2 . \tag{B.1}$$

If each contact surface is topographically smooth on both micro and macro scales, and the surface function is continuous up to its pth derivative in the contact area, the contact surface in Eq.(B.1) can be expressed by its Taylor series at the point $o(0,0,0)$, which gives

$$
\begin{aligned}
z_i &\approx \sum_{n+m=0}^{p} \frac{1}{(n+m)!} \frac{\partial^{n+m} f_i(x_i, y_i)}{\partial x_i^{\,n} \partial y_i^{\,m}} x_i^{\,n} y_i^{\,m} \\
&= f_i(0,0) \\
&+ \left(\frac{\partial f_i}{\partial x_i} x_i + \frac{\partial f_i}{\partial y_i} y_i \right) \\
&+ \frac{1}{2} \left(\frac{\partial^2 f_i}{\partial x_i^{\,2}} x_i^{\,2} + \frac{\partial^2 f_i}{\partial x_i \partial y_i} x_i y_i + \frac{\partial^2 f_i}{\partial y_i^{\,2}} y_i^{\,2} \right) \\
&+ \cdots \\
&+ \frac{1}{p!} \sum_{m=0}^{p} \frac{\partial^p f_i}{\partial x_i^{\,p-m} \partial y_i^{\,m}} x_i^{\,p-m} y_i^{\,m}
\end{aligned}
\quad . \qquad \text{(B.2)}
$$

Due to the flat tangent plane at the origin, the zero and first derivative terms in Eq.(B.2) are equal to zero:

$$
f_i(0,0) = \left.\frac{\partial f_i}{\partial x}\right|_{0,0} = \left.\frac{\partial f_i}{\partial y}\right|_{0,0} = 0 \, . \qquad \text{(B.3)}
$$

The higher order terms ($p > 2$) can also be neglected, since x_i and y_i in the contact area are very small. Thus, Eq.(B.2) can be reduced to

$$
z_i \approx \frac{1}{2} \left(\frac{\partial^2 f_i}{\partial x_i^{\,2}} x_i^{\,2} + \frac{\partial^2 f_i}{\partial x_i \partial y_i} x_i y_i + \frac{\partial^2 f_i}{\partial y_i^{\,2}} y_i^{\,2} \right) . \qquad \text{(B.4)}
$$

If choosing appropriate coordinates (including x-axis and y-axis in the principal planes), the second term in Eq.(B.4) can be eliminated to give

$$
z_i = \frac{1}{2} \left(\frac{\partial^2 f_i}{\partial x_i^{\,2}} x_i^{\,2} + \frac{\partial^2 f_i}{\partial y_i^{\,2}} y_i^{\,2} \right) . \qquad \text{(B.5)}
$$

The extent of a curve is normally represented by its radius of curvature, which by definition is the inverse of the curvature. Eliminating the first derivative at the contact point ***o*** gives the following relations:

$$
\frac{1}{R_i'} \equiv \left| \frac{\dfrac{\partial^2 f_i}{\partial x_i^{\,2}}}{\left(1 + \dfrac{\partial f_i}{\partial x_i} \right)^{3/2}} \right| = \left| \frac{\partial^2 f_i}{\partial x_i^{\,2}} \right| , \qquad \text{(B.6)}
$$

and

$$\frac{1}{R_i''} \equiv \left| \frac{\dfrac{\partial^2 f_i}{\partial y_i^{\,2}}}{\left(1+\dfrac{\partial f_i}{\partial y_i}\right)^{3/2}} \right| = \left| \frac{\partial^2 f_i}{\partial y_i^{\,2}} \right|. \tag{B.7}$$

where R_i' and R_i'' are principal radii of curvature, corresponding to the minimum and maximum curvatures at the contact point. The radius of curvature is assumed positive. Thus, for contact surface (1),

$$\frac{\partial^2 f_1}{\partial x_1^{\,2}} = \frac{1}{R_1'},\ \frac{\partial^2 f_1}{\partial y_1^{\,2}} = \frac{1}{R_1''},\ \text{and}\ \frac{1}{R_1'} \le \frac{1}{R_1''}, \tag{B.8}$$

and for contact surface (2), since $f_2 \le 0$,

$$\frac{\partial^2 f_2}{\partial x_2^{\,2}} = -\frac{1}{R_2'},\ \frac{\partial^2 f_2}{\partial y_2^{\,2}} = -\frac{1}{R_2''},\ \text{and}\ \frac{1}{R_2'} \le \frac{1}{R_2''}. \tag{B.9}$$

Substitution of Eq.(B.8) and Eq.(B.9) into Eq.(B.5) gives

$$z_1 = \frac{x_1^{\,2}}{2R_1'} + \frac{y_1^{\,2}}{2R_1''}, \tag{B.10}$$

and

$$z_2 = -\left(\frac{x_2^{\,2}}{2R_2'} + \frac{y_2^{\,2}}{2R_2''} \right). \tag{B.11}$$

The separation between the two surfaces (before deformation) can be written as

$$\begin{aligned} h &= z_1 - z_2 \\ &= \left(\frac{x_1^{\,2}}{2R_1'} + \frac{y_1^{\,2}}{2R_1''} \right) + \left(\frac{x_2^{\,2}}{2R_2'} + \frac{y_2^{\,2}}{2R_2''} \right). \end{aligned} \tag{B.12}$$

This separation between two surfaces can be expressed in the system frame ***oxyz***:

$$h = Ax^2 + By^2 + Cxy. \tag{B.13}$$

By a suitable choice of axes, the coefficient C can be eliminated to give

$$h = Ax^2 + By^2 = \frac{1}{2R'}x^2 + \frac{1}{2R''}y^2, \tag{B.14}$$

where A and B are positive constants to ensure the separation is a positive value under the condition of non-conforming contact.

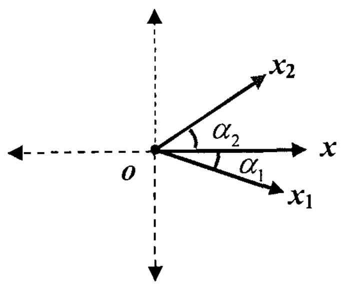

Figure B-2 Relationship between the system frame and local frames of contacting bodies [74].

The relationship between the system frame and the local frames can be assumed, as shown in Figure B-2 [74]. The angles between the x_i-axis of the local frame of body (i) and the x-axis of the system frame are $\alpha_1 \leq 0$, $\alpha_2 \geq 0$, and $\theta = \alpha_2 - \alpha_1 \geq 0$. Hence, the following relations exist [74]:

$$A + B = \frac{1}{2}\left(\frac{1}{R_1'} + \frac{1}{R_1''} + \frac{1}{R_2'} + \frac{1}{R_2''}\right), \tag{B.15}$$

and

$$B - A = \frac{1}{2}\left(\left(\frac{1}{R_1''} - \frac{1}{R_1'}\right)^2 + \left(\frac{1}{R_2''} - \frac{1}{R_2'}\right)^2 + 2\left(\frac{1}{R_1''} - \frac{1}{R_1'}\right)\left(\frac{1}{R_2''} - \frac{1}{R_2'}\right)\cos(2\theta)\right)^{1/2} . \tag{B.16}$$

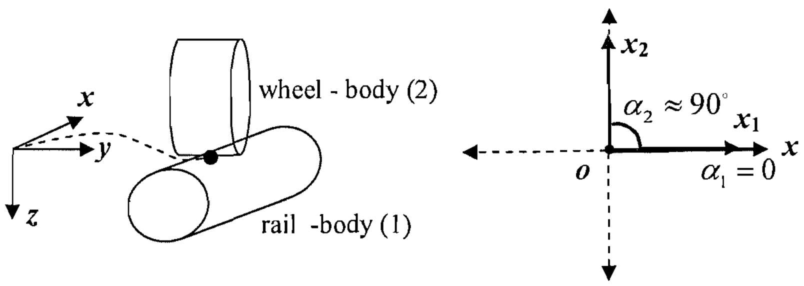

Figure B-3 Wheel/rail contact.

For a case of wheel/rail contact, the rail is contacting body (1) and wheel is contacting body (2), as shown in Figure B-3. The x-axis of the local frame is assumed to be in a plane where the minimum (or maximum) curvature of the contact surface exists. Hence, the x_1 -axis of the rail frame coincides with the x-axis, with $\alpha_1 = 0$, $R_1' = \infty$ and $R_1'' = R_r > 0$. The x_2-axis of the wheel frame is almost coincident with to the y-axis as the yaw angle is normally very small, less than 2°, with $\alpha_2 = 90^\circ$, $R_2' = R_w$ and $R_2'' = r_0$ (the nominal wheel radius). The angle between the x_2 -axis and x_1 -axis is then $\theta = \alpha_2 - \alpha_1 = 90^\circ$. Substitution of these parameters into Eq.(B.15) and Eq.(B.16) gives

$$A + B = \frac{1}{2}\left(\frac{1}{R_r} + \frac{1}{R_w} + \frac{1}{r_0}\right), \tag{B.17}$$

and

$$B - A = \frac{1}{2}\left|\frac{1}{R_r} + \frac{1}{R_w} - \frac{1}{r_0}\right|. \tag{.B.18}$$

The wheel may have a concave profile especially in the flange zone due to wear, which results in the curve centre being outside the contacting body and the radius being negative $R_2' < 0$.

B.2 Assumptions in Hertzian elasticity

Non-conforming elastic bodies in contact with sufficiently small deformation can be treated using linear elasticity theory. The contact stresses are highly concentrated close to the contact area and decrease rapidly in intensity with distance from the point of contact, so that the region of practical interest lies close to the contact interface. Thus, if the dimensions of the bodies are large compared with the dimensions of the contact area, the stresses in this region are not critically dependent upon the shape of the bodies distant from the contact area, or upon the precise way in which they are supported [35]. The stresses may be calculated to good approximation by considering each body as a semi-infinite elastic solid bounded by a plane surface: i.e. an elastic half-space. Denoting the significant dimension of the contact area by a, the significant relative radius of curvature by R, and the significant dimensions of the bodies by l, the assumptions of Hertz theory can be summarised as follows [35]:

1. The surfaces are continuous and non-conforming - *ellipse contact region*;
2. The strains are small: $a << R$ - *linear elasticity theory applicable*;
3. Each solid body can be considered as an elastic half-space: $a << R$ and $a << l$ - *no influence from the body shape*;
4. The surfaces are frictionless: $q_x = q_y = 0$ - *only normal stress in the contact region.*

B.3 Hertz elastic mechanics

The shape of the contact area is elliptical in shape, having semi-axes a and b:

$$\left(\frac{x}{a}\right)^2 + \left(\frac{y}{b}\right)^2 - 1 = 0. \tag{B.19}$$

If $A < B$, as in the case discussed in Section B.1, the major semi-axis is on the x-axis, giving $a > b$. From the assumption of Hertz, the normal pressure distribution over this elliptical contact region is a semi-ellipsoid:

$$p = p_0 \left\{1 - \left(\frac{x}{a}\right)^2 - \left(\frac{y}{b}\right)^2\right\}^{1/2}, \tag{B.20}$$

where the maximum normal pressure p_0 will be found in the centre of contact ellipse: $x = y = 0$.

According to the elastic stress-strain relationship, via elliptical integration in the contact area, the surface displacement, pressure distribution and shape of the contact ellipse within the loaded region can be represented in terms of A, B and the normal force P. The following results, from Eq.(B.21) to Eq.(B.43), are given by Johnson [35] (pp.65

and pp.95-99). Due to the semi-ellipsoid pressure in Eq.(B.20), the distribution of surface displacement $\bar{u}_z$ in the contact area is

$$\bar{u}_z = \frac{L - Mx^2 - Ny^2}{\pi E^*}, \tag{B.21}$$

where

$$M = \frac{\pi p_0 ab}{2} \int_0^\infty \frac{dw}{\left\{(a^2+w)^3(b^2+w)w\right\}^{1/2}} = \frac{\pi p_0 b}{e^2 a^2} \{\mathbf{K}(e) - \mathbf{E}(e)\}, \tag{B.22}$$

$$N = \frac{\pi p_0 ab}{2} \int_0^\infty \frac{dw}{\left\{(a^2+w)(b^2+w)^3 w\right\}^{1/2}} = \frac{\pi p_0 b}{e^2 a^2} \left\{(a/b)^2 \mathbf{E}(e) - \mathbf{K}(e)\right\}, \tag{B.23}$$

$$L = \frac{\pi p_0 ab}{2} \int_0^\infty \frac{dw}{\left\{(a^2+w)(b^2+w)w\right\}^{1/2}} = \pi p_0 b \mathbf{K}(e), \tag{B.24}$$

$\mathbf{K}(e), \mathbf{E}(e)$ are complete elliptical integrals of argument

$$e = (1 - (b/a)^2)^{1/2}, \quad a > b, \tag{B.25}$$

and the composite elastic modulus E^* is determined by the elastic modulus E_i and Poisson's ratio ν_i of each body i, $i = 1,2$:

$$\frac{1}{E^*} = \frac{1-\nu_1^{\,2}}{E_1} + \frac{1-\nu_2^{\,2}}{E_2}. \tag{B.26}$$

The total load on the contact patch is

$$P = \frac{2}{3} p_0 \pi ab. \tag{B.27}$$

Hence, the maximum pressure is given by

$$p_0 = \frac{3P}{2\pi ab}. \tag{B.28}$$

The separation is given by Eq.(B.14), $h = Ax^2 + By^2$. Within the contact patch, the surface elastic displacement for both bodies after deformation is

$$\begin{aligned}\bar{u}_z &= \delta - h \\ &= \delta - Ax^2 - By^2\end{aligned}, \tag{B.29}$$

where δ is the compression displacement of both bodies.

To find the shape and size of the ellipse of contact patch, combining Eq.(B.29) and Eq.(B.21) gives

$$\frac{B}{A} = \frac{N}{M} = \frac{(a/b)^2 \mathbf{E}(e) - \mathbf{K}(e)}{\mathbf{K}(e) - \mathbf{E}(e)}. \tag{B.30}$$

Writing the equivalent relative curvature radius R_e

$$\begin{aligned}\frac{1}{2R_e} &= \frac{1}{2}\left(\frac{1}{R'R''}\right)^{1/2} = (AB)^{1/2} \\ &= \frac{MN}{(\pi E^*)^2} \\ &= \frac{p_0}{E^*}\frac{b}{a^2e^2}\left[\left\{(a/b)^2\mathbf{E}(e) - \mathbf{K}(e)\right\}\left\{\mathbf{K}(e) - \mathbf{E}(e)\right\}\right]^{1/2}\end{aligned} \tag{B.31}$$

and

$$\delta = \frac{L}{\pi E^*} = \frac{p_0 b \mathbf{K}(e)}{E^*}. \tag{B.32}$$

From Eq.(B.30), the eccentricity of the contact ellipse (b/a) is independent of the load and depends only on the ratio of the relative curvatures B/A. The size of the ellipse of contact patch is related with Eq.(B.31).

Writing $c = (ab)^{1/2}$, substituting for p_0 from Eq.(B.28) into Eq.(B.31) to obtain

$$c = \left(\frac{3PR_e}{4E^*}\right)^{1/3} F_1(e), \tag{B.33}$$

where $F_1(e)$ is a function in terms of (b/a):

$$F_1(e) = \left(\frac{4}{\pi e^2}\right)^{1/3}\left(\left[\left\{(b/a)\mathbf{E}(e) - (b/a)^3\mathbf{K}(e)\right\}\left\{\mathbf{K}(e) - \mathbf{E}(e)\right\}\right]^{1/2}\right)^{1/3}. \tag{B.34}$$

Thus, the size of the contact ellipse is given by Eq.(B.33). The displacement between the contact bodies, as shown in Eq.(B.32), can also be expressed by the normal force P and a function in terms of (b/a):

$$\begin{aligned}\delta &= \frac{3P}{2\pi ab}\frac{b\mathbf{K}(e)}{E^*} \\ &= \frac{3P}{2\pi E^*}\left\{\frac{\mathbf{K}(e)}{(ab)^{1/2}}(b/a)^{1/2}\right\}\end{aligned} \tag{B.35}$$

Substituting for $(ab)^{1/2}$ from Eq.(B.33) into Eq.(B.35) gives

$$\begin{aligned}\delta &= \left(\frac{9P^2}{16R_e E^{*2}}\right)^{1/3}\left\{\frac{2}{\pi}\frac{\mathbf{K}(e)}{F_1(e)}(b/a)^{1/2}\right\} \\ &= \left(\frac{9P^2}{16R_e E^{*2}}\right)^{1/3} F_2(e)\end{aligned} \tag{B.36}$$

The maximum pressure in Eq.(B.28)

$$p_0 = \left(\frac{6PE^{*2}}{\pi^3 R_e^{\ 2}}\right)^{1/3}\{F_1(e)\}^{-2}. \tag{B.37}$$

The detailed results for contact area in terms of normal force and curvatures of contact bodies are quite complicated. For ease of numerical computation various authors, e.g. Brewe and Hamrock in 1977 [75], Greenwood in 1985 [76], have produced approximate algebraic expressions in terms of the ratio (A/B) to replace the elliptical integrals in Eq.(B.33), Eq.(B.36) and Eq.(B.37).

B.4 Routine for the calculation of wheel/rail Hertzian contact

A traditional routine for Hertzian contact calculation is provided here [74].

Eq.(B.21) gives

$$A+B = \frac{M+N}{\pi E^*} = \frac{\pi p_0 b}{e^2 a^2}\frac{\{\mathbf{K}(e)-\mathbf{E}(e)\}+\{(a/b)^2\mathbf{E}(e)-\mathbf{K}(e)\}}{\pi E^*} = \frac{3}{2}\frac{P}{e^2 a^3}\frac{((a/b)^2-1)\mathbf{E}(e)}{\pi E^*}. \tag{B.38}$$

Considering $e^2 = 1 - b^2/a^2$, Eq.(B.38) can be arranged to be

$$\begin{aligned} a^3 &= \left\{\frac{3}{2}\frac{P}{(A+B)2E^*}\right\}\left\{\frac{2((a/b)^2-1)\mathbf{E}(e)}{\pi e^2}\right\} \\ &= \left\{\frac{3}{2}\frac{P}{(A+B)2E^*}\right\}\left\{\frac{2((a/b)^2-1)b^2\mathbf{E}(e)}{\pi(1-(b/a)^2)a^2}\frac{a^2}{b^2}\right\} \\ &= \left\{\frac{3}{2}\frac{P}{(A+B)2E^*}\right\}\left\{\frac{2\mathbf{E}(e)}{\pi(1-e^2)}\right\} = \left\{\frac{3}{2}\frac{P}{(A+B)2E^*}\right\}m^3 \end{aligned} \tag{B.39}$$

where

$$m = \left\{\frac{2\mathbf{E}(e)}{\pi(1-e^2)}\right\}^{1/3}. \tag{B.40}$$

From the definition of e in Eq.(B.25),

$$b^3 = a^3(1-e^2)^{3/2} = \left\{\frac{3}{2}\frac{P}{\{2(A+B)\}E^*}\right\}n^3, \tag{B.41}$$

where

$$n = m(1-e^2)^{1/2} = \left\{\frac{2\mathbf{E}(e)}{\pi}\right\}^{1/3}(1-e^2)^{1/6}. \tag{B.42}$$

Hence, combining Eq.(B.39) and Eq.(B.41) gives following relation:

$$\left(\frac{a}{m}\right)^3 = \left(\frac{b}{n}\right)^3 = \left\{\frac{3}{2}\frac{P}{\{2(A+B)\}E^*}\right\}^3. \tag{B.43}$$

A and B can be represented by an intermediate angle η, (0, $\pi/2$), substituting Eq.(B.30) for (B/A), $\cos\eta$ is

$$\cos\eta = \frac{B-A}{A+B} = \frac{B/A-1}{B/A+1} = \frac{\left(1+\frac{1}{1-e^2}\right)\mathbf{E}(e) - 2\mathbf{K}(e)}{\left(\frac{1}{1-e^2}-1\right)\mathbf{E}(e)}. \tag{B.44}$$

If $(A+B)$ and $(B-A)$ have been determined by the principal curvatures of the contact surfaces, the intermediate angle η can be calculated. The relationship between the angle η and e is established in Eq.(B.44). Furthermore, m and n are determined by e, as given in Eq.(B.40) and Eq.(B.42), so that m and n can be found in terms of η. Hence, a, b can be calculated with Eq.(B.43), ($a > b$ with $A < B$). The best way in applications is to use tables of the related parameters to avoid evaluating the elliptical integrals. Table B-1 gives examples, which are also plotted in Figure B-4.

Table B-1 Parameters for Hertz contact calculation. [11]

b/a	e^2	E(e)	K(e)	m	n	η/(°)
0.01	1.00	1	5.9915	18.5336	0.1853	2.6
0.1	0.99	1.0160	3.6956	4.0141	0.4014	18.8
0.2	0.96	1.0505	3.0161	2.5570	0.5114	32.4
0.3	0.91	1.0965	2.6278	1.9795	0.5938	43.6
0.4	0.84	1.1507	2.3593	1.6605	0.6642	53.1
0.5	0.75	1.2111	2.1565	1.4556	0.7278	61.3
0.6	0.64	1.2763	1.9953	1.3117	0.7870	68.5
0.7	0.51	1.3456	1.8626	1.2047	0.8433	74.8
0.8	0.36	1.4181	1.7508	1.1215	0.8972	80.5
0.9	0.19	1.4933	1.6546	1.0548	0.9493	85.5
1.0	0.00	1.5708	1.5708	1.0000	1.0000	90.0

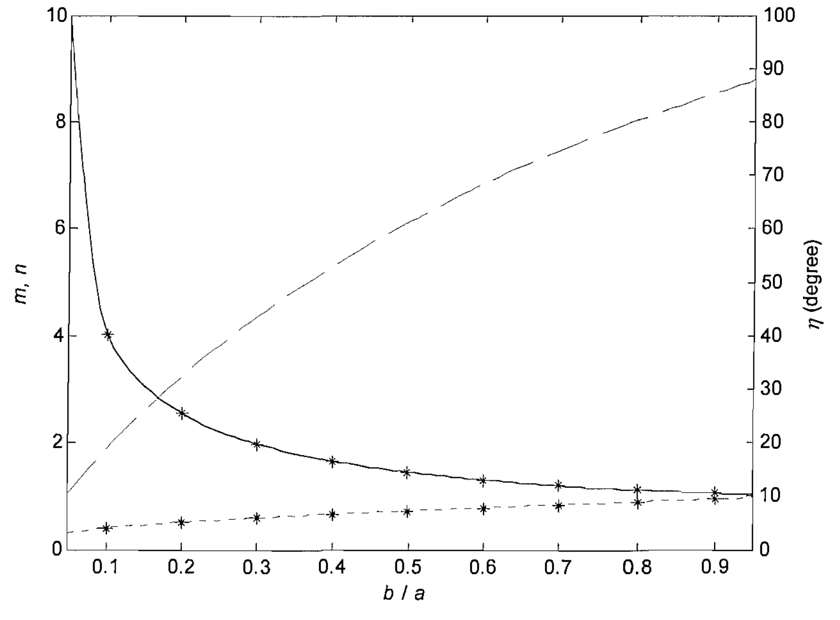

Figure B-4 Interpolation of the parameters for Hertz contact calculation: m, n and η with respect to b/a (in the range from 0.05 to 0.95), —— m, ----- n, — — η.

---

[11] The complete elliptical integrals are obtained from Table E1 in Kalker's book [71].

APPENDIX C. FASTSIM

Kalker's FASTSIM algorithm [36] is based on his 'simplified theory', which offers a quick approach to calculating the total tangential forces in rolling contact from given creepages and spin. In this appendix, the simplified theory and the FASTSIM algorithm are briefly restated. Then a falling friction coefficient for large creepage is introduced into FASTSIM, as used by Xie *et al* [51] for studying curve squeal noise.

C.1 Description

In the original publication of FASTSIM [36], it is limited to Hertz contact, which means the assumptions for Hertz contact should be satisfied, as given in Appendix B. Hence, the contact surface is elliptical, and the distribution of normal pressure is a semi-ellipsoid. It is assumed that this will not be influenced by the traction in the contact.

The elliptical contact area is divided into independent longitudinal parallel strips with equal width, as shown in Figure C-1. Each strip is divided equally into the same number of elements. According to the simplified theory, the traction in each strip is independent, while the tractions in the elements of one strip are dependent each other.

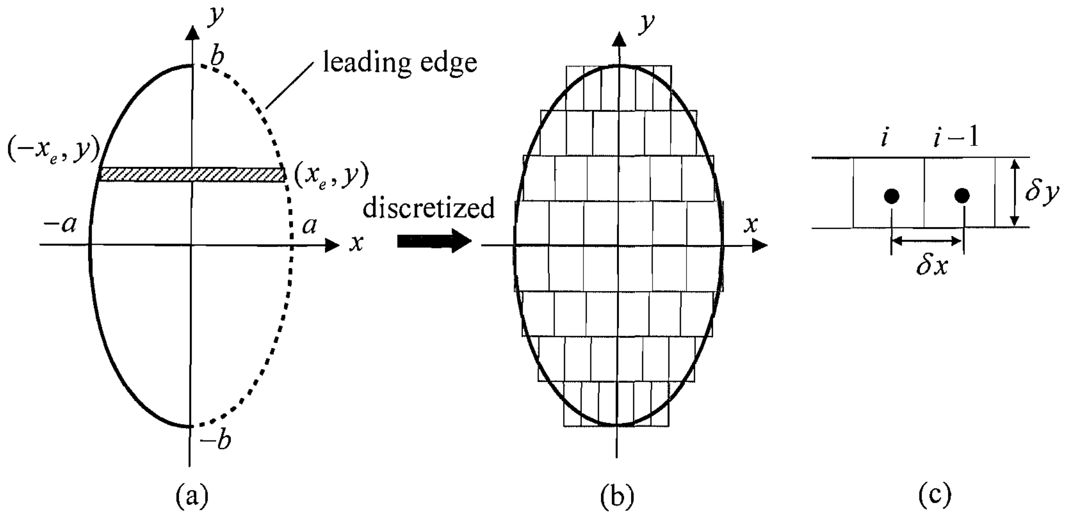

Figure C-1 (a) Contact ellipse, (b) strips and elements in the contact ellipse, and (c) two neighbouring elements in a strip.

The tractions in each strip can be calculated starting from the element at the leading edge. The leading boundary is under 'stick'. Since the simplified theory assumes a local elastic deformation corresponding to a local force, the traction of each element can be calculated by the averaged deformation of this element and a set of equivalent springs. The values of the equivalent springs are obtained from Kalker's linear theory for small creepages and spin.

If the resultant traction is found to be greater than the limiting value (which is the Coulomb force in terms of the local normal stress), this element will slip with the discounted traction. Integration of the traction in all elements gives the tangential forces and spin moment of the contact ellipse in terms of the creepages and spin.

Kalker [36] compared FASTSIM with Duvorol (based on Kalker's exact theory) and found that the error is usually less than 5%, rising to 10% for pure spin.

C.2 Algorithm

The FASTSIM algorithm is an approach to realise the simplified theory [71]. Kalker reduced the contact ellipse to a circular area with unit radius and made terms involved in the problem dimensionless. This can offer general and simple formulae but it is not necessary for the numerical calculation.

In Figure C-1(b), the elliptical contact area is evenly divided into N_y slices parallel to the x-axis with equal width

$$\delta y = 2b / N_y . \tag{C.1}$$

The sequence of slices is from $-b$ to b. Let the y-coordinate of the centreline of slice j be $y(j)$. In each slice, there are N_x elements with equal length δx

$$\delta x(j) = 2a\left[1-\left(y(j)/b\right)^2\right]^{1/2} / N_x . \tag{C.2}$$

Hence, the length of the elements varies from one slice to another due to the elliptical contact area. The element at the leading contact position is denoted $i=1$. Let the x-coordinate of the centre point in element (i,j) be $x(i,j)$, giving

$$\delta x(j) = x(i-1,j) - x(i,j) > 0\,. \tag{C.3}$$

The initial traction at the edge, denoted $q_k(0,j)$, should be zero

$$q_k(0,j) = 0, \quad k = 1,2\,. \tag{C.4}$$

The longitudinal ($k=1$) and lateral ($k=2$) surface (sliding) velocities of the leading element $(1,j)$ are

$$w_k(1,j) = g_k(1,j) + \frac{q_k(1,j)}{\delta x(j)/2}, \qquad k=1,2 \tag{C.5}$$

where the rigid components $g_{1,2}$ for an element (i,j) are represented by the creepages $\gamma_1, \gamma_2, \gamma_6$ and the flexibilities in terms of Kalker's coefficients: $L_1 = 8a/3GC_{11}$, $L_2 = 8a/3GC_{22}$ and $L_3 = \pi a^{3/2} b^{-1/2}/4GC_{23}$, giving

$$\begin{aligned} g_1(i,j) &= \frac{\gamma_1}{L_1} - \frac{\gamma_6}{L_3} y(j) \\ g_2(i,j) &= \frac{\gamma_2}{L_2} + \frac{\gamma_6}{L_3} x(i,j) \end{aligned}\,. \tag{C.6}$$

These surface velocities can be rearranged to give

$$q_k(1,j) = w_k(1,j)\delta x(j)/2 - g_k(1,j)\delta x(j)/2, \tag{C.7}$$

where g_k, q_k are all evaluated at the centre of element (i,j). For other elements (i,j), $i = 2,3 \ldots N_x$, the surface velocity is

$$w_k(i,j) = g_k(i,j) - \frac{q_k(i,j) - q_k(i-1,j)}{x(i,j) - x(i-1,j)}, \quad k=1,2 \tag{C.8}$$

which is arranged to be

$$q_k(i,j) = w_k(i,j)\delta x(j) - g_k(i,j)\delta x(j) + q_k(i-1,j)\,. \tag{C.9}$$

Assuming an element i in strip j is in the 'stick' zone, $w_k(i,j)=0$, the hypothetical traction $q_k^H(i,j)$ can be calculated through the integration from $q_k(i-1,j)$:

$$for\ i=1,\ q_k^H(1,j)=-g_k(1,j)\delta x(j)/2, \qquad k=1,2 \tag{C.10}$$

$$for\ i=2,3..,N_x,\ q_k^H(i,j)=q_k(i-1,j)-g_k(i,j)\delta x(j), \quad k=1,2. \tag{C.11}$$

For elements in the 'stick' zone, nevertheless the hypothetical resultant traction $q^H(i,j)$ should not be greater than the limiting Coulomb force at this element, which is

$$\left|q^H(i,j)\right|=\left[(q_1^H(i,j))^2+(q_2^H(i,j))^2\right]^{1/2}\le\mu_0 p^s(i,j), \tag{C.12}$$

where the normal pressure $p^s(i,j)$ is provided by the simplified theory

$$p^s(i,j)=\frac{2P}{\pi ab}\left(1-\frac{x^2(i,j)}{a^2}-\frac{y^2(j)}{b^2}\right). \tag{C.13}$$

If the condition in Eq.(C.12) is not satisfied, the element is actually under 'slip'. The traction should be discounted by a ratio ε:

$$\varepsilon(i,j)=\frac{\mu_0 p^s(i,j)}{\left|q^H(i,j)\right|}<1. \tag{C.14}$$

The discounted traction is

$$q_k(i,j)=q_k^H(i,j)\varepsilon(i,j). \qquad k=1,2 \tag{C.15}$$

As the element may 'stick' or 'slip', the term related with slip velocity $w_k(i,j)$ is not always zero. For the leading element $(1,j)$, from Eq.(C.5), Eq.(C.15) and Eq.(C.10),

$$w_k(1,j)=g_k(1,j)\left[1-\varepsilon(1,j)\right]. \qquad k=1,2 \tag{C.16}$$

For other elements (i,j), $i=2,3,...,N_x$, substituting $q_k^H(i,j)$ in Eq.(C.15) and Eq.(C.11) for $q_k(i-1,j)$ and $q_k(i,j)$ in Eq.(C.8), $w_k(i,j)$ is represented by the hypothetical traction and discount ratio

$$w_k(i,j)=-\frac{q_k^H(i,j)}{\delta x(j)}\left[1-\varepsilon(i,j)\right], \qquad k=1,2. \tag{C.17}$$

The total tangential forces can then be calculated by integrating the traction of all elements in the contact ellipse:

$$Q_k = \sum_{j=1}^{N_y} \sum_{i=1}^{N_x} q_k(i,j)\delta x(j)\delta y, \qquad k = 1,2 \tag{C.18}$$

and the spin moment is

$$M = \sum_{j=1}^{N_y} \sum_{i=1}^{N_x} \left[-q_1(i,j)y(j) + q_2(i,j)x(i,j)\right]\delta x(j)\delta y. \tag{C.19}$$

C.3 Results

Parameters are chosen to represent the wheel and rail in contact, as listed in Table C-1. The materials of wheel and rail are assumed quasi-identical.

Table C-1 Parameters for non-dimensional friction force curves

Parameters	Symbol (units)	Value
normal contact force	P (kN)	42
longitudinal semi-axis of contact ellipse	a (mm)	10
lateral semi-axis of contact ellipse	b (mm)	5
Poisson's ratio	ν	0.27
shear modulus	G (Pa)	7.9×10^{10}
Coulomb friction coefficient	μ_0	0.3
Kalker's coefficients:	C_{11}	5.2
	C_{22}	5.0
	C_{23}	2.7
	C_{33}	0.82
number of elements in each strip in FASTSIM	N_x	30
number of strips in FASTSIM	N_y	20
nominal radius of wheel	r_0 (m)	0.48
wheel/rail contact angle (flange contact)	θ (°)	70

Results from FASTSIM of the surface condition of the contact ellipse are shown in Figure C-2 for a longitudinal creepage $\gamma_1 = 0.001$. The distribution of traction in the centre strip shows that 'slip' happens at the position where the resultant traction reaches the limiting Coulomb friction. Figure C-3 shows the surface condition of the contact ellipse under a lateral creepage $\gamma_2 = 0.001$. The boundary of the stick region and the value of traction are almost the same as those for the longitudinal case with the same creepage $\gamma_1 = 0.001$, as shown in Figure C-2 (since $C_{11} \approx C_{22}$ in this case).

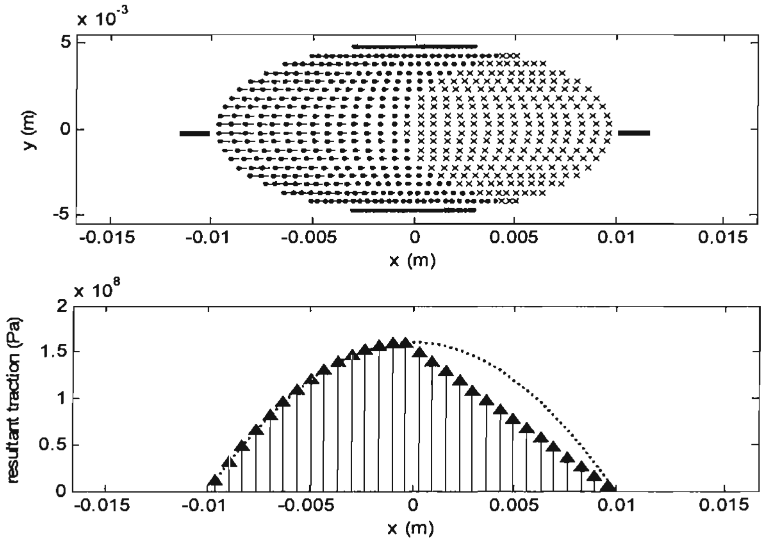

Figure C-2 Contact ellipse under $\gamma_1 = 0.001$ by FASTSIM: (a) × stick element, • slip element, – slip direction, — show traction in this slice; (b) ↑ resultant traction, ----- limiting traction.

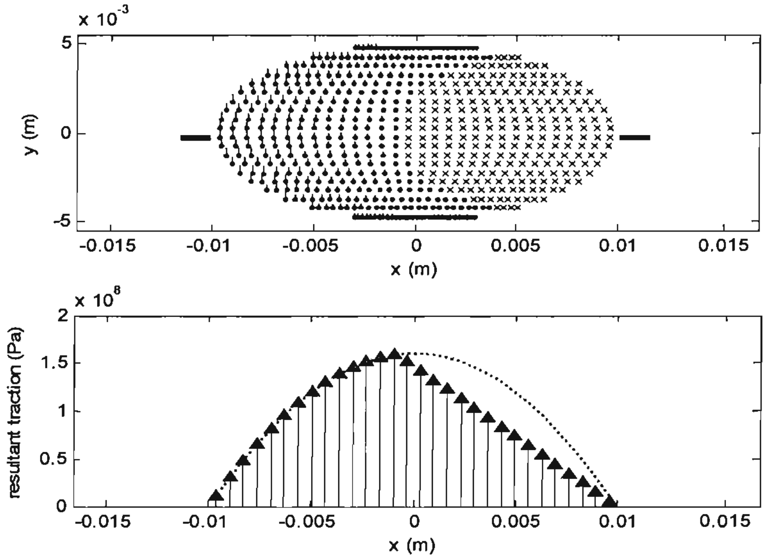

Figure C-3 Contact ellipse under $\gamma_2 = 0.001$, FASTSIM: (a) × stick element, • slip element, – slip direction, — show traction in this slice; (b) ↑ resultant traction, ----- limiting traction.

In the wheel and rail contact system, the spin is determined by the wheel/rail contact angle θ, and has units m^{-1}:

$$\gamma_6 = \sin\theta / r_0 . \tag{C.20}$$

When the wheel and rail are in tread contact, the contact angle is quite small, typically about 2° or $\gamma_6 = 0.076$ m^{-1}. The corresponding condition of the contact surface is shown in Figure C-4. However, flange contact will lead to a large contact angle, up to 70° or $\gamma_6 = 2.0$ m^{-1}. The corresponding condition of the contact surface is shown in Figure C-5. Spin may lead to complex condition of contact surface. One case combining creepages and spin, $\gamma_1 = \gamma_2 = 0.001$, $\gamma_6 = 0.076$ m^{-1}, is shown in Figure C-6.

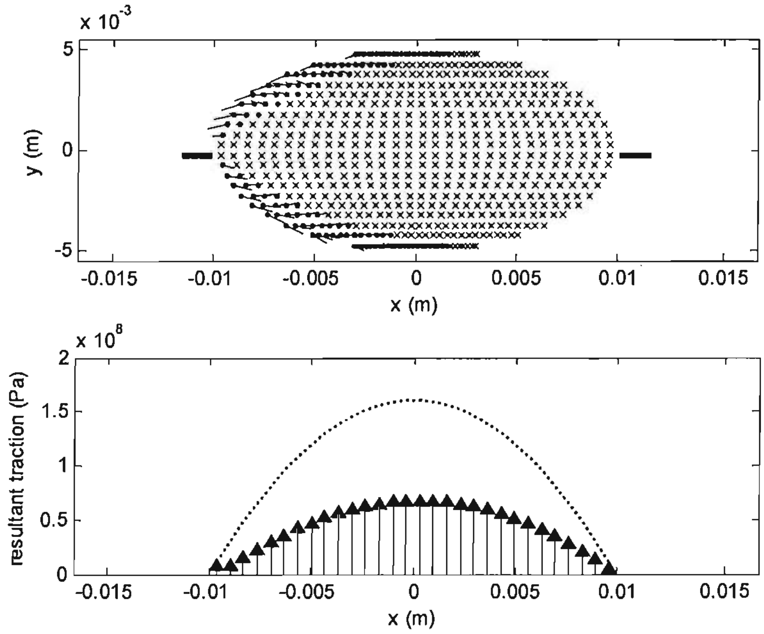

Figure C-4 Contact ellipse under a small spin, $\gamma_6 = 0.076$ m^{-1}, by FASTSIM: (a) × stick element, • slip element, – slip direction, — show traction in this slice; (b) ↑ resultant traction, ----- limiting traction.

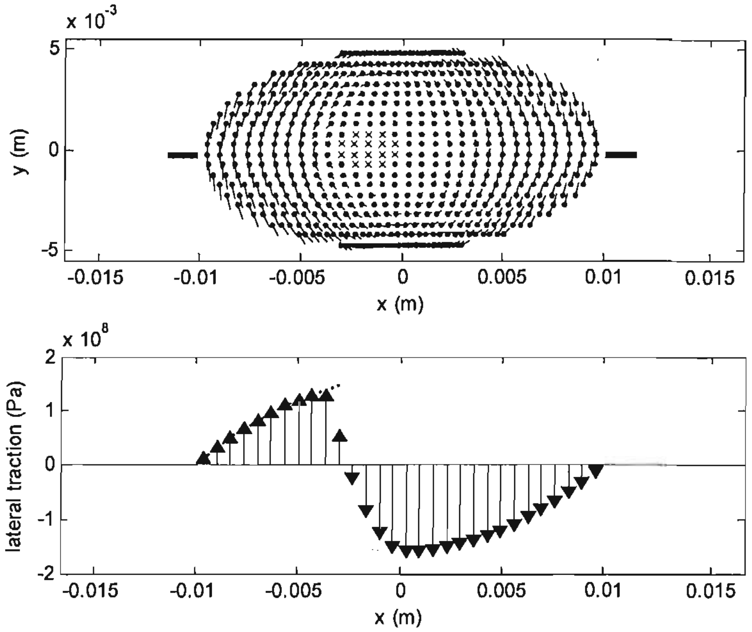

Figure C-5 Contact ellipse under a large spin, $\gamma_6 = 2.0$ m^{-1}, calculated by FASTSIM: (a) × stick element, • slip element, – slip direction, — show traction in this slice; (b) ↑ lateral traction, ----- limiting traction.

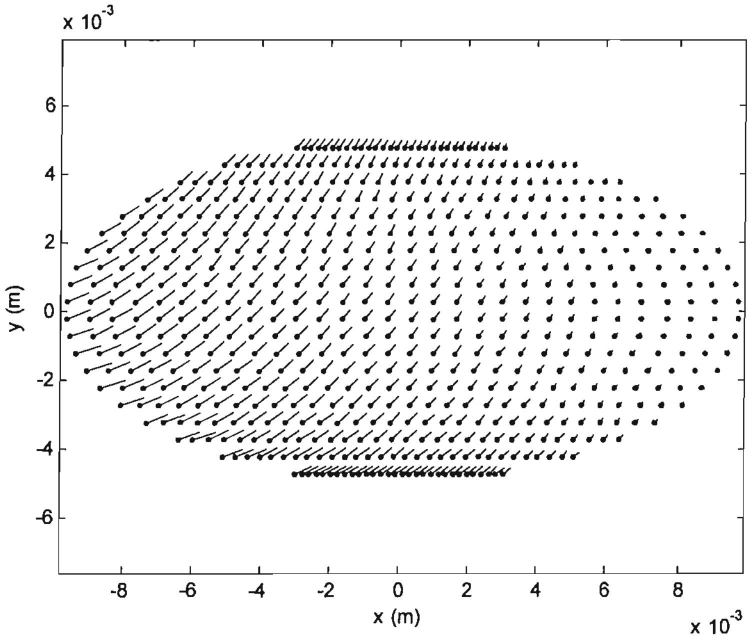

Figure C-6 Contact ellipse under creepages and spin, $\gamma_1 = \gamma_2 = 0.001$, $\gamma_6 = 0.076$ m^{-1}, by FASTSIM: × stick element, • slip element, – slip direction.

APPENDIX D. VEHICLE PARAMETERS AND MATRICES

D.1 Vehicle parameters

In Table D-1, **A** is a set of parameters for a conventional bogied vehicle, provided by Wickens [40]. **B** is a set of parameters for the Class 158 DMU, obtained from the sample vehicle of Vampire [47] with equivalent suspension stiffnesses for 17 DOF.

Table D-1 Parameters of the bogied vehicles with 17 DOF

		A	B	
nominal wheel radius	r_0	0.45	0.42	m
half distance of the track gauge	l_0	0.75	0.75	m
half distance between two wheelsets in a bogie	h	1.25	1.30	m
half distance between two bogies in a vehicle	c	8.75	8.00	m
vertical distance between the bogie and primary suspensions	d_1	0.20	-0.07	m
vertical distance between the bogie and secondary suspensions	d_2	0.40	0.42	m
vertical distance between the vehicle body and secondary suspensions	d_3	1.00	0.70	m
mass of the wheelset	m_w	1250	1528	kg
yaw inertia of the wheelset	I_{zw}	700	815	kgm^2
mass of the bogie	m_b	2500	2192	kg
yaw inertia of the bogie	I_{zb}	3500	2740	kgm^2
roll inertia of the bogie	I_{xb}	1000	1460	kgm^2
mass of the vehicle body	m_c	22000	39561	kg
yaw inertia of the vehicle body	I_{zc}	1	1.53	Mkgm^2
roll inertia of the vehicle body	I_{xc}	30000	39493	kgm^2
lateral stiffness of the primary suspensions	k_y	40[12]	40	MN/m
lateral damping of the primary suspensions	C_y	0	0	kNs/m
yaw stiffness of the primary suspensions	k_ψ	40	43	MNm
yaw damping of the primary suspensions	C_ψ	0	0	kNms
roll stiffness of the primary suspensions	k_φ	1	1.26	MNm
roll damping of the primary suspensions	C_φ	10	10	kNms
lateral stiffness of the secondary suspensions	k_{yb}	0.45	0.15	MN/m
lateral damping of the secondary suspensions	C_{yb}	1	1	kNs/m
yaw stiffness of the secondary suspensions	$k_{\psi b}$	0	0	MNm
yaw damping of the secondary suspensions	$C_{\psi b}$	0	0	kNms
roll stiffness of the secondary suspensions	$k_{\varphi b}$	1	0.25	MNm
roll damping of the secondary suspensions	$C_{\varphi b}$	60	60	kNms

---

[12] It is assumed that a printing error exists in Table 6.1 of Wickens' book which gives $k_y = 40$ N/m.

D.2 Vehicle matrices

The vectors and matrices in the equations of motion given in Eq.(3.21) are

(i) the inertia matrix

$$[\mathbf{A}_{\mathrm{v}}]=\mathrm{diag}(m_w\ I_{zw}\ m_b\ I_{xb}\ I_{zb}\ m_w\ I_{zw}\ m_c\ I_{xc}\ I_{zc}\ m_w\ I_{zw}\ m_b\ I_{xb}\ I_{zb}\ m_w\ I_{zw}), \tag{D. 1}$$

(ii) the damping matrix $[\mathbf{D}_{\mathrm{v}}]$, see Table D-2,

(iii) the stiffness matrix $[\mathbf{E}_{\mathrm{v}}]$, see Table D-3,

(iv) and the external force vector

$$\{\mathbf{F}_{\mathrm{v}}\}=\begin{bmatrix} T_{y,l}^1+T_{y,r}^1+m_w g\sin\phi_0-m_w a\cos\phi_0 \\ T_{x,l}^1 l_0-T_{x,r}^1 l_0-k_\psi(h/R_0) \\ m_b g\sin\phi_0-m_b a\cos\phi_0 \\ 0 \\ -k_{\psi b}(c/R_0) \\ T_{y,l}^2+T_{y,r}^2+m_w g\sin\phi_0-m_w a\cos\phi_0 \\ T_{x,l}^2 l_0-T_{x,r}^2 l_0+k_\psi(h/R_0) \\ m_c g\sin\phi_0-m_c a\cos\phi_0 \\ 0 \\ 0 \\ T_{y,l}^3+T_{y,r}^3+m_w g\sin\phi_0-m_w a\cos\phi_0 \\ T_{x,l}^3 l_0-T_{x,r}^3 l_0-k_\psi(h/R_0) \\ m_b g\sin\phi_0-m_b a\cos\phi_0 \\ 0 \\ k_{\psi b}(c/R_0) \\ T_{y,l}^4+T_{y,r}^4+m_w g\sin\phi_0-m_w a\cos\phi_0 \\ T_{x,l}^4 l_0-T_{x,r}^4 l_0+k_\psi(h/R_0) \end{bmatrix}, \tag{D. 2}$$

where the wheel/rail interaction forces acting on the wheelset i ($i=1,2,3,4$) are

$$\begin{aligned} T_{y,l}^i &= f_{2l}^i\cos\delta_l^i-f_{3l}^i\sin\delta_l^i \\ T_{y,r}^i &= f_{2r}^i\cos\delta_r^i-f_{3r}^i\sin\delta_r^i \\ T_{x,l}^i &= f_{1l}^i \\ T_{x,r}^i &= f_{1r}^i \end{aligned}, \tag{D. 3}$$

where $f_{j(l\text{ or }r)}^i$, are the longitudinal friction force ($j=1$), the transverse friction force ($j=2$) and the normal contact force ($j=3$) at the left (*l*) or the right (*r*) wheel/rail contact in the wheelset i.

Table D-2 Damping matrix of the bogied vehicle $[\mathbf{D}_v]$

	y_1	ψ_1	y_b	φ_b	ψ_b	y_2	ψ_2	y_c	φ_c	ψ_c	y_3	ψ_3	y_d	φ_d	ψ_d	y_4	ψ_4
y_1	C_y		$-C_y$	$C_y d_1$	$-C_y h$												
ψ_1		C_ψ			$-C_\psi$												
y_b	$-C_y$		$D_{3,3}$	$D_{3,4}$		$-C_y$		$-C_{yb}$	$C_{yb} d_3$	$-C_{yb} c$							
φ_b	$C_y d_1$		$D_{3,4}$	$D_{4,4}$		$C_y d_1$		$-C_{yb} d_2$	$D_{4,9}$	$-C_{yb} c d_2$							
ψ_b	$-C_y h$	$-C_\psi$			$D_{5,5}$	$C_y h$	$-C_\psi$			$-C_{\psi b}$							
y_2			$-C_y$	$C_y d_1$	$C_y h$	C_y											
ψ_2					$-C_\psi$		C_ψ										
y_c			$-C_{yb}$	$-C_{yb} d_2$				$2C_{yb}$	$-C_{yb} d_3$				$-C_{yb}$	$-C_{yb} d_2$			
φ_c			$C_{yb} d_3$	$D_{4,9}$				$-C_{yb} d_3$	$2C_{\varphi b}$				$C_{yb} d_3$	$D_{9,14}$			
ψ_c			$-C_{yb} c$	$-C_{yb} c d_2$	$-C_{\psi b}$					$D_{10,10}$			$C_{yb} c$	$c_{yb} d_2 c$	$-C_{\psi b}$		
y_3											C_y		$-C_y$	$c_y d_1$	$-C_y h$		
ψ_3												C_ψ			$-C_\psi$		
y_d								$-C_{yb}$	$C_{yb} d_3$	$C_{yb} c$	$-C_y$		$D_{13,13}$	$D_{13,14}$		$-C_y$	
φ_d								$-C_{yb} d_2$	$D_{9,14}$	$C_{yb} d_2 c$	$C_y d_1$		$D_{13,14}$	$D_{14,14}$		$C_y d_1$	
ψ_d										$-C_{\psi b}$	$-C_y h$	$-C_\psi$			$D_{15,15}$	$C_y h$	$-C_\psi$
y_4													$-C_y$	$C_y d_1$	$C_y h$	C_y	
ψ_4															$-C_\psi$		C_ψ

$D_{3,3} = C_{yb} + 2C_y$

$D_{3,4} = C_{yb} d_2 - 2C_y d_1$

$D_{4,4} = 2C_y d_1^2 + C_{yb} d_2^2 + C_\varphi + C_{\varphi b}$

$D_{4,9} = C_{yb} d_2 d_3 - C_{\varphi b}$

$D_{5,5} = C_{\psi b} + 2C_\psi + 2h^2 C_y$

$D_{9,14} = C_{yb} d_2 d_3 - C_{\varphi b}$

$D_{10,10} = 2C_{yb} c^2 + 2C_{\psi b}$

$D_{13,13} = C_{yb} + 2C_y$

$D_{13,14} = C_{yb} d_2 - 2C_y d_1$

$D_{14,14} = 2C_y d_1^2 + C_{yb} d_2^2 + C_\varphi + C_{\varphi b}$

$D_{15,15} = C_{\psi b} + 2C_\psi + 2h^2 C_y$

Table D-3 Stiffness matrix of the bogied vehicle $[\mathbf{E}_v]$

	y_1	ψ_1	y_b	φ_b	ψ_b	y_2	ψ_2	y_c	φ_c	ψ_c	y_3	ψ_3	y_d	φ_d	ψ_d	y_4	ψ_4
y_1	k_y		$-k_y$	$k_y d_1$	$-k_y h$												
ψ_1		k_ψ			$-k_\psi$												
y_b	$-k_y$		$E_{3,3}$	$E_{3,4}$		$-k_y$		$-k_{yb}$	$k_{yb} d_3$	$-k_{yb} c$							
φ_b	$k_y d_1$		$E_{3,4}$	$E_{4,4}$		$k_y d_1$		$-k_{yb} d_2$	$E_{4,9}$	$-k_{yb} c d_2$							
ψ_b	$-k_y h$	$-k_\psi$			$E_{5,5}$	$k_y h$	$-k_\psi$			$-k_{\psi b}$							
y_2			$-k_y$	$k_y d_1$	$k_y h$	k_y											
ψ_2					$-k_\psi$		k_ψ										
y_c			$-k_{yb}$	$-k_{yb} d_2$				$2k_{yb}$	$-k_{yb} d_3$				$-k_{yb}$	$-k_{yb} d_2$			
φ_c			$k_{yb} d_3$	$E_{4,9}$				$-k_{yb} d_3$	$2k_{\varphi b}$				$k_{yb} d_3$	$E_{9,14}$			
ψ_c			$-k_{yb} c$	$-k_{yb} c d_2$	$-k_{\psi b}$					$E_{10,10}$			$k_{yb} c$	$k_{yb} d_2 c$	$-k_{\psi b}$		
y_3											k_y		$-k_y$	$k_y d_1$	$-k_y h$		
ψ_3												k_ψ			$-k_\psi$		
y_d								$-k_{yb}$	$k_{yb} d_3$	$k_{yb} c$	$-k_y$		$E_{13,13}$	$E_{13,14}$		$-k_y$	
φ_d								$-k_{yb} d_2$	$E_{9,14}$	$k_{yb} d_2 c$	$k_y d_1$		$E_{13,14}$	$E_{14,14}$		$k_y d_1$	
ψ_d										$-k_{\psi b}$	$-k_y h$	$-k_\psi$			$E_{15,15}$	$k_y h$	$-k_\psi$
y_4													$-k_y$	$k_y d_1$	$k_y h$	k_y	
ψ_4															$-k_\psi$		k_ψ

$E_{3,3} = k_{yb} + 2k_y$

$E_{3,4} = k_{yb} d_2 - 2k_y d_1$

$E_{4,4} = 2k_y d_1^2 + k_{yb} d_2^2 + k_\varphi + k_{\varphi b}$

$E_{4,9} = k_{yb} d_2 d_3 - k_{\varphi b}$

$E_{5,5} = k_{\psi b} + 2k_\psi + 2h^2 k_y$

$E_{9,14} = k_{yb} d_2 d_3 - k_{\varphi b}$

$E_{10,10} = 2k_{yb} c^2 + 2k_{\psi b}$

$E_{13,13} = k_{yb} + 2k_y$

$E_{13,14} = k_{yb} d_2 - 2k_y d_1$

$E_{14,14} = 2k_y d_1^2 + k_{yb} d_2^2 + k_\varphi + k_{\varphi b}$

$E_{15,15} = k_{\psi b} + 2k_\psi + 2h^2 k_y$

APPENDIX E. PARAMETERS OF A STANDARD UIC 60 TRACK

A standard UIC 60 rail is positioned on pads with moderate stiffness. The stiffness of pad is replaced by an equivalent continuous stiffness averaged over the sleeper spacing. The ballast is continuous along the rail. The related parameters for analytical modelling of the rail are given in Table E-1.

Table E-1 Parameters for the calculation of standard UIC 60 track

	rail type	**UIC 60**	
rail [77]	Young's modulus E	2.1×10^{11}	Nm^{-2}
	Poisson's ratio ν	0.3	
	shear modulus G	8.1×10^{10}	Nm^{-2}
	density of rail ρ	7860	kgm^{-3}
	area of cross-section A	7.7×10^{-3}	m^2
	mass of rail per metre m_r	60.3	kgm^{-1}
	loss factor of rail η_r	0.02	
	second moment of area I_z	5.1×10^{-6}	m^4
	lateral bending stiffness EI_z	1.1×10^{6}	Nm^2
	second moment of area I_y	3.05×10^{-5}	m^4
	vertical bending stiffness EI_y	6.4×10^{6}	Nm^2
	Timoshenko shear coefficient κ [78]	0.4	
	sleeper type	**concrete monobloc**	
sleeper	sleeper spacing	0.6	m
	mass per half sleeper	162	kg
	sleeper mass per metre of a rail	270	kgm^{-1}
rail pad	longitudinal stiffness of pad per metre	1.7×10^{7}	Nm^{-1}
	lateral stiffness of pad per metre	1.7×10^{7}	Nm^{-1}
	vertical stiffness of pad per metre	5.8×10^{8}	Nm^{-1}
	loss factor of pad	0.25	
ballast	longitudinal stiffness of ballast	5×10^{7}	Nm^{-1}
	lateral stiffness of ballast	5×10^{7}	Nm^{-1}
	vertical stiffness of ballast	4×10^{7}	Nm^{-1}
	loss factor of ballast	1.0	

APPENDIX F. NORMAL CONTACT FORCE CHECK

To calculate the creep forces, the normal force acting on the contact patch is required. The left and right normal contact forces can initially be assumed equal, which is valid if the contact angles are approximately equal and cant deficiency (or cant excess) is not too large. However, if the contact point of one wheel is close to the flange, the difference between left and right contact angles can be great enough to make the normal force on each contact patch different. The assumed normal force should be adjusted to satisfy the real condition.

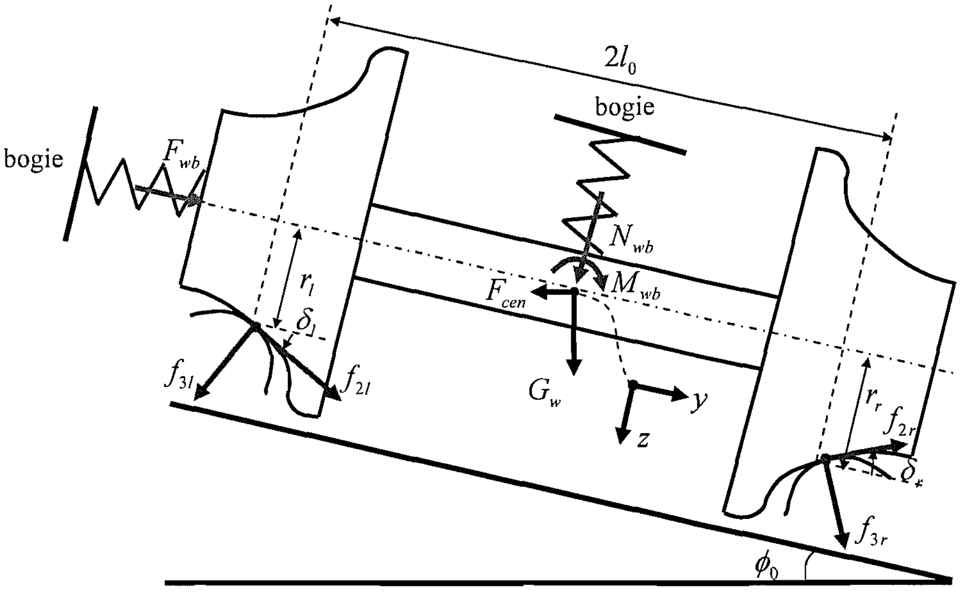

Figure F-1 Left and right contact forces in their own contact frames, and the force balance for the wheelset.

With some of the wheelset force equations, the normal force can be adjusted using an iteration process. In the steady-state curving analysis, the wheelset is assumed to remain in contact with the rails and without obvious roll deflection, which means the static force analysis in the wheelset frame, along the *z*-axis and about the *x*-axis, can be used to check the normal forces. The force and moment balance equations on a track with a cant of ϕ_0, as shown in Figure F-1, are expressed as

$$f_{2l}\sin\delta_l + f_{3l}\cos\delta_l + f_{2r}\sin\delta_r + f_{3r}\cos\delta_r + F_{wb}\sin\phi_0 + G_w\cos\phi_0 + N_{wb}\cos\phi_0 = 0, \qquad (F.1)$$

and

$$\begin{aligned}&(f_{2r}\sin\delta_r + f_{3r}\cos\delta_r)l_0 - (f_{2l}\sin\delta_l + f_{3l}\cos\delta_l)l_0\\&-(f_{2r}\cos\delta_r - f_{3r}\sin\delta_r)r_r - (f_{2l}\cos\delta_l - f_{3l}\sin\delta_l)r_l + M_{wb} = 0\end{aligned} \quad \text{(F.2)}$$

In these equations, F_{wb}, N_{wb} and M_{wb} are the spring forces and moment between the wheelset and the bogie. The relative motions between the wheelset and the bogie determine these spring forces (and possible damping forces in parallel). If the mass of the wheelset is m_w, the gravity force acting on the wheelset is $G_w = m_w g$, and the centripetal force acting on the wheelset is $F_{cen} = m_w V_0^2 / R_0$. The friction forces f_{2l}, f_{2r} are determined by the lateral creepages and the initial normal forces f_{3l}, f_{3r}. In the step-by-step integration for steady-state curving behaviour, the normal force must be checked at each step as follows:

(1) Assuming the initial values of normal forces are the same as the last step, for step n, having

$$f_{3l}^0 = f_{3l}(n-1),\ f_{3r}^0 = f_{3r}(n-1) \quad \text{(F.3),(F.4)}$$

where

$$f_{3l}(0) = f_{3r}(0) = N_{wb} + G_w / \cos\phi_0,\ n = 1 \quad \text{(F.5)}$$

(2) With the initial normal forces in check f_{3l}^0, f_{3r}^0, the lateral friction forces f_{2l}, f_{2r} are obtained.

(3) Checking the force and moment balance of the wheelset in the lateral and rolling directions: substituting the lateral friction forces and suspension forces into Eq.(F.1) and Eq.(F.2), the new normal forces f_{3l}, f_{3r} can be obtained.

(4) Comparing the new normal forces and the previous normal forces: if the difference is larger than the tolerance, updating the normal forces with the new normal forces, $f_{3l}^0 = f_{3l}, f_{3r}^0 = f_{3r}$, then go to step (3); if the difference is inside the tolerance, the iteration is finished and the normal forces are obtained: $f_{3l}(n) = f_{3l}, f_{3r}(n) = f_{3r}$.

APPENDIX G. CALCULATING THE ACOUSTIC RADIATION OF WHEEL

G.1 Introduction to the method

The acoustic radiation from a vibrating structure is described by two important acoustical quantities. The first quantity is the radiation ratio, which evaluates the relative conversion efficiency from the structural vibration to the sound radiation with respect to the frequency. The second quantity is the directivity of acoustic radiation, which describes the spatial distribution of the sound field, and allows the sound pressure at a receiver point in the far field to be derived from the sound power. As a practical wheel has considerably complex geometry, however, its acoustical quantities are normally obtained by some numerical methods. For ease of calculating the acoustic radiation of a wheel, it is meaningful to find some formulae for the acoustical quantities in terms of some parameters of the wheel structure. This work has been realised by Thompson and Jones [62]. They proposed simple formulae for the radiation ratio and directivity after investigating the sound radiation characteristics of a railway wheel by using boundary element calculations. With these formulae, if the characteristics of one mode, i.e. the numbers of nodal circles and nodal diameters, and the geometrical dimensions of the wheel, i.e. the wheel radius, the thickness of the web and the rim, are known, the acoustical quantities of this mode can be obtained approximately. Hence, using these acoustical quantities, the sound power radiation due to the vibration in each individual wheel mode can be calculated, and then the whole sound radiation can be obtained by summing them. Assuming the acoustical quantities for each mode are known, the noise radiation calculation can proceed as follows.

G.2 Calculation

The radiation ratio σ is defined as the sound power produced by a vibrating structure, normalised by the sound power that would be radiated by the same mean square spatially averaged velocity if the surface were part of an infinite plane, all vibrating in phase:

$$\sigma \equiv \frac{W_{rad}}{\rho_0 c_0 S \overline{\langle v^2 \rangle}}, \tag{G.1}$$

where W_{rad} is the radiated sound power, ρ_0 is the density of air, c_0 is the speed of sound in air, S is the surface area of the structure and v^2 is the squared normal velocity of the surface, which is both temporally $(\overline{\ })$ and spatially $(\langle\ \rangle)$ averaged. If the radiation ratio σ is available, the radiated sound power can be calculated from $\overline{\langle v^2 \rangle}$ by rearranging Eq.(G.1) to give

$$W_{rad} = \rho_0 c_0 S \sigma \overline{\langle v^2 \rangle}. \tag{G.2}$$

The wheel has two radiation directions: the lateral direction due to the axial vibration from the two sides of the web and tyre (excluding the axle), and the radial direction due to the radial vibration of the outer and inner tread surfaces (excluding the thickness of the web in the inner surface), as shown in Figure G-1.

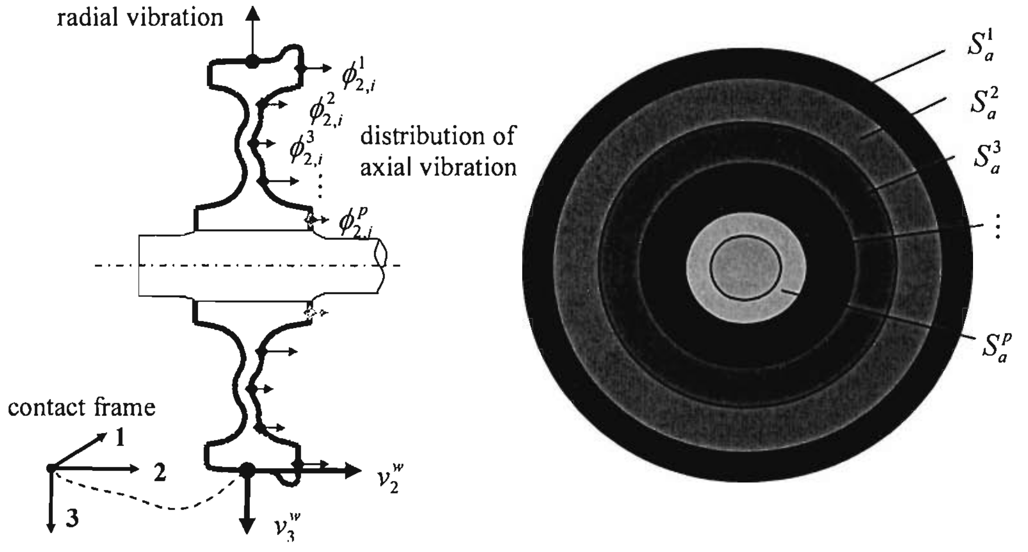

(a) (b)

Figure G-1 (a) Cross section of a typical railway wheel; (b) radiation rings on the web area.

For the wheel mode i with natural frequency f_i, the radiated sound power in the axial direction (denoted with an index 'a') and in the radial direction (denoted with an index 'r') are given as

$$W_a(i) = \rho_0 c_0 \sigma_a(i) S_a \overline{\langle v_a^2(i) \rangle}, \qquad \text{(G.3)}$$

and

$$W_r(i) = \rho_0 c_0 \sigma_r(i) S_r \overline{\langle v_r^2(i) \rangle}. \qquad \text{(G.4)}$$

In these radiation equations, the vibration $\overline{\langle v_{a,r}^2(i) \rangle}$ may not be equally distributed over the corresponding radiation surface $S_{a,r}$. If the wheel is assumed to have steady-state distribution of vibration over the radiation surfaces, $\langle v_{a,r}^2(i) \rangle$ can be represented by the velocities at the contact point and the distribution of the modeshape as follows.

In the axial direction (also the lateral direction in the contact frame), the lateral modeshapes, $\phi_{2,i}^j$, $j = 1, 2, \cdots, p$, are determined at p points, distributed on a radial line from a position close to the contact to a position close to the axle, see Figure G-1. The velocity at the point of wheel rim, $v_a^1(i)$, is equal to the velocity at the contact position, $v_2^w(i)$, which steadily oscillates at the natural frequency of mode i, giving $v_a^1(i) = v_2^w(i)$. Hence, the axial velocity at each point is proportional to the contact velocity according to the ratio of their modeshapes:

$$\frac{v_a^j(i)}{v_2^w(i)} = \frac{v_a^j(i)}{v_2^1(i)} = \frac{\phi_{2,i}^j}{\phi_{2,i}^1}, \; j = 1 \sim p. \qquad \text{(G.5)}$$

If the number of the points is large enough, e.g. $p \geq 5$, the axial velocity v_a^j can be considered as the averaged velocity of the ring area S_a^j. The term related to the spatial averaged velocity in Eq.(G.3) can then be expressed as

$$\overline{\langle v_a^2(i) \rangle} = \frac{\sum_{j=1}^{p} S_a^j \overline{\left(v_a^j(i)\right)^2}}{S_a} = \frac{\sum_{j=1}^{p} S_a^j \left(\phi_{2,i}^j / \phi_{2,i}^1\right)^2}{S_a} \overline{\left(v_2^w(i)\right)^2}. \qquad \text{(G.6)}$$

Thus, substituting Eq.(G.6) into Eq.(G.3), in the axial direction, the radiated sound power from the vibration of mode i can be rewritten as

$$W_a(i) = \rho_0 c_0 \sigma_a(i) \left(\sum_{j=1}^{p} S_a^j \left(\phi_{2,i}^j / \phi_{2,i}^1\right)^2 \right) \overline{\left(v_2^w(i)\right)^2} . \qquad \text{(G.7)}$$

A similar treatment can be applied to the radial direction. However, since the contact point is located around the centre point of the tread, the spatially averaged velocity in the radial direction is approximately equal to the steady vertical contact velocity, giving

$$\overline{\left\langle v_r^2(i) \right\rangle} = \overline{\left(v_3^w(i)\right)^2} . \qquad \text{(G.8)}$$

Substituting Eq.(G.8) into Eq.(G.4), in the radial direction, the radiated sound power from the vibration of mode i can be rewritten as

$$W_r(i) = \rho_0 c_0 \sigma_r(i) S_r \overline{\left(v_3^w(i)\right)^2} . \qquad \text{(G.9)}$$

The velocity in one mode can be decomposed from the steady-state velocity by using spectra analyses, e.g. Fourier transform. Parseval's theorem tells that the vibration energy in the time domain is equal to that in the frequency domain, giving

$$\int_{-\infty}^{\infty} v^2(t) dt = \int_{-\infty}^{\infty} \left| V(f) \right|^2 df , \qquad \text{(G.10)}$$

where $V(f)$ is the spectrum of the time domain vibration $v(t)$. If the time-domain vibration is a band-limited steady-state signal, with the lower cut-off frequency f_l and the upper cut-off frequency f_u, the time-averaged vibration $\overline{v^2(t)}$ is equal to the sum of 'power' $P(f) = \left| V(f) \right|^2$ in this frequency range $[f_l, f_u]$, which is expressed as

$$\overline{v^2(t)} = \int_{f_l}^{f_u} P(f) df . \qquad \text{(G.11)}$$

In the acoustic analysis, the vibration can be analysed in the preferred 1/3-octave bands, so that the power in the frequency band k, denoted $P(k)$, can be defined as the integration of the power in this frequency band, $[f_l^k, f_u^k]$, which is

$$P(k) \equiv \int_{f_l^k}^{f_u^k} P(f) df . \qquad \text{(G.12)}$$

If one of the frequency band m, $(m \in k)$ includes only one mode i, having

$$f_l^m \le f_i \le f_u^m, \tag{G.13}$$

the time-averaged squared velocity in this mode, $\overline{v^2(i)}$, can be considered as forming the whole power in this frequency band

$$\overline{v^2(i)} = P(m). \tag{G.14}$$

In this way, the contact velocities in each mode, $\overline{\left(v_2^w(i)\right)^2}$ and $\overline{\left(v_3^w(i)\right)^2}$, can be decomposed from the corresponding time-domain contact velocities $\overline{\left(v_2^w\right)^2}$ and $\overline{\left(v_3^w\right)^2}$. Thus, the axial and radial sound power of all n modes in the frequency range of interest can be calculated and summed to get the whole sound radiation W_s, which is

$$W_s = \sum_{i=1}^{n} \left(W_a(i) + W_r(i)\right). \tag{G.15}$$

The sound power level is defined as

$$L_W \equiv 10 \log_{10} \frac{W_s}{1 \times 10^{-12}}, \tag{G.16}$$

with the units dB (re 1×10^{-12} W)

For a point monopole source, in free space (ignoring the ground effect and air absorption), the sound intensity at a distance r (far from the source) is

$$\langle I \rangle = \frac{W_s}{4\pi r^2}. \tag{G.17}$$

Then, the sound pressure is

$$\overline{p^2} = \rho_0 c_0 \langle I \rangle. \tag{G.18}$$

In the far field, the sound field can be approximated as having a dependence on distance, and a directivity factor D_ϑ, which is defined as the ratio of intensity in one spatial direction ϑ to the mean intensity:

$$D_\vartheta \equiv I_\vartheta / \langle I \rangle, \tag{G.19}$$

and the directivity index can be defined as

$$DI \equiv 10\log_{10} D_\vartheta . \qquad \text{(G.20)}$$

The sound radiation of an axial mode is mainly from the two web surfaces, so the directivity index of this mode is calculated using a dipole sound source [62]. If the sound radiation is from a radial mode, a monopole sound source can be used to obtain the directivity index. Thus, in the far field, in the direction ϑ, the sound pressure is

$$\overline{p_\vartheta^2} = \rho_0 c_0 I_\vartheta = \rho_0 c_0 D_\vartheta \langle I \rangle = \rho_0 c_0 D_\vartheta \frac{W_s}{4\pi r^2} , \qquad \text{(G.21)}$$

and the sound pressure level L_p can be approximately related with the sound power level L_W, the distance r and the directivity index $DI = 10\log_{10} D_\vartheta$ as follows

$$L_p \equiv 10\log_{10} \frac{\left(\overline{p_\vartheta^2}\right)}{\left(2\times10^{-5}\right)^2} = L_W - 20\log_{10} r + DI - 11 , \qquad \text{(G.22)}$$

with the units: dB (re 2×10^{-5} Pa).

APPENDIX H. FE MODEL OF CLASS 158 WHEEL

A Class 158 wheel including the axle is modelled by FE analysis. The model has a plane of symmetry at the centre of the axle. The frequency range covered by this model is up to 16 kHz. The modal parameters of all wheel modes below 5000 Hz are listed in Table H-1. The predominant out-of-plane and radial modes below 5000 Hz are identified and numbered in Table H-1. Their modeshapes are shown in Figure H-1.

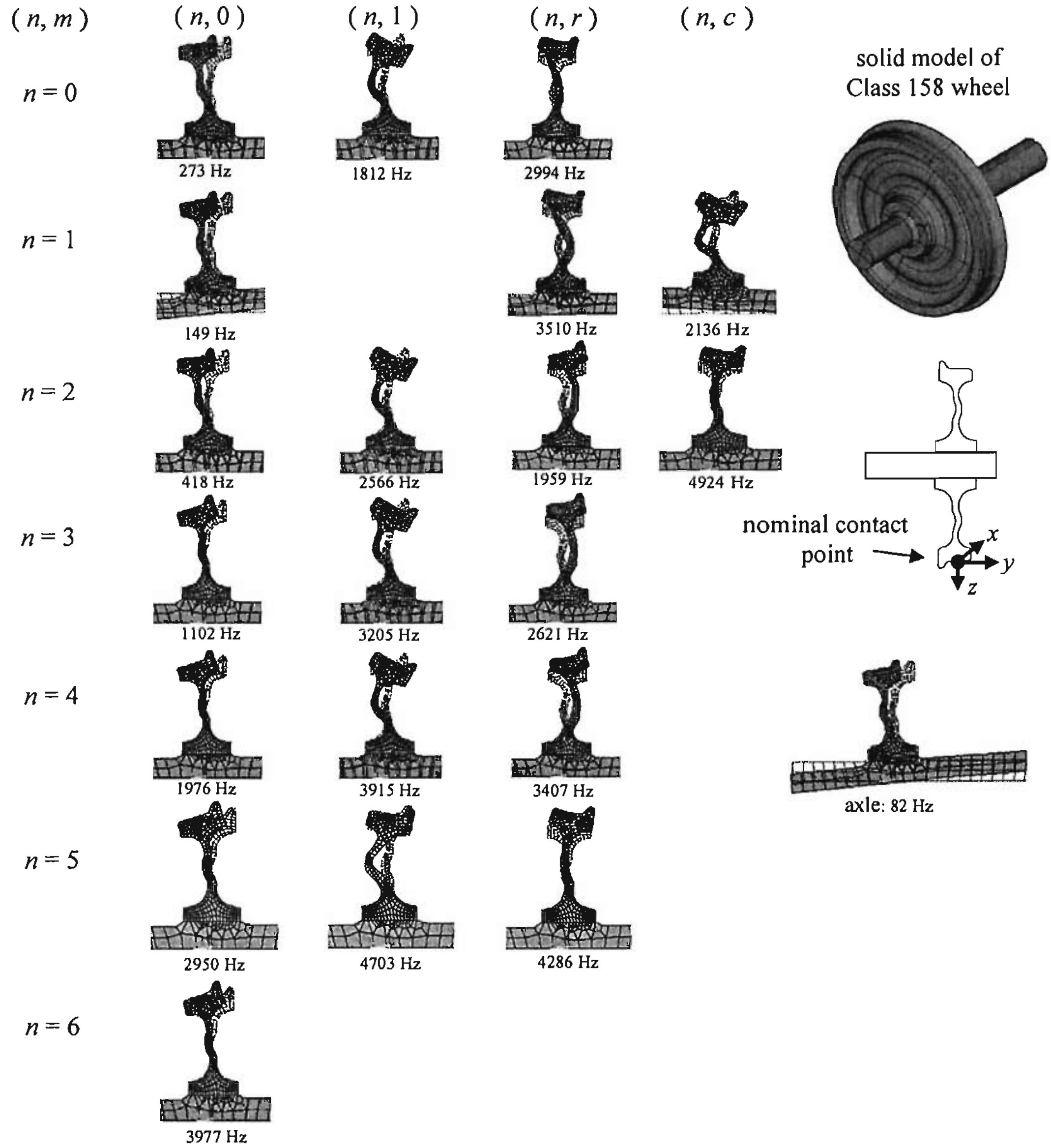

Figure H-1 FE model of a Class 158 wheel: modeshapes of the identified predominant modes up to 5 kHz, *n*: number of the nodal diameters, *m* = 0, 1, number of the nodal circles, *m*: *r*, radial mode, *m*: *c*, circumferential mode.

In Table H-1, the modeshapes are described in 6 DOF. Their directions are defined in the wheel/rail contact frame, as shown in Figure H-1. The damping ratio ζ_i of each mode is assumed in terms of previous measurement results with rounded values [64].

Table H-1 Modal parameters of a Class 158 wheel

Identified modes.	(n,m)[13]	f_i [Hz]	M_i [kg]	ζ_i [-]	ϕ_1 [-]	ϕ_2 [-]	ϕ_3 [-]	ϕ_4 [-]	ϕ_5 [-]	ϕ_6 [-]
1	rigid	10	1250	10^{-1}	0	0	1	0	0	0
2	rigid	15	1250	10^{-1}	1	0	0	0	0	0
3	rigid	20	675	10^{-1}	7.5×10^{-1}	4.2×10^{-1}	0	0	0	1
4	rigid	25	675	10^{-1}	0	0	-7.5×10^{-1}	-1	0	0
5	rigid	30	1250	10^{-1}	0	1	0	0	0	0
6	(0,c)	70	2.0	10^{-3}	-7.3×10^{-2}	1.6×10^{-13}	1.3×10^{-15}	-1.0×10^{-12}	-1.7×10^{-1}	-4.1×10^{-3}
7	axle	82	1.0	10^{-2}	5.9×10^{-3}	6.1×10^{-2}	-6.0×10^{-3}	-1.5×10^{-1}	-3.7×10^{-2}	-1.4×10^{-1}
8	(1,0)	149	1.0	10^{-2}	-9.5×10^{-3}	7.1×10^{-2}	9.4×10^{-3}	-2.0×10^{-1}	-4.3×10^{-2}	-1.6×10^{-1}
9	(0,0)	273	2.0	10^{-3}	7.8×10^{-13}	7.3×10^{-2}	1.4×10^{-4}	-1.1×10^{-1}	1.8×10^{-12}	3.7×10^{-14}
	(1,x)	340	1.0	10^{-2}	-8.7×10^{-3}	4.8×10^{-2}	8.2×10^{-3}	-2.1×10^{-1}	-2.9×10^{-2}	-1.0×10^{-1}
	(0,x)	402	2.0	10^{-3}	2.0×10^{-13}	5.8×10^{-2}	3.0×10^{-4}	-1.8×10^{-1}	4.8×10^{-13}	2.3×10^{-14}
10	(2,0)	418	0.5	10^{-4}	1.4×10^{-4}	8.1×10^{-2}	1.9×10^{-3}	-4.2×10^{-1}	-6.9×10^{-2}	-3.0×10^{-1}
	(1,x)	569	1.0	10^{-2}	-6.4×10^{-4}	-2.8×10^{-2}	9.6×10^{-4}	2.0×10^{-1}	1.4×10^{-2}	4.8×10^{-2}
	(0,x)	953	2.0	10^{-3}	6.2×10^{-14}	-1.9×10^{-2}	-1.0×10^{-3}	2.5×10^{-1}	1.5×10^{-13}	1.7×10^{-14}
11	(3,0)	1102	0.5	10^{-4}	1.4×10^{-3}	8.2×10^{-2}	3.7×10^{-3}	-5.3×10^{1}	-6.4×10^{-2}	-3.4×10^{-1}
	(0,x)	1788	2.0	10^{-3}	-2.6×10^{-14}	-4.4×10^{-2}	-4.8×10^{-3}	1.3×10^{0}	-5.0×10^{-14}	1.4×10^{-14}
12	(0,1)	1812	2.0	10^{-3}	-9.5×10^{-16}	-4.3×10^{-2}	-4.4×10^{-3}	1.3×10^{0}	-1.1×10^{-14}	-1.6×10^{-14}
	(1,x)	1852.5	1.0	10^{-2}	2.9×10^{-2}	-2.6×10^{-2}	-9.4×10^{-3}	9.3×10^{-1}	4.7×10^{-2}	-4.6×10^{-2}
	(1,x)	1853.4	1.0	10^{-2}	3.0×10^{-2}	-2.6×10^{-2}	-9.7×10^{-3}	9.1×10^{-1}	4.8×10^{-2}	-4.5×10^{-2}
13	(2,r)	1959	0.5	10^{-4}	-2.4×10^{-2}	3.5×10^{-3}	5.4×10^{-2}	-3.1×10^{-1}	2.0×10^{-1}	5.7×10^{-2}
14	(4,0)	1976	0.5	10^{-4}	2.8×10^{-3}	8.2×10^{-2}	6.2×10^{-3}	-6.2×10^{-1}	-2.9×10^{-2}	-3.3×10^{-1}
15	(1,c)	2136	1.0	10^{-2}	-4.3×10^{-2}	-2.9×10^{-2}	1.4×10^{-2}	9.3×10^{-1}	-8.1×10^{-2}	-4.4×10^{-2}
	(1,x)	2211	1.0	10^{-2}	-4.4×10^{-2}	-2.7×10^{-2}	1.3×10^{-2}	9.2×10^{-1}	-9.0×10^{-2}	-4.7×10^{-2}
16	(2,1)	2566	0.5	10^{-4}	-1.1×10^{-2}	-3.0×10^{-2}	2.8×10^{-2}	1.2×10^{0}	8.2×10^{-2}	-1.4×10^{-1}
17	(3,r)	2621	0.5	10^{-4}	-8.3×10^{-3}	-3.6×10^{-3}	5.9×10^{-2}	-1.6×10^{-1}	4.0×10^{-1}	7.4×10^{-2}
18	(5,0)	2950	0.5	10^{-4}	4.4×10^{-3}	8.0×10^{-2}	9.1×10^{-3}	-6.9×10^{-1}	3.2×10^{-2}	-2.8×10^{-1}
	(0,x)	2989	2.0	10^{-3}	4.6×10^{-15}	-1.3×10^{-2}	6.7×10^{-2}	4.8×10^{-1}	2.2×10^{-14}	-1.1×10^{-14}
19	(0,r)	2994	2.0	10^{-3}	-3.3×10^{-15}	-1.3×10^{-2}	6.7×10^{-2}	4.7×10^{-1}	-4.0×10^{-15}	1.7×10^{-16}
20	(3,1)	3205	0.5	10^{-4}	-2.6×10^{-3}	-2.4×10^{-2}	2.8×10^{-2}	1.1×10^{0}	1.5×10^{-1}	-2.2×10^{-1}
21	(4,r)	3407	0.5	10^{-4}	1.7×10^{-3}	-1.1×10^{-2}	6.3×10^{-2}	2.4×10^{-4}	5.8×10^{-1}	6.5×10^{-2}
	(0,x)	3455	2.0	10^{-3}	2.3×10^{-2}	5.7×10^{-15}	-1.9×10^{-14}	-1.1×10^{-13}	8.2×10^{-2}	1.1×10^{-2}
22	(1,r)	3510	0.5	10^{-2}	4.3×10^{-2}	-9.8×10^{-3}	5.3×10^{-2}	4.6×10^{-1}	2.5×10^{-1}	-2.3×10^{-2}
	(0,x)	3714	2.0	10^{-3}	2.3×10^{-2}	1.6×10^{-15}	-1.9×10^{-14}	-1.5×10^{-13}	8.5×10^{-2}	1.3×10^{-2}
23	(4,1)	3915	0.5	10^{-4}	1.5×10^{-3}	-2.0×10^{-2}	2.2×10^{-2}	9.9×10^{-1}	1.7×10^{-1}	-2.7×10^{-1}
24	(6,0)	3977	0.5	10^{-4}	6.3×10^{-3}	7.8×10^{-2}	1.2×10^{-2}	-7.3×10^{-1}	1.1×10^{-1}	-2.0×10^{-1}
	(1,0)	4199	1.0	10^{-2}	1.4×10^{-2}	4.2×10^{-3}	1.3×10^{-2}	4.9×10^{-1}	9.3×10^{-2}	6.2×10^{-2}
25	(5,r)	4286	0.5	10^{-4}	9.3×10^{-3}	-1.9×10^{-2}	6.5×10^{-2}	2.0×10^{-1}	7.4×10^{-1}	2.3×10^{-2}
	(0,x)	4361	2.0	10^{-3}	3.7×10^{-15}	3.4×10^{-3}	1.4×10^{-2}	-5.2×10^{-1}	5.4×10^{-15}	-1.5×10^{-15}
	(2,x)	4389	0.5	10^{-4}	-2.7×10^{-2}	7.1×10^{-3}	-8.0×10^{-3}	-7.0×10^{-1}	-9.1×10^{-2}	1.4×10^{-1}
	(0,x)	4403	2.0	10^{-3}	4.0×10^{-16}	3.4×10^{-3}	1.3×10^{-2}	-5.2×10^{-1}	6.0×10^{-15}	1.3×10^{-14}
	(1,x)	4606	1.0	10^{-2}	1.2×10^{-2}	2.2×10^{-3}	1.8×10^{-2}	-4.8×10^{-1}	9.8×10^{-2}	6.7×10^{-2}
26	(5,1)	4703	0.5	10^{-4}	2.6×10^{-3}	-1.4×10^{-2}	1.3×10^{-2}	8.6×10^{-1}	1.1×10^{-1}	-3.0×10^{-1}
27	(2,c)	4924	0.5	10^{-4}	-6.9×10^{-2}	1.3×10^{-5}	2.7×10^{-2}	-1.4×10^{-1}	-3.7×10^{-1}	-5.4×10^{-2}
	(3,x)	4931	0.5	10^{-4}	-8.5×10^{-3}	6.5×10^{-3}	4.7×10^{-4}	-8.2×10^{-1}	2.7×10^{-2}	2.5×10^{-1}

---

[13] *n*: number of nodal diameters; *m* = 0,1: number of nodal circles; *m*: r, radial mode; *m*: c, circumferential mode; *m*: x, others. The natural frequencies of those rigid modes are determined by the suspension stiffness of the vehicle.

The mobilities at the nominal contact point of the wheel FE model are calculated from the modal parameters of both all the modes up to 10 kHz and the 27 identified modes below 5 kHz (see Table H-1). Generally good agreement is found fro frequencies up to 4 kHz using only the selected modes.

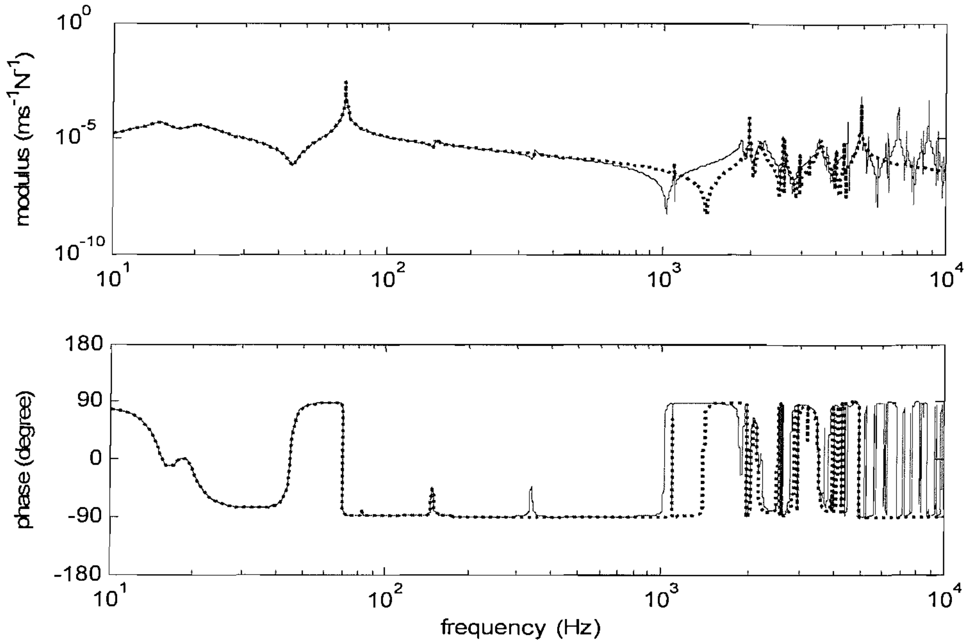

Figure H-2 Longitudinal mobility Y_{11}^{w} of a Class 158 wheel at the nominal contact point: —— all modes up to 10 kHz, ····· identified modes below 5 kHz.

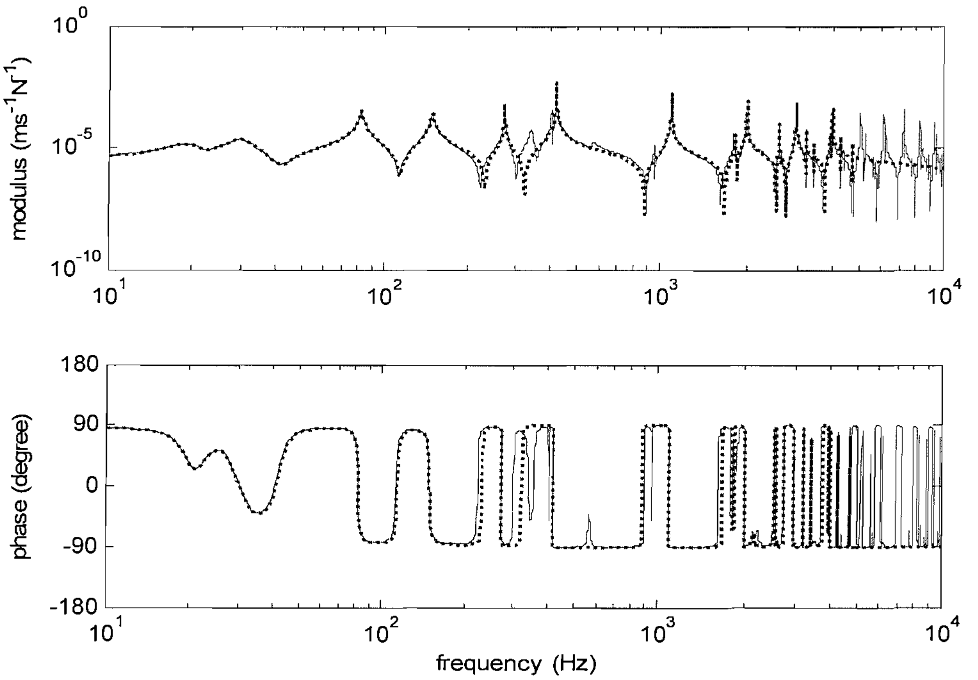

Figure H-3 Lateral mobility Y_{22}^{w} of a Class 158 wheel at the nominal contact point: —— all modes up to 10 kHz, ····· identified modes below 5 kHz.

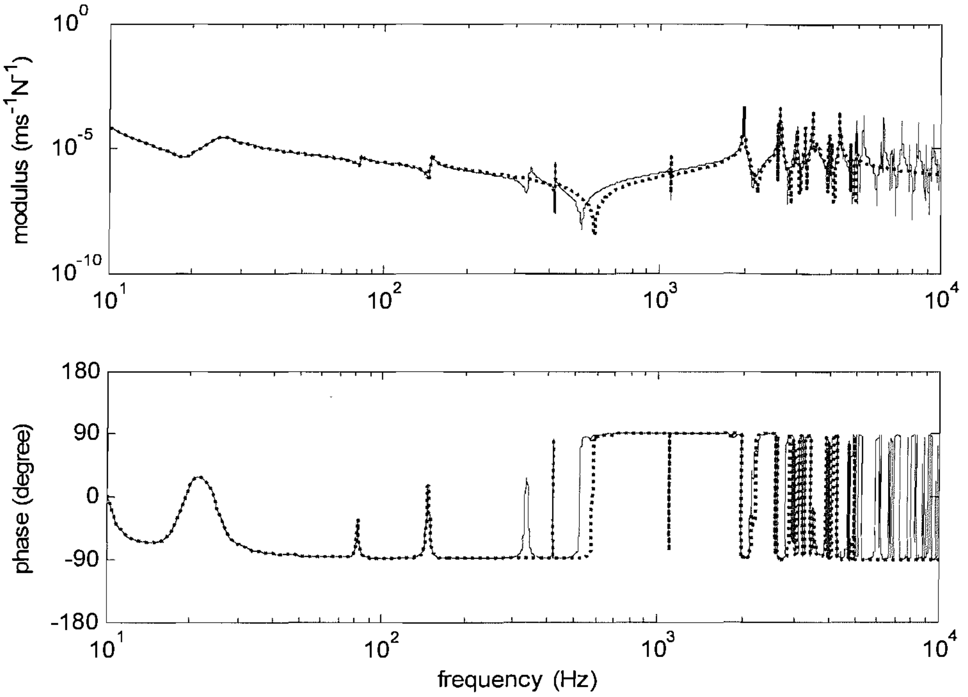

Figure H-4 Vertical mobility Y_{33}^{w} of a Class 158 wheel at the nominal contact point: —— all modes up to 10 kHz, ····· identified modes below 5 kHz.

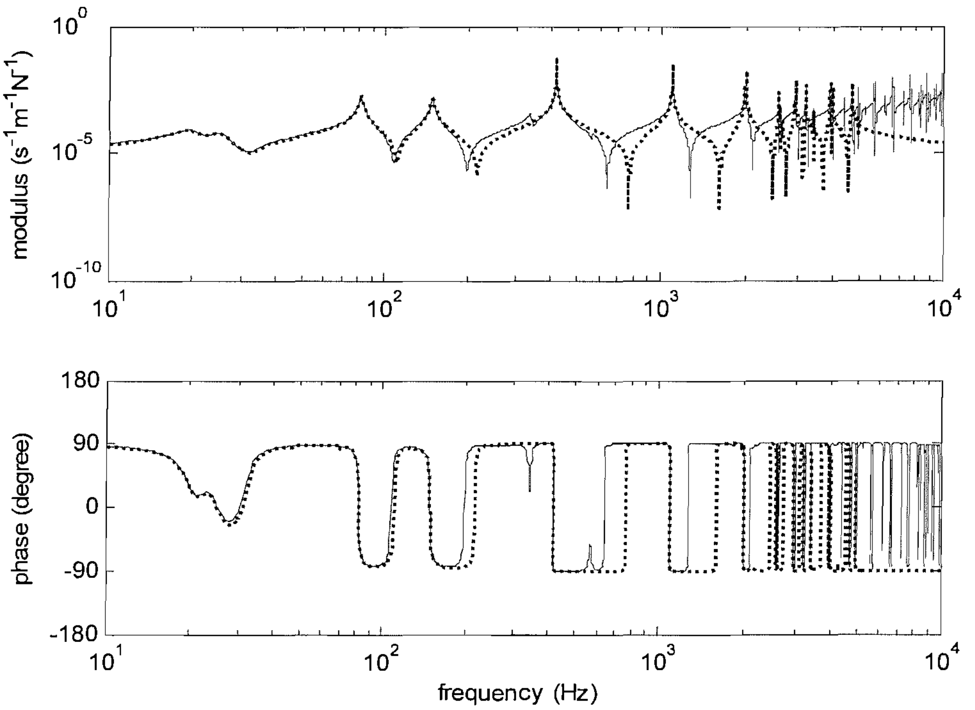

Figure H-5 Spin mobility Y_{66}^{w} of a Class 158 wheel at the nominal contact point: —— all modes up to 10 kHz, ····· identified modes below 5 kHz.

APPENDIX I. EQUIVALENT LUMPED-PARAMETER SYSTEM

A lumped-parameter system can be designed to have the equivalent dynamic characteristics to a wheel. It is chosen to have the form shown in Figure I-1, which induces n mass-spring-damper sub-systems in the system. Only the mass m_1 is connected to ground through the spring k_1 and the dashpot c_1, and is in contact with the belt surface with the normal force N and the friction force f_y. The other $n-1$ masses m_i, $i=2\cdots n$ are connected to the mass m_1 through their springs and dashpots separately and experience no friction force. If the frequency response function of m_1 in the lateral direction is equal to that of the continuous wheel system in a particular frequency band, this lumped-parameter system can be used as an equivalent model to simulate the self-excited vibration of the multi-mode wheel on the rigid belt (rail). The method of finding suitable parameter values is described below.

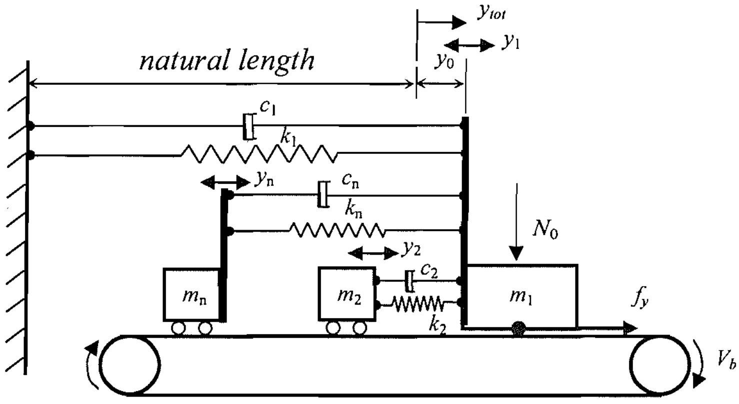

Figure I-1 Equivalent lumped-parameter system of the wheel.

The equations of motion of this n-DOF system are

$$
\begin{aligned}
& m_1\ddot{y}_1 + c_1\dot{y}_1 + k_1 y_1 + \sum_{i=2}^{n}\left(c_i(\dot{y}_1 - \dot{y}_i) + k_i(y_1 - y_i)\right) = f_y \\
& m_2\ddot{y}_2 + c_2(\dot{y}_2 - \dot{y}_1) + k_2(y_2 - y_1) = 0 \\
& \qquad \vdots \\
& m_n\ddot{y}_n + c_n(\dot{y}_n - \dot{y}_1) + k_n(y_n - y_1) = 0
\end{aligned}
\quad . \qquad (I.1)
$$

The system can be described using a $2n$th-order state-space model as follows:

$$\begin{bmatrix} \dot{x}_1 \\ \dot{x}_2 \\ \dot{x}_3 \\ \vdots \\ \dot{x}_n \\ \hline \dot{x}_{n+1} \\ \dot{x}_{n+2} \\ \\ \\ \dot{x}_{2n} \end{bmatrix} = \left[\begin{array}{ccccc|ccccc} -\frac{c_1+\cdots+c_n}{m_1} & \frac{c_2}{m_1} & \frac{c_3}{m_1} & \cdots & \frac{c_n}{m_1} & -\frac{k_1+\cdots+k_n}{m_1} & \frac{k_2}{m_1} & \frac{k_3}{m_1} & \cdots & \frac{k_n}{m_1} \\ \frac{c_2}{m_2} & -\frac{c_2}{m_2} & 0 & \cdots & 0 & \frac{k_2}{m_2} & -\frac{k_2}{m_2} & 0 & \cdots & 0 \\ \frac{c_3}{m_3} & 0 & -\frac{c_3}{m_3} & & 0 & \frac{k_3}{m_3} & 0 & -\frac{k_3}{m_3} & & 0 \\ \vdots & \vdots & & \ddots & & \vdots & \vdots & & \ddots & \\ \frac{c_n}{m_n} & 0 & 0 & & -\frac{c_n}{m_n} & \frac{k_n}{m_n} & 0 & 0 & & -\frac{k_n}{m_n} \\ \hline 1 & & & & & & & & & \\ & 1 & & & & & & & & \\ & & 1 & & & & & & & \\ & & & \ddots & & & & & & \\ & & & & 1 & & & & & \end{array}\right] \begin{bmatrix} x_1 \\ x_2 \\ x_3 \\ \vdots \\ x_n \\ \hline x_{n+1} \\ x_{n+2} \\ x_{n+3} \\ \vdots \\ x_{2n} \end{bmatrix} + \begin{bmatrix} \frac{1}{m_1} \\ 0 \\ 0 \\ \vdots \\ \vdots \\ \vdots \\ \vdots \\ \vdots \\ 0 \end{bmatrix} f_y \tag{I.2}$$

where the state vector is

$$\{\mathbf{x}\} \equiv \left[x_1 \; x_2 \; \cdots \; x_n \; x_{n+1} \; \cdots \; x_{2n}\right]^{\mathrm{T}}, \tag{I.3}$$

with

$$\begin{array}{l} x_1 \equiv \dot{y}_1 \quad x_2 \equiv \dot{y}_2 \quad \cdots \quad x_n \equiv \dot{y}_n \\ x_{n+1} \equiv y_1 \; x_{n+2} \equiv y_2 \; \cdots \; x_{2n} \equiv y_n \end{array} . \tag{I.4}$$

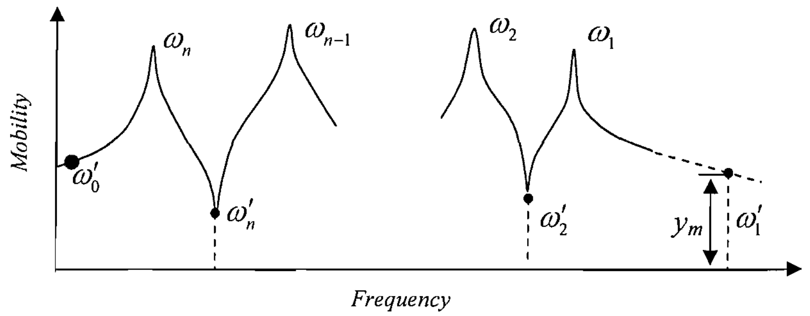

Figure I-2 Mobility (modulus) curve of an *n*-DOF system.

The parameters in Eq.(I.2) are determined from the given frequency response curve. If the curve is a point mobility with n modes, as shown in Figure I-2, n resonances and $n-1$ anti-resonances can be found with frequencies: $\omega_1 > \cdots > \omega_n$, and $\omega_2' > \cdots > \omega_n'$. In addition, one point is selected on the mass-like line with the frequency ω_1' and amplitude y_m (ω_1' should be much higher than the highest natural frequency ω_1, e.g. $\omega_1' > 10\omega_1$) and one point at very low frequency $\omega_0' \approx 0$. Thus, the point mobility at m_1

can be obtained from Eq.(I.1) by assuming the harmonic displacement $y_1 = Y_1 e^{j\omega t}$ and force $f_y = F_1 e^{j\omega t}$:

$$Y_{yy} \equiv \frac{(j\omega)Y_1}{F_1} = (j\omega)/T\,, \tag{I.5}$$

where the term in the denominator is

$$T \equiv \left(-m_1\omega^2 + k_1 + j\omega c_1\right) + \sum_{r=2}^{n}\left(\frac{-m_r\omega^2\left(k_r + j\omega c_r\right)}{-m_r\omega^2 + k_r + j\omega c_r}\right). \tag{I.6}$$

If the damping is very small, eliminating the damping parts in Eq.(I.6) gives:

$$T = \left(-m_1\omega^2 + k_1\right) + \sum_{r=2}^{n}\left(\frac{-m_r\omega^2 k_r}{-m_r\omega^2 + k_r}\right). \tag{I.7}$$

At the anti-resonance frequencies ω'_r, there are the following relationships between m_r and k_r, $r = 2\cdots n$:

$$T(\omega'_r) \rightarrow \infty \;\Rightarrow\; -m_r{\omega'_r}^2 + k_r = 0,\; r = 2\cdots n. \tag{I.8}$$

Thus, Eq.(I.7) can be written as

$$T = \left(-m_1\omega^2 + k_1\right) + \sum_{r=2}^{n}\left(\frac{k_r}{1-(\omega'_r/\omega)^2}\right). \tag{I.9}$$

The denominator of the mobility function is close to zero at the resonance frequencies for small structural damping, which gives

$$T(\omega_i) = 0 \;\Rightarrow\; \left(-m_1\omega_i^2 + k_1\right) + \sum_{r=2}^{n}\left(\frac{k_r}{1-(\omega'_r/\omega_i)^2}\right) = 0,\; i = 1\cdots n, \tag{I.10}$$

where m_1 is obtained at the mass-like line at frequency ω'_1 ($\omega'_1 >> \omega_1$)

$$m_1 = \frac{1}{y_m\omega'_1}. \tag{I.11}$$

From Eq.(I.10), $k_r, r = 1\cdots n$, are determined from the resonance and anti-resonance frequencies

$$\begin{bmatrix} k_1 \\ k_2 \\ \vdots \\ k_n \end{bmatrix} = \begin{bmatrix} 1 & 1/\left(1-(\omega_2^{'}/\omega_1)^2\right) & \cdots & 1/\left(1-(\omega_n^{'}/\omega_1)^2\right) \\ 1 & 1/\left(1-(\omega_2^{'}/\omega_2)^2\right) & \cdots & 1/\left(1-(\omega_n^{'}/\omega_2)^2\right) \\ \vdots & \vdots & \cdots & \vdots \\ 1 & 1/\left(1-(\omega_2^{'}/\omega_n)^2\right) & \cdots & 1/\left(1-(\omega_n^{'}/\omega_n)^2\right) \end{bmatrix}^{\mathrm{T}} \begin{bmatrix} m_1\omega_1^2 \\ m_1\omega_2^2 \\ \vdots \\ m_1\omega_n^2 \end{bmatrix}. \qquad (I.12)$$

Then, m_r, $r = 2\cdots n$ are calculated from Eq.(I.8)

$$m_r = k_r / \omega_r^{'2}, \ r = 2\cdots n. \qquad (I.13)$$

At the resonance frequencies, the mobilities are real values, which are related with the damping coefficients $c_i, i = 1\cdots n$, allowing c_i to be determined. Combining Eqs.(I.5) and (I.6), after some algebraic manipulations, the real part of the inverse of the mobility can be obtained

$$R(\omega) \equiv \mathrm{Re}\{1/Y_{yy}\} = c_1 + \sum_{r=2}^{n} \frac{c_r}{\left(1-\left(\frac{\omega_r^{'}}{\omega}\right)^2\right)^2 + \left(\frac{\omega_r^{'}}{\omega}\right)^2 \left(\frac{c_r^2}{m_r k_r}\right)}. \qquad (I.14)$$

Considering the mobilities at particular frequencies, Eq.(I.14) can be reduced to include only several damping coefficients with the following approximations for the denominator of the right part in Eq.(I.14):

$$\omega << \omega_r^{'}, \ \left(1-\left(\frac{\omega_r^{'}}{\omega}\right)^2\right)^2 + \left(\frac{\omega_r^{'}}{\omega}\right)^2 \left(\frac{c_r^2}{m_r k_r}\right) \rightarrow \infty, \qquad (I.15)$$

$$\omega >> \omega_r^{'}, \ \left(1-\left(\frac{\omega_r^{'}}{\omega}\right)^2\right)^2 + \left(\frac{\omega_r^{'}}{\omega}\right)^2 \left(\frac{c_r^2}{m_r k_r}\right) \rightarrow 1, \qquad (I.16)$$

$$\omega = \omega_r^{'}, \ \left(1-\left(\frac{\omega_r^{'}}{\omega}\right)^2\right)^2 + \left(\frac{\omega_r^{'}}{\omega}\right)^2 \left(\frac{c_r^2}{m_r k_r}\right) \rightarrow \frac{c_r^2}{m_r k_r}. \qquad (I.17)$$

At $\omega = \omega_0$, $\omega_n^{'}$, $\omega_{n-1}^{'} \ldots \omega_2^{'}$, the damping coefficients c_i, $i = 1\cdots n$ can be obtained one by one as follows

$$
\begin{aligned}
&R(\omega_0') = c_1 \\
&R(\omega_n') = c_1 + \frac{m_n k_n}{c_n} \\
&R(\omega_{n-1}') = c_1 + \frac{m_{n-1} k_{n-1}}{c_{n-1}} + c_n \, . \\
&\vdots \\
&R(\omega_2') = c_1 + \frac{m_2 k_2}{c_2} + \sum_{r=3}^{n} c_r
\end{aligned}
\tag{I.18}
$$

This equivalent model is applicable only to those mobilities expressed by FRF curves with anti-resonances between each pair of close resonances (i.e. for point mobilities but not cross or transfer mobilities). Moreover, the model is only suitable for simulating SISO dynamic systems.

APPENDIX J. MODAL DECOMPOSITION IN STATE-SPACE

For a wheel with n modes, the following relationships apply between the motion in the spatial coordinates (6 DOF) and the modal coordinates (n DOF):

$$\{\mathbf{s}(t)\} = [\boldsymbol{\phi}]\{\mathbf{q}(t)\}, \tag{J.1}$$

where the vector of spatial displacements is

$$\{\mathbf{s}(t)\} \equiv \begin{bmatrix} u_1^w(t) & u_2^w(t) & \cdots & u_6^w(t) \end{bmatrix}^{\mathrm{T}}, \tag{J.2}$$

the vector of displacements in the modal coordinates is

$$\{\mathbf{q}(t)\} \equiv \begin{bmatrix} q_1^w(t) & q_2^w(t) & \cdots & q_n^w(t) \end{bmatrix}^{\mathrm{T}}, \tag{J.3}$$

and the modal matrix is formed of the mass normalised modeshape parameters:

$$[\boldsymbol{\phi}] \equiv \begin{bmatrix} \phi_{1,1} & \phi_{1,2} & \cdots & \phi_{1,n} \\ \phi_{2,1} & \phi_{2,2} & \cdots & \phi_{2,n} \\ \vdots & \vdots & \ddots & \vdots \\ \phi_{6,1} & \phi_{6,2} & \cdots & \phi_{6,n} \end{bmatrix}. \tag{J.4}$$

Since the modal matrix is time invariant, the spatial velocities and accelerations are the derivatives of spatial displacements in Eq.(J.1):

$$\{\dot{\mathbf{s}}(t)\} = [\boldsymbol{\phi}]\{\dot{\mathbf{q}}(t)\}, \tag{J.5}$$

$$\{\ddot{\mathbf{s}}(t)\} = [\boldsymbol{\phi}]\{\ddot{\mathbf{q}}(t)\}. \tag{J.6}$$

The modal forces for each mode can be transformed from the spatial forces as follows

$$\{\mathbf{Q}(t)\} = [\boldsymbol{\phi}]^{\mathrm{T}}\{\mathbf{f}(t)\}. \tag{J.7}$$

where the vector of spatial forces (and moments) is

$$\{\mathbf{f}(t)\} \equiv [f_1(t) \quad f_2(t) \quad \cdots \quad f_6(t)]^{\mathrm{T}}, \tag{J.8}$$

the vector of modal forces in their modal coordinates is

$$\{\mathbf{Q}(t)\} = \begin{bmatrix} Q_1(t) & Q_2(t) & \cdots & Q_n(t) \end{bmatrix}^{\mathrm{T}}. \tag{J.9}$$

In the modal coordinates, the equation of motion for mode i is

$$\ddot{q}_i + 2\zeta_i\omega_i\dot{q}_i + \omega_i^2 q_i = Q_i, \tag{J.10}$$

where ζ_i is the damping ratio, ω_i is the natural frequency and Q_i is the modal force. The vector of state variables is written as

$$\{\mathbf{w}\} \equiv \left[w_1, w_2, \cdots, w_{2n}\right]^{\mathrm{T}}, \tag{J.11}$$

where

$$\begin{array}{llll} w_1 \equiv \dot{q}_1 & w_2 \equiv \dot{q}_2 & \cdots & w_n \equiv \dot{q}_n \\ w_{n+1} \equiv q_1 & w_{n+2} \equiv q_2 & \cdots & w_{2n} \equiv q_n \end{array}. \tag{J.12}$$

Eq.(J.10) can be expressed as a set of first-order equations in terms of the state variables:

$$\left[\begin{array}{c}\dot{w}_1\\ \dot{w}_2\\ \vdots\\ \dot{w}_n\\ \hline \dot{w}_{n+1}\\ \dot{w}_{n+2}\\ \vdots\\ \dot{w}_{2n}\end{array}\right]=\left[\begin{array}{cccc|cccc} -2\zeta_1\omega_1 & & & & -\omega_1^2 & & & \\ & -2\zeta_2\omega_2 & & & & -\omega_2^2 & & \\ & & \ddots & & & & \ddots & \\ & & & -2\zeta_n\omega_n & & & & -\omega_n^2 \\ \hline 1 & & & & & & & \\ & 1 & & & & [0] & & \\ & & \ddots & & & & & \\ & & & 1 & & & & \end{array}\right]\left[\begin{array}{c}w_1\\ w_2\\ \vdots\\ w_n\\ \hline w_{n+1}\\ w_{n+2}\\ \vdots\\ w_{2n}\end{array}\right]+\left[\begin{array}{c}Q_1\\ Q_2\\ \vdots\\ Q_n\\ \hline 0\\ 0\\ \vdots\\ 0\end{array}\right]. \tag{J.13}$$

Defining the modal forces vector:

$$\{\mathbf{f}_{\mathrm{m}}\} \equiv \left[\underbrace{Q_1 \quad Q_2 \quad \cdots \quad Q_n}_{n}, \quad \underbrace{0 \quad 0 \quad \cdots \quad 0}_{n}\right]^{\mathrm{T}}, \tag{J.14}$$

and the system matrix:

$$[\mathbf{A}^{\mathrm{w}}] \equiv \left[\begin{array}{cccc|cccc} -2\zeta_1\omega_1 & & & & -\omega_1^2 & & & \\ & -2\zeta_2\omega_2 & & & & -\omega_2^2 & & \\ & & \ddots & & & & \ddots & \\ & & & -2\zeta_n\omega_n & & & & -\omega_n^2 \\ \hline 1 & & & & & & & \\ & 1 & & & & & & \\ & & \ddots & & & & & \\ & & & 1 & & & & \end{array}\right], \tag{J.15}$$

Eq.(J.13) is rewritten as

$$\{\dot{\mathbf{w}}\} = [\mathbf{A}^{\mathrm{w}}]\{\mathbf{w}\} + \{\mathbf{f}_{\mathrm{m}}\}. \tag{J.16}$$

In the state-space model, the relationships between the input forces and the responses are shown in Figure J-1. The vectors and matrices in the loop are defined as follows.

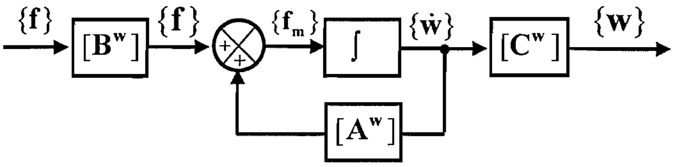

Figure J-1 Wheel model in the state-space form

The vector of wheel velocities, (6×1), is

$$\{\mathbf{r}^{\mathrm{w}}\} \equiv \begin{bmatrix} v_1^w & v_2^w & v_3^w & v_4^w & v_5^w & v_6^w \end{bmatrix}^{\mathrm{T}}. \tag{J.17}$$

The vector of dynamic forces (moments), (6×1) is

$$\{\mathbf{f}\} \equiv \begin{bmatrix} f_1 & f_2 & \cdots & f_6 \end{bmatrix}^{\mathrm{T}}. \tag{J.18}$$

The matrix $[\mathbf{B}^{\mathrm{w}}]$ is extended from the modal matrix in Eq.(J.4) by zero padding,

$$[\mathbf{B}^{\mathrm{w}}] \equiv \left[\begin{array}{cccc|cccc} \phi_{1,1} & \phi_{1,2} & \cdots & \phi_{1,n} & 0 & 0 & \cdots & 0 \\ \phi_{2,1} & \phi_{2,2} & \cdots & \phi_{2,n} & 0 & 0 & \cdots & 0 \\ \vdots & \vdots & & \vdots & \vdots & \vdots & & \vdots \\ \phi_{6,1} & \phi_{6,2} & \cdots & \phi_{6,n} & 0 & 0 & \cdots & 0 \end{array}\right]^{\mathrm{T}}, \tag{J.19}$$

which transfers the spatial forces to the modal forces as follows

$$\{\mathbf{f}_{\mathrm{m}}\} = [\mathbf{B}^{\mathrm{w}}]\{\mathbf{f}\}. \tag{J.20}$$

The output matrix $[\mathbf{C}^{\mathrm{w}}]$ is also related to the modal matrix in Eq.(J.4) by zero padding,

$$[\mathbf{C}^{\mathrm{w}}] \equiv \left[\begin{array}{cccc|cccc} \phi_{1,1} & \phi_{1,2} & \cdots & \phi_{1,n} & 0 & 0 & \cdots & 0 \\ \phi_{2,1} & \phi_{2,2} & \cdots & \phi_{2,n} & 0 & 0 & \cdots & 0 \\ \vdots & \vdots & \ddots & \vdots & \vdots & \vdots & \ddots & \vdots \\ \phi_{6,1} & \phi_{6,2} & \cdots & \phi_{6,n} & 0 & 0 & \cdots & 0 \end{array}\right], \tag{J.21}$$

which transfers the state-space variables (the movements in the modal coordinates of the wheel) to the spatial velocities

$$\{\mathbf{r}^{\mathrm{w}}\} = [\mathbf{C}^{\mathrm{w}}]\{\mathbf{w}\}. \tag{J.22}$$

APPENDIX K. RAIL MODEL IN THE SPIN DIRECTION

The rail can be considered as an infinite uniform beam installed on the rail pads, as shown in Figure K-1. The free vibration of the beam in the xy-plane (i.e. laterally) is treated as a Timoshenko beam [79], as shown in Figure K-2, where the spring mattress connected with the rail represents the effect of rail pads.

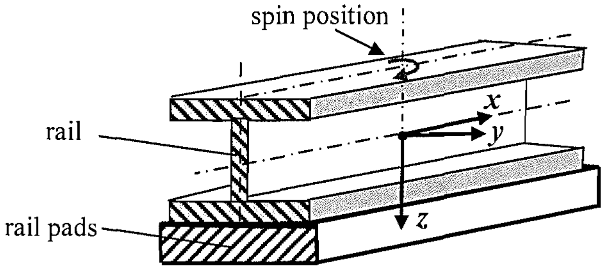

Figure K-1 Spin on the top of rail.

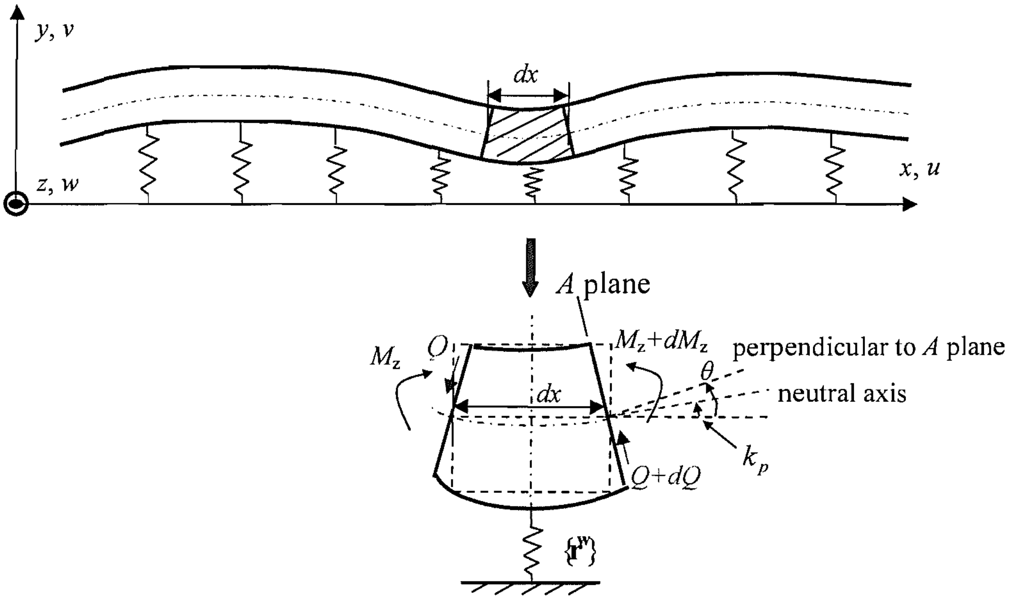

Figure K-2 Free vibration of the Timoshenko beam on the elastic foundation.

K.1 Equations of motion

In the x-y plane, the rotation of a cross-section is due to the bending angle $\theta_b = \partial v / \partial x$ and shear angle θ_s:

$$\theta = \theta_b + \theta_s . \tag{K.1}$$

The axial deformation can be expressed by the rotation angle

$$u = -y\theta,\ \frac{\partial u}{\partial y} = -\theta\,. \tag{K.2}$$

This gives the shear strain:

$$\gamma_{xy} = \frac{\partial v}{\partial x} + \frac{\delta u}{\delta y} = \frac{\partial v}{\partial x} - \theta\,. \tag{K.3}$$

Then, the shear stress is

$$\tau_{xy} = G\gamma_{xy} = G\left(\frac{\partial v}{\partial x} - \theta\right), \tag{K.4}$$

where the shear modulus is

$$G = \frac{E}{2(1+\nu)}\,. \tag{K.5}$$

Actually, the shear stress is not constant over the cross-section. In order to compensate for this, a numerical factor κ, (geometrical) Timoshenko shear coefficient, is introduced, so that

$$\tau_{xy} = \kappa G\left(\frac{\partial v}{\partial x} - \theta\right), \tag{K.6}$$

where the value of the factor κ depends on the shape of the cross-section, and is given by the ratio of the average shear stress and the maximum shear stress over the cross-section area:

$$\kappa \equiv \frac{\text{average shear stress}}{\text{maximum shear stress}}\,. \tag{K.7}$$

The shear force can be obtained from the averaged shear stress:

$$Q = A\tau_{xy} = \kappa AG\left(\frac{\partial v}{\partial x} - \theta\right). \tag{K.8}$$

The bending moment M_z results from the normal stress (forces) σ_{xx}:

$$M_z = -y \int_A \sigma_{xx} dA \,, \tag{K.9}$$

where the normal stress can be expressed in terms of the rotation θ with following deductions.

With the assumption of no axial load (in the longitudinal direction of the rail), the strain along the x-direction is

$$\varepsilon_{xx} = \frac{1}{E}[\sigma_{xx} - \nu(\sigma_{yy} + \sigma_{zz})] \,. \tag{K.10}$$

Only the stress along the x-direction is important and other stresses can be ignored, therefore Eq.(K.10) is reduced to

$$\varepsilon_{xx} = \sigma_{xx} / E \,. \tag{K.11}$$

Since the relationship between the deflection and stress is

$$\varepsilon_{xx} = \partial u / \partial x \,, \tag{K.12}$$

substitution of u from Eq.(K.2) gives

$$\varepsilon_{xx} = -y(\partial \theta / \partial x) \,. \tag{K.13}$$

Combination of Eq.(K.13) and Eq.(K.11) obtains the stress in terms of the rotation:

$$\sigma_{xx} = -Ey(\partial \theta / \partial x) \,. \tag{K.14}$$

Substituting the stress from Eq.(K.14) into Eq.(K.9), the bending moment is

$$M_z = E(\partial \theta / \partial x) \int_A y^2 dA \,. \tag{K.15}$$

With the assumption that the cross-section is symmetric, Eq.(K.15) can be rewritten as

$$M_z = E(\partial \theta / \partial x) I_z \,, \tag{K.16}$$

where the second moment of area about the z axis is:

$$I_z = \int_A y^2 dA \,. \tag{K.17}$$

The angular motion around the centre of the isolated body of length dx satisfies (Newton's 2nd law of motion):

$$\rho I_z dx(\frac{\partial^2\theta}{\partial t^2}) = -M_z + \left(M_z + \frac{\partial M_z}{\partial x}dx\right) + Q\frac{dx}{2} + \left(Q + \frac{\partial Q}{\partial x}dx\right)\frac{dx}{2}, \qquad \text{(K.18)}$$

where Q is the shear force.

Ignoring the terms involving $(dx)^2$ in Eq.(K.18), substituting the shear force Q from Eq.(K.8) and the bending moment from Eq.(K.16), the angular motion is rewritten as

$$GA\kappa\left(\theta - \frac{\partial v}{\partial x}\right) + \rho I_z \frac{\partial^2\theta}{\partial t^2} - EI_z \frac{\partial^2\theta}{\partial x^2} = 0\,. \qquad \text{(K.19)}$$

Since the rail pads give the spring effect on the rail, the linear motion in the y-direction satisfies (Newton's 2nd law of motion):

$$\rho A dx \frac{\partial^2 v}{\partial t^2} + (k_p dx)v = -Q + \left(Q + \frac{\partial Q}{\partial x}dx\right), \qquad \text{(K.20)}$$

where k_p is averaged transverse stiffness of rail pads per metre.

Substituting the shear force Q from Eq.(K.8) into Eq.(K.20), the linear motion is

$$GA\kappa\frac{\partial}{\partial x}\left(\theta - \frac{\partial v}{\partial x}\right) + k_p v + \rho A \frac{\partial^2 v}{\partial t^2} = 0\,. \qquad \text{(K.21)}$$

The equations of motion for a Timoshenko beam on an elastic foundation of stiffness per unit length k_p are given by Eq.(K.19) and Eq.(K.21).

K.2 Free wave solutions

The free wave solutions of the Timoshenko beam can exist in the form:

$$v(x,t) = Ve^{j\omega t}e^{jkx}, \qquad \text{(K.22)}$$

$$\theta(x,t) = \Theta e^{j\omega t}e^{jkx}, \qquad \text{(K.23)}$$

where V and Θ are the complex amplitude of v and θ respectively.

Substituting Eq.(K.22) and Eq.(K.23) into the equations of motion Eq.(K.19) and Eq.(K.21), both can provide the ratio between V and Θ as follows:

$$\frac{V}{\Theta}=\frac{-jk\left(GA\kappa\right)}{-\rho A\omega^2+k_p+\left(GA\kappa\right)k^2}, \tag{K.24}$$

$$\frac{V}{\Theta}=\frac{-\rho I_z\omega^2+\left(GA\kappa\right)+EI_Zk^2}{jk\left(GA\kappa\right)}. \tag{K.25}$$

Combining Eq.(K.24) and Eq.(K.25), after some algebra, gives a quadratic for k^2:

$$k^4+C_2(\omega)k^2+C_3(\omega)=0, \tag{K.26}$$

where

$$C_2(\omega)\equiv\left(\frac{k_p-\rho A\omega^2}{GA\kappa}\right)-\left(\frac{\rho I_z\omega^2}{EI_z}\right), \tag{K.27}$$

$$C_3(\omega)\equiv\left(\frac{k_p-\rho A\omega^2}{EI_z}\right)\left(1-\frac{\rho I_z\omega^2}{GA\kappa}\right). \tag{K.28}$$

K.3 Mobility for the spin direction

The equation of bending motion in Eq.(K.19) can be extended to include excitation by a moment at $x=0$, which gives:

$$GA\kappa\left(\theta-\frac{\partial v}{\partial x}\right)+\rho I_z\frac{\partial^2\theta}{\partial t^2}-EI_z\frac{\partial^2\theta}{\partial x^2}=M\delta(0)e^{j\omega t}. \tag{K.29}$$

Taking Fourier transforms of Eq.(K.29) with respect to x gives:

$$GA\kappa\left(\Theta-Vjk\right)-\rho I_z\omega^2\Theta+EI_zk^2\Theta=M. \tag{K.30}$$

Combining Eq.(K.24) and Eq.(K.30), after some algebra, gives the rotational receptance:

$$\frac{\Theta}{M}=\frac{1}{EI_z}\frac{k^2+C_1(\omega)}{k^4+C_2(\omega)k^2+C_3(\omega)} \tag{K.31}$$

where

$$C_1(\omega) \equiv \frac{k_p - \rho A \omega^2}{GA\kappa}. \tag{K.32}$$

Taking the inverse Fourier transform, the receptance for the spin motion about the z-axis is given as

$$\alpha_{66}(x) \equiv \frac{\theta(x)}{M} = \frac{1}{2\pi} \int_{-\infty}^{+\infty} \left(\frac{1}{EI_z} \frac{k^2 + C_1(\omega)}{k^4 + C_2(\omega)k^2 + C_3(\omega)} \right) e^{jkx} dk. \tag{K.33}$$

To solve the integral, an appropriate contour integration is adopted. The contour should be closed at infinity in the upper half plane of k, and include the real axis. The poles enclosed in the contour should have positive imaginary parts. The integral is equal to $2\pi j$ times the sum of the residues of the poles enclosed:

$$\alpha_{66}(x) = \frac{2\pi j}{2\pi} \sum_{\substack{n \text{ with} \\ \mathrm{Im}(k_n)>0}} \mathrm{Res}(k_n), \tag{K.34}$$

where the residue is

$$\mathrm{Res}(k_n) = \frac{e^{jk_n x}}{EI_z} \left(\frac{k_n^2 + C_1(\omega)}{4k_n^3 + 2C_2(\omega)k_n} \right). \tag{K.35}$$

The mobility for the spin direction at $x = 0$ is thus

$$Y_{66} = -\frac{\omega}{EI_z} \sum_{\substack{n \text{ with} \\ \mathrm{Im}(k_n)>0}} \left(\frac{k_n^2 + C_1(\omega)}{4k_n^3 + 2C_2(\omega)k_n} \right). \tag{K.36}$$

This spin mobility can also be modelled using Euler-Bernoulli beam theory, which is directly provided here:

$$Y_{66}^E = \frac{(1+j)\omega^{1/2}}{4(EI_z)^{3/4}\left(\rho A - k_p/\omega^2\right)^{1/4}}. \tag{K.37}$$

In Figure K-3, two spin mobility curves are shown, based on the Timoshenko beam and Euler-Bernoulli beam respectively. These are calculated up to 10 kHz using the same parameters of a standard UIC 60 rail, see Table E-1. The two results are consistent with each other up to 2 kHz. At higher frequency, the mobility of the Timoshenko beam is more flexible. Timoshenko beam theory constitutes an improvement over Euler-Bernoulli theory, in that it incorporates shear deformation and rotational inertia effects. The shear effect plays an important role at high frequency, making the beam more flexible. In the squeal analysis, the frequency range of interest extends up to 5000 Hz, so the spin mobility from the Timoshenko beam theory is preferred.

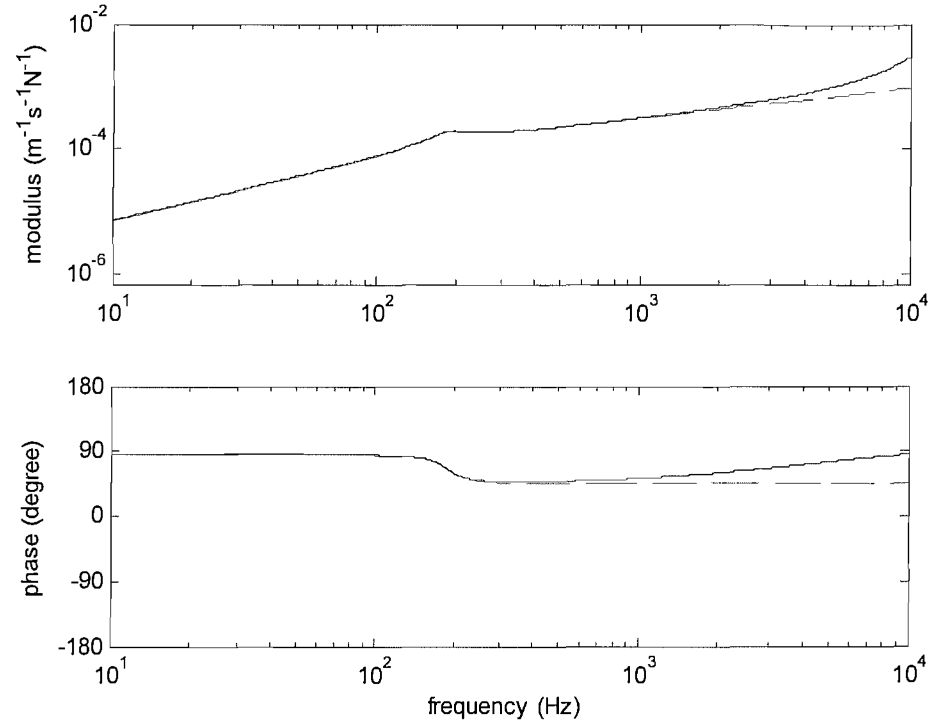

Figure K-3 Spin mobility of a standard UIC 60 rail: —— Timoshenko beam, — — Euler-Bernoulli beam.

APPENDIX L. EQUIVALENT SYSTEMS OF A UIC 60 RAIL

For an arbitrary FRF curve, it is always possible to find an equivalent system with a transfer function expressed in the form of a ratio of two polynomials

$$H(s)=\frac{B(s)}{A(s)}=\frac{b_1 s^{m-1}+b_2 s^{m-2}+\cdots+b_m}{s^m+a_1 s^{m-1}+a_2 s^{m-2}+\cdots+a_m}. \tag{L.1}$$

The Signal Processing Toolbox of MATLAB provides the function '*invfreqs*', which can be used to find a continuous-time transfer function that corresponds to a given complex frequency response.

With this method, after trial-and-error in terms of the orders required, the equivalent systems corresponding to the mobilities of a standard UIC 60 rail (see Table E-1), in the longitudinal, lateral, vertical and spin directions, are obtained. The coefficients of the equivalent systems are provided in Table L-1. The equivalent systems are compared with the rail mobilities in Figure L-1 to Figure L-4.

Table L-1 Coefficients of the equivalent systems of a UIC 60 rail

i	Y_{11}^r		Y_{22}^r		Y_{33}^r		Y_{66}^r	
	a_i	b_i	a_i	b_i	a_i	b_i	a_i	b_i
1	4.80×10^4	7.50×10^{-2}	4.47×10^4	0.56	8.13×10^4	-2.30×10^{-2}	9.20×10^4	1.70×10^2
2	6.96×10^7	9.07×10^1	1.34×10^9	8.50×10^3	9.90×10^9	2.89×10^4	6.67×10^9	2.50×10^6
3	1.21×10^{11}	1.54×10^5	3.91×10^{13}	5.37×10^8	1.71×10^{14}	6.56×10^8	3.61×10^{13}	4.98×10^9
4	7.45×10^{13}	1.58×10^6	5.09×10^{17}	6.02×10^{12}	3.78×10^{17}	3.04×10^{12}	4.12×10^{16}	5.36×10^{12}
5			9.21×10^{21}	1.44×10^{17}	2.04×10^{21}	4.19×10^{15}	4.65×10^{19}	1.86×10^{14}
6			5.06×10^{25}	1.03×10^{21}	1.03×10^{24}	5.41×10^{18}		
7			5.48×10^{29}	8.97×10^{24}	6.92×10^{26}	5.23×10^{20}		
8			1.15×10^{33}	4.26×10^{28}				
9			3.33×10^{36}	5.72×10^{31}				
10			2.45×10^{39}	1.18×10^{35}				
11			2.35×10^{42}	2.67×10^{36}				

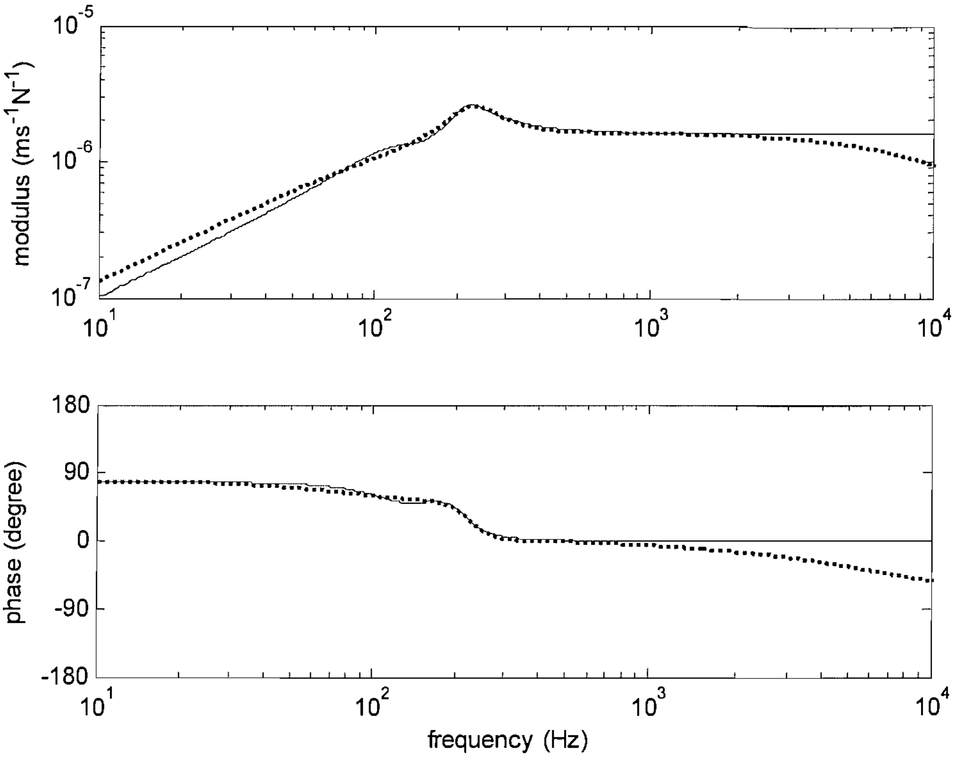

Figure L-1 Longitudinal mobility Y_{11}^{r} of a UIC60 rail at the nominal contact point: —— analytical system [53], ····· fourth order equivalent system.

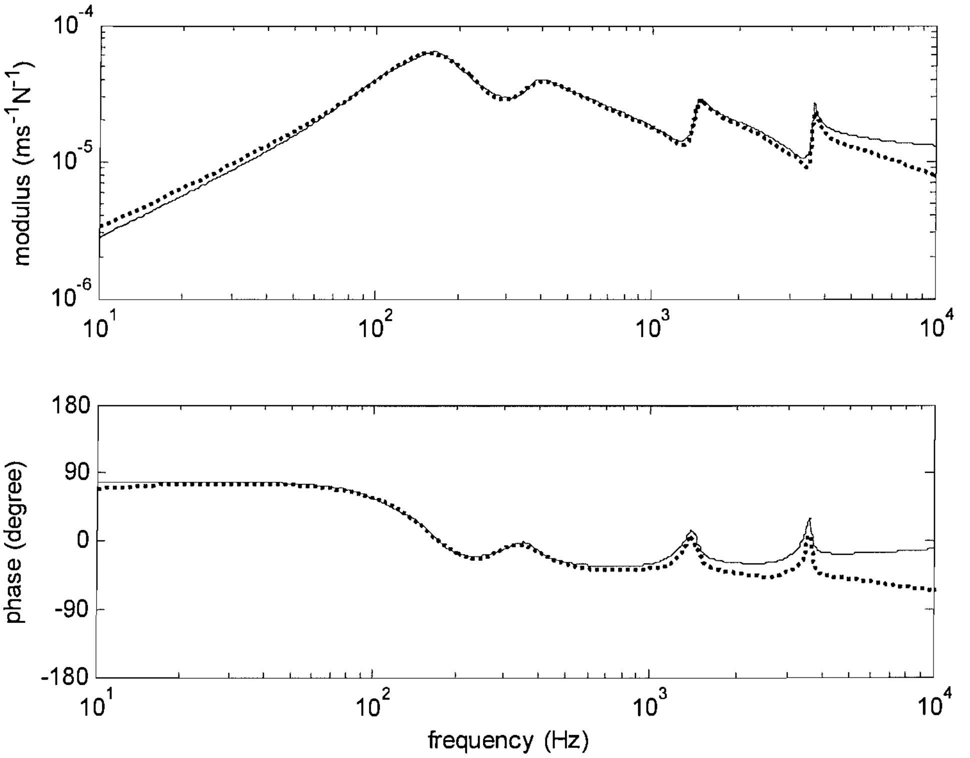

Figure L-2 Lateral mobility Y_{22}^{r} of a UIC60 rail at the nominal contact point: —— analytical system [52], ····· 11th order equivalent system.

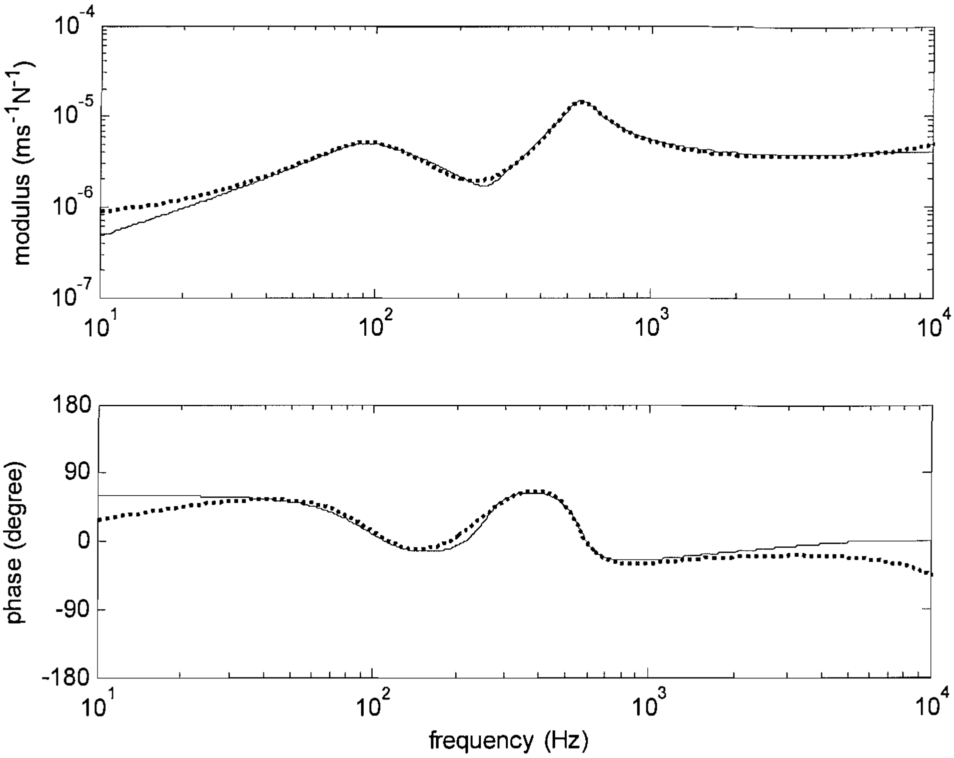

Figure L-3 Vertical mobility Y_{33}^{r} of a UIC60 rail at the nominal contact point: —— analytical system [52], ····· seventh order equivalent system.

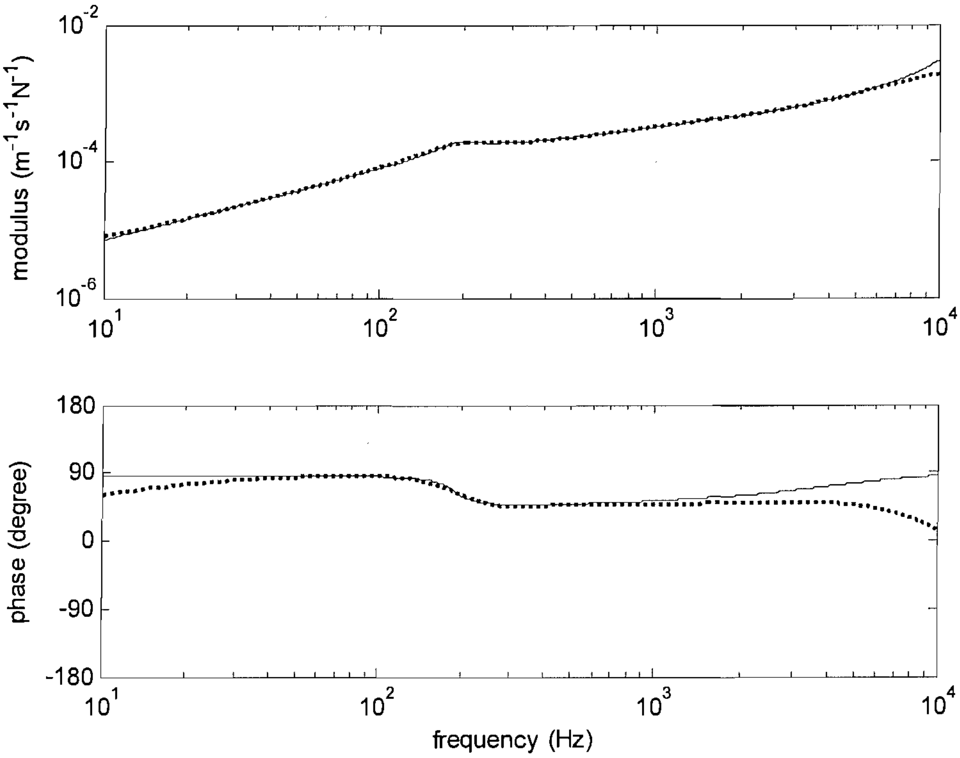

Figure L-4 Spin mobility Y_{66}^{r} of a UIC60 rail at the nominal contact point: —— analytical system (Appendix K), ····· fifth order equivalent system.

APPENDIX M. CONTINUOUS-TIME SYSTEMS IN STATE-SPACE

For a continuous-time system, different forms of state-space system can be obtained by choosing different sets of state-variable vectors. Here a continuous-time system, which has the same form as that of Direct II digital filter [80], is introduced as follows. The transfer function $H(s)$ in Eq.(M.1) has the same physical meaning of an ARMA (autoregressive and moving-average) digital system, which can be broken into a product of two transfer functions $H_1(s)$ (AR component) and $H_2(s)$ (MA component):

$$H(s) = H_1(s) \cdot H_2(s), \tag{M.1}$$

where $H_1(s)$ contains the denominator and $H_2(s)$ contains the numerator ($b_k = 0$, $k \leq m-n$):

$$H_1(s) \equiv \frac{1}{s^m + a_1 s^{m-1} + \cdots + a_m}, \tag{M.2}$$

$$H_2(s) \equiv b_1 s^{m-1} + \cdots + b_m. \tag{M.3}$$

The output of the system is obtained by calculating an intermediate result $P(s)$ as follows:

$$P(s) = H_1(s) \cdot X(s) \tag{M.4}$$

$$Y(s) = H_2(s) \cdot P(s). \tag{M.5}$$

The time function $p(t)$ corresponding to $P(s)$ can be obtained from Eq.(M.4) by applying the inverse Laplace transform:

$$\begin{gathered} P(s)\left(s^m + a_1 s^{m-1} + \cdots + a_m\right) = X(s) \xrightarrow{L^{-1}} \\ D^m p(t) = x(t) - \sum_{k=1}^{m} a_k \left(D^{m-k} p(t)\right), \text{ if } (D^{k-1} p(0)) = 0,\ k = 1, 2, \cdots, m \end{gathered} \tag{M.6}$$

where D represents the differential operator d/dt.

The vector of state variables is defined as

$$\{\mathbf{r}\} \equiv [r_1, r_2, \cdots, r_m]^{\mathrm{T}}, \tag{M.7}$$

where

$$r_1 \equiv D^{m-1}p(t) \quad r_2 \equiv D^{m-2}p(t) \quad \cdots \quad r_m \equiv p(t). \tag{M.8}$$

Thus, from Eq.(M.6), the state equation takes the following form:

$$\begin{bmatrix} \dot{r}_1 \\ \dot{r}_2 \\ \dot{r}_3 \\ \vdots \\ \dot{r}_m \end{bmatrix} = \begin{bmatrix} -a_1 & -a_2 & \cdots & -a_{m-1} & -a_m \\ 1 & 0 & \cdots & 0 & 0 \\ 0 & 1 & & 0 & 0 \\ \vdots & & \ddots & \vdots & \vdots \\ 0 & 0 & \cdots & 1 & 0 \end{bmatrix} \begin{bmatrix} r_1 \\ r_2 \\ r_3 \\ \vdots \\ r_m \end{bmatrix} + \begin{bmatrix} 1 \\ 0 \\ 0 \\ \vdots \\ 0 \end{bmatrix} x(t). \tag{M.9}$$

The output $y(t)$ can be obtained from Eq.(M.5) via inverse Laplace transform:

$$\begin{aligned} &Y(s) = P(s)\left(b_1 s^{m-1} + \cdots + b_m\right) \xrightarrow{L^{-1}} \\ &y(t) = \sum_{k=1}^{m} b_k \left(D^{m-k}p(t)\right), \text{ if } (D^{k-1}p(0)) = 0,\ k = 1,2\cdots,m \end{aligned}. \tag{M.10}$$

Hence, the output can be represented by the state vector:

$$y(t) = \left[b_1, \quad b_2, \quad \cdots, \quad b_m\right]\{\mathbf{r}\}. \tag{M.11}$$

Using matrix notation, Eq.(M.9) and Eq.(M.11) can be written as

$$\{\dot{\mathbf{r}}\} = [\mathbf{A}]\{\mathbf{r}\} + [\mathbf{B}]x, \tag{M.12}$$

$$y = [\mathbf{C}]\{\mathbf{r}\}, \tag{M.13}$$

where the system matrix is

$$[\mathbf{A}] = \begin{bmatrix} -a_1 & -a_2 & \cdots & -a_{m-1} & -a_m \\ 1 & 0 & \cdots & 0 & 0 \\ 0 & 1 & & 0 & 0 \\ \vdots & & \ddots & \vdots & \vdots \\ 0 & 0 & \cdots & 1 & 0 \end{bmatrix}, \tag{M.14}$$

the input matrix is

$$[\mathbf{B}] = \left[1 \quad 0, \quad \cdots, \quad 0\right]^{\mathrm{T}}, \tag{M.15}$$

and the output matrix is

$$[\mathbf{C}] = \left[b_1, \quad b_2, \quad \cdots, \quad b_m\right]. \tag{M.16}$$

REFERENCES.

1. Thompson, D.J. and Jones, C.J.C., Chapter 10. Noise and vibration from railway vehicles; Iwnicki, S. (ed.), Handbook of railway vehicle dynamics. CRC Press, 2006.
2. Thompson, D.J. and Jones, C.J.C., A review of the modelling of wheel/rail noise generation. *Journal of Sound and Vibration*, 231, 519-536, 2000.
3. Müller, B. and Oertli, J., Combatting curve squeal: Monitoring applications. *Journal of Sound and Vibration*, 293, 728-734, 2006.
4. Eadie, D.T., Santoro, M., Top-of-rail friction control for curve noise mitigation and corrugation rate reduction. *Journal of Sound and Vibration*, 293, 747-757, 2006.
5. Wetta, P. and Demilly, F., Reduction of wheel squeal noise generated on curves or during braking. *11th International of Wheelset Congress*, Paris, 301-306, June, 1995.
6. Von Stappenbeck, H., Streetcar curve noise (in German). Zeitschrift V.D.I. 96, 1954.
7. Rudd, M.J., Wheel/rail noise – Part II: wheel squeal. *Journal of Sound and Vibration*, 46, 381-394, 1976.
8. Van Ruiten, C.J.M., Mechanism of squeal noise generated by trams. *Journal of Sound and Vibration*, 120, 245-253, 1988.
9. Remington, P.J., Wheel/rail squeal and impact noise: What do we know? What don't we know? Where do we go from here? *Journal of Sound and Vibration*, 116, 339-353, 1985.
10. Schneider, E., Popp, K., Irretier, H., Noise generation in railway wheels due to rail-wheel contact forces. *Journal of Sound and Vibration*, 120, 227-244, 1988.
11. Fingberg, U., A model of wheel-rail squealing noise. *Journal of Sound and Vibration*, 143, 365-377, 1990.
12. Périard, F., Wheel-rail noise generation: curve squealing by trams. *Ph.D. Dissertation, Technische Universiteit Delft*, ISBN 90-9011964-7, NUGI 834, 1998.
13. Heckl, M.A. and Abrahams, I.D., Curve squeal of train wheels, part 1: Mathematical model for its generation. *Journal of Sound and Vibration*, 229, 669-693, 2000.
14. De Beer, F.G., Janssens, M.H.A. and Kooijman, P.P., Squeal noise of rail-bound vehicles influenced by lateral contact position. *Journal of Sound and Vibration*, 267,

497-507, 2003.

15. Monk-Steel, A. and Thompson, D.J., Models for railway curve squeal noise. *8th Conf. on Recent Advances in Structural Dynamics*, Southampton, UK, July, 2003.

16. Chiello, O., Ayasse, J.-B., Vincent, N. and Koch, J.-R., Curve squeal of urban rolling stock- Part 3: Theoretical model. *Journal of Sound and Vibration*, 293, 710-727, 2006.

17. Cataldi-Spinola, E., Glocker, C., Curve squealing of railroad vehicles. ENOC-2005, Eindhoven, Netherlands, Aug. 2005.

18. Kraft, K., Der Einfluß der Fahrgeschwindigkeit auf den Haftwert zwischen Rad und Schiene. *AET 22 addendum to ETR*, 58-78, 1967.

19. Kalker, J.J., Survey of wheel-rail rolling contact theory. *Vehicle System Dynamics,* 5, 317-358, 1979.

20. Heckl, M.A., Curve squeal of train wheels, part 2: Which wheel modes are prone to squeal? *Journal of Sound and Vibration*, 229, 695-707, 2000.

21. Heckl, M.A. and Huang, X.Y., Curve squeal of train wheels, part 3: Active control. *Journal of Sound and Vibration*, 229, 709-735, 2000.

22. Thompson, D.J. and Janssens, M.H.A, Theoretical manual, version 2.4. TNO report TPD-HAG-RPT-930214. *TWINS – Track-wheel interaction noise software*, 1997.

23. Koch, J.R., Vincent, N., Chollet, H. and Chiello, O., Curve squeal of urban rolling stock-Part 2: Parametric study on a ¼ scale test rig. *Journal of Sound and Vibration*, 293, 701-709, 2006.

24. Kinkaid, N.M., O'Reilly, O.M., Papadopoulos, P., Automotive disc brake squeal. *Journal of Sound and Vibration*, 267, 105-166, 2003.

25. Mills, H.R., Brake squeak. Technical Report 9000 B, Institution of Automobile Engineers, 1938.

26. Bowden, F.P. and Leben, L., The nature of sliding and the analysis of friction. *Royal Society of London Proceedings Series A Mathematics Physics and Engineering Science*, 169, 371-391, 1939.

27. Blok, H., Fundamental mechanical aspects of boundary lubrication. *SAE Journal*, 46, 54-68, 1940.

28. Eriksson, M. and Jacobson, S., Friction behaviour and squeal generation of disc brakes at low speeds. *Proceedings of the Institution of Mechanical Engineers D*, 215 (D12), 1245-1256, 2001.

29. Spurr, R.T., A theory of brake squeal. *Proceedings of the Automobile Division, Institution of Mechanical Engineers*,1961 1962, 33-52, 1961.

30. North, M.R., Disc brake squeal — a theoretical model. Technical Report 1972/5, Motor Industry Research Association, Warwickshire, England, 1972.

31. Ouyang, H., Mottershead, J.E., Brookfield, D.J., James, S., Cartmell, M.P., Kaster, T., Treyde, T., Hirst, B. and Allen, R., Dynamic instabilities in a simple model of a car disc brake. Technical Report 1999-01-3409, SAE, Warrendale, PA, 1999.

32. Bowden, F.P. and Tabor, D., The friction and lubrication of solids Part I. Oxford University Press, 1950.

33. Hertz, H., Über die Berührung fester elastischer Körper (On the contact of elastic solids). *Journal für die Reine und Angewandte Mathematik*, 92, 156-171, 1881.

34. Hertz, H., On the contact of elastic solids. Papers by Hertz H., Jones and Schott Macmillan London, 166-171, 1896.

35. Johnson, K.L., Contact Mechanics. Cambridge University Press, 1987.

36. Kalker, J.J., A fast algorithm for the simplified theory of rolling contact. *Vehicle System Dynamics*, 11, 1-13, 1982.

37. Kalker, J.J., Simplified theory of rolling contact. Delft Progress Report 1, 1-10, 1973.

38. Shen, Z.Y., Hedrick, J.K., Elkins, J.A., A comparison of alternative creep-force models for rail vehicle dynamic analysis. IAVSD, Cambridge, Ma. USA, 591-605, 1984

39. Monk-Steel, A.D., Thompson, D.J., de Beer, F.G. and Janssens, M.H.A., An investigation into the influence of longitudinal creepage on railway squeal noise due to lateral creepage. *Journal of Sound and Vibration*, 293, 766-776, 2006.

40. Wickens, A.H., Fundamentals of Rail Vehicle Dynamics – Guidance and Stability. Swets & Zeitlinger Publishers, Lisse, 2003.

41. Redtenbacher, F.J., Die Gesetze des locomotiv-Baues. Verlag von Friedrich

Bassermann, Mannheim, 22, 1855.

42. Mackenzie, J., Resistance on railway curves as an element of danger. *Proc. Inst. Civ. Engs.*, 74, 1-57, 1883.
43. Porter, S.R.M., The mechanics of a locomotive on curved track. *The railway Gazette*, London, 1935.
44. Boocock, D., Steady-state motion of railway vehicles on curved track. *Journal Mech. Eng. Sci.*, 11, 556-566, 1969.
45. Newland, D.E., Steering characteristics of bogies. *The Railway Gazette*, 124, 745-750, 1968.
46. Elkins, J.A. and Gostlling, R.J., A general quasi-static curving theory for railway vehicles. In: A. Slibar and H. Springer (Eds.): The Dynamics of Vehicles on Roads and Tracks, *Proc. 5th IAVSD Symposium*, Vienna, September 1977. Swets and Zeitlinger Publishers, Lisse, 388-406, 1978.
47. VAMPIRE user manual, version 4.2. AEA Technology plc.
48. Nayak, P.R. and Paul, I.L., A new theory of rolling contact. MIT Report DSR-76109-7, 1968.
49. Kalker, J.J., A simplified theory for non-Hertzian contact. In: J.K. Hedrick (Ed.): The Dynamics of Vehicles on Roads and Tracks, *Proc. 8th IAVSD Symposium*, Cambridge, Mass., August 1983, 295-302. Swets and Zeitlinger Publishers, Lisse, 1984.
50. Thompson, D.J. and Monk-Steel, A.D., A theoretical model for curve squeal. Technical Memorandum 904, ISVR, University of Southampton, 2003.
51. Xie, G., Allen, P.D., Iwnichi, S.D., Alonso, A., Thompson, D.J., Jones, C.J.C. and Huang, Z.Y., The introduction of falling coefficients into curving calculations for studying curve squeal noise. *IAVSD*, Milan, Italy, 2005.
52. Wu, T.X. and Thompson, D.J., Theoretical investigation of wheel/rail non-linear interaction due to roughness excitation. *Vehicle System Dynamics*, 34, 261 - 282, 2000.
53. Lurcock, D.E.J., An investigation into the longitudinal vibration properties of railway track. BEng Thesis, ISVR, University of Southampton, 2004.

54. Signal Processing Toolbox User's Guide. Matlab® 2006a, The Mathworks, 2006.

55. Dahlberg T., Chapter 6. Track issues; Iwnicki, S. (ed), Handbook of railway vehicle dynamics. CRC Press, 2006.

56. Dutton, K., The Art of Control Engineering. Prentice Hall, 120-125, 1997.

57. Barman, J.F. and Katzenelson, J., A generalized Nyquist-type stability criterion for multivariable feedback systems. *International Journal of Control*, 20, 593-622, 1974.

58. MacFarlane, A.G.J. and Postlethwaite, I., The generalized Nyquist stability criterion and multivariable root loci. *International Journal of Control*, 25, 81-127, 1977.

59. Desoer, C.A. and Wang, Y., On the generalized Nyquist stability criterion. *IEEE Transactions on Automatic Control*, 25, 187-196, 1980.

60. Brockett, R.W. and Byrnes, C.I., Multivariable Nyquist criteria, root loci, and pole placement: A geometric viewpoint. *IEEE Transactions on Automatic Control*, 26, 271-284, 1981.

61. Postlethwaite, I., Edmunds, J.M. and MacFarlane, A.G.J., Principal gains and principal phases in the analysis of linear multivariable feedback systems. *IEEE Transactions on Automatic Control*, 26, 32-46, 1981.

62. Thompson, D.J. and Jones, C.J.C., Sound radiation from a vibrating railway wheel. *Journal of Sound and Vibration*, 253, 401 - 419, 2002.

63. Hsu, S.S., Huang, Z.Y., Iwnicki, S.D., Thompson, D.J., Jones, C.J.C., Xie, G. and Allen, P.D., Experimental and theoretical investigation of railway wheel squeal. *Proceedings of the Institution of Mechanical Engineers*, 221 Part F, 59-73, 2007.

64. Jones, C.J.C., Thompson, D.J., Rolling noise generated by railway wheels with visco-elastic layers. *Journal of Sound and Vibration*, 231, 779-790, 2000.

65. Ewins, D.J., Modal testing: theory, practice and application. Taylor & Francis Group, 2nd edition 2001.

66. Kootwijk-Damman, C.M., Industrial noise in railway yards; the problem of squeal noise. *Journal of Sound and Vibration*, 193, 451-452, 1996.

67. Carter, F.W., On the action of a locomotive driving wheel. *Proceedings of the Royal Society of London, Series A*, 112, 151-157, 1926.

68. Johnson, K.L., The effect of a tangential contact force upon the rolling motion of an elastic sphere on a plane. *Trans ASME, Journal of Applied Mechanics*, 25, 339-346, 1958.

69. Haines, D.J. and Ollerton, E., Contact stress distribution on elliptical contact surfaces subjected to radial and tangential forces. *Proceedings of the Institution of Mechanical Engineers*, 177, 261-265, 1963.

70. Vermeulen, P.J. and Johnson, K.L., Contact of non-spherical elastic bodies transmitting tangential forces. *Trans. ASME, Journal of Applied Mechanics*, 31, 338-340, 1964.

71. Kalker, J.J., Three-dimensional Elastic Bodies in Rolling Contact. The Netherlands: Dordrecht, Kluwer Academic Publishers, 1990.

72. Johnson, K.L., The effect of spin upon the rolling motion of an elastic sphere on a plane, *Trans ASME, Journal of Applied Mechanics*, 25, 332-338, 1958.

73. Kalker, J.J., On the rolling contact of two elastic bodies in the presence of dry friction. PhD. Thesis, the Netherlands, Delft University, 1967.

74. Jin, X. and Liu, Q., Tribology of wheel and rail (in Chinese). Chinese Railway Press, 2004.

75. Brewe, D.E. and Hamrock, B.J., Simplified solution for elliptical-contact deformation between two elastic solids. *ASME, Journal of Lubrication Technology*, 99, 485-487, 1977.

76. Greenwood, J.A., Formulas for moderately elliptical Hertzian contacts. *ASME Journal of Tribology*, 107, 501-504, 1985.

77. Technical handbook (rail products), Corus, 2005.

78. Dahlberg, T., Vertical dynamic train/track interaction – verifying a theoretical model by full-scale experiments. *Vehicle System Dynamics*, Supplement 24, 45-57, 1995.

79. Timoshenko, S. and Goodier, J.N., Theory of Elasticity. 2nd Ed. McGraw-Hill, New York, 377-379, 1951.

80. Orfanidis, S.J., Introduction to Signal Processing. Prentice Hall, 1996.